

INFORMATION TO USERS

This manuscript has been reproduced from the microfilm master. UMI films the text directly from the original or copy submitted. Thus, some thesis and dissertation copies are in typewriter face, while others may be from any type of computer printer.

The quality of this reproduction is dependent upon the quality of the copy submitted. Broken or indistinct print, colored or poor quality illustrations and photographs, print bleedthrough, substandard margins, and improper alignment can adversely affect reproduction.

In the unlikely event that the author did not send UMI a complete manuscript and there are missing pages, these will be noted. Also, if unauthorized copyright material had to be removed, a note will indicate the deletion.

Oversize materials (e.g., maps, drawings, charts) are reproduced by sectioning the original, beginning at the upper left-hand corner and continuing from left to right in equal sections with small overlaps. Each original is also photographed in one exposure and is included in reduced form at the back of the book.

Photographs included in the original manuscript have been reproduced xerographically in this copy. Higher quality 6" x 9" black and white photographic prints are available for any photographs or illustrations appearing in this copy for an additional charge. Contact UMI directly to order.

UMI

A Bell & Howell Information Company
300 North Zeeb Road, Ann Arbor MI 48106-1346 USA
313/761-4700 800/521-0600

**HYDRODYNAMIC LOADS ON OFFSHORE STRUCTURES IN
BICHROMATIC BIDIRECTIONAL SEAS**

A Dissertation

Presented to

the Faculty of the Department of Civil and Environmental Engineering

University of Houston

In Partial Fulfillment

of the Requirements for the Degree

Doctor of Philosophy

by

Jose H. Vazquez

August 1995


UMI Number: 9619121

UMI Microform 9619121
Copyright 1996, by UMI Company. All rights reserved.

**This microform edition is protected against unauthorized
copying under Title 17, United States Code.**


UMI
300 North Zeeb Road
Ann Arbor, MI 48103

HYDRODYNAMIC LOADS ON OFFSHORE STRUCTURES IN BICHROMATIC BIDIRECTIONAL SEAS



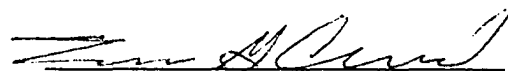
Jose H. Vazquez

Approved:

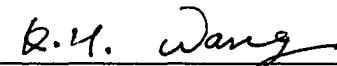


Chairman of the Committee
A.N. Williams, Professor,
Civil Engineering


Committee Members:




T.G. Cleveland, Assistant Professor,
Civil Engineering




K.H. Wang, Assistant Professor,
Civil Engineering




C. Dalton, Professor,
Mechanical Engineering



S.J. Kleis, Associate Professor,
Mechanical Engineering



C. Dalton, Associate Dean,
Cullen College of Engineering



S.T. Mau, Professor and Chairman,
Civil and Environmental Engineering

This dissertation is dedicated to my family

My parents: Layo and Lupina

My brother: Cesar

My sister and her family: Mary, Pablo, Dayan, Marisol and Marlene.

and to all the people who directly or indirectly encouraged me to do it.

ACKNOWLEDGEMENT

I would like to express my appreciation to Dr. A. N. Williams, my graduate advisor, for his suggestions and indispensable guidance during the course of this study. Thanks are also due to Dr. C. Dalton, Dr. S. J. Kleis, Dr. T. G. Cleveland, and Dr. K. H. Wang for serving on my dissertation committee.

I would also like to thank my fellow members of the Computational Hydrodynamics Laboratory for their insights and discussions. Special thanks are in order to Dr. Chang for his patience and support. Finally, I would like to express my sincere gratitude to my brother for his support and understanding during the course of this study.

**HYDRODYNAMIC LOADS ON OFFSHORE STRUCTURES IN
BICHROMATIC BIDIRECTIONAL SEAS**

An Abstract of A Dissertation

Presented to

the Faculty of the Department of Civil and Environmental Engineering

University of Houston

In Partial Fulfillment

of the Requirements for the Degree

Doctor of Philosophy

by

Jose H. Vazquez

August 1995

ABSTRACT

A complete second-order solution is given for the hydrodynamic loads on ocean structures in bichromatic, bidirectional waves. The solution to the first-order problem is obtained utilizing a Green's function approach using higher order boundary elements. The second-order hydrodynamic loads explicitly due to the second-order potential components are computed using the indirect, assisting radiation potential approach. An efficient numerical technique, that accounts for the directionality of the waves, is presented to treat the free-surface integral which appears in the second-order load formulation. Numerical results are presented which illustrate the sensitivity to wave directionality of the second-order sum- and difference-frequency hydrodynamic loads on example structures. In particular, arrays of bottom-mounted, surface piercing cylinders and tension-leg platforms are considered. It is found that wave directionality may have a significant influence on the second-order hydrodynamic loads on these structures at both sum- and difference-frequencies and that the assumption of unidirectional waves does not always lead to conservative estimates of the second-order loading.

TABLE OF CONTENTS

Dedication	iii
Acknowledgment	iv
Abstract	v
Table of Contents	vii
List of Figures	x
List of Tables	xvii
1. INTRODUCTION	1
2. LITERATURE REVIEW	7
3. HYDRODYNAMIC LOADS ON DEEPWATER STRUCTURES IN BICHROMATIC BIDIRECTIONAL WAVES	11
3.1 First-Order Potential	13
3.1.1 Boundary-Value Problem for First-Order Potential	13
3.1.2 Decomposition of First-Order Potential	14
3.1.3 Solution of the BVP Using Source Distribution Method	16
3.2 Second-Order Potential	19
3.2.1 Boundary-Value Problem for Second-Order Potential	19
3.2.2 Decomposition of the Second-Order Potential	20
3.3 Linear Equation of Motion for Rigid Structures	23
3.3.1 Exciting Loads	23
3.3.2 Added Mass and Damping	24
3.3.3 Mass and Stiffness Matrices	25
3.4 First- and Second-Order Hydrodynamic Loads	29
3.4.1 Derivation	29
3.4.2 Second-Order Loads due to Second-Order Potential	31
3.4.3 Transfer Functions	33
3.5 Asymptotic Forms of the First-Order Potentials	34

3.6	The Free-Surface Integral	35
3.6.1	Numerical Integration on S_{F1}	36
3.6.2	Analytical Integration on S_{F2}	39
3.7	The Double Gradient Body Integral	44
4.	IMPLEMENTING NUMERICAL COMPUTATION OF SECOND- ORDER SUM-AND DIFFERENCE-FREQUENCY LOADS ON ISSC TLP IN BICHROMATIC BIDIRECTIONAL WAVES	45
4.1	Convergence of First-Order Potentials	45
4.2	Sum- and Difference-frequency Loads on ISSC TLP	51
5.	ARRAYS OF BOTTOM-MOUNTED, SURFACE- PIERCING CYLINDERS IN BICHROMATIC BIDIRECTIONAL WAVES	108
5.1	First-Order Scattered Potential Solution	110
5.2	Radiated Potential Solution	114
5.3	Approximation of Hydrodynamic Loads on Deep Draft Floating Structures	119
5.4	Second-Order Hydrodynamic Loads	121
6.	IMPLEMENTING NUMERICAL COMPUTATION OF SECOND- ORDER SUM-FREQUENCY LOADS ON A FOUR-CYLINDER STRUCTURE	123
6.1	Convergence of Linear Solutions	123
6.2	Element Convergence on S_{F11}	135
6.3	Convergence of Free-Surface Integral	139
6.4	Numerical Results and Discussion	143
7.	SUMMARY AND CONCLUSIONS	162
	REFERENCES	164
	APPENDIX A: QUADRATIC SHAPE FUNCTIONS FOR SURFACE AND LINE ELEMENTS	168

APPENDIX B: REDUCTION OF $O(1/R)$ SINGULARITY BY POLAR COORDINATE TRANSFORMATION	177
APPENDIX C: GEOMETRICAL SYMMETRY	181
APPENDIX D: STIFFNESS MATRIX FOR TETHERED STRUCTURE	191
APPENDIX E: FRESNEL INTEGRALS	195

LIST OF FIGURES

Fig. 3.1 Definition Sketch.	12
Fig. 4.1 Distribution of points to check convergence of velocity potentials. There are three sets of points corresponding to $\theta = 45^\circ$, 135° , 225° , and 315° , at three different levels: $z = 0$, $z = -b/2$, and $z = -b$.	47
Fig. 4.2 Element distribution on one eighth-model of circular cylinder of radius $a = 10$ m. and draft $b = 30$ m.	48
Fig. 4.3 Different mesh discretizations of one-eighth model for the ISSC TLP.	53
Fig. 4.4a Variation of scattered potential amplitude around the water line of column 1 with TLP discretization.	54
Fig. 4.4b Variation of surge radiated potential amplitude around the water line of column 1 with TLP discretization.	55
Fig. 4.4c Variation of heave radiated potential amplitude around the water line of column 1 with TLP discretization.	56
Fig. 4.4d Variation of pitch radiated potential amplitude around the water line of column 1 with TLP discretization.	57
Fig. 4.5 Exciting load amplitudes on the ISSC TLP in dimensional (SI) units for (a) $\beta = 0^\circ$ and (b) $\beta = 45^\circ$.	59
Fig. 4.6 (a) Added mass and (b) radiation damping on ISSC TLP in dimensional (SI) units.	60
Fig. 4.7 Sum-frequency hydrodynamic surge force QTF, $H^+(\omega_j, \omega_k; \beta_j, \beta_k)$, for the ISSC TLP with $\beta_j = 0^\circ$, $\beta_k = 45^\circ$. Notation: (a) Fixed TLP, (b) Tethered TLP.	64
Fig. 4.8 Sum-frequency hydrodynamic surge force QTF, $H^+(\omega_j, \omega_k; \beta_j, \beta_k)$, for the ISSC TLP with $\beta_j = 45^\circ$, $\beta_k = 0^\circ$. Notation: (a) Fixed TLP, (b) Tethered TLP.	65
Fig. 4.9 Sum-frequency hydrodynamic surge force QTF, $H^+(\omega_j, \omega_k; \beta_j, \beta_k)$, for the ISSC TLP with $\beta_j = \beta_k = 22.5^\circ$. Notation: (a) Fixed TLP, (b) Tethered TLP.	66

Fig. 4.10 Sum-frequency hydrodynamic sway force QTF, $H^+(\omega_j, \omega_k; \beta_j, \beta_k)$, for the ISSC TLP with $\beta_j = 0^\circ$, $\beta_k = 45^\circ$. Notation: (a) Fixed TLP, (b) Tethered TLP.	68
Fig. 4.11 Sum-frequency hydrodynamic sway force QTF, $H^+(\omega_j, \omega_k; \beta_j, \beta_k)$, for the ISSC TLP with $\beta_j = 45^\circ$, $\beta_k = 0^\circ$. Notation: (a) Fixed TLP, (b) Tethered TLP.	69
Fig. 4.12 Sum-frequency hydrodynamic sway force QTF, $H^+(\omega_j, \omega_k; \beta_j, \beta_k)$, for the ISSC TLP with $\beta_j = \beta_k = 22.5^\circ$. Notation: (a) Fixed TLP, (b) Tethered TLP.	70
Fig. 4.13 Sum-frequency hydrodynamic heave force QTF, $H^+(\omega_j, \omega_k; \beta_j, \beta_k)$, for the ISSC TLP with $\beta_j = 0^\circ$, $\beta_k = 45^\circ$. Notation: (a) Fixed TLP, (b) Tethered TLP.	72
Fig. 4.14 Sum-frequency hydrodynamic heave force QTF, $H^+(\omega_j, \omega_k; \beta_j, \beta_k)$, for the ISSC TLP with $\beta_j = 45^\circ$, $\beta_k = 0^\circ$. Notation: (a) Fixed TLP, (b) Tethered TLP.	73
Fig. 4.15 Sum-frequency hydrodynamic heave force QTF, $H^+(\omega_j, \omega_k; \beta_j, \beta_k)$, for the ISSC TLP with $\beta_j = \beta_k = 22.5^\circ$. Notation: (a) Fixed TLP, (b) Tethered TLP.	74
Fig. 4.16 Sum-frequency hydrodynamic roll moment QTF, $H^+(\omega_j, \omega_k; \beta_j, \beta_k)$, for the ISSC TLP with $\beta_j = 0^\circ$, $\beta_k = 45^\circ$. Notation: (a) Fixed TLP, (b) Tethered TLP.	76
Fig. 4.17 Sum-frequency hydrodynamic roll moment QTF, $H^+(\omega_j, \omega_k; \beta_j, \beta_k)$, for the ISSC TLP with $\beta_j = 45^\circ$, $\beta_k = 0^\circ$. Notation: (a) Fixed TLP, (b) Tethered TLP.	77
Fig. 4.18 Sum-frequency hydrodynamic roll moment QTF, $H^+(\omega_j, \omega_k; \beta_j, \beta_k)$, for the ISSC TLP with $\beta_j = \beta_k = 22.5^\circ$. Notation: (a) Fixed TLP, (b) Tethered TLP.	78
Fig. 4.19 Sum-frequency hydrodynamic pitch moment QTF, $H^+(\omega_j, \omega_k; \beta_j, \beta_k)$, for the ISSC TLP with $\beta_j = 0^\circ$, $\beta_k = 45^\circ$. Notation: (a) Fixed TLP, (b) Tethered TLP.	79
Fig. 4.20 Sum-frequency hydrodynamic pitch moment QTF, $H^+(\omega_j, \omega_k; \beta_j, \beta_k)$, for the ISSC TLP with $\beta_j = 45^\circ$, $\beta_k = 0^\circ$. Notation: (a) Fixed TLP, (b) Tethered TLP.	80
Fig. 4.21 Sum-frequency hydrodynamic pitch moment QTF, $H^+(\omega_j, \omega_k; \beta_j, \beta_k)$, for the ISSC TLP with $\beta_j = \beta_k = 22.5^\circ$. Notation: (a) Fixed TLP, (b) Tethered TLP.	81
Fig. 4.22 Sum-frequency hydrodynamic yaw moment QTF, $H^+(\omega_j, \omega_k; \beta_j, \beta_k)$, for the ISSC TLP with $\beta_j = 0^\circ$, $\beta_k = 45^\circ$. Notation: (a) Fixed TLP, (b) Tethered TLP.	82

Fig. 4.23 Sum-frequency hydrodynamic yaw moment QTF, $H^+(\omega_j, \omega_k; \beta_j, \beta_k)$, for the ISSC TLP with $\beta_j = 45^\circ$, $\beta_k = 0^\circ$. Notation: (a) Fixed TLP, (b) Tethered TLP.	83
Fig. 4.24 Sum-frequency hydrodynamic yaw moment QTF, $H^+(\omega_j, \omega_k; \beta_j, \beta_k)$, for the ISSC TLP with $\beta_j = \beta_k = 22.5^\circ$. Notation: (a) Fixed TLP, (b) Tethered TLP.	84
Fig. 4.25 Difference-frequency hydrodynamic surge force QTF, $H^-(\omega_j, \omega_k; \beta_j, \beta_k)$, for the ISSC TLP with $\beta_j = 0^\circ$, $\beta_k = 45^\circ$. Notation: (a) Fixed TLP, (b) Tethered TLP.	87
Fig. 4.26 Difference-frequency hydrodynamic surge force QTF, $H^-(\omega_j, \omega_k; \beta_j, \beta_k)$, for the ISSC TLP with $\beta_j = 45^\circ$, $\beta_k = 0^\circ$. Notation: (a) Fixed TLP, (b) Tethered TLP.	88
Fig. 4.27 Difference-frequency hydrodynamic surge force QTF, $H^-(\omega_j, \omega_k; \beta_j, \beta_k)$, for the ISSC TLP with $\beta_j = \beta_k = 22.5^\circ$. Notation: (a) Fixed TLP, (b) Tethered TLP.	89
Fig. 4.28 Difference-frequency hydrodynamic sway force QTF, $H^-(\omega_j, \omega_k; \beta_j, \beta_k)$, for the ISSC TLP with $\beta_j = 0^\circ$, $\beta_k = 45^\circ$. Notation: (a) Fixed TLP, (b) Tethered TLP.	90
Fig. 4.29 Difference-frequency hydrodynamic sway force QTF, $H^-(\omega_j, \omega_k; \beta_j, \beta_k)$, for the ISSC TLP with $\beta_j = 45^\circ$, $\beta_k = 0^\circ$. Notation: (a) Fixed TLP, (b) Tethered TLP.	91
Fig. 4.30 Difference-frequency hydrodynamic sway force QTF, $H^-(\omega_j, \omega_k; \beta_j, \beta_k)$, for the ISSC TLP with $\beta_j = \beta_k = 22.5^\circ$. Notation: (a) Fixed TLP, (b) Tethered TLP.	92
Fig. 4.31 Difference-frequency hydrodynamic heave force QTF, $H^-(\omega_j, \omega_k; \beta_j, \beta_k)$, for the ISSC TLP with $\beta_j = 0^\circ$, $\beta_k = 45^\circ$. Notation: (a) Fixed TLP, (b) Tethered TLP.	93

Fig. 4.32 Difference-frequency hydrodynamic heave force QTF, $H^*(\omega_j, \omega_k; \beta_j, \beta_k)$, for the ISSC TLP with $\beta_j = 45^\circ$, $\beta_k = 0^\circ$. Notation: (a) Fixed TLP, (b) Tethered TLP.	94
Fig. 4.33 Difference-frequency hydrodynamic heave force QTF, $H^*(\omega_j, \omega_k; \beta_j, \beta_k)$, for the ISSC TLP with $\beta_j = \beta_k = 22.5^\circ$. Notation: (a) Fixed TLP, (b) Tethered TLP.	95
Fig. 4.34 Difference-frequency hydrodynamic roll moment QTF, $H^*(\omega_j, \omega_k; \beta_j, \beta_k)$, for the ISSC TLP with $\beta_j = 0^\circ$, $\beta_k = 45^\circ$. Notation: (a) Fixed TLP, (b) Tethered TLP.	96
Fig. 4.35 Difference-frequency hydrodynamic roll moment QTF, $H^*(\omega_j, \omega_k; \beta_j, \beta_k)$, for the ISSC TLP with $\beta_j = 45^\circ$, $\beta_k = 0^\circ$. Notation: (a) Fixed TLP, (b) Tethered TLP.	97
Fig. 4.36 Difference-frequency hydrodynamic roll moment QTF, $H^*(\omega_j, \omega_k; \beta_j, \beta_k)$, for the ISSC TLP with $\beta_j = \beta_k = 22.5^\circ$. Notation: (a) Fixed TLP, (b) Tethered TLP.	98
Fig. 4.37 Difference-frequency hydrodynamic pitch moment QTF, $H^*(\omega_j, \omega_k; \beta_j, \beta_k)$, for the ISSC TLP with $\beta_j = 0^\circ$, $\beta_k = 45^\circ$. Notation: (a) Fixed TLP, (b) Tethered TLP.	99
Fig. 4.38 Difference-frequency hydrodynamic pitch moment QTF, $H^*(\omega_j, \omega_k; \beta_j, \beta_k)$, for the ISSC TLP with $\beta_j = 45^\circ$, $\beta_k = 0^\circ$. Notation: (a) Fixed TLP, (b) Tethered TLP.	100
Fig. 4.39 Difference-frequency hydrodynamic pitch moment QTF, $H^*(\omega_j, \omega_k; \beta_j, \beta_k)$, for the ISSC TLP with $\beta_j = \beta_k = 22.5^\circ$. Notation: (a) Fixed TLP, (b) Tethered TLP.	101
Fig. 4.40 Difference-frequency hydrodynamic yaw moment QTF, $H^*(\omega_j, \omega_k; \beta_j, \beta_k)$, for the ISSC TLP with $\beta_j = 0^\circ$, $\beta_k = 45^\circ$. Notation: (a) Fixed TLP, (b) Tethered TLP.	102

Fig. 4.41 Difference-frequency hydrodynamic yaw moment $QTF, H^-(\omega_j, \omega_k; \beta_j, \beta_k)$, for the ISSC TLP with $\beta_j = 45^\circ, \beta_k = 0^\circ$. Notation: (a) Fixed TLP, (b) Tethered TLP.	103
Fig. 4.42 Difference-frequency hydrodynamic yaw moment $QTF, H^-(\omega_j, \omega_k; \beta_j, \beta_k)$, for the ISSC TLP with $\beta_j = \beta_k = 22.5^\circ$. Notation: (a) Fixed TLP, (b) Tethered TLP.	104
Fig. 5.1 Definition sketch.	109
Fig. 6.1 Four cylinder array as an approximation to a four column, deep draft TLP.	125
Fig. 6.2a Variation of scattered potential on cylinder 1 with body discretization for $\beta = 22.5^\circ$. Notation: four elements per cylinder, --- 16 elements per cylinder, and —— 64 elements per cylinder.	126
Fig. 6.2b Variation of scattered potential on cylinder 2 with body discretization for $\beta = 22.5^\circ$. Notation: four elements per cylinder, --- 16 elements per cylinder, and —— 64 elements per cylinder.	157
Fig. 6.2c Variation of scattered potential on cylinder 3 with body discretization for $\beta = 22.5^\circ$. Notation: four elements per cylinder, --- 16 elements per cylinder, and —— 64 elements per cylinder.	128
Fig. 6.2d Variation of scattered potential on cylinder 4 with body discretization for $\beta = 22.5^\circ$. Notation: four elements per cylinder, --- 16 elements per cylinder, and —— 64 elements per cylinder.	129
Fig. 6.3a Variation of surge radiated potential on cylinder 1 with body discretization. Notation: four elements per cylinder, --- 16 elements per cylinder, and —— 64 elements per cylinder.	131
Fig. 6.3b Variation of pitch radiated potential on cylinder 1 with body discretization. Notation: four elements per cylinder, --- 16 elements per cylinder, and —— 64 elements per cylinder.	132

Fig. 6.3c Variation of yaw radiated potential on cylinder 1 with body discretization. Notation: $\cdots\cdots$ four elements per cylinder, $---$ 16 elements per cylinder, and $---$ 64 elements per cylinder.	133
Fig. 6.4 Variation of the real part of surge/pitch potential on cylinder 1 with different number of evanescent modes \bar{Q} . Notation: $---$ $\bar{Q}=0$, $\cdots\cdots$ $\bar{Q}=2$, $---$ $\bar{Q}=5$, and $---$ $\bar{Q}=20$.	134
Fig. 6.5a One-eighth interior free-surface mesh for four-cylinder array. Mesh 1: 354 nodes, 608 linear elements.	136
Fig. 6.5b One-eighth interior free-surface mesh for four-cylinder array. Mesh 2: 766 nodes, 1382 linear elements.	137
Fig. 6.5c One-eighth interior free-surface mesh for four-cylinder array. Mesh 3: 1396 nodes, 2592 linear elements.	138
Fig. 6.5d One-eighth interior free-surface mesh for four-cylinder array. Mesh 4: 2043 nodes, 3828 linear elements.	139
Fig. 6.6 Variation of the amplitude of the free-surface contribution to the sum-frequency moment QTF, $ I_F^+ $, with partition distance, R/a , for the four cylinder structure at $v_j = 1.4$, $v_k = 1.2$.	142
Fig. 6.7 Hydrodynamic sum-frequency surge force QTF, $H^+(\omega_j, \omega_k; \beta_j, \beta_k)$, for four-cylinder structure with $\beta_j = 0^\circ$, $\beta_k = 45^\circ$.	145
Fig. 6.8 Hydrodynamic sum-frequency surge force QTF, $H^+(\omega_j, \omega_k; \beta_j, \beta_k)$, for four-cylinder structure with $\beta_j = 45^\circ$, $\beta_k = 0$.	146
Fig. 6.9 Hydrodynamic sum-frequency surge force QTF, $H^+(\omega_j, \omega_k; \beta_j, \beta_k)$, for four-cylinder structure with $\beta_j = \beta_k = 22.5^\circ$.	147
Fig. 6.10 Hydrodynamic sum-frequency sway force QTF, $H^+(\omega_j, \omega_k; \beta_j, \beta_k)$, for four-cylinder structure with $\beta_j = 0^\circ$, $\beta_k = 45^\circ$.	149
Fig. 6.11 Hydrodynamic sum-frequency sway force QTF, $H^+(\omega_j, \omega_k; \beta_j, \beta_k)$, for four-cylinder structure with $\beta_j = 45^\circ$, $\beta_k = 0$.	150

Fig. 6.12 Hydrodynamic sum-frequency sway force $QTF, H^+(\omega_j, \omega_k; \beta_j, \beta_k)$, for four-cylinder structure with $\beta_j = \beta_k = 22.5^\circ$.	151
Fig. 6.13 Hydrodynamic sum-frequency roll moment $QTF, H^+(\omega_j, \omega_k; \beta_j, \beta_k)$, for four-cylinder structure with $\beta_j = 0^\circ, \beta_k = 45^\circ$.	152
Fig. 6.14 Hydrodynamic sum-frequency roll moment $QTF, H^+(\omega_j, \omega_k; \beta_j, \beta_k)$, for four-cylinder structure with $\beta_j = 45^\circ, \beta_k = 0$.	153
Fig. 6.15 Hydrodynamic sum-frequency roll moment $QTF, H^+(\omega_j, \omega_k; \beta_j, \beta_k)$, for four-cylinder structure with $\beta_j = \beta_k = 22.5^\circ$.	154
Fig. 6.16 Hydrodynamic sum-frequency pitch moment $QTF, H^+(\omega_j, \omega_k; \beta_j, \beta_k)$, for four-cylinder structure with $\beta_j = 0^\circ, \beta_k = 45^\circ$.	155
Fig. 6.17 Hydrodynamic sum-frequency pitch moment $QTF, H^+(\omega_j, \omega_k; \beta_j, \beta_k)$, for four-cylinder structure with $\beta_j = 45^\circ, \beta_k = 0$.	156
Fig. 6.18 Hydrodynamic sum-frequency pitch moment $QTF, H^+(\omega_j, \omega_k; \beta_j, \beta_k)$, for four-cylinder structure with $\beta_j = \beta_k = 22.5^\circ$.	157
Fig. 6.19 Hydrodynamic sum-frequency yaw moment $QTF, H^+(\omega_j, \omega_k; \beta_j, \beta_k)$, for four-cylinder structure with $\beta_j = 0^\circ, \beta_k = 45^\circ$.	159
Fig. 6.20 Hydrodynamic sum-frequency yaw moment $QTF, H^+(\omega_j, \omega_k; \beta_j, \beta_k)$, for four-cylinder structure with $\beta_j = 45^\circ, \beta_k = 0$.	160
Fig. 6.21 Hydrodynamic sum-frequency yaw moment $QTF, H^+(\omega_j, \omega_k; \beta_j, \beta_k)$, for four-cylinder structure with $\beta_j = \beta_k = 22.5^\circ$.	161
Fig. A.1 Quadratic quadrilateral and triangular elements.	171
Fig. A.2 Natural triangular coordinates.	173
Fig. B.1 Triangular polar coordinate transformation.	178
Fig. B.2 Distribution of the integration points for 2x2 and 4x4 Gauss quadrature.	180
Fig. C.1 Planes of symmetry.	182

LIST OF TABLES

<p>Table 4.1a Convergence of complex surge radiated potential and scattered potential at different points on a circular cylinder with radius $a = 10$ m., and draft $b = 30$ m. for $\omega = 1.0$ rad/sec and $\beta = 30^\circ$ with element/node distribution and number of Gauss points used for the integration. Also shown are relative cpu times required.</p>	49
<p>Table 4.1b Convergence of complex surge radiated potential and scattered potential at different points on a circular cylinder with radius $a = 10$ m., and draft $b = 30$ m. for $\omega = 1.0$ rad/sec and $\beta = 30^\circ$ with element/node distribution and number of Gauss points used for the integration. Also shown are relative cpu times required.</p>	50
<p>Table 4.2 Geometric dimensions and structural properties of the ISSC TLP (Eatock Taylor and Jeffreys, 1986).</p>	52
<p>Table 4.3 Ratio of the maximum second-order sum-frequency vertical force QTF with different angles of wave incidence, $H^+(\omega_j, \omega_k; \beta_j, \beta_k)$, to those resulting from unidirectional waves, $H^+(\omega_q, \omega_q; \beta_q, \beta_q)$. The upper right triangular matrix contains the QTF ratios for a tethered ISSC TLP, the lower left triangle contains the QTF ratios for a fixed ISSC TLP. In row 1, $\beta_j = 0^\circ$, $\beta_k = 45^\circ$, and $\beta_q = 0^\circ$; in row 2, $\beta_j = 45^\circ$, $\beta_k = 0^\circ$, and $\beta_q = 0^\circ$; in row 3, $\beta_j = 0^\circ$, $\beta_k = 45^\circ$, and $\beta_q = 45^\circ$, in row 4, $\beta_j = 45^\circ$, $\beta_k = 0^\circ$, and $\beta_q = 45^\circ$.</p>	105

<p>Table 4.4 Ratio of the maximum second-order sum-frequency overturning moment QTF with different angles of wave incidence, $H^+(\omega_j, \omega_k; \beta_j, \beta_k)$, to those resulting from unidirectional waves, $H^+(\omega_q, \omega_q; \beta_q, \beta_q)$. The upper right triangular matrix contains the QTF ratios for a tethered ISSC TLP, the lower left triangle contains the QTF ratios for a fixed ISSC TLP. In row 1, $\beta_j = 0^\circ$, $\beta_k = 45^\circ$, and $\beta_q = 0^\circ$; in row 2, $\beta_j = 45^\circ$, $\beta_k = 0^\circ$, and $\beta_q = 0^\circ$; in row 3, $\beta_j = 0^\circ$, $\beta_k = 45^\circ$, and $\beta_q = 45^\circ$; in row 4, $\beta_j = 45^\circ$, $\beta_k = 0^\circ$, and $\beta_q = 45^\circ$.</p>	<p>106</p>
<p>Table 4.5 Ratio of the maximum second-order difference-frequency horizontal force QTF with different angles of wave incidence, $H^-(\omega_j, \omega_k; \beta_j, \beta_k)$, to those resulting from unidirectional waves, $H^-(\omega_q, \omega_q; \beta_q, \beta_q)$. The upper right triangular matrix contains the QTF ratios for a tethered ISSC TLP, the lower left triangle contains the QTF ratios for a fixed ISSC TLP. In row 1, $\beta_j = 0^\circ$, $\beta_k = 45^\circ$, and $\beta_q = 0^\circ$; in row 2, $\beta_j = 45^\circ$, $\beta_k = 0^\circ$, and $\beta_q = 0^\circ$; in row 3, $\beta_j = 0^\circ$, $\beta_k = 45^\circ$, and $\beta_q = 45^\circ$; in row 4, $\beta_j = 45^\circ$, $\beta_k = 0^\circ$, and $\beta_q = 45^\circ$.</p>	<p>107</p>
<p>Table 6.1 Variation of the sum-frequency free-surface integral on the interior region with different mesh discretizations. Hydrodynamic load components are computed at $v_j = 1.4$, $v_k = 1.2$.</p>	<p>141</p>

CHAPTER ONE

INTRODUCTION

As the search for offshore oil and gas reserves moves into deeper waters, a new generation of offshore platforms is being designed to meet the operational challenges of exploration and production in these increased water depths. One concept which has achieved considerable success is the tension-leg platform (TLP) which is a large displacement, multi-column, floating structure anchored to the sea bed by an array of tendons (tethers) kept under tension by the excess buoyancy of the hull. Due to their compliant nature, TLPs are much more sensitive to environmental load effects than conventional fixed, jacket structures and exhibit complex responses to wave loading. In particular, although a TLP system is designed so that the natural frequencies of its vertical plane motions (heave, roll, pitch) are significantly higher than that of most of the ocean wave energy, recent model tests and full-scale measurements of TLPs have indicated high frequency resonant responses. In addition to sudden bursts of highly amplified resonant activity, a modulating resonant response component of moderate amplitude has also been observed. This latter response, termed "springing", may have a significant impact on tendon fatigue life. In the horizontal modes (surge, sway, yaw), TLPs have very long natural periods, and so also exhibit resonant response at low frequencies. Therefore, the low-frequency wave loading is also an important consideration and may provide the design values of the platform set down and offset. In an irregular sea that is assumed to consist of a superposition of linear wave components, these high and low frequency loads are second-order effects arising from products of linear (first-order) terms. For a structure such as a TLP which consists exclusively of large diameter columns and pontoons, the high and low frequency hydrodynamic loading may be predicted on the basis of second-order potential theory.

The present research may be conveniently divided into two parts in accordance with the level of integration required to obtain the solution of the first-order velocity potential. Due to the large computational effort required to obtain the hydrodynamic loads on arbitrarily shaped structures in the ocean, solutions to two special cases are presented in this dissertation, namely:

(1) the computation of sum- and difference-frequency hydrodynamic loads on arbitrarily shaped three-dimensional structures such as TLPs in bichromatic, bidirectional waves. The water depth is assumed infinite. Attention is focused on the effect of wave directionality as well as the effect of body motions on the hydrodynamic loads on the structure.

(2) the computation of the sum- and difference-frequency hydrodynamic loads on arrays of bottom-mounted, surface-piercing cylinders in bichromatic, bidirectional waves in water of uniform finite depth. Particular attention is given to the effect of wave directionality on the second-order hydrodynamic loads experienced by the cylinders. The possibility of using this geometry, which requires considerably less computational effort, to estimate the sum-frequency loads on a deep draft TLP is also investigated.

For both cases, the solution is based on a source distribution approach which yields the first-order velocity potential at any point in the fluid domain as the integral of a Green's function and a source strength over the wetted surface of the structure. For the case of arbitrarily shaped structures, a three-dimensional deep water Green's function which satisfies the first-order free-surface condition, is utilized together with higher-order surface elements on the structure. For structures with constant cross-section extending from the sea bed to the free surface, the constant cross-section is exploited to express the vertical dependency of the solution in terms of eigenfunction expansions, thereby rendering the

problem two-dimensional in the horizontal plane. For these structures, a suitable two-dimensional Green's function is utilized together with higher-order line elements.

These two parts of the research share several common aspects. For instance, the general expression for the second-order hydrodynamic loads at both the sum- and difference-frequency has the same form regardless of the structure being considered. This results in similar treatment of the free-surface integral present in the expressions for the hydrodynamic loads. The accurate computation of the sum- and difference-frequency hydrodynamic loads depends on a robust solution for the first-order potentials. Taking this into account, the following format is used for this dissertation:

Chapter One consists of an introduction and a dissertation outline. In Chapter Two a review of the literature relating to areas (1) and (2) above is covered. Chapter Three starts with the solution to the first-order problem for an arbitrarily shaped structure situated in infinite water depth. Numerical solutions for first-order potentials may be obtained utilizing a boundary integral method using a suitable Green's function. This solution may be achieved in one of two ways. The first method is to apply Green's second identity to both the scattered (radiated) potential and the Green's function, discretize the surface of the structure and describe the variation of both the velocity potential and the normal component of the velocity over each element in terms of corresponding values at the nodes and shape functions. This procedure results in a system of linear equations which may be solved for the unknown velocity potentials at the nodes. Through the application of Green's second identity, now with the velocity potentials on the structure known, the potentials anywhere in the fluid domain may be determined. The second method is to describe the scattered (radiated) potential as the integral over the wetted surface of the structure of a suitable Green's function and a source distribution. The derivative of the scattered (radiated) potential (which is known in terms of the structural boundary condition) in a direction

normal to the structural surface results in an integral equation relating the source strength at a point on the structure to the normal scattered (radiated) velocities. Discretizing the surface of the structure such that the source strength variation over each element is described in terms of the nodal strengths and shape functions results in a set of linear equations which may be solved for the nodal source strengths. Once the nodal source strengths are determined, the velocity potential, and water particle velocities anywhere in the fluid domain may be obtained. One of the advantages of the source distribution method is that it provides for a more accurate computation of the water particle velocities since numerical differentiation of the potentials is avoided. For this reason, this method is employed to compute the first-order velocity potentials in the present work.

The derivation of the second-order hydrodynamic sum- and difference-frequency loads on an arbitrarily shaped structure in deep water subject to bichromatic bidirectional waves is also presented in Chapter Three. The indirect, assisting radiation potential approach is used to determine the second-order hydrodynamic loading due to the second-order potential without the explicit calculation of that potential. The second-order hydrodynamic loads consist of a free-surface integral and body integrals. The integral over the free-surface appearing in the formulation for the second-order hydrodynamic loads due to the second-order potential is divided into two regions, an interior region containing the structure and an exterior region extending to infinity in the horizontal plane. The integral over the interior region is performed numerically and, by utilizing the asymptotic forms of the potentials, the integration over the exterior region is carried out analytically in terms of Fresnel functions.

Chapter Four addresses the numerical convergence of the solution presented in Chapter Three. In particular, the accuracy of the first-order solution is investigated. Also in Chapter Four, numerical examples for the ISSC TLP, which illustrate the effect of wave

directionality as well as the effect of first-order body motions on the second-order sum- and difference-frequency loads are presented. The numerical convergence of the free-surface integral is not discussed in this chapter. Rather, it is addressed in Chapter Six when computing the sum-frequency loads on a structure consisting of four bottom-mounted, surface-piercing cylinders.

Chapter Five initially presents the solution for the first-order diffraction and radiated potentials for an array of bottom-mounted, surface-piercing cylinders of arbitrary cross-section. The constant structural cross-section of the array may be exploited to provide a computationally efficient form for the first-order solution. The vertical dependency of the first-order diffracted potential and the associated linearized radiation potentials may be expressed in terms of eigenfunction expansions and a two-dimensional Green's function approach utilized to obtain the solution at this order. Chapter Five continues with the derivation of the expressions for the sum- and difference-frequency hydrodynamic loads on arrays of bottom mounted cylinders of arbitrary cross-section. As was mentioned above, the form for these loads is very similar to those derived in Chapter Three for an arbitrarily shaped three-dimensional ocean structure. The main difference is that for arrays of bottom mounted cylinders, no body motions are present. Also, since the cylinders are independent of each other, it may be of interest to obtain the hydrodynamic loads on each of the cylinder. This is accomplished by calculating the assisting radiated potential due to the oscillation of an individual cylinder with all others stationary.

The method derived in Chapter Five is applied to obtain the sum-frequency hydrodynamic loads on a four-cylinder structure. This structure is chosen because it may be used to model a deep draft TLP. Chapter Six begins by discussing the numerical convergence of the first-order solution for the four-cylinder structure, as well as the free-surface integral. After this discussion, numerical results for the sum-frequency

hydrodynamic loads are presented. Although the derivation of Chapter Five allows for the computation of the hydrodynamic loads on each of the cylinders, the four cylinders are treated as a rigid structure because they are used to model a deep draft TLP. One of the advantages of using this two dimensional idealization is that it allows for the efficient computation of the hydrodynamic loads on deep draft TLPs over a much higher range of frequencies since it does not require a large number of nodes to describe the structure.

Finally, the conclusions of this research and a discussion of their significance are presented in Chapter Seven. References and appendices follow the text and complete the dissertation.

CHAPTER TWO

LITERATURE REVIEW

The computation of second-order hydrodynamic loads on arbitrarily shaped bodies depends on a robust solution to the linear diffraction problem. Accurate first-order solutions may be obtained using a boundary element approach using a suitable free-surface Green's function whose form is well-known. At the second-order, either a direct approach in which the second-order potential is computed explicitly, or an indirect approach based on the assisting radiation potential technique may be used (Lee *et al.*, 1991; Eatock Taylor and Chau, 1991; Kim, 1991; Zaraphonitis and Papanikolaou, 1993). Most previous work on the effects of wave directionality has been restricted to low-frequency loads (Eatock Taylor *et al.*, 1988; Kim and Yue, 1989; Kim, 1992). It has been found that the assumption of wave unidirectionality is not necessarily conservative as far as low-frequency loading is concerned and that a simple superposition of directional wave components may not yield reliable results. Recently, Vazquez and Williams (1994) investigated the second-order sum- and difference-frequency forces due to bidirectional waves on an array of bottom-mounted, surface-piercing cylinders. The analysis was an extension of the unidirectional waves solution of Moubayed and Williams (1992a) and is based on a two-dimensional boundary element approach in the horizontal plane. The above conclusions regarding the effects of wave directionality on low-frequency forces were also shown to be true for the sum-frequency case.

Although the general form for the computation of the second-order hydrodynamic loads on ocean structures seems relatively straightforward, it should be noted that it is in fact computationally intensive. Newman and Lee (1992) discuss the sensitivity of wave loads to the discretization of bodies. Techniques aimed at improving the efficiency by

which converged first- and second-order results for arbitrary three-dimensional bodies may be obtained have been discussed by Eatock Taylor and Chau (1991). However, even though significant advances have been made in the numerical techniques associated with these approaches, they remain computationally intensive and require considerable amounts of CPU and disk storage. For this reason, several investigators have considered idealized geometries consisting of arrays of vertical, circular cylinders (either bottom-mounted or floating), to approximate floating ocean structures. Chen and Molin (1990) developed an efficient technique to examine the influence of the high-frequency interactions between TLP columns on second-order wave loads where the first-order diffraction solution for the array was obtained by the eigenfunction expansion approach of Linton and Evans (1990). Abul-Azm and Williams (1989a, 1989b) have developed a computationally efficient semi-analytical approximate method to study second-order interference effects in structural arrays and have presented numerical results in regular waves for arrays of bottom-mounted, surface-piercing and semi-immersed, truncated cylinders, respectively. The first-order solution is obtained via the modified plane wave method (McIver and Evans, 1984), and so the technique is essentially a large spacing approximation. Second-order wave loads are obtained utilizing the indirect approach due to Molin (1979). Williams *et al.* (1990) compared the results from this approximate approach with those from an exact second-order solution for an array of surface-piercing cylinders based on a two-dimensional Green's function approach. Very good agreement was found over the parameter range where the large-spacing approximation was valid.

Ghalayini and Williams (1989, 1991) presented an exact second-order solution to predict the hydrodynamic forces to second-order on bottom-mounted, surface-piercing, vertical cylinders of arbitrary cross-section in the presence of regular waves. The constant cross-sections of the array members are used to render the problem two-dimensional. An efficient numerical technique was presented to treat the free-surface integral appearing in the

second-order force formulation. This analysis was extended to deal with a bichromatic, unidirectional incident wave field by Moubayed and Williams (1992b).

Previous work on the effect of wave directionality has been restricted to the study of low-frequency wave loads and associated motions. Kim and Yue (1989) investigated slowly-varying drift forces in short-crested irregular seas. Newman's approximation (Newman, 1974) was used for the second-order force quadratic transfer function (QTF) but the directional spreading was treated exactly. They found that the slowly-varying forces on an axisymmetric body can be greatly amplified when the wave systems are incident from opposing directions. Kim (1992) computed the complete second-order difference-frequency force and moment QTFs for the ISSC TLP. His numerical results indicate that the assumption of wave unidirectionality is not necessarily conservative as far as low-frequency loading is concerned. Also, Kim (1993) obtained the second-harmonic vertical wave loads on arrays of deep-draft cylinders in monochromatic uni- and multi-directional waves. Arrays of circular bottom-mounted surface-piercing cylinders were used in the computation of the second-order potential. The vertical loads were obtained by multiplying the second-order pressure at the desired level on each of the cylinders by the corresponding cross-sectional area. His observations were similar to those found for the difference-frequency load QTFs for the ISSC TLP, namely that the exciting loads on multiple columns are very sensitive to wave headings. The influence of wave directionality and the role of the second-order velocity potential on low-frequency hydrodynamic forces has been discussed by Eatock Taylor *et al.* (1988). Practical engineering approximations to the bi-directional, quadratic second-order surge force transfer function were assessed. In particular, it was shown that a simple superposition of directional wave components may not yield reliable results at second-order. Maeda *et al.* (1986, 1988, 1992) have published a series of papers on the effects of wave directionality on the low-frequency motions of semi-submersible structures, and validated their theoretical approach through laboratory

experiments. In their work the influence of the second-order velocity potential and second-order structural motions were neglected. Nwogu and Isaacson (1991) presented the results of both a theoretical and experimental investigation of the slow drift oscillations of a moored barge in random multi-directional waves. The Newman approximation was used for the second-order force quadratic transfer function and wave directionality was treated by averaging the corresponding unidirectional QTFs.

Therefore, a review of the open literature reveals that, at the current time, there exists no comprehensive solution for the calculation of the sum- and difference-frequency hydrodynamic loads on arbitrary three-dimensional floating structures in bichromatic, bidirectional waves. Furthermore, as suggested by Natvig (1994), a computationally efficient two-dimensional solution for an array of bottom-mounted, surface-piercing vertical cylinders will be analyzed as an approximation to the solution for deep-draft multi-column structures.

CHAPTER THREE

HYDRODYNAMIC LOADS ON DEEPWATER STRUCTURES IN BICHROMATIC BIDIRECTIONAL WAVES

Consider an arbitrarily shaped ocean structure in deep water (Fig. 3.1). The theoretical formulation of the wave-structure interaction problem is based on the assumption of a homogeneous, ideal, incompressible, inviscid fluid. The irrotational motion of the fluid may be described in terms of a velocity potential $\phi(\underline{X},t)$, where $\underline{X} = (x,y,z)$ and t denotes time. The potential $\phi(\underline{X},t)$ and surface elevation $\eta(\underline{X}_{FS},t)$, where $\underline{X}_{FS} = (x,y,0)$, are assumed expressible in a Stokes series, namely,

$$\phi(\underline{X},t) = \varepsilon \phi^{(1)}(\underline{X},t) + \varepsilon^2 \phi^{(2)}(\underline{X},t) + \dots, \quad (3.1a)$$

$$\eta(\underline{X}_{FS},t) = \varepsilon \Gamma^{(1)}(\underline{X}_{FS},t) + \varepsilon^2 \Gamma^{(2)}(\underline{X}_{FS},t) + \dots, \quad (3.1b)$$

where ε is a small parameter of the order of the incident wave steepness.

If it is assumed that the bichromatic incident wave system may be represented by a superposition of two monochromatic waves of amplitudes Γ_j with frequencies ω_j , and incident direction β_j $j = 1, 2$, then the time-dependency in all dynamic quantities may be separated explicitly,

$$\phi^{(1)}(\underline{X};t) \underset{\text{Re}}{=} \sum_{j=1}^2 \Phi_j^{(1)}(\underline{X}) e^{-i\omega_j t}, \quad (3.2a)$$

$$\phi^{(2)}(\underline{X};t) \underset{\text{Re}}{=} \sum_{j=1}^2 \sum_{k=1}^2 \left\{ \Phi_{jk}^+(\underline{X}) e^{-i(\omega_j + \omega_k)t} + \Phi_{jk}^-(\underline{X}) e^{-i(\omega_j - \omega_k)t} \right\} + \delta^{(2)}t, \quad (3.2b)$$

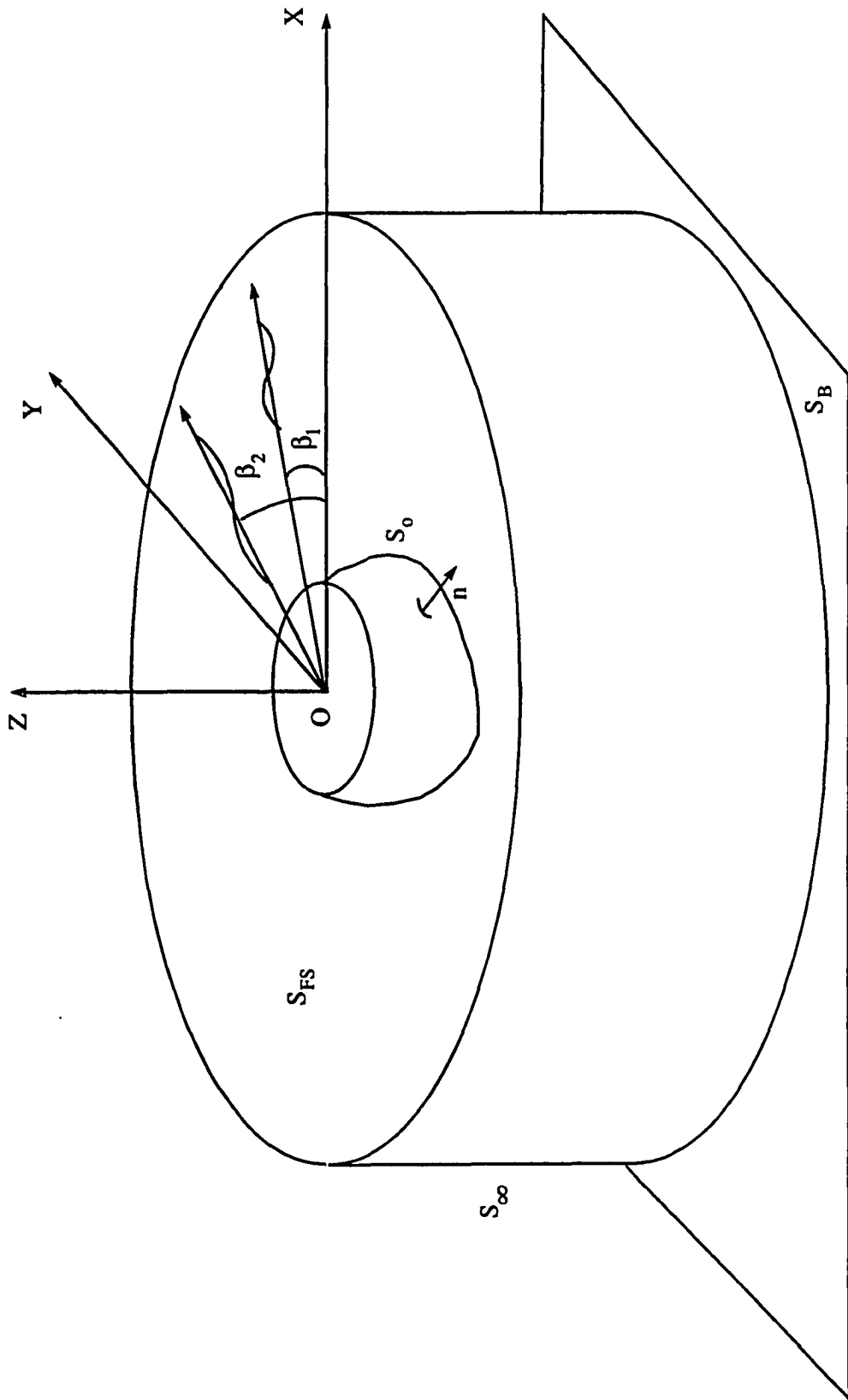


Fig 3.1 Definition sketch.

$$\eta^{(1)}(\underline{X}_{FS};t) = \sum_{\text{Re}} \sum_{j=1}^2 \Gamma_j^{(1)}(\underline{X}_{FS}) e^{-i\omega_j t}, \quad (3.3a)$$

$$\eta^{(2)}(\underline{X}_{FS};t) = \sum_{\text{Re}} \sum_{j=1}^2 \sum_{k=1}^2 \left\{ \Gamma_{jk}^+(\underline{X}_{FS}) e^{-i(\omega_j + \omega_k)t} + \Gamma_{jk}^-(\underline{X}_{FS}) e^{-i(\omega_j - \omega_k)t} \right\}, \quad (3.3b)$$

$$\underline{\Delta}^{(1)}(t) = \sum_{\text{Re}} \sum_{j=1}^2 \underline{\xi}_j^{(1)} e^{-i\omega_j t}, \quad (3.4a)$$

$$\underline{\Delta}^{(2)}(t) = \sum_{\text{Re}} \sum_{j=1}^2 \sum_{k=1}^2 \left\{ \underline{\xi}_{jk}^+ e^{-i(\omega_j + \omega_k)t} + \underline{\xi}_{jk}^- e^{-i(\omega_j - \omega_k)t} \right\}, \quad (3.4b)$$

$$\underline{\Omega}^{(1)}(t) = \sum_{\text{Re}} \sum_{j=1}^2 \underline{\alpha}_j^{(1)} e^{-i\omega_j t}, \quad (3.5a)$$

$$\underline{\Omega}^{(2)}(t) = \sum_{\text{Re}} \sum_{j=1}^2 \sum_{k=1}^2 \left\{ \underline{\alpha}_{jk}^+ e^{-i(\omega_j + \omega_k)t} + \underline{\alpha}_{jk}^- e^{-i(\omega_j - \omega_k)t} \right\}, \quad (3.5b)$$

where $\delta^{(2)}$ is a constant (Stoker, 1957).

3.1 First-Order Potential

3.1.1 Boundary-Value Problem for First-Order Potential

The boundary-value problem for the first-order potential is given by

$$\nabla^2 \phi^{(1)} = 0 \quad \text{in the fluid domain, } V, \quad (3.6)$$

$$\frac{\partial^2 \phi^{(1)}}{\partial t^2} + g \frac{\partial \phi^{(1)}}{\partial z} = 0 \quad \text{on the mean free surface, } S_F, \quad (3.7)$$

$$\frac{\partial \phi^{(1)}}{\partial n} = \underline{V}^{(1)} \cdot \underline{n} \quad \text{on the equilibrium structural surface, } S_o, \quad (3.8)$$

$$\frac{\partial \phi^{(1)}}{\partial z} = 0 \quad \text{as } z \rightarrow -\infty, \quad (3.9)$$

$$\text{where } \underline{V}^{(1)} = \frac{\partial}{\partial t} \{ \underline{\Delta}^{(1)} + \underline{\Omega}^{(1)} \times [\underline{r} - \underline{r}_G] \}, \quad (3.10)$$

g is the acceleration due to gravity, $\underline{n} = (n_1, n_2, n_3)$ is the unit normal away from the structure in its equilibrium position, $\underline{\Delta}^{(1)}$ and $\underline{\Omega}^{(1)}$ are the first-order translation and rotational motions of the structure, respectively, \underline{r}_G is the location of the center of gravity of the structure at equilibrium, and \underline{r} is the position vector of any point on the body surface.

3.1.2 Decomposition of First-Order Potential

The total first-order potential may be decomposed into incident, scattered, and radiated wave terms. Therefore, the total first-order potential is

$$\phi^{(1)} = \phi_I^{(1)} + \phi_S^{(1)} + \phi_R^{(1)}. \quad (3.11)$$

The scattered component results from the interaction of the incident wave field with a stationary body, while the radiated components arise from the prescribed harmonic oscillation of the structure in an otherwise quiescent fluid. The radiated wave potential may be further decomposed into components explicitly associated with the various translational and rotational modes of oscillation, that is,

$$\phi_R^{(1)} = \sum_{p=1}^6 \phi_{Rp}^{(1)}. \quad (3.12)$$

The radiation potential components in Eq. (3.12) may be further decomposed into

$$\Phi_{Rp}^{(1)} = \text{Re} \sum_{j=1}^2 \xi_{jp}^{(1)} \Psi_{jp}^{(1)} e^{-i\omega_j t} \quad (3.13a)$$

and

$$\Phi_{Rp+3}^{(1)} = \text{Re} \sum_{j=1}^2 \alpha_{jp}^{(1)} \Psi_{jp+3}^{(1)} e^{-i\omega_j t} \quad (3.13b)$$

for $p = 1, 2, 3$ and so the complex radiation potential amplitudes $\Psi_{jp}^{(1)}$ $p = 1, 2, \dots, 6; j = 1, 2$, are associated with unit amplitude motions of the structure at frequency ω_j in the p th mode of oscillation.

In addition, the scattered and radiated waves must satisfy a radiation condition at large distances from the body. This is best expressed in terms of the individual potential component amplitudes as

$$\lim_{\gamma \rightarrow \infty} \sqrt{\gamma} \left\{ \frac{\partial}{\partial \gamma} - ik_{oj} \right\} (\Phi_j^{(1)} - \Phi_{Ij}^{(1)}) = 0, \quad (3.14)$$

in which $\gamma = \sqrt{x^2 + y^2}$, k_{oj} is the incident wave number given by the positive real root of the dispersion relation $\omega_j^2 = gk_{oj}$ and $\Phi_{Ij}^{(1)}$ is the spatial component of the linear incident wave potential given by

$$\Phi_{Ij}^{(1)} = -\frac{ig\Gamma_j^{(1)}}{\omega_j} e^{k_{oj}z} e^{ik_{oj}(x \cos \beta_j + y \sin \beta_j)}, \quad (3.15)$$

where $\Gamma_j^{(1)}$ is the first-order amplitude of the j th incident wave component.

Numerical solutions for $\Phi_{jS}^{(1)}$ and $\Psi_{jp}^{(1)}$ may be obtained utilizing a boundary integral method using a suitable Green's function and the appropriate structural boundary conditions.

3.1.3 Solution of the BVP Using Source Distribution Method

For wave diffraction and radiation of an arbitrarily shaped structure, the j th component of the first-order potential may be written as a distribution of sources of unknown strength over the equilibrium body surface, i.e.,

$$[\Phi_{jS}^{(1)}(\underline{X}), \Psi_{jp}^{(1)}(\underline{X})] = \int_{S_0} [\sigma_{jS}(\underline{X}'), \sigma_{jp}(\underline{X}')] G(\omega_j, \underline{X}; \underline{X}') dS. \quad (3.16)$$

A suitable expression for $G(\omega_j, \underline{X}; \underline{X}') = G(\omega_j, x, y, z; x', y', z')$ is given by the following integral form:

$$G(\omega_j, \underline{X}; \underline{X}') = \frac{1}{R} \text{PV} \int_0^\infty \frac{\mu + v_j}{\mu - v_j} e^{\mu(z+\zeta)} J_0(\mu r) d\mu + 2\pi i v_j e^{v_j(z+z')} J_0(v_j r), \quad (3.17a)$$

where

$$v_j = \frac{\omega_j^2}{g}, \quad (3.17b)$$

$$R = [(x - x')^2 + (y - y')^2 + (z - z')^2]^{1/2}, \quad (3.17c)$$

$$r = [(x - x')^2 + (y - y')^2]^{1/2}. \quad (3.17d)$$

In Eq. (3.17a), J_0 denotes the Bessel function of the first kind of zero order and PV denotes the principal value of the integral (Wehausen J.V. and Laitone, E.V., 1960). Telste and Noblesse (1986) derived expressions to obtain accurate values of the above Green's function which are more computationally efficient than the above form. Their coded form to compute the Green's function is used throughout the present study.

Letting \underline{X}_0 be a point on S_0 , then Eq. (3.16) may be used to express the velocity normal to the structure at \underline{X}_0 as

$$\left[\frac{\partial \Phi_{iS}^{(1)}}{\partial n}, \frac{\partial \Psi_{jP}^{(1)}}{\partial n} \right] (\underline{X}_0) = \gamma(\underline{X}_0) [\sigma_{jS}(\underline{X}_0), \sigma_{jP}(\underline{X}_0)] + \int_{S_0} [\sigma_{jS}^{(1)}(\underline{X}'), \sigma_{jP}^{(1)}(\underline{X}')] \frac{\partial G_j}{\partial n} (\omega_j, \underline{X}_0; \underline{X}) dS, \quad (3.18)$$

in which $\gamma(\underline{X}_0)$ is the interior solid angle at \underline{X}_0 . For smooth surfaces, $\gamma(\underline{X}_0)$ has a value of 2π .

The surface of the structure S_0 is now discretized into a total of M higher-order surface elements each described in terms of N_e nodes for a total of N_T nodes on the structure. Next, the variation of the source distribution over each of these elements is expressed in terms of its corresponding values at the nodes and appropriate shape functions, N_i (see Appendix A). For \underline{X}_0 at the n^{th} node ($\underline{X}_0 = \underline{X}_n$), and after applying the structural boundary condition, Eq. (3.8), the above expression becomes

$$\left[\frac{\partial \Phi_{iS_n}^{(1)}}{\partial n}, \frac{\partial \Psi_{jP_n}^{(1)}}{\partial n} \right] = \gamma(\underline{X}_n) [\sigma_{jS_n}^{(1)}, \sigma_{jP_n}^{(1)}] + \sum_{m=1}^M \sum_{i=1}^{N_e} [\sigma_{jS_{i^*}}^{(1)}, \sigma_{jP_{i^*}}^{(1)}] \int_{\Delta S_m} N_i \frac{\partial G}{\partial n} (\omega_j, \underline{X}_n; \underline{X}') dS, \quad (3.19)$$

where i^* is the node number associated with the i^{th} node of the m^{th} element in the global system.

Allowing n to vary from $n = 1$ to $n = N_T$ results in a system of $N_T \times N_T$ linear equations which can be solved for the unknown source distributions at the nodes, namely

$$[C]_{N_T \times N_T} \{ S_{jS}, S_{jP} \}_{N_T} = \{ R_{jS}, R_{jP} \}_{N_T}, \quad (3.20)$$

where $[C]$ is the coefficient matrix, $\{S_{js}, S_{jp}\}$ is the unknown source distribution matrix (scattered and radiation components), and $\{R_{js}, R_{jp}\}$ is the corresponding right-hand side. The coefficient matrix $[C]$ is defined by

$$C_{nm} = \sum_{m=1}^M \sum_{i=1}^{N_e} \delta_{mi^*} \int_{\Delta S_m} N_i \frac{\partial G}{\partial n}(\omega_j, \underline{X}_n; \underline{X}') dS + \delta_{nm} \gamma(\underline{X}_n). \quad (3.21)$$

where δ is the Kronecker delta.

The integrals in Eq. (3.21) and in the discretized form of Eq. (3.16) contain singularities of order $O(1/R^2)$ and $O(1/R)$, respectively, when the node n is on element m . The order of these singularities may be reduced by performing the integrations in a polar coordinate system. Details of this transformation are given in Appendix B.

Once the source strength values at the nodes are computed, the velocity potential at any point \underline{X}_n in the fluid domain may be determined from the discretized version of Eq. (3.16), namely

$$[\Phi_{js_n}^{(1)}, \Phi_{jp_n}^{(1)}] = \sum_{m=1}^M \sum_{i=1}^{N_e} [\sigma_{js_{i^*}}^{(1)}, \sigma_{jp_{i^*}}^{(1)}] \int_{\Delta S_m} N_i G(\omega_j, \underline{X}_n; \underline{X}') dS. \quad (3.22)$$

The velocity gradient at any point \underline{X}_n , $[q_{js_n}^{(1)}, q_{jp_n}^{(1)}] = [\nabla \Phi_{js_n}^{(1)}, \nabla \Phi_{jp_n}^{(1)}]$, strictly inside the fluid domain is then given by

$$[\nabla \Phi_{js_n}^{(1)}, \nabla \Psi_{jp_n}^{(1)}] = \sum_{m=1}^M \sum_{i=1}^{N_e} [\sigma_{js_{i^*}}^{(1)}, \sigma_{jp_{i^*}}^{(1)}] \int_{\Delta S_m} N_i \nabla G(\omega_j, \underline{X}_n; \underline{X}') dS, \quad (3.23a)$$

whereas for \underline{X}_n on the boundary S_o , the velocity gradient is given by

$$[\nabla \Phi_{jS_n}^{(1)}, \nabla \Psi_{jP_n}^{(1)}] = \sum_{m=1}^M \sum_{i=1}^{N_e} [\sigma_{jS_{i^*}}^{(1)}, \sigma_{jP_{i^*}}^{(1)}] \int_{\Delta S_m} N_i \nabla G(\omega_j, \underline{X}_n; \underline{X}') dS + \gamma(\underline{X}_n) [\sigma_{jS_n}^{(1)}, \sigma_{jP_n}^{(1)}] \underline{n}, \quad (3.23b)$$

where \underline{n} is the unit normal vector at point \underline{X}_n .

For the most part, ocean structures have geometrical symmetry dividing the structure into two, four or eight similar parts. The existence of this geometrical symmetry may be used to reduce the computational effort even for cases when the wave system does not possess symmetry. Details of this procedure are given in Appendix C.

3.2 Second-Order Potential

3.2.1 Boundary-Value Problem for Second-Order Potential

The second-order problem, obtained by gathering terms of $O(\epsilon^2)$, may be written as

$$\nabla^2 \phi^{(2)} = 0 \quad \text{in the fluid domain, } V, \quad (3.24)$$

$$\frac{\partial^2 \phi^{(2)}}{\partial t^2} + g \frac{\partial \phi^{(2)}}{\partial z} = \frac{1}{g} \frac{\partial \phi^{(1)}}{\partial t} \frac{\partial}{\partial z} \left\{ \frac{\partial^2 \phi^{(1)}}{\partial t^2} + g \frac{\partial \phi^{(1)}}{\partial z} \right\} - \frac{\partial}{\partial t} (\nabla \phi^{(1)})^2 \quad \text{on } S_F, \quad (3.25)$$

and

$$\begin{aligned} \frac{\partial \phi^{(2)}}{\partial n} = & \underline{V}^{(2)} \cdot \underline{n} + \left[\frac{1}{2} \underline{n} \cdot \left(\frac{\partial \underline{R}^{(2)}}{\partial t} [\underline{I} - \underline{I}_G] \right) \right. \\ & - \underline{n} \cdot \left\{ (\underline{\Delta}^{(1)} + \underline{\Omega}^{(1)} \times [\underline{I} - \underline{I}_G]) \cdot \underline{\nabla} \right\} \underline{\nabla} \phi^{(1)} \\ & \left. + (\underline{\Omega}^{(1)} \times \underline{n}) \cdot (\underline{V}^{(1)} - \underline{\nabla} \phi^{(1)}) \right] \quad \text{on } S_o, \quad (3.26) \end{aligned}$$

where

$$\underline{\mathbf{V}}^{(2)} = \frac{\partial}{\partial t} \left\{ \underline{\Delta}^{(2)} + \underline{\Omega}^{(2)} \times [\underline{\mathbf{r}} - \underline{\mathbf{r}}_G] \right\}, \quad (3.27)$$

and $\underline{\mathbf{R}}^{(2)}$ is a second-order matrix whose entries are products of first-order rotational displacements, namely:

$$\underline{\mathbf{R}}^{(2)} = - \begin{bmatrix} (\Omega_2^2 + \Omega_3^2) & 0 & 0 \\ -2\Omega_1\Omega_2 & (\Omega_1^2 + \Omega_3^2) & 0 \\ -2\Omega_1\Omega_3 & -2\Omega_2\Omega_3 & (\Omega_1^2 + \Omega_2^2) \end{bmatrix}. \quad (3.28)$$

It should be noted that the form of $\underline{\mathbf{R}}^{(2)}$ depends on the sequence of angular motions. In the present case, the sequence roll-pitch-yaw has been used. Finally, a suitable radiation condition must be imposed on $\phi^{(2)}$, to ensure the correct behavior of the solution at large distances from the structure.

3.2.2 Decomposition of the Second-Order Potential

Similar to the first-order potential, the second-order potential may also be decomposed into incident, scattered and radiated wave components, thus

$$\phi^{(2)} = \phi_I^{(2)} + \phi_S^{(2)} + \phi_R^{(2)}. \quad (3.29)$$

The spatial variation of the second-order incident potential is given by

$$\Phi_{ijk}^{\pm} = \left[\frac{I_{jk}^{\pm} + I_{kj}^{\pm*}}{2} \right] e^{(\kappa^{\pm} z)} e^{i(\mathbf{k}_j \pm \mathbf{k}_k) \cdot (x, y)}, \quad (3.30a)$$

where

$$I_{jk} = - \frac{ig\Gamma_j\Gamma_k}{2\omega_j} \left\{ \frac{-1 \pm 2k_{oj}k_{ok} [\cos(\beta_j - \beta_k)]}{v^{\pm} - \kappa^{\pm}} \right\}, \quad (3.30b)$$

and

$$\mathbf{k}_j = (k_{oj} \cos \beta_j, k_{oj} \sin \beta_j), \quad v^{\pm} = \frac{(\omega_j \pm \omega_k)^2}{g} \quad \text{and} \quad \kappa^{\pm} = |\mathbf{k}_j \pm \mathbf{k}_k|.$$

Unlike the first-order problem, this decomposition is not unique. It is convenient to let the second-order scattered potential, $\phi_S^{(2)}$, be associated with the second-order incident wave field and also all forcing due to quadratic contributions of first-order quantities both on the free-surface and on the structural surface.

Following the decomposition defined in Eq. (3.29), the boundary-value problem for the second-order scattered potential may be written as

$$\nabla^2 \phi_S^{(2)} = 0 \quad \text{in the fluid domain, } V, \quad (3.31)$$

$$\begin{aligned} \frac{\partial^2 \phi_S^{(2)}}{\partial t^2} + g \frac{\partial \phi_S^{(2)}}{\partial z} &= \frac{1}{g} \frac{\partial \phi^{(1)}}{\partial t} \frac{\partial}{\partial z} \left\{ \frac{\partial^2 \phi^{(1)}}{\partial t^2} + g \frac{\partial \phi^{(1)}}{\partial z} \right\} \\ &\quad - \frac{\partial}{\partial t} (\nabla \phi^{(1)})^2 - \left(\frac{\partial^2 \phi_1^{(2)}}{\partial t^2} + g \frac{\partial \phi_1^{(2)}}{\partial z} \right) \quad \text{on } S_F, \end{aligned} \quad (3.32)$$

$$\begin{aligned} \frac{\partial \phi_S^{(2)}}{\partial n} &= \frac{1}{2} \underline{n} \cdot \left(\frac{\partial \underline{R}^{(2)}}{\partial t} [\underline{r} - \underline{r}_G] \right) - \underline{n} \cdot \left\{ (\underline{\Delta}^{(1)} + \underline{\Omega}^{(1)} \times [\underline{r} - \underline{r}_G]) \cdot \underline{\nabla} \right\} \nabla \phi^{(1)} \\ &+ (\underline{\Omega}^{(1)} \times \underline{n}) \cdot (\underline{V}^{(1)} - \underline{\nabla} \phi^{(1)}) - \frac{\partial \phi_I^{(2)}}{\partial n} \quad \text{on } S_o. \end{aligned} \quad (3.33)$$

The second-order radiated potential may be expressed as

$$\phi_{Rp}^{(2)}(\underline{X}; t) = \sum_{j=1}^2 \sum_{k=1}^2 \left\{ \Psi_p^+(\underline{X}) e^{-i(\omega_j + \omega_k)t} + \Psi_p^-(\underline{X}) e^{-i(\omega_j - \omega_k)t} \right\}. \quad (3.34)$$

Then, the boundary-value problem for the second-order radiation potential in the p th mode ($p = 1, 2, \dots, 6$) may be written as

$$\nabla^2 \Psi_p^\pm = 0 \quad \text{in the fluid domain, } V, \quad (3.35)$$

$$-(\omega_j \pm \omega_k)^2 \Psi_p^\pm + g \frac{\partial \Psi_p^\pm}{\partial z} = 0 \quad \text{on the mean free surface, } S_F, \quad (3.36)$$

$$\frac{\partial \Psi_p^\pm}{\partial n} = -i(\omega_j \pm \omega_k) n_p \quad \text{on } S_o, \quad (3.37)$$

$$\lim_{\gamma \rightarrow \infty} \sqrt{\gamma} \left\{ \frac{\partial}{\partial \gamma} - i\lambda_o^\pm \right\} \Psi_p^\pm = 0. \quad (3.38)$$

In Eq. (3.38), λ_o^\pm is the sum- difference-frequency wave number given by the dispersion relation $(\omega_j \pm \omega_k)^2 = g \lambda_o^\pm$ and $\{n_4, n_5, n_6\} = \underline{n} \times [\underline{r} - \underline{r}_G]$.

3.3 Linear Equation of Motion for Rigid Structures

In response to wave excitation, the structure experiences small amplitude translations given by $\underline{\Delta}^{(1)}$ in surge, sway and heave, and small rotations about the center of gravity of the structure of $\underline{\Omega}^{(1)}$ in roll, pitch and yaw. Because of the linearity of the problem, the analysis for a monochromatic wave train is presented below. For simplicity, all superscripts denoting first-order, as well as all subscripts denoting wave component are dropped in this section.

Assuming that the structural response has the same time dependency as the exciting loads, the equation of motion may be described in terms of the unknown structural displacements. In general, the solution of the equation of motion requires the calculation of the load vector acting on the structure as well as the properties of the structural system (i.e., the mass, damping and stiffness matrices).

3.3.1 Exciting Loads

Once the scattered and radiated potential components on the structure have been calculated, various quantities of engineering interest may be determined. The hydrodynamic pressure may be calculated from the linearized form of Bernoulli's equation according to

$$P = \rho i \omega \Phi, \quad (3.39)$$

where $p(x,y,z,t) = \text{Re}[P(x,y,z) e^{-i\omega t}]$ and ρ is the fluid density. This pressure can be broken down into an incident wave component, a scattered wave component (due to the disturbance associated with waves impinging on a fixed structure), and a radiated wave component (due to the oscillation of the structure in otherwise calm water). These first two pressure components (incident and scattered) may be integrated over the wetted surface of

the structure to give the complex amplitude of the exciting loads at each of the 6 modes (surge, sway, heave, roll, pitch and yaw), namely

$$F_p^E = - \int_{S_0} (P_I + P_S) n_p dS = - \rho i \omega \int_{S_0} (\Phi_I + \Phi_S) n_p dS. \quad (3.40)$$

3.3.2 Added Mass and Damping Coefficients

In a similar manner, the hydrodynamic reaction loads may be defined in terms of the oscillation-induced pressures experienced by the structure,

$$F_p^R = - \int_{S_0} P_R n_p dS = - \rho i \omega \int_{S_0} \Phi_R n_p dS \quad (3.41a)$$

$$= - \rho i \omega \int_{S_0} \sum_{q=1}^3 [\Psi_{Rq} \xi_q + \Psi_{Rq+3} \alpha_q] n_p dS. \quad (3.41b)$$

For convenience, the above expression may also be written as

$$F_p^R = \sum_{q=1}^6 F_{pq}^R, \quad (3.42)$$

where

$$F_{pq}^R = - \rho i \omega \xi_q \int_{S_0} \Psi_{Rq} n_p dS \quad q = 1, 2, 3; \quad p = 1, 2, \dots, 6 \quad (3.43a)$$

$$= - \rho i \omega \alpha_{q-3} \int_{S_0} \Psi_{Rq} n_p dS \quad q = 4, 5, 6 \quad p = 1, 2, \dots, 6. \quad (3.43b)$$

Real symmetric added mass and radiation damping matrices \underline{A} and \underline{B} with entries A_{pq} and B_{pq} are now defined as those components of the reaction force in phase with the acceleration and velocity of the structure, respectively. Thus, we have

$$F_{pq}^R = [\omega^2 A_{pq} + i \omega B_{pq}] \xi_q \quad q = 1, 2, 3; p = 1, 2, \dots, 6 \quad (3.44)$$

$$F_{pq+3}^R = [\omega^2 A_{pq+3} + i \omega B_{pq+3}] \alpha_q \quad q = 1, 2, 3; p = 1, 2, \dots, 6 \quad (3.45)$$

3.3.3 Mass and Stiffness Matrices

Consider a rigid structure whose center of gravity G relative to O is given by $\underline{r}_G = [x_G, y_G, z_G]$. If the mooring line or tendon forces and moments are represented by the six-component vector \underline{T} and the fluid loading (both hydrodynamic and hydrostatic) by \underline{P} , then the rigid body equations of motion of the structure, referred to the mass center G , may be written as

$$\underline{M} \underline{\ddot{x}} = \underline{T} + \underline{F}^E + \underline{F}^R, \quad (3.46)$$

where $[\underline{x}] = [\underline{\xi}, \underline{\alpha}]$ and \underline{M} is the mass matrix, given by

$$\underline{M} = \begin{bmatrix} m & 0 & 0 & 0 & 0 & 0 \\ 0 & m & 0 & 0 & 0 & 0 \\ 0 & 0 & m & 0 & 0 & 0 \\ 0 & 0 & 0 & I_{xx} & -I_{xy} & -I_{xz} \\ 0 & 0 & 0 & -I_{xy} & I_{yy} & -I_{yz} \\ 0 & 0 & 0 & -I_{xz} & -I_{yz} & I_{zz} \end{bmatrix}. \quad (3.47)$$

Here m is the structural mass; I_{xx} , I_{yy} , and I_{zz} are its moments of inertia, and I_{xy} , I_{xz} , and I_{yz} are the products of inertia relative to axes through G parallel to the coordinate axes.

The fluid exerts a pressure P on the structure; this pressure consists of a hydrostatic component P_0 and a hydrodynamic component P' , so that the total pressure may be written as

$$P = P_0 + P'. \quad (3.48)$$

The hydrostatic pressure gives rise to a steady buoyancy force, which determines the static equilibrium state of the structure, and also to oscillatory forces and moments caused by changes in the submerged volume of the structure as it heaves, rolls, and pitches (note that surge, sway, and yaw have a zero contribution to this component). The oscillatory load due to hydrostatic effects, \underline{E}_0 , may be written as

$$F_p = - \int_{\Delta S} P' n_p dS, \quad (3.49)$$

in which ΔS represents the change in submerged area S from the static equilibrium position (i.e., in calm water). The hydrostatic load vector may be written as

$$\underline{E}_0 = - \underline{J} \underline{x}, \quad (3.50)$$

where

$$\underline{J} = \rho g \begin{bmatrix} 0 & 0 & 0 & 0 & 0 & 0 \\ 0 & 0 & 0 & 0 & 0 & 0 \\ 0 & 0 & \alpha_{00} & \alpha_{01} & -\alpha_{10} & 0 \\ 0 & 0 & \alpha_{01} & V(z_B - z_G) + \alpha_{02} & -\alpha_{11} & \alpha_{01} & -V(x_B - x_G) \\ 0 & 0 & -\alpha_{10} & -\alpha_{11} & V(z_B - z_G) + \alpha_{20} & -V(y_B - y_G) \\ 0 & 0 & 0 & 0 & 0 & 0 \end{bmatrix}, \quad (3.51)$$

in which ρ is the fluid density, g the acceleration due to gravity, V the displacement volume of the structure, and $(x_B, y_B, z_B) = \underline{r}_B$ is the location, B , of the structure center of buoyancy. The quantities α_{00} , α_{10} , and α_{01} are the water plane area and first moments of the water plane area about G , respectively, that is,

$$\alpha_{00} = \int_A dA, \quad (3.52a)$$

$$\alpha_{10} = \int_A (x - x_G) dA, \quad (3.52b)$$

$$\alpha_{01} = \int_A (y - y_G) dA. \quad (3.52c)$$

The quantities α_{11} , α_{20} , and α_{02} are the product and second moments of water plane area, respectively, and are defined by

$$\alpha_{11} = \int_A (x - x_G)(y - y_G) dA, \quad (3.53a)$$

$$\alpha_{20} = \int_A (x - x_G)^2 dA, \quad (3.53b)$$

$$\alpha_{02} = \int_A (y - y_G)^2 dA. \quad (3.53c)$$

The hydrodynamic pressure component P' can be broken down into an incident wave component, P_I ; a component due to wave scattering by a fixed structure, P_S ; and a component due to the waves radiated by the structure in otherwise calm water, P_R . Thus, we get

$$\mathbf{P}' = \mathbf{P}_I + \mathbf{P}_S + \mathbf{P}_R. \quad (3.54)$$

Integrating the first two components over the immersed surface of the structure yields the exciting loads (forces and moments about G in the pth mode), F_p^E . Similarly, integrating the radiated pressure component over S_0 results in the hydrodynamic reaction loads, F_p^R , which may be decomposed into components in phase with the acceleration and velocity of the structure to define the added mass and radiation damping matrices \mathbf{A} and \mathbf{B} , respectively. Thus the fluid loading vector may finally be written as

$$\mathbf{F} = \mathbf{F}_E - \mathbf{A} \ddot{\mathbf{x}} - \mathbf{B} \dot{\mathbf{x}} - \mathbf{J} \mathbf{x}, \quad (3.55)$$

where \mathbf{F}_E is the vector of the exciting forces and moments about G, \mathbf{A} and \mathbf{B} are the added mass and radiation damping matrices and \mathbf{x} is the vector containing the structural translational and rotational displacements at r_G , i.e., $[\mathbf{x}] = [\xi, \alpha]$.

The final contribution to the equations of motion comes from the mooring forces and moments represented by the vector \mathbf{T} . In estimating the entries of \mathbf{T} , the mooring cables will be assumed weightless, taut, and of constant stiffness. The model proposed herein includes both "elastic" effects due to linear extension of the cables and also "pendulum" effects due to the static pre-tension in the cable under lateral displacement. The vector \mathbf{T} may be expressed in terms of a cable stiffness matrix \mathbf{K} so that

$$\mathbf{T} = -\mathbf{K} \mathbf{x}. \quad (3.56)$$

Expressions for the entries of the matrix \mathbf{K} are given in Appendix D.

The complete equation of motion for the structure is obtained by equating the hydrodynamic loading components (excitations and reactions), hydrostatic loads and mooring terms to the product of the mass matrix and the acceleration vector to yield

$$\underline{\mathbf{M}} \ddot{\underline{\mathbf{x}}} = \underline{\mathbf{F}}_E - \underline{\mathbf{A}} \ddot{\underline{\mathbf{x}}} - \underline{\mathbf{B}} \dot{\underline{\mathbf{x}}} - \underline{\mathbf{J}} \underline{\mathbf{x}} - \underline{\mathbf{K}} \underline{\mathbf{x}} \quad (3.57a)$$

or

$$(\underline{\mathbf{M}} + \underline{\mathbf{A}}) \ddot{\underline{\mathbf{x}}} + \underline{\mathbf{B}} \dot{\underline{\mathbf{x}}} + (\underline{\mathbf{J}} + \underline{\mathbf{K}}) \underline{\mathbf{x}} = \underline{\mathbf{F}}_E, \quad (3.57b)$$

where $\underline{\mathbf{F}}_E$ is the exciting load vector, evaluated about the center of mass G.

3.4 First- and Second-Order Hydrodynamic Loads

3.4.1 Derivation

Similar to the expansion of the velocity potential and free-surface elevation, the hydrodynamic loads on the structure in a direction aligned with the pth mode may be expressed as

$$F_p(t) = \varepsilon F_p^{(1)}(t) + \varepsilon^2 F_p^{(2)}(t) + \dots \quad (3.58)$$

For structures with vertical walls at the still-water level, the diffracted hydrodynamic loads in the pth mode at first- and second-order are given by

$$F_p^{(1)} = -\rho \int_{S_0} \left[\frac{\partial(\phi_i^{(1)} + \phi_s^{(1)})}{\partial t} \right] n_p \, dS, \quad (3.59)$$

$$\begin{aligned}
F_p^{(2)} = & -\rho \int_{S_o} \left[\frac{\partial(\phi_1^{(2)} + \phi_3^{(2)})}{\partial t} + \frac{1}{2} (\nabla\phi^{(1)})^2 \right. \\
& + (\underline{\Delta}^{(1)} + \underline{\Omega}^{(1)} \times [\underline{r} - \underline{r}_G]) \cdot \frac{\partial}{\partial t} (\nabla\phi^{(1)}) \left. \right] n_p \, dS \\
& + \frac{1}{2} \rho g \int_{L_o} (\eta_r^{(1)})^2 n_p \, dL + \underline{\Omega}^{(1)} \times F_p^{(1)}, \tag{3.60}
\end{aligned}$$

in which L_o is the water line contour around the structure and $\eta_r^{(1)}$ is the spatial component of the first-order relative wave elevation defined by

$$\eta_r^{(1)} = \eta^{(1)} - \Delta_3^{(1)} + (\underline{r}_G \times \underline{\Omega}^{(1)}) \cdot (0,0,1). \tag{3.61}$$

An examination of the expressions for the second-order diffraction-induced loads given by Eq. (3.60) reveals that every component except one may be determined from the known second-order incident potential, or from first-order quantities alone. The one exception is the contribution due explicitly to the second-order scattered potential which may be written as

$$F_{Sp}^{(2)} \underset{\text{Re}}{=} \sum_{j=1}^2 \sum_{k=1}^2 \left\{ F_{Sp}^+ e^{-i(\omega_j + \omega_k)t} + F_{Sp}^- e^{-i(\omega_j - \omega_k)t} \right\}, \tag{3.62a}$$

where

$$F_{Sp}^{\pm} = -i\rho (\omega_j \pm \omega_k) \int_{S_o} \Phi_S^{\pm} n_p \, dS. \tag{3.62b}$$

3.4.2 Second-Order Loads Due to Second-Order Potential

The method utilized to calculate the second-order hydrodynamic loading components explicitly due to the second-order scattered potential in Eq. (3.64), does not involve the explicit calculation of this potential. Instead, the loading components due to Φ_S^\pm are obtained by solving a series of associated linearized radiation problems corresponding to the prescribed oscillation of the structure at the sum-frequency, $(\omega_j + \omega_k)$, or difference-frequency, $(\omega_j - \omega_k)$, of interest. The solutions of these problems are linked to the required loading components through Green's second identity (Lighthill, 1979; Molin, 1979).

Let us define the domain V^* bounded by the surface S^* , consisting of S_o , S_F , S_∞ , and a horizontal boundary S_B , where the vertical scattered and radiated velocities may be taken as zero (see Fig. 3.1). Then, applying Green's second identity to Φ_S^\pm and Ψ_p^\pm over the region V^* gives

$$\int_{S^*} \left[\Phi_S^\pm \frac{\partial \Psi_p^\pm}{\partial n} - \Psi_p^\pm \frac{\partial \Phi_S^\pm}{\partial n} \right] dS = \int_{V^*} \left[\Phi_S^\pm \nabla^2 \Psi_p^\pm - \Psi_p^\pm \nabla^2 \Phi_S^\pm \right] dV. \quad (3.63)$$

Since Φ_S^\pm and Φ_p^\pm both satisfy Laplace's equation, the right-hand side of Eq. (3.63) is zero. By imposing the boundary conditions on S_B and S_o , Eq. (3.63) may be written as

$$\begin{aligned} \int_{S_o} \Phi_S^\pm \frac{\partial \Psi_p^\pm}{\partial n} dS &= \int_{S_o} \Psi_p^\pm \left[\frac{1}{4} \underline{n} \cdot \underline{\Sigma}^\pm [\underline{r} - \underline{r}_G] \right. \\ &\quad \left. - \frac{1}{2} \underline{n} \cdot \{ (\xi_j^{(1)} + \alpha_j^{(1)}) \times [\underline{r} - \underline{r}_G] \cdot \underline{\nabla} \} \underline{\nabla} \Phi_k^{(1)*} \right. \\ &\quad \left. + \frac{1}{2} (\xi_j^{(1)} \times \underline{n}) \cdot (\underline{U}_k^{(1)} - \underline{\nabla} \Phi_k^{(1)*}) - \frac{\partial \Phi_1^\pm}{\partial n} \right] dS \\ &\quad - \int_{S_\infty \cup S_F} \left[\Phi_S^\pm \frac{\partial \Psi_p^\pm}{\partial n} - \Psi_p^\pm \frac{\partial \Phi_S^\pm}{\partial n} \right] dS, \end{aligned} \quad (3.64)$$

in which the matrices \underline{S}^{\pm} are defined by the relationship.

$$\frac{\partial \underline{R}^{(2)}}{\partial t} \Big|_{\text{Re}} = \sum_{j=1}^2 \sum_{k=1}^2 \left\{ \underline{S}^+ e^{-i(\omega_j + \omega_k)t} + \underline{S}^- e^{-i(\omega_j - \omega_k)t} \right\}, \quad (3.65)$$

and $\underline{U}_k^{(1)}$ is defined by $\underline{V}^{(1)} \Big|_{\text{Re}} = \sum_{k=1}^2 \{ \underline{U}_k^{(1)} e^{-i\omega_k t} \}$, where $\underline{V}^{(1)}$ is given by Eq. (3.10). In

Eq. (3.64), the symbol * denotes the complex conjugate which is to be applied only to the difference-frequency component.

The quantity on the left-hand side of Eq. (3.64) is now recognized as being related to the p th component of the second-order load on the structure due to Φ_S^{\pm} , that is, from Eqs. (3.62) and (3.37),

$$F_{S_p}^{\pm} = -i\rho (\omega_j \pm \omega_k) \int_{S_m} \Phi_S^{\pm} n_p \, dS = \rho \int_{S_o} \Phi_S^{\pm} \frac{\partial \Psi_p^{\pm}}{\partial n} \, dS \quad p=1, 2, \dots, 6. \quad (3.66)$$

Also the integral over S_F in Eq. (3.64) may be simplified, utilizing the boundary condition for Ψ_p^{\pm} on that surface and the complex form of Eq. (3.32), to give

$$\frac{i\rho (\omega_j \pm \omega_k)}{g} \int_{S_F} Q^{\pm} \Psi_p^{\pm} \, dS, \quad (3.67)$$

in which

$$Q^{\pm} = \frac{1}{2} (q_{jk}^{\pm} + q_{kj}^{\pm*}), \quad (3.68a)$$

where * denotes complex conjugate. Again, it is noted that the conjugate operator is to be applied only in the difference-frequency case. In Eq. (3.68), we have

$$q_{jk}^{\pm} = \pm \frac{i\omega_k}{2g} \Phi_k^{(1)*} \left(\omega_j^2 \frac{\partial \Phi_j^{(1)}}{\partial z} - g \frac{\partial^2 \Phi_j^{(1)}}{\partial z^2} \right) \pm i\omega_k \nabla \Phi_j^{(1)} \cdot \nabla \Phi_k^{(1)*}. \quad (3.68b)$$

Solving the linearized boundary value problems at each sum / difference frequency, yields the appropriate radiation potentials for use in calculating the second-order hydrodynamic loads on the structure.

3.4.3 Transfer Functions

The first and second-order hydrodynamic loads may be expressed in terms of linear and quadratic load transfer functions. The first-order wave excitation loads on the structure in the p th mode (surge, sway, ..., yaw) are proportional to the wave amplitudes and may be written as

$$F_p^{(1)}(t) = \sum_{\text{Re}} \sum_{j=1}^2 \Gamma_j G_p(\omega_j, \beta_j) e^{-i\omega_j t}, \quad (3.69)$$

where $G_p(\omega_j, \beta_j)$ is the appropriate linear transfer function. The analogous expression for the second-order load in the p th mode is

$$F_p^{(2)}(t) = \frac{1}{\text{Re}} \sum_{j=1}^2 \sum_{k=1}^2 \left\{ \Gamma_j \Gamma_k^* H_p^-(\omega_j, \omega_k; \beta_j, \beta_k) e^{-i(\omega_j - \omega_k)t} \right. \\ \left. + \Gamma_j \Gamma_k H_p^+(\omega_j, \omega_k; \beta_j, \beta_k) e^{-i(\omega_j + \omega_k)t} \right\}, \quad (3.70)$$

where the $H_p^\pm(\omega_j, \omega_k; \beta_j, \beta_k)$ are the quadratic sum and difference load transfer functions in bidirectional waves.

3.5 Asymptotic Forms of the First-Order Potentials

A separation of variables solution of the governing Laplace equation in cylindrical polar coordinates (r, θ, z) yields the following analytical form for the first-order scattered potential, which is consistent with the free-surface, sea-bed and radiation boundary conditions,

$$\phi_{jS}^{(1)} = e^{k_{oj}z} \sum_{n=0}^{\infty} \varepsilon_n \left\{ A_{noj} \cos n\theta + B_{noj} \sin n\theta \right\} H_n^{(1)}(k_{oj}r) e^{-i\omega_j t}, \quad (3.71)$$

where $\varepsilon_0 = 1$ and $\varepsilon_n = 2$ for $n \geq 1$, the A_{noj} and B_{noj} are complex coefficients, and $H_n^{(1)}$ denotes the Hankel function of the first kind of order n . The first-order incident potential may be written in polar coordinates as

$$\phi_{jI}^{(1)} = -\frac{ig\Gamma_i}{\omega_j} e^{k_{oj}z} e^{ik_{oj}r \cos(\theta-\beta_j)} e^{-i\omega_j t} \quad (3.72a)$$

$$= -\frac{ig\Gamma_i}{\omega_j} e^{k_{oj}z} \sum_{n=0}^{\infty} \varepsilon_n i^n J_n(k_{oj}r) \cos n(\theta-\beta_j) e^{-i\omega_j t}, \quad (3.72b)$$

where J_n denotes the Bessel function of the first kind of order n .

A separation of variables solution of Laplace's equation in cylindrical coordinates, which is consistent with the boundary conditions for Φ_{Rp} , is given by

$$\Psi_{jP} = \sum_{n=0}^{\infty} \varepsilon_n H_n^{(1)}(k_{oj}r) e^{k_{oj}z} \left\{ D_{no}^{pj} \cos n\theta + E_{no}^{pj} \sin n\theta \right\}, \quad (3.73)$$

since at large distances, only a propagating mode of the radiation potential is needed.

The form of this radiation potential is also valid for the assisting radiation potential with proper substitution of the wave frequency and wavenumber at the sum- or difference-frequency.

3.6 The Free-Surface Integral

The numerical evaluation of the free-surface integral appearing in Eq. (3.67) constitutes the major computational effort in obtaining the second-order load component $F_p^{(2)}$. It has been shown analytically (Eatock Taylor and Hung, 1987; Abul-Azm and Williams, 1988) that at large radial distances r from the structure this integral exhibits oscillatory behavior, decaying as $r^{-1/2}$. For an axisymmetric structure, this integral may be expressed in polar coordinates (r, θ) , the angular-integration carried out explicitly, and the remaining r -integral evaluated by a suitable quadrature rule (Eatock Taylor and Hung, 1987; Abul-Azm and Williams, 1988; Moubayed and Williams, 1992a).

However, for an arbitrarily shaped structure, the angular and radial dependency in the free-surface integral will not be separable. Therefore, in the present work, the method of Moubayed and Williams(1992b) for cylinders of arbitrary cross-section in uni-directional, bichromatic waves will be extended to deal with the bidirectional wave case. The free-surface integral is divided into two parts, an interior, near-field region S_{F_1} encompassing the structure and bounded by a fictitious circular boundary C_R situated at $r = R$ and an exterior, far-field region S_{F_2} extending from $r = R$ to infinity. Thus, the free-surface integral contribution I_F may be written as

$$I_{Fp}^{\pm} = \int_{S_{F_1}} Q_{p1}^{\pm}(x,y) dS + \int_{S_{F_2}} Q_{p2}^{\pm}(x,y) dS. \quad (3.74)$$

The boundary C_R is chosen sufficiently far from the structure that analytical asymptotic forms for the potentials are valid for $r \geq R$. The asymptotic forms of the potentials may now be substituted into the free-surface integral on S_{F_2} and the θ -integrations evaluated analytically. The remaining r -integrand may be integrated explicitly in terms of Fresnel functions to yield an explicit form for the integral over the exterior free-surface region.

3.6.1 Numerical Integration on S_{F1}

The interior free-surface integral over the domain S_{F_1} , which extends to $r = R$ and contains the structure, is evaluated numerically. The domain S_{F_1} is subdivided into a large number of triangular or quadrilateral elements. The number of nodes utilized to represent each element, N_e , depends on the order of variation desired within the element for the different dynamic quantities such as velocity potential and water particle velocities. The general element is first mapped onto a right triangular element or a square element, then the quantity of interest on each element is expressed in terms of shape functions N_i and the corresponding nodal values $[\]_i$ as

$$[\Phi_j^{(1)}, \Phi_{jI}^{(1)}, \Psi_p^\pm] (v, \xi) = \sum_{i=1}^{N_e} N_i [\Phi_j^{(1)}, \Phi_{jI}^{(1)}, \Psi_p^\pm]_i, \quad (3.75a)$$

$$[(\Phi_j^{(1)})_x, (\Phi_{jI}^{(1)})_x, (\Psi_p^\pm)_x] (v, \xi) = \sum_{i=1}^{N_e} N_i [(\Phi_j^{(1)})_x, (\Phi_{jI}^{(1)})_x, (\Psi_p^\pm)_x]_i, \quad (3.75b)$$

$$[(\Phi_j^{(1)})_y, (\Phi_{jI}^{(1)})_y, (\Psi_p^\pm)_y] (v, \xi) = \sum_{i=1}^{N_e} N_i [(\Phi_j^{(1)})_y, (\Phi_{jI}^{(1)})_y, (\Psi_p^\pm)_y]_i, \quad (3.75c)$$

$$[(\Phi_j^{(1)})_z, (\Phi_{jI}^{(1)})_z, (\Psi_p^\pm)_z] (v, \xi) = \sum_{i=1}^{N_e} N_i [(\Phi_j^{(1)})_z, (\Phi_{jI}^{(1)})_z, (\Psi_p^\pm)_z]_i. \quad (3.75d)$$

In order to evaluate the quantity $Q_1^\pm(x,y)$ on an element, the second partial derivative with respect to z of the potentials is required. For the incident potential it may be obtained analytically, while for the scattered and radiation components of the potential it may be obtained through application of the governing Laplace equation as

$$\begin{aligned} \frac{\partial^2 \Phi_{jS}^{(1)}}{\partial z^2} &= - \left\{ \frac{\partial^2 \Phi_{jS}^{(1)}}{\partial x^2} + \frac{\partial^2 \Phi_{jS}^{(1)}}{\partial y^2} \right\} \\ &= - \left\{ \sum_{i=1}^{\bar{N}} \frac{\partial N_i}{\partial x} [(\Phi_{jS}^{(1)})_{x}]_i + \sum_{i=1}^{N_e} \frac{\partial N_i}{\partial y} [(\Phi_{jS}^{(1)})_{y}]_i \right\}, \end{aligned} \quad (3.76a)$$

and

$$\begin{aligned} \frac{\partial^2 \Psi_{jp}^{(1)}}{\partial z^2} &= - \left\{ \frac{\partial^2 \Psi_{jp}^{(1)}}{\partial x^2} + \frac{\partial^2 \Psi_{jp}^{(1)}}{\partial y^2} \right\} \\ &= - \left\{ \sum_{i=1}^{\bar{N}} \frac{\partial N_i}{\partial x} [(\Psi_{jp}^{(1)})_{x}]_i + \sum_{i=1}^{N_e} \frac{\partial N_i}{\partial y} [(\Psi_{jp}^{(1)})_{y}]_i \right\}. \end{aligned} \quad (3.76a)$$

The partial derivatives with respect to the global (x,y) coordinates are related to the partial derivatives with respect to the local (v,ξ) coordinates through the Jacobian matrix (see Appendix A).

For convenience, in the subsequent discussion, the subscript p , which is associated with the p th mode, will be dropped from the expressions, and only the \pm will be written.

Dividing the integration domain S_{F_1} into M' elements yields

$$\begin{aligned}
 I_{F_1}^{\pm} &= \int_{S_{F_1}} Q_i^{\pm}(x,y) \, dS \\
 &= \sum_{n=1}^{M'} \int_0^1 \int_0^{1-\xi} Q_i^{n\pm}(\xi,v) |\underline{I}_{1n}| \, dv \, d\xi \quad \text{for triangular elements} \quad (3.77a)
 \end{aligned}$$

and

$$\begin{aligned}
 I_{F_1}^{\pm} &= \int_{S_{F_1}} Q_i^{\pm}(x,y) \, dS \\
 &= \sum_{n=1}^{M'} \int_{-1}^1 \int_{-1}^1 Q_i^{n\pm}(\xi,v) |\underline{I}_{1n}| \, dv \, d\xi \quad \text{for quadrilateral elements,} \quad (3.77b)
 \end{aligned}$$

in which

$$Q_i^{n\pm}(\xi,v) = \frac{i p g(\omega_j \pm \omega_k)}{2V^{\pm}} \sum_{i=1}^{\bar{N}} ([\Psi^{\pm}]_i^n \{ d\bar{q}_{jk}^{\pm}(\xi,v) + d\bar{q}_{kj}^{\pm*}(\xi,v) \}). \quad (3.78)$$

The integration of the function $Q_i^{n\pm}(\xi,v)$ over an element on S_{F_1} is carried out utilizing Gaussian quadrature.

3.6.2 Analytical Integration on S_{F2}

Choosing the boundary C_R sufficiently far from the structure, the asymptotic forms of the incident, scattered, and radiated potentials on the free-surface ($z=0$) will be valid on S_{F2} , thus using polar coordinates, (r, θ) ,

$$\Phi_{jI}^{(1)} \sim \sum_{n=0}^{\infty} \varepsilon_n I_{nj} \cos n(\theta - \beta_j) \sqrt{\frac{2}{\pi k_{oj} r}} \cos(k_{oj} r - \omega_n), \quad (3.79)$$

$$\Phi_{jS}^{(1)} + \Phi_{jR}^{(1)} \sim \sum_{n=0}^{\infty} \varepsilon_n \{ A_{noj} \cos n\theta + B_{noj} \sin n\theta \} \sqrt{\frac{2}{\pi k_{oj} r}} e^{i(k_{oj} r - \omega_n)}, \quad (3.80)$$

$$\Psi^{\pm} \sim \sum_{n=0}^{\infty} \varepsilon_n \{ D_{no}^{\pm} \cos n\theta + E_{no}^{\pm} \sin n\theta \} \sqrt{\frac{2}{\pi \lambda_o^{\pm} r}} e^{i(\lambda_o^{\pm} r - \omega_n)}, \quad (3.81)$$

in which $I_n = i^n$ and $\omega_n = (2n + 1)\pi/4$. Utilizing the orthogonality properties of the trigonometric functions, the potential coefficients A_{noj} , B_{noj} , D_{no}^{\pm} , and E_{no}^{\pm} for $n \geq 0$ may be expressed in terms of the values of the radiated and scattered potentials on C_R according to

$$A_{noj} = \sqrt{\frac{k_{oj} R}{8\pi}} e^{-i(k_{oj} R - \omega_n)} \int_0^{2\pi} [\Phi_{jS}^{(1)}(R, \theta) + \Phi_{jR}^{(1)}(R, \theta)] \cos n\theta \, d\theta, \quad (3.82)$$

$$B_{noj} = \sqrt{\frac{k_{oj} R}{8\pi}} e^{-i(k_{oj} R - \omega_n)} \int_0^{2\pi} [\Phi_{jS}^{(1)}(R, \theta) + \Phi_{jR}^{(1)}(R, \theta)] \sin n\theta \, d\theta, \quad (3.83)$$

$$D_{no}^{\pm} = \sqrt{\frac{\lambda_o^{\pm} R}{8\pi}} e^{-i(\lambda_o^{\pm} R - \omega_n)} \int_0^{2\pi} \Psi^{\pm}(R, \theta) \cos n\theta \, d\theta, \quad (3.84)$$

$$E_{no}^{\pm} = \sqrt{\frac{\lambda_o^{\pm} R}{8\pi}} e^{-i(\lambda_o^{\pm} R - \omega_n)} \int_0^{2\pi} \Psi^{\pm}(R, \theta) \sin n\theta \, d\theta. \quad (3.85)$$

After substitution of the asymptotic forms given by Eqs. (3.82)-(3.85) into Eq. (3.67) for $r > R$, the θ -integrations may be evaluated analytically. The integrand also contains oscillatory components of the form $r^{-1/2} \exp\{i\lambda_0^\pm r\}$ and $r^{-1/2} \exp\{i(\lambda_0^\pm \pm k_{oj} \pm k_{ok}) r\}$, these terms may be integrated explicitly in terms of Fresnel sine and cosine functions $C(x)$ and $S(x)$, defined by Abramowitz and Stegun (1972).

After dropping the common subscript 'o' on the potential coefficients for convenience, and maintaining a format suitable for the more general case of finite water depth, the final explicit form for the integral over the exterior region S_{F_2} is

$$\begin{aligned}
I_{F_2}^\pm = & -8\rho (\omega_j \pm \omega_k) \frac{1}{\sqrt{k_{oj}k_{ok}}} \frac{1}{\sqrt{\lambda_0^\pm}} \left[\frac{1}{2} (C_1^\pm \mp k_{oj} k_{ok} (\omega_j \pm \omega_k)) \right. \\
& \left[\frac{1}{2} A_{oj} I_{ok}^* D_o^\pm e^{-i(2\omega_o \pm \omega_o)} + \sum_{p=0}^{\infty} \sum_{q=1}^{\infty} \{ (A_{pj} D_{p+q}^\pm + B_{p+qj} E_p^\pm) \right. \\
& I_{qk}^* \cos q\beta e^{-i(\pm\omega_q + \omega_p + \omega_{p+q})} + [(A_{p+qj} D_q^\pm + B_{qj} E_{p+q}^\pm) \cos p\beta_k \\
& + (B_{p+qj} D_q^\pm - B_{qj} D_{p+q}^\pm + A_{qj} E_{p+q}^\pm - A_{p+qj} E_q^\pm) \sin p\beta_k] I_{pk}^* e^{-i(\omega_q \pm \omega_p + \omega_{p+q})} \\
& + [(A_{qj} D_p^\pm - B_{qj} E_p^\pm) \cos (p+q)\beta_k \\
& + (B_{qj} D_p^\pm + A_{pj} E_q^\pm) \sin (p+q)\beta_k] I_{p+qk}^* e^{-i(\omega_q + \omega_p \pm \omega_{p+q})} \} \left. \right] \\
& \left. \frac{1}{\sqrt{\lambda_0^\pm + k_{oj} \pm k_{ok}}} \left\{ \left(\frac{1}{2} - c \left(\sqrt{\frac{2(\lambda_0^\pm + k_{oj} \pm k_{ok})R}{\pi}} \right) \right) \right\} \right)
\end{aligned}$$

$$\begin{aligned}
& + i \left(\frac{1}{2} - S \left(\sqrt{\frac{2(\lambda_0^\pm + k_{0j} \pm k_{0k})R}{\pi}} \right) \right) \Big\} \\
& + \frac{1}{2} (C_1^\pm \pm k_{0j} k_{0k} (\omega_j \pm \omega_k)) \left[\frac{1}{2} A_{0j} I_{0k}^* D_0^\pm e^{-i(2\omega_0 \mp \omega_0)} \right. \\
& + \sum_{p=0}^{\infty} \sum_{q=1}^{\infty} \left\{ (A_{pj} D_{p+q}^\pm + B_{p+qj} E_p^\pm) I_{qk}^* \cos q\beta_k e^{i(\pm\omega_q - \omega_p - \omega_{p+q})} \right. \\
& + \left[(A_{qj} D_p^\pm - B_{qj} E_p^\pm) \cos (p+q)\beta_k \right. \\
& + \left. (B_{qj} D_p^\pm + A_{pj} E_q^\pm) \sin (p+q)\beta_k \right] I_{p+qk}^* e^{i(-\omega_q - \omega_p \pm \omega_{p+q})} \\
& + \left[(B_{p+qj} D_q^\pm - B_{qj} D_{p+q}^\pm + A_{qj} E_{p+q}^\pm - A_{p+qj} E_q^\pm) \sin p\beta_k \right. \\
& + \left. (B_{qj} E_{p+q}^\pm + A_{p+qj} D_q^\pm) \cos p\beta \right] I_{pk}^* e^{i(-\omega_q \pm \omega_p - \omega_{q+p})} \Big\} \Big] \\
& \frac{1}{\sqrt{\lambda_0^\pm + \kappa_j \mp \kappa_k}} \left\{ \left(\frac{1}{2} - C \left(\sqrt{\frac{2(\lambda_0^\pm + k_{0j} \mp k_{0k})R}{\pi}} \right) \right) \right. \\
& + i \left(\frac{1}{2} - S \left(\sqrt{\frac{2(\lambda_0^\pm + k_{0j} \mp k_{0k})R}{\pi}} \right) \right) \Big\} \\
& + \frac{1}{2} (C_1^\pm \pm k_{0j} k_{0k} (\omega_j \pm \omega_k)) \left[\frac{1}{2} A_{0k}^* I_{0j} D_0^\pm e^{\mp i\omega_0} \right. \\
& + \sum_{p=0}^{\infty} \sum_{q=1}^{\infty} \left\{ A_{pk}^* I_{qj} D_{p+q}^\pm \cos q\beta_j e^{i(\mp\omega_p + \omega_q - \omega_{p+q})} \right. \\
& + \left. A_{pk}^* I_{p+qj} E_q^\pm \sin (p+q)\beta_j e^{i(\mp\omega_p + \omega_{p+q} - \omega_q)} \right\}
\end{aligned}$$

$$\begin{aligned}
& + \left[(A_{qk}^* D_p^\pm - B_{qk}^* E_p^\pm) \cos (p+q)\beta_j \right. \\
& + \left. B_{qk}^* D_p^\pm \sin (p+q)\beta_j \right] I_{p+qj} e^{i(-\omega_p \mp \omega_q + \omega_{p+q})} \\
& + \left[(A_{qk}^* E_{p+q}^\pm - B_{qk}^* D_{p+q}^\pm) \sin p\beta_j + B_{qk}^* E_{p+q}^\pm \cos p\beta_j \right] I_{pj} e^{i(\mp \omega_q + \omega_p - \omega_{p+q})} \\
& + \left[(B_{p+qk}^* D_q^\pm - A_{p+qk}^* E_q^\pm) \sin p\beta_j + A_{p+qk}^* D_q^\pm \cos n\beta_j \right] I_{pj} e^{i(-\omega_q + \omega_p \mp \omega_{p+q})} \\
& + \left. B_{p+qk}^* I_{qj} E_p^\pm \cos m\beta_j e^{i(+\omega_q - \omega_p \mp \omega_{p+q})} \right\} \frac{1}{\sqrt{\lambda_o^\pm - k_{oj} \pm k_{ok}}} \\
& \left\{ \left(\frac{1}{2} - c \left(\sqrt{\frac{2(\lambda_o^\pm - k_{oj} \pm k_{ok})R}{\pi}} \right) \right) \right. \\
& + \left. i \left(\frac{1}{2} - s \left(\sqrt{\frac{2(\lambda_o^\pm - k_{oj} + k_{ok})R}{\pi}} \right) \right) \right\} \\
& + \frac{1}{2} C_2^\pm \cdot \left[\frac{1}{2} A_{ok}^* I_{oj} D_o^\pm e^{-i(2\omega_o \pm \omega_o)} \right. \\
& + \sum_{p=0}^{\infty} \sum_{q=1}^{\infty} \left\{ (I_{qj} D_{p+q}^\pm \cos q\beta_j + I_{p+qj} E_q^\pm \sin (p+q)\beta_j) A_{pk}^* e^{-i(\pm \omega_p + \omega_{p+q} + \omega_q)} \right. \\
& + \left[(A_{qk}^* D_p^\pm - B_{qk}^* E_p^\pm) I_{p+qj} \cos (p+q)\beta_j + (A_{qk}^* E_{p+q}^\pm - B_{qk}^* D_p^\pm) I_{pj} \sin p\beta_j \right. \\
& + \left. (I_{p+qj} D_p^\pm \sin (p+q)\beta_j + I_{pj} E_{p+q}^\pm \cos p\beta_j) B_{qk}^* \right] e^{-i(\pm \omega_q + \omega_{p+q} + \omega_p)} \\
& + \left. (I_{pj} D_q^\pm \sin p\beta_j + I_{qj} E_p^\pm \cos q\beta_j) B_{p+qk}^* \right\}
\end{aligned}$$

$$\begin{aligned}
& + A_{p+qk}^* (D_q^\pm \cos p\beta_j - E_q^\pm \sin p\beta_j) I_{p_j} \left] e^{-i(\omega_q \pm \omega_{p+q} + \omega_p)} \right\} \\
& \frac{1}{\sqrt{\lambda_o^\pm + k_{oj} \pm k_{ok}}} \left\{ \left(\frac{1}{2} - C \left(\sqrt{\frac{2(\lambda_o^\pm + k_{oj} \pm k_{ok})R}{\pi}} \right) \right) \right. \\
& \left. + i \left(\frac{1}{2} - S \left(\sqrt{\frac{2(\lambda_o^\pm + k_{oj} \pm k_{ok})R}{\pi}} \right) \right) \right\} \\
& + C_2^\pm \left[\frac{1}{2} A_{o_j} A_{o_k}^* D_o^\pm e^{-i(2\omega_o \pm \omega_o)} \right. \\
& \left. + \sum_{p=0}^{\infty} \sum_{q=1}^{\infty} \left\{ (A_{p+q_j} D_q^\pm + B_{q_j} E_{p+q}^\pm) A_{p_k}^* e^{-i(\omega_q + \omega_{p+q} \pm \omega_p)} \right. \right. \\
& \left. + (A_{p+q_k}^* A_{q_j} D_p^\pm + B_{p+q_k}^* B_{p_j} D_q^\pm + B_{p+q_k}^* A_{q_j} E_p^\pm \right. \\
& \left. - B_{q_j} A_{p+q_k}^* E_p^\pm) e^{-i(\omega_q \pm \omega_{p+q} + \omega_p)} + \left[(A_{p_j} D_{p+q}^\pm + B_{p+q_j} E_p^\pm) A_{q_k}^* \right. \right. \\
& \left. \left. + (B_{p+q_j} D_p^\pm - B_{p_j} D_{p+q}^\pm + A_{p_j} E_{p+q}^\pm - A_{p+q_j} E_p^\pm) B_{q_k}^* \right] e^{-i(\pm \omega_q + \omega_{p+q} + \omega_p)} \right\} \\
& \frac{1}{\sqrt{\lambda_o^\pm + k_{oj} \pm k_{ok}}} \left\{ \left(\frac{1}{2} - C \left(\sqrt{\frac{2(\lambda_o^\pm + k_{oj} \pm k_{ok})R}{\pi}} \right) \right) \right. \\
& \left. + i \left(\frac{1}{2} - S \left(\sqrt{\frac{2(\lambda_o^\pm + k_{oj} \pm k_{ok})R}{\pi}} \right) \right) \right\} \left. \right], \tag{3.86a}
\end{aligned}$$

where

$$C_1^\pm = (\omega_j \pm \omega_k) k_{oj} k_{ok} \quad \text{and} \quad C_2^\pm = C_1^\pm \mp (\omega_j \pm \omega_k) k_{oj} k_{ok}.$$

3.7 The Double Gradient Body Integral

When the ocean structure being analyzed undergoes motion, the expression for the second-order hydrodynamic loads contains terms requiring the computation of double gradients of the potential which are integrated over the mean position of the structure, S_0 . Since the potentials satisfy the Laplace equation, a transformation utilizing Stokes' theorem may be performed to change the integral into a combination of line integrals and surface integrals involving only first derivatives of the velocity potential. From Eq. (3.64), the term requiring the computation of the double gradient may be modified as shown by Matsui *et al.* (1992) to take the form:

$$\begin{aligned}
 B_{jkp}^{\pm} &= \int_{S_0} \Psi_p^{\pm} \left[\mathbf{n} \cdot \left\{ (\underline{\Delta}_j^{(1)} + \underline{\Omega}_j^{(1)} \times [\mathbf{r} - \mathbf{r}_G]) \cdot \underline{\nabla} \right\} \underline{\nabla} \Phi_k^{(1)*} \right] dS \\
 &= \int_{S_0} \Psi_p^{\pm} \left[\mathbf{n} \cdot \left\{ \underline{x}_{Gj}^{(1)} \cdot \underline{\nabla} \right\} \underline{\nabla} \Phi_k^{(1)*} \right] dS \\
 &= \int_{S_0} \left[\left(\underline{x}_{Gj}^{(1)} \cdot \mathbf{n} \right) \left(\underline{\nabla} \Psi_p^{\pm} \cdot \underline{\nabla} \Phi_k^{(1)*} \right) - \left(\underline{x}_{Gj}^{(1)} \cdot \underline{\nabla} \Psi_p^{\pm} \right) \left(\mathbf{n} \cdot \underline{\nabla} \Phi_k^{(1)*} \right) \right. \\
 &\quad \left. - \Psi_p^{\pm} \left(\underline{\Omega}_j^{(1)} \times \mathbf{n} \right) \cdot \underline{\nabla} \Phi_k^{(1)*} \right] dS - \oint_{C_w} \Psi_p^{\pm} \underline{x}_{Gj}^{(1)} \times \underline{\nabla} \Phi_k^{(1)*} \cdot d\mathbf{l}, \quad (3.87)
 \end{aligned}$$

where $\underline{x}_{Gj}^{(1)} = (\underline{\Delta}_j^{(1)} + \underline{\Omega}_j^{(1)} \times [\mathbf{r} - \mathbf{r}_G])$, and the last term is the integral over the closed path defined by the intersection of the mean free-surface and the mean structural surface.

This form is preferred since it requires only first derivatives of the first-order potential and assisting radiated potential which may be obtained directly from the source distribution approach used to solve the first-order problem.

CHAPTER FOUR

IMPLEMENTING NUMERICAL COMPUTATION OF SECOND-ORDER SUM- AND DIFFERENCE-FREQUENCY LOADS ON ISSC TLP IN BICHROMATIC BIDIRECTIONAL WAVES

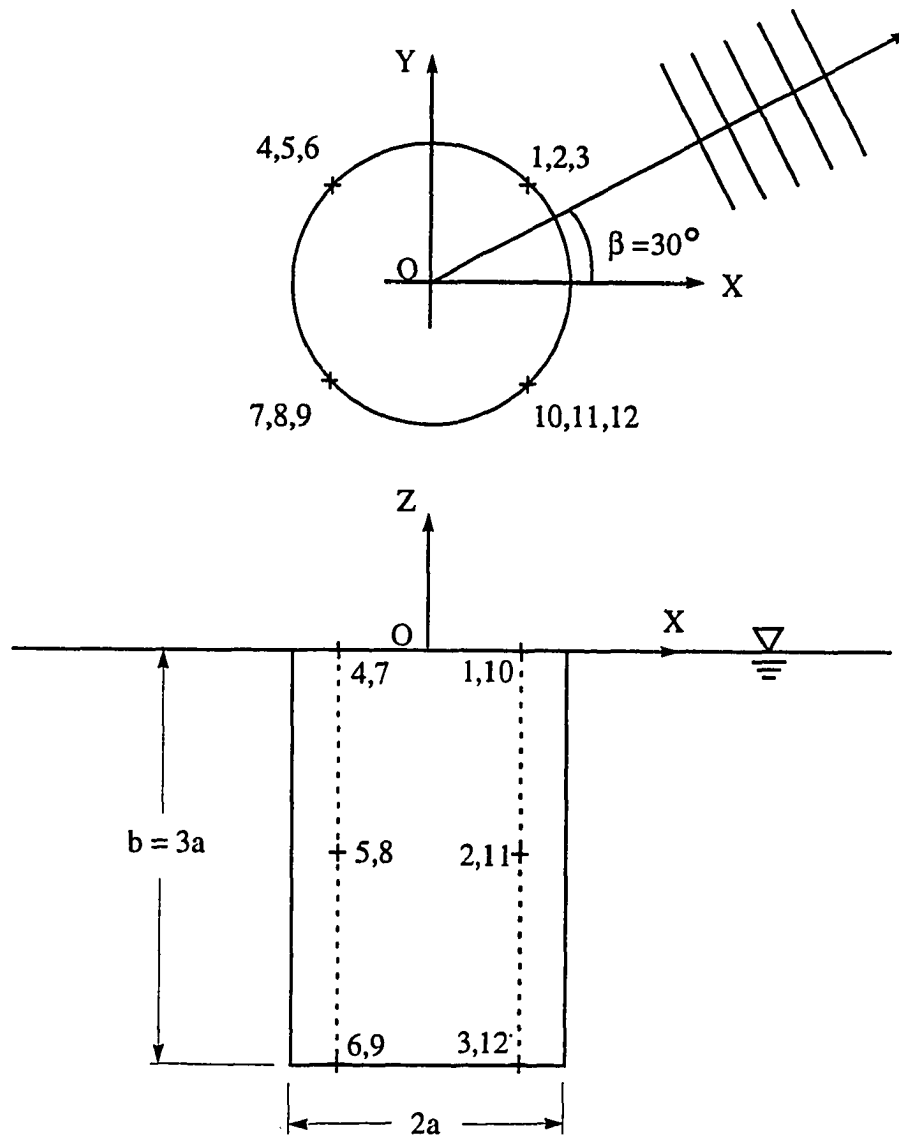
The theory developed in Chapter Three was coded utilizing quadratic elements and taking advantage of the triple symmetry exhibited by typical ocean structures. The ISSC TLP (Eatock Taylor and Jeffreys, 1986) will be used to illustrate the solution methodology and demonstrate the effect of wave directionality and first-order body motions on the second-order sum- and difference-frequency hydrodynamic loads. However, before results for the sum- and difference-frequency loads on the ISSC TLP are presented, the convergence of the first-order solution is addressed. As stated earlier, the accurate computation of the second-order loads is directly related to the accuracy of the first-order solution. Since the two dimensional solution for the array of cylinders is much more computationally efficient than the solution for an arbitrarily-shaped three-dimensional structure, the convergence of the free-surface integral will not be discussed in this chapter, rather it will be addressed in Chapter Six, after the derivation of the solution for the array of cylinders is presented in the next chapter.

4.1 Convergence of First-Order Potentials

In this section, the numerical convergence of the diffraction and radiation problems is investigated. A truncated circular cylinder of draft $b = 30$ m. and radius $a = 10$ m. situated in deep water is used to show the convergence of the solution. The dimensions of this cylinder are chosen in such a way that they correspond to a typical column of a TLP. One of the biggest problems in showing numerical convergence on

three-dimensional structures is the lack of a simple way to present the velocity potentials on the structural surface for different numbers of elements. One could conceivably argue that convergence of the first-order loads would be a good indicator of the convergence of the velocity potential. However, the final computed values for the loads, which are obtained through integration of the velocity potentials, may be the result of error cancellations leading to false convergence estimates. For this reason, the convergence test results are presented in terms of the velocity potentials themselves, along four vertical lines on the side of the cylinder corresponding to $x = y$ and $x = -y$ (see Fig. 4.1).

Figure 4.2 shows the different meshes (1 - 8) used for the convergence test. In all cases, the corner nodes were assumed to have unit normals in the directions bisecting the normals of each of the elements (i.e., in the same direction of an equivalent rounded element) (Eatock Taylor and Teng, 1993). Tables 4.1 show the variation at selected points of the scattering potential (with an incident wave angle of 30°), and the surge radiation potential with structure discretization. A typical wave frequency $\omega = 1.0$ rad/sec was used. Also shown in the tables are the relative cpu times required to obtain the solution with each of the different cylinder discretizations. As can be seen, the computational effort increases greatly with the number of nodes used to discretize the structure. It can also be seen that there are two factors that affect the convergence of the solution. The first is the distance between the nodes used to describe the structure geometry, and the second is the number of Gauss points used to carry out the integrations within each of the elements. From the results in Tables 4.1, it is seen that Mesh 6 is adequate for the frequency of interest. Also, 4×4 Gaussian integration results in accurate values for the velocity potentials. Aside from the accuracy issue, it should be noted that, as expected, the potentials for the surge radiation problem are equal (or opposite) at points located across the x - and y -axes. This confirms the validity of the solution obtained utilizing symmetry considerations.



Point	Cylindrical Coordinates	Point	Cylindrical Coordinates	Point	Cylindrical Coordinates
1	$(a, \pi/4, 0)$	2	$(a, \pi/4, -b/2)$	3	$(a, \pi/4, -b)$
4	$(a, 3\pi/4, 0)$	5	$(a, 3\pi/4, -b/2)$	6	$(a, 3\pi/4, -b)$
7	$(a, 5\pi/4, 0)$	8	$(a, 5\pi/4, -b/2)$	9	$(a, 5\pi/4, -b)$
10	$(a, 7\pi/4, 0)$	11	$(a, 7\pi/4, -b/2)$	12	$(a, 7\pi/4, -b)$

Fig. 4.1 Distribution of points to check convergence of velocity potentials. There are three sets of points corresponding to $\theta = 45^\circ, 135^\circ, 215^\circ,$ and 315° , at three different levels: $z=0, z=-b/2,$ and $z=-b.$

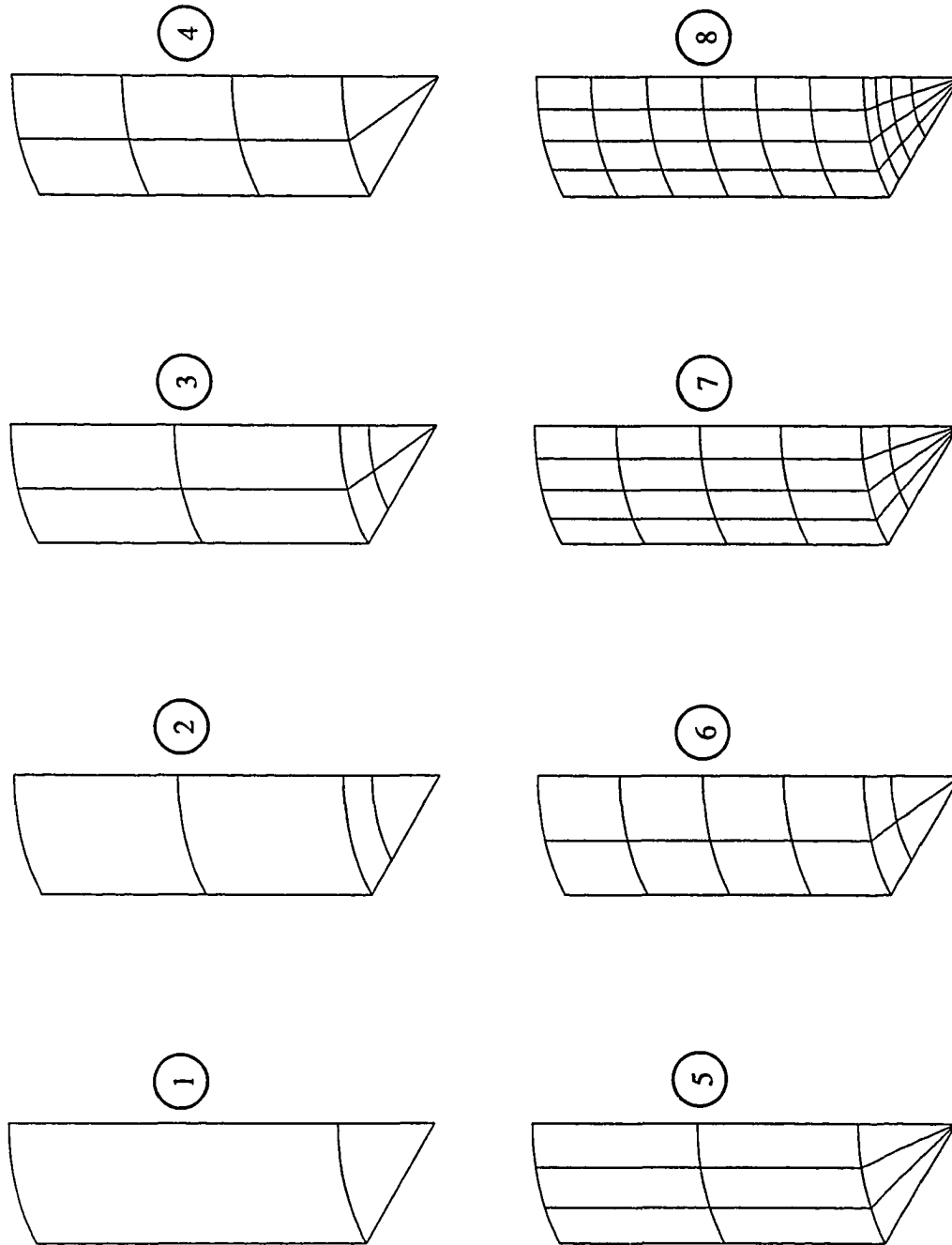


Fig. 4.2 Element distribution on one eighth-model of circular cylinder of radius $a = 10$ m. and draft $b = 30$ m.

Table 4.1a Convergence of complex surge radiated potential and scattered potential at different points on a circular cylinder with radius $a = 10$ m, and draft $b = 30$ m. for $\omega = 1.0$ rad/sec and $\beta = 30^\circ$ with element/node distribution and number of Gauss points used for the integration. Also shown are relative cpu times required.

Mesh	Num. of elements	Num. of nodes	Num. of Integ. Pts.	Normalized cpu time	Point 1	Point 2	Point 3	Point 4	Point 5	Point 6
1	2	11	4x4	1.0	(-9.792, 5.190) (-0.528, 8.926)	(-2.091, 3.775) (-0.174, 1.929)	(-0.288, 1.242) (-0.216, 0.258)	(9.792, -5.190) (-4.434, -2.384)	(2.091, -3.775) (-0.964, -0.553)	(0.288, -1.242) (-0.143, 0.007)
2	4	21	4x4	3.2	(-9.714, 5.175) (-0.444, 8.407)	(-2.085, 4.119) (-0.121, 1.806)	(-0.296, 1.248) (-0.174, 0.294)	(9.714, -5.175) (-4.394, -2.228)	(2.085, -4.119) (-0.946, -0.475)	(0.296, -1.248) (-0.118, 0.048)
3	8	33	4x4	8.2	(-9.826, 5.203) (-0.455, 8.431)	(-2.110, 4.166) (-0.122, 1.810)	(-0.299, 1.241) (-0.175, 0.293)	(9.826, -5.203) (-4.421, -2.231)	(2.110, -4.166) (-0.952, -0.474)	(0.299, -1.241) (-0.119, 0.048)
4	8	33	4x4	8.3	(-9.862, 5.198) (-0.453, 8.368)	(-2.126, 4.153) (-0.112, 1.806)	(-0.336, 1.661) (-0.146, 0.299)	(9.862, -5.198) (-4.407, -2.207)	(2.126, -4.153) (-0.951, -0.474)	(0.336, -1.661) (-0.144, 0.008)
5	9	34	4x4	9.0	(-9.953, 5.203) (-0.460, 8.503)	(-2.142, 4.215) (-0.119, 1.827)	(-0.330, 1.479) (-0.156, 0.295)	(9.953, -5.203) (-4.427, -2.244)	(2.142, -4.215) (-0.956, -0.481)	(0.330, -1.479) (-0.142, 0.013)
6	12	49	4x4	17.7	(-9.860, 5.218) (-0.454, 8.352)	(-2.125, 4.146) (-0.111, 1.805)	(-0.314, 1.480) (-0.162, 0.299)	(9.860, -5.218) (-4.410, -2.204)	(2.125, -4.146) (-0.950, -0.470)	(0.314, -1.480) (-0.126, 0.037)
7	24	85	4x4	56.5	(-9.878, 5.221) (-0.457, 8.360)	(-2.129, 4.151) (-0.111, 1.807)	(-0.315, 1.467) (-0.162, 0.299)	(9.878, -5.221) (-4.413, -2.204)	(2.129, -4.151) (-0.951, -0.470)	(0.315, -1.467) (-0.126, 0.036)
8	40	141	4x4	162.2	(-9.877, 5.223) (-0.456, 8.347)	(-2.130, 4.152) (-0.110, 1.806)	(-0.310, 1.463) (-0.164, 0.299)	(9.877, -5.223) (-4.411, -2.200)	(2.130, -4.152) (-0.950, -0.470)	(0.310, -1.463) (-0.123, 0.042)
6	12	49	2x2	10.9	(-9.934, 5.243) (-0.429, 8.448)	(-2.137, 4.175) (-0.109, 1.817)	(-0.314, 1.503) (-0.163, 0.301)	(9.934, -5.243) (-4.424, -2.233)	(2.137, -4.175) (-0.951, -0.473)	(0.314, -1.503) (-0.125, 0.038)
6	12	49	8x8	44.8	(-9.852, 5.218) (-0.455, 8.347)	(-2.124, 4.143) (-0.111, 1.805)	(-0.314, 1.440) (-0.162, 0.298)	(9.852, -5.218) (-4.410, -2.202)	(2.124, -4.143) (-0.950, -0.470)	(0.314, -1.440) (-0.126, 0.036)
8	40	141	8x8	409.5	(-9.877, 5.224) (-0.456, 8.349)	(-2.130, 4.152) (-0.110, 1.806)	(-0.310, 1.434) (-0.165, 0.298)	(9.877, -5.224) (-4.411, -2.201)	(2.130, -4.152) (-0.950, -0.470)	(0.310, -1.434) (-0.123, 0.042)

Table 4.1b Convergence of complex surge radiated potential and scattered potential at different points on a circular cylinder with radius $a = 10$ m, and draft $b = 30$ m. for $\omega = 1.0$ rad/sec and $\beta = 30^\circ$ with element/node distribution and number of Gauss points used for the integration. Also shown are relative cpu times required.

Mesh	Num. of elements	Num. of nodes	Num. of Integ. Pts.	Normalized cpu time	Point 7	Point 8	Point 9	Point 10	Point 11	Point 12
1	2	11	4x4	1.0	(-9.792, 5.190) (-0.528, 8.926)	(-2.091, 3.775) (-0.174, 1.929)	(-0.288, 1.242) (-0.216, 0.258)	(9.792, -5.190) (-4.434, -2.384)	(2.091, -3.775) (-0.964, -0.553)	(0.288, -1.242) (-0.143, 0.007)
2	4	21	4x4	3.2	(-9.714, 5.175) (-0.444, 8.407)	(-2.085, 4.119) (-0.121, 1.806)	(-0.296, 1.248) (-0.174, 0.294)	(9.714, -5.175) (-4.394, -2.228)	(2.085, -4.119) (-0.946, -0.475)	(0.296, -1.248) (-0.118, 0.048)
3	8	33	4x4	8.2	(-9.826, 5.203) (-0.455, 8.431)	(-2.110, 4.166) (-0.122, 1.810)	(-0.299, 1.241) (-0.175, 0.293)	(9.826, -5.203) (-4.421, -2.231)	(2.110, -4.166) (-0.952, -0.474)	(0.299, -1.241) (-0.119, 0.048)
4	8	33	4x4	8.3	(-9.862, 5.198) (-0.453, 8.368)	(-2.126, 4.153) (-0.112, 1.806)	(-0.336, 1.661) (-0.146, 0.299)	(9.862, -5.198) (-4.407, -2.207)	(2.126, -4.153) (-0.951, -0.474)	(0.336, -1.661) (-0.144, 0.008)
5	9	34	4x4	9.0	(-9.953, 5.203) (-0.460, 8.503)	(-2.142, 4.215) (-0.119, 1.827)	(-0.330, 1.479) (-0.156, 0.295)	(9.953, -5.203) (-4.427, -2.244)	(2.142, -4.215) (-0.956, -0.481)	(0.330, -1.479) (-0.142, 0.013)
6	12	49	4x4	17.7	(-9.860, 5.218) (-0.454, 8.352)	(-2.125, 4.146) (-0.111, 1.805)	(-0.314, 1.480) (-0.162, 0.299)	(9.860, -5.218) (-4.410, -2.204)	(2.125, -4.146) (-0.950, -0.470)	(0.314, -1.480) (-0.126, 0.037)
7	24	85	4x4	56.5	(-9.878, 5.221) (-0.457, 8.360)	(-2.129, 4.151) (-0.111, 1.807)	(-0.315, 1.467) (-0.162, 0.299)	(9.878, -5.221) (-4.413, -2.204)	(2.129, -4.151) (-0.951, -0.470)	(0.315, -1.467) (-0.126, 0.036)
8	40	141	4x4	162.2	(-9.877, 5.223) (-0.456, 8.347)	(-2.130, 4.152) (-0.110, 1.806)	(-0.310, 1.463) (-0.164, 0.299)	(9.877, -5.223) (-4.411, -2.200)	(2.130, -4.152) (-0.950, -0.470)	(0.310, -1.463) (-0.123, 0.042)
6	12	49	2x2	10.9	(-9.934, 5.243) (-0.429, 8.448)	(-2.137, 4.175) (-0.109, 1.817)	(-0.314, 1.503) (-0.163, 0.301)	(9.934, -5.243) (-4.424, -2.233)	(2.137, -4.175) (-0.951, -0.473)	(0.314, -1.503) (-0.125, 0.038)
6	12	49	8x8	44.8	(-9.852, 5.218) (-0.455, 8.347)	(-2.124, 4.143) (-0.111, 1.805)	(-0.314, 1.440) (-0.162, 0.298)	(9.852, -5.218) (-4.410, -2.202)	(2.124, -4.143) (-0.950, -0.470)	(0.314, -1.440) (-0.126, 0.036)
8	40	141	8x8	409.5	(-9.877, 5.224) (-0.456, 8.349)	(-2.130, 4.152) (-0.110, 1.806)	(-0.310, 1.434) (-0.165, 0.298)	(9.877, -5.224) (-4.411, -2.201)	(2.130, -4.152) (-0.950, -0.470)	(0.310, -1.434) (-0.123, 0.042)

4.2 Sum- and Difference-frequency Loads on ISSC TLP

The ISSC TLP is a fictitious TLP created to allow the ocean engineering community to have a common structure to compare and validate different techniques developed to better understand the response of ocean structures to wave loading (Eatock Taylor and Jeffreys, 1986). The properties of the ISSC TLP are presented in Table 4.2. As can be seen, the TLP has three planes of symmetry, and has columns that are comparable in size to the cylinder used to show convergence of the first-order scattered and radiation problems in the previous section.

In this section results will be presented for the second-order sum- and difference-frequency hydrodynamic loads on the ISSC TLP. Although the Green's function utilized is only valid for deep water, the tethered TLP will be assumed to still be anchored at a distance of 450 m. below the still water level, which results in tether lengths of 415 m. In order to observe the significance of the first-order body motions on the second-order hydrodynamic loads, a fixed (stationary) ISSC TLP is also considered.

The frequency range considered in the computation of the second-order, sum- and difference-frequency loads on the ISSC TLP in bichromatic bidirectional deep water waves is $0.5 \leq \nu = \omega^2 a / g \leq 1.5$, where a is the column radius. Before these loads are computed, the issue of TLP discretization is addressed. Figure 4.3 shows four different discretizations (meshes 1 - 4) of the ISSC TLP having 208, 393, 500, and 604 nodes respectively. These four discretizations are used to obtain the surge, heave, and pitch radiated potentials as well as the scattered potential along the water line of the column located on the first quadrant (column 1). Results for two dimensionless frequencies are presented. These frequencies correspond to the smallest frequency (i.e., $\nu = 0.5$) and the largest sum-frequency (i.e., the double frequency associated with $\nu = 1.5$) in the range for

Table 4.2 Geometric Dimensions and Structural Properties of the ISSC TLP (Eatock Talyor and Jeffreys, 1986).

<u>Parameter</u>	<u>Value</u>
Spacing between column centers	86.25 m
Column radius	8.44 m
Pontoon width	7.5 m
Pontoon height	10.5 m
Draft	35.0 m
Wave height	2.0 m
Weight	40.5×10^6 Kg
Displacement	54.5×10^6 Kg
Tether pretension per group	4.5×10^6 Kg
Tether axial stiffness per group	2.0325×10^5 kN/m
Tether length	415.0 m
Waterplane area	894.0 m^2
First moments of waterplane area	0.0 m^3
Second moments of waterplane area	$1.6787 \times 10^6 \text{ m}^4$
Product moment of waterplane area	0.0 m^3
Roll & pitch moments of inertia	$82.37 \times 10^9 \text{ Kg m}^2$
Yaw moment of inertia	$98.07 \times 10^9 \text{ Kg m}^2$
Vertical position of center of gravity above keel	38.0 m
Vertical position of center of buoyancy above keel	9.0 m
Vertical position of center of rotation above keel	38.0 m

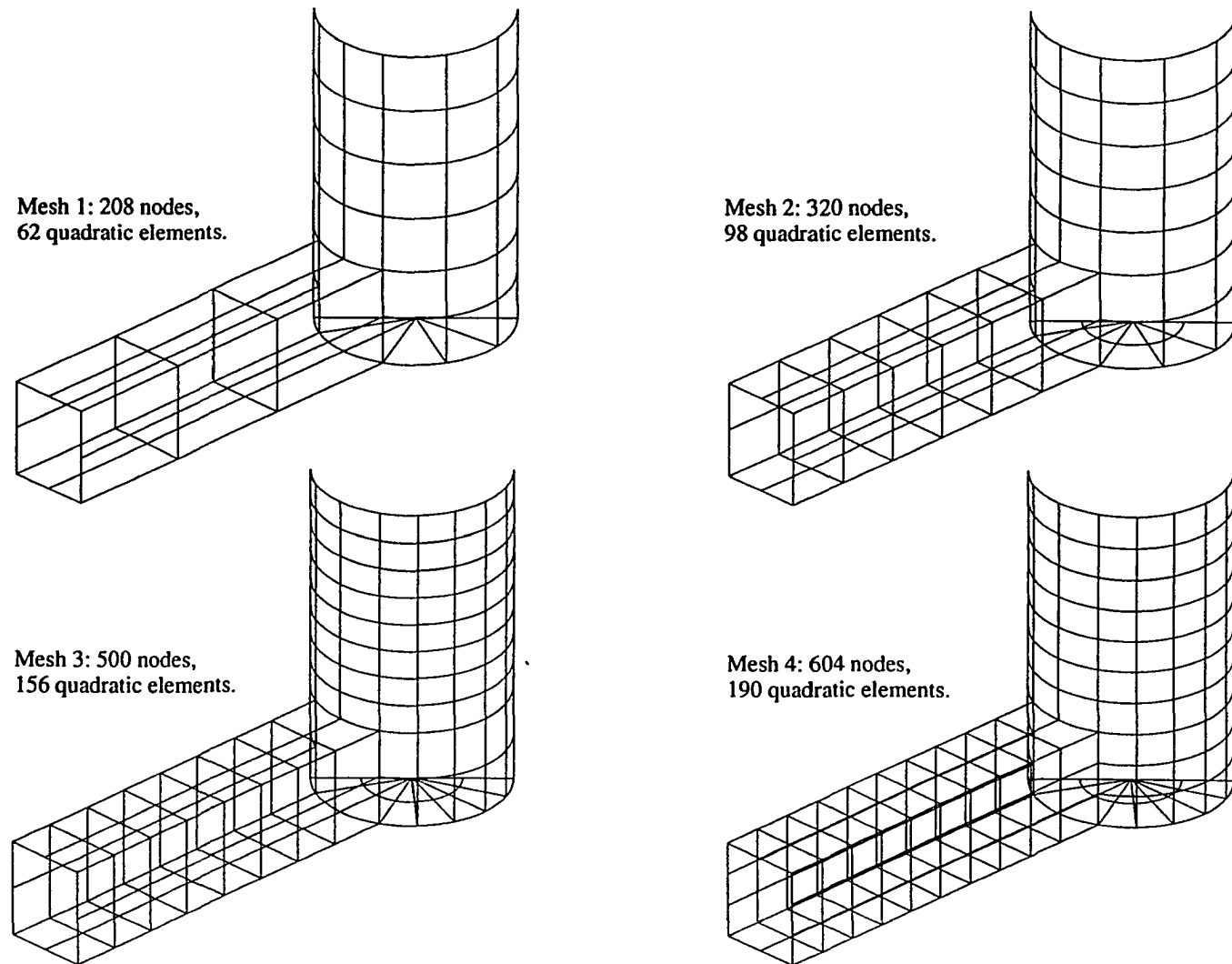


Fig. 4.3 Different mesh discretizations of one-eighth model for ISSC TLP.

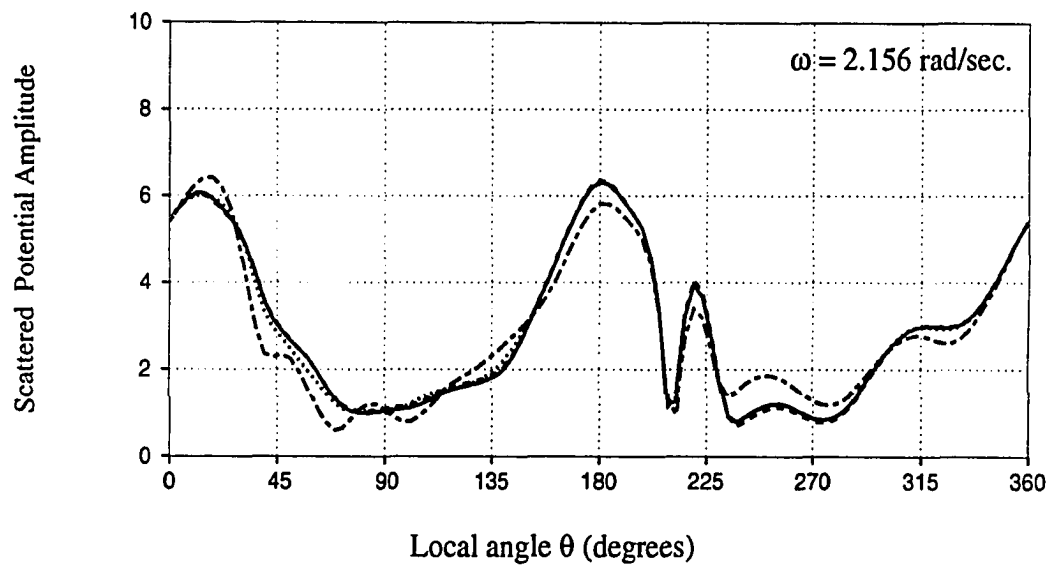
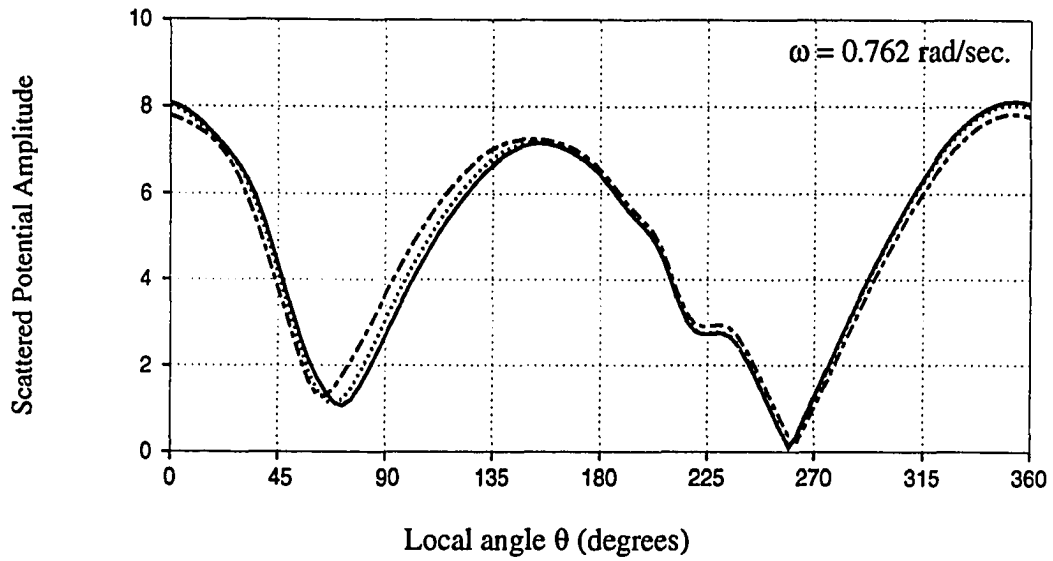


Fig. 4.4a Variation of scattered potential amplitude around the water line of column 1 with TLP discretization. Notation: - - - Mesh 1, Mesh 2, - . - Mesh 3, and — Mesh 4.

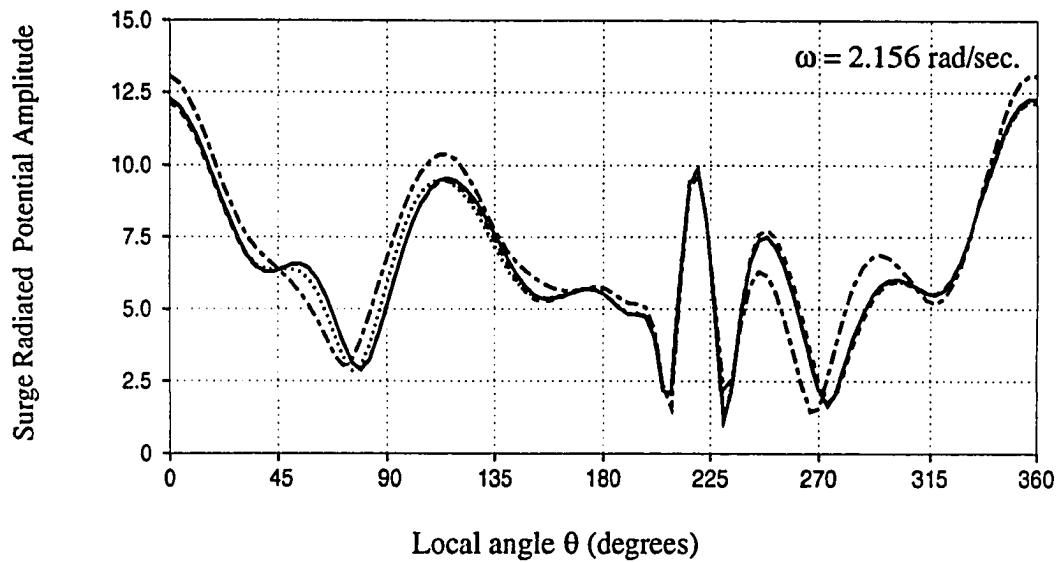
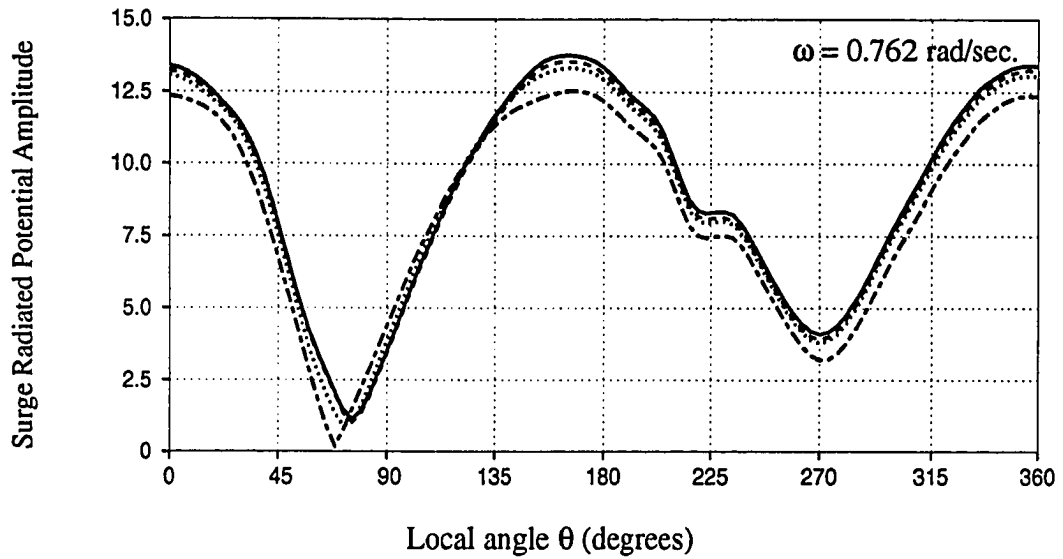


Fig. 4.4b Variation of surge radiated potential amplitude around the water line of column 1 with TLP discretization. Notation: - - - Mesh 1, Mesh 2, - . - Mesh 3, and ——— Mesh 4.

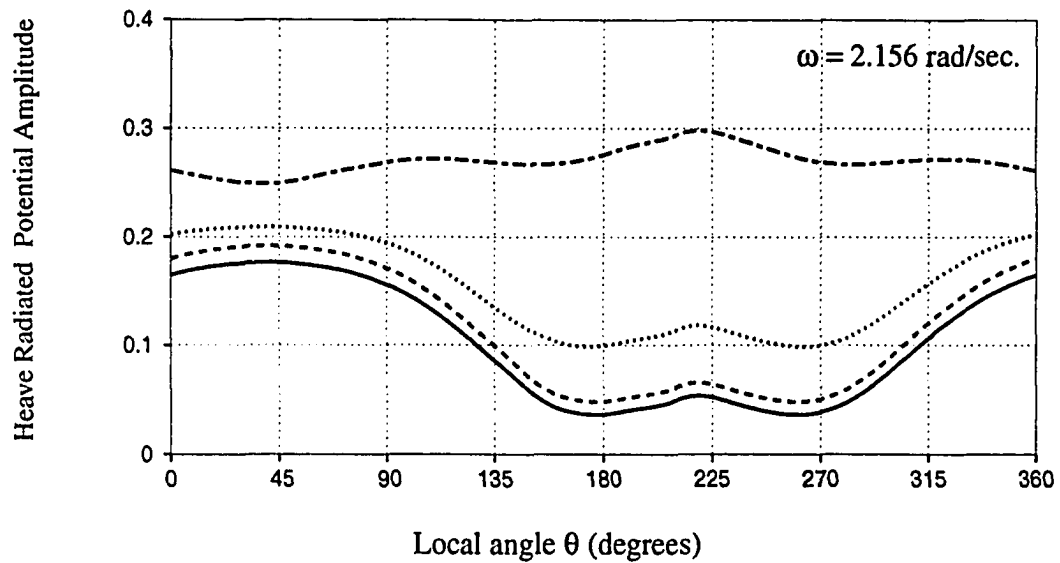
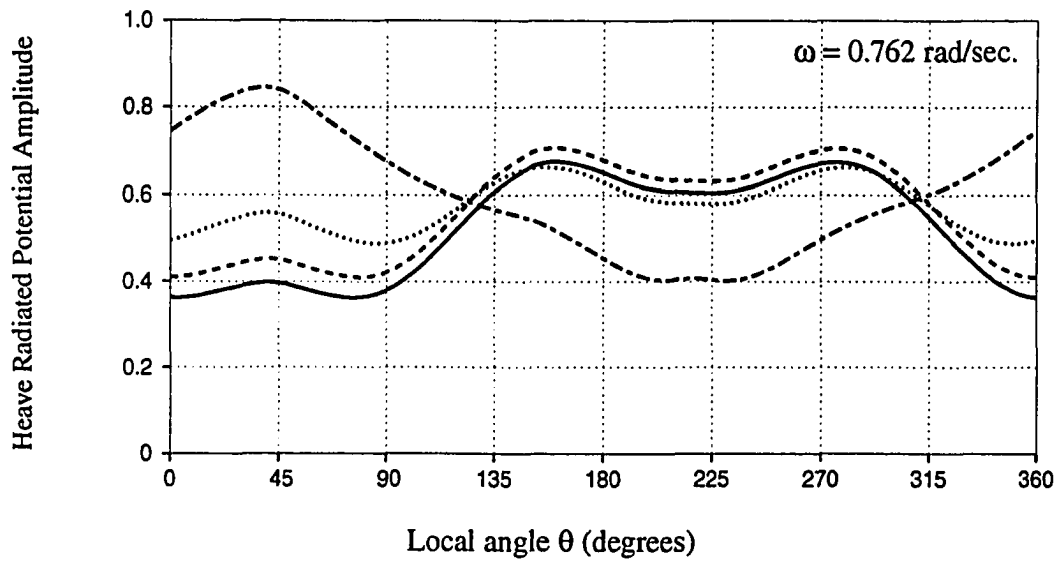


Fig. 4.4c Variation of heave radiated potential amplitude around the water line of column 1 with TLP discretization. Notation: - - - Mesh 1, Mesh 2, - . - Mesh 3, and — Mesh 4.

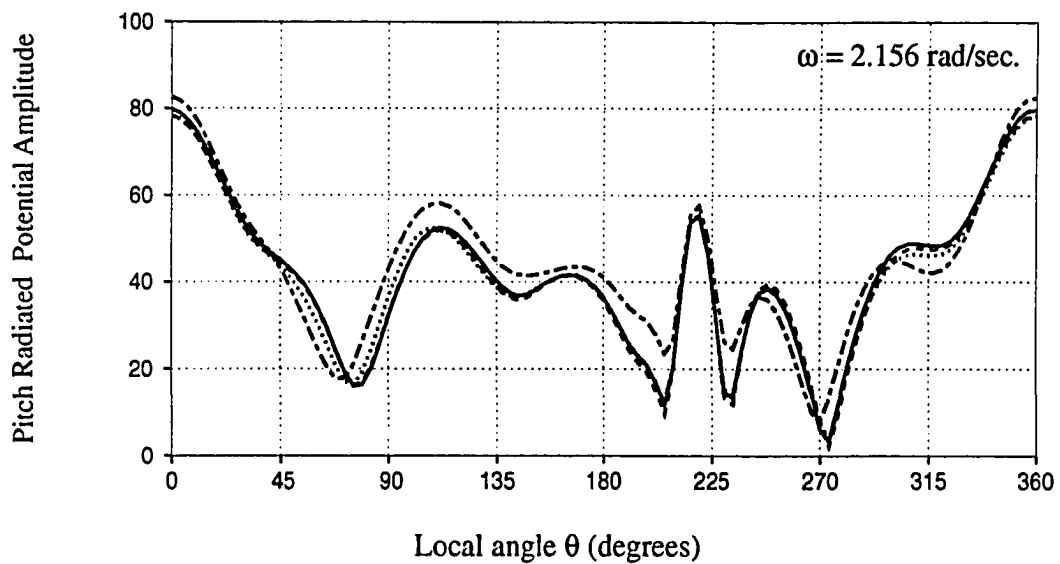
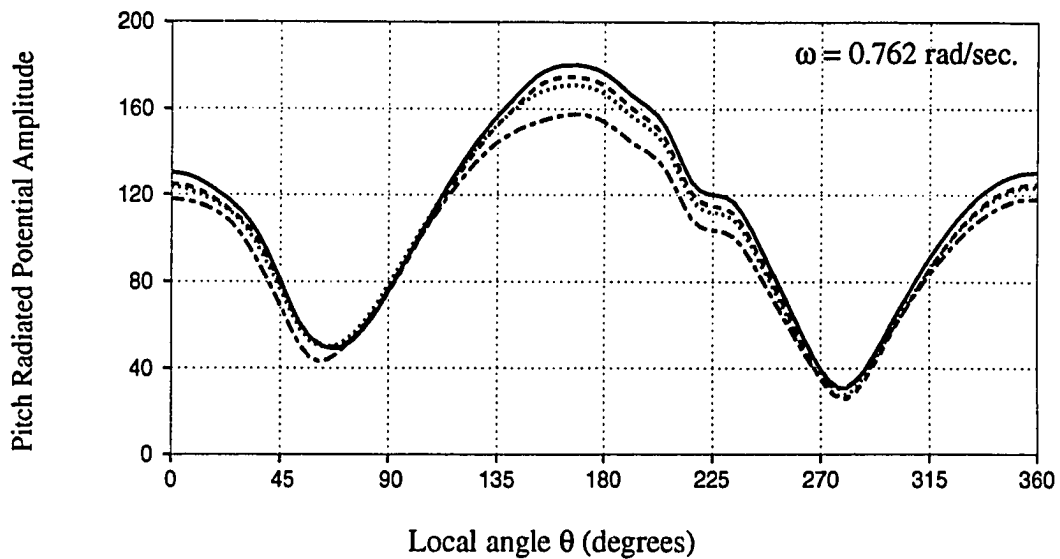


Fig. 4.4d Variation of pitch radiated potential amplitude around the water line of column 1 with TLP discretization. Notation: - - - - Mesh 1, Mesh 2, - · - · Mesh 3, and ——— Mesh 4.

associated with $\nu = 1.5$) in the range for which second-order loads are to be computed. The results are presented in Figs. 4.4 as plots of the amplitude of the potential around the column. From the figures it can be seen that there is significantly more oscillation of the velocity potential for the higher frequency. This suggests that the wave frequency plays a role in the selection of mesh discretization. It is also seen that the heave mode requires a finer mesh for convergence of the potentials as compared with the other modes.

Next, a comparison with published results of the first-order loads is presented. It should be noted that the specifications of the ISSC TLP place it in water depth of 450 m., not in deep water as will be assumed in this study. For this reason, small differences between the present results and published results for the ISSC TLP in finite water depth are to be expected, especially at low frequencies. The magnitudes of the exciting forces and moments and the added mass and radiation damping components in the various modes of oscillation are compared with the corresponding estimates of Korsmeyer *et al.* (1988) who used the computer program WAMIT. Utilizing a mesh of 4048 constant panels (over the entire TLP), they obtained the exciting forces and moments and the added mass and radiation damping values at seven specific wave periods (2, 6, 10, 14, 18, 20, and 22 secs.) The results presented herein are given as plots in the dimensionless frequency range $\nu = \omega^2 a/g < 1.5$ (a being the column radius). With the exception of the 2-second period, the results given by Korsmeyer *et al.* fall within this dimensionless frequency range. For the results presented, both the mesh containing 320 nodes (mesh 2) and the one containing 604 nodes (mesh 4) were used to perform the calculations producing similar results throughout the frequency range considered. For the coarser mesh, mesh 2, the number of nodes results in a 2560×2560 system of equations for the source strengths, compared to the 4048×4048 system resulting from the constant panel method. This again shows the benefit of utilizing higher order elements for the solution of the first-order problem. An examination of Figs. 4.5 and 4.6 shows that, there is good

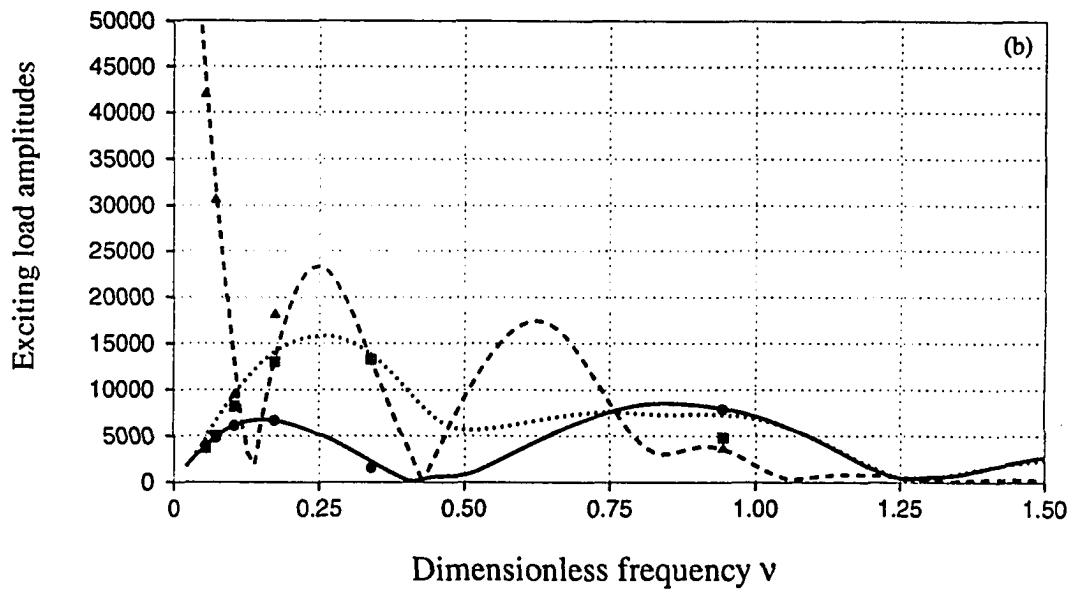
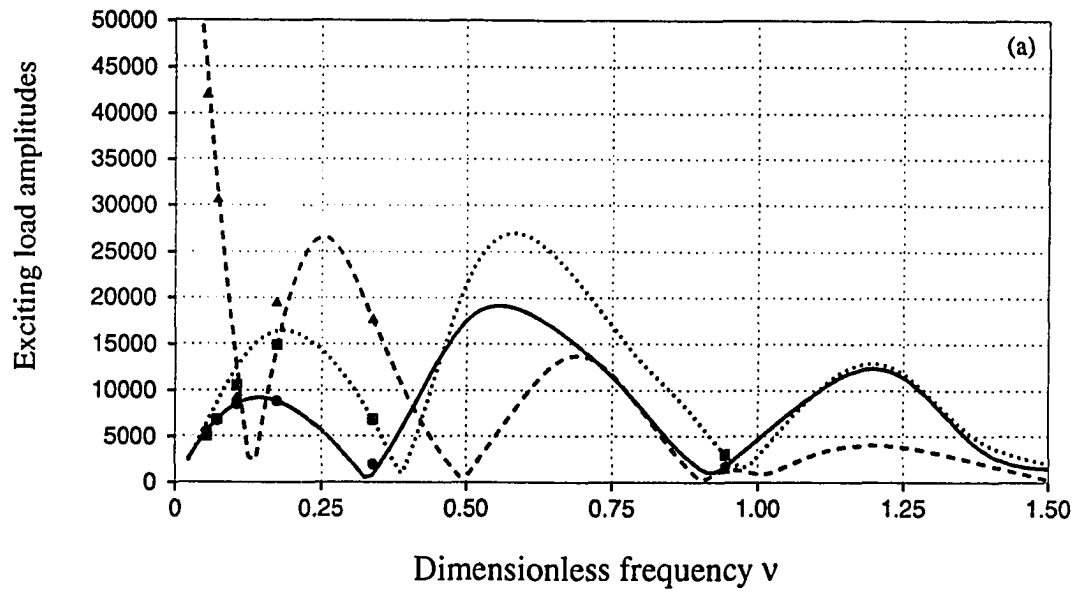


Fig. 4.5 Exciting load amplitudes on the ISSC TLP in dimensional (SI) units for (a) $\beta = 0^\circ$ and (b) $\beta = 45^\circ$. Notation: $\text{—}\bullet\text{—}$ F_x , $\text{--}\blacktriangle\text{--}$ $10 F_z$, $\cdots\blacksquare\cdots$ $M_y/10$. Symbols represent the results obtained by Korsmeyer *et al.*

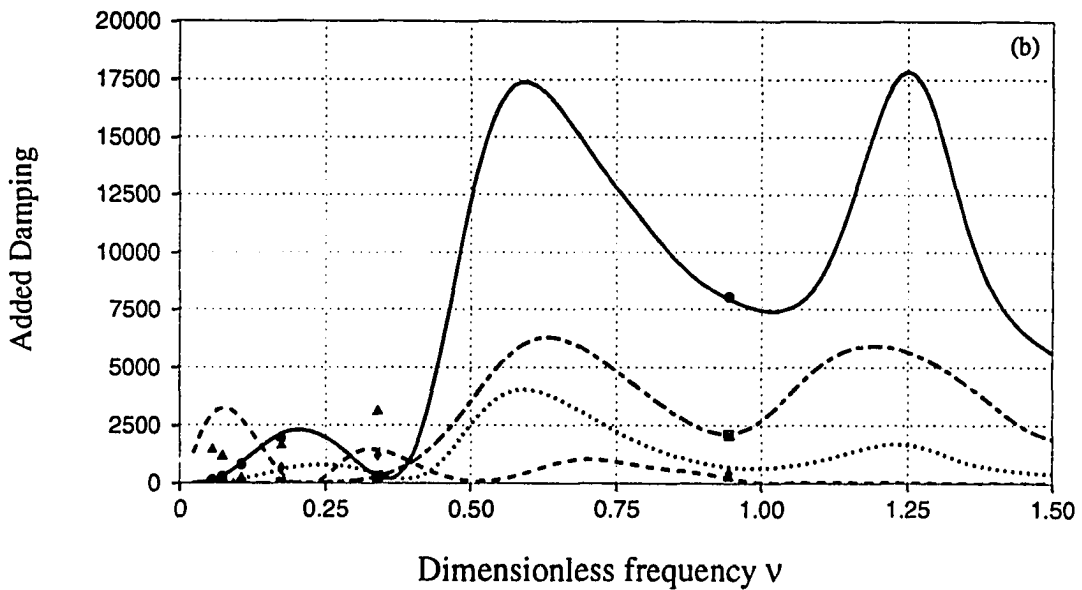
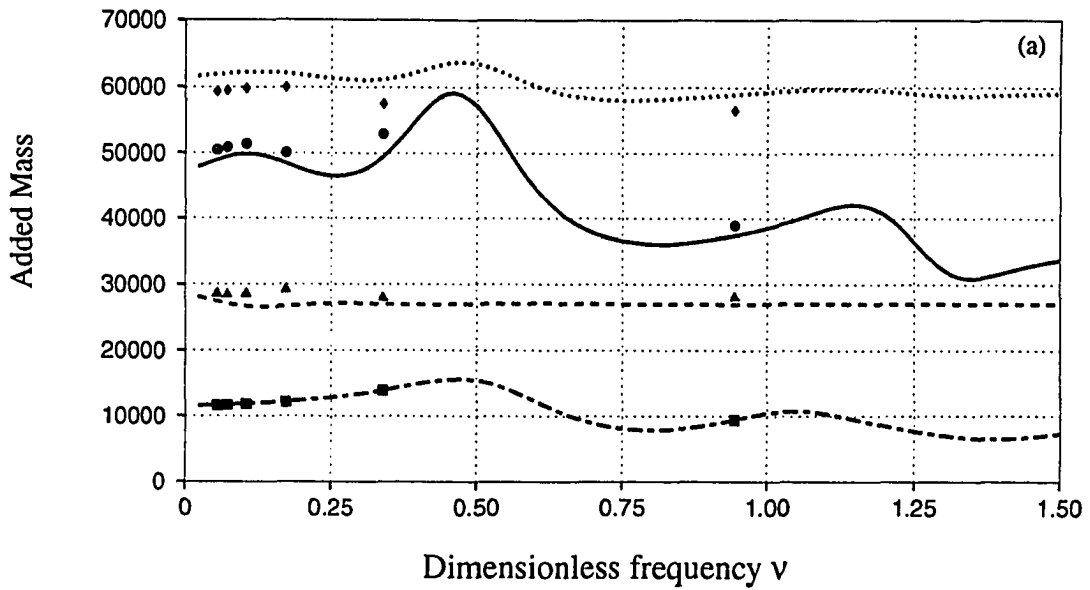


Fig. 4.6 (a) Added mass and (b) radiated damping on ISSC TLP in dimensional (SI) units. Notation: \bullet — A_{11}, B_{11} , \blacktriangle — $A_{33}, 10 B_{33}$, \blacklozenge — $A_{55}/1000, B_{55}/1000$, \blacksquare — $A_{66}/10000, B_{66}/10000$. Symbols represent the results obtained by Korsmeyer *et al.*

agreement between the two methodologies at the larger frequencies (where the influence of the sea bed is insignificant), and that the agreement for the added mass and radiation damping values is not as good. This slight discrepancy results from the fact that the structure discretization is more critical in the radiation problem since the structure itself is responsible for generating the wave field as opposed to the scattering problem, when its contribution to the wave field is less due to the presence of the incident wave field. Overall, however, the results shown are seen to be in agreement with those obtained from the WAMIT program. It should be emphasized again that the present numerical technique is valid in deep water, whereas the results presented by Krosmeier *et al.* were obtained for the ISSC TLP situated in water depth of 450 m. From part (b) of Fig. 4.6, it is seen that there is a discrepancy in the results for heave added damping. However, the values themselves are small, and the discrepancies occur at the relatively low frequencies where the finite water depth still plays a role.

As was discussed in Section 4.1, an accurate solution to the first-order problem depends on proper discretization of the structure. An adequate discretization will be one that is able to accommodate the smallest waves to be studied. For this reason, two meshes are used in the computation of the second-order hydrodynamic loads: a fine mesh (604 nodes) for the sum-frequency loads, and a coarser mesh (320 nodes) for the difference-frequency loads. The selection of these meshes is in accordance with the practice of having a minimum number of nodes per wavelength. In this study a dimensionless frequency range $0.5 \leq \nu = \omega^2 a/g \leq 1.5$ is used. For the sum-frequency case, this results in the wavelengths in the range 8.84 m. to 106.06 m. These wavelengths are critical in the selection of the mesh discretization, and in the selection of the radial distance R delineating the numerical and analytical integration domains of the free-surface integral (Kim, 1992, Lee *et al.*, 1991, and Newman and Lee, 1992).

Results for the second-order sum-frequency loads on the ISSC TLP in bichromatic bidirectional waves are presented to illustrate the effect of wave directionality on the hydrodynamic loads. For this reason, three incident wave angle combinations are selected: $\beta_j = 0^\circ, \beta_k = 45^\circ$; $\beta_j = 45^\circ, \beta_k = 0^\circ$; and $\beta_j = \beta_k = 22.5^\circ$. Unidirectional loads were also computed for 0 and 45 degrees, but are not presented herein in the same format. Due to the large number of figures generated from this study, the unidirectional results are only used to obtain ratios for the different loads from the bidirectional cases. Although the results will be discussed from different perspectives, the discussion will be focused primarily on the effect of directionality on the second-order hydrodynamic loads.

The hydrodynamic loads are presented as quadratic transfer functions (QTFs) which are shown as surface plots (and corresponding contour plots) of the dimensionless frequency components v_j, v_k , for different combinations of wave incidence. In all cases, the QTFs satisfy the symmetry relation resulting in surface plots that are symmetric about the line $v_j = v_k$. The figures are ordered to facilitate comparisons between similar load components (i.e., surge, sway, etc.) for different combinations of incident wave directions. For every mode of loading, three sets of (a) and (b) figures may be compared to investigate the effect of wave directionality and first-order body motions. Each of these sets corresponds to a particular pair of angles of wave incidence. The effect of body motions may be easily seen by comparing parts (a) and (b) in each of the figures. The effect of wave directionality may be quantified by comparing sets of three consecutive figures corresponding to the incident wave combinations: $\beta_j = 0^\circ, \beta_k = 45^\circ$; $\beta_j = 45^\circ, \beta_k = 0^\circ$; and $\beta_j = \beta_k = 22.5^\circ$. The unidirectional set is presented to show that the hydrodynamic load QTFs resulting from waves at 0° and 45° are not equal to those arising from those at the "average angle" of 22.5° . All load QTFs are presented in dimensionless form. The

non-dimensionalization factor for the forces is $\rho g a \Gamma_j \Gamma_k$, while for the moments, the factor is $\rho g a^2 \Gamma_j \Gamma_k$, with a equal to the column radius of 8.44 m.

Figure 4.7 presents the second-order sum-frequency surge QTFs for a fixed and tethered ISSC TLP for incident wave combinations of $\beta_j = 0^\circ$, $\beta_k = 45^\circ$. It can be seen from the figure that the QTFs are oscillatory and that, in general, they increase with increasing frequency. The oscillatory nature of the curves is caused by hydrodynamic interaction effects between the TLP columns. In comparing the surge QTFs for the fixed and tethered cases [parts (a) and (b) of the figure], it is seen that while there are slight differences in the QTF values, their magnitude and general behavior is very similar. Figure 4.8 presents similar results as those in Fig. 4.7, but for a different wave incidence angle combination of $\beta_j = 45^\circ$, $\beta_k = 0^\circ$. As for the $\beta_j = 0^\circ$, $\beta_k = 45^\circ$ case, the QTFs are again oscillatory and increasing with frequency, and the QTF values for the latter wave incidence combination are, in general, higher in magnitude. It should be noted that the QTFs from Figs. 4.7 and 4.8 do agree with each other when $\nu_j = \nu_k$ (i.e., for monochromatic waves). However, for bichromatic waves, they differ significantly. For example, for values along $\nu_k = 0.5$, (i.e. along the left edge of the surfaces), the QTF values in Fig. 4.7 oscillate in the range 0.0 to 2.0. In Fig. 4.8 the QTF values are seen to reach values greater than 8.0 along the same constant-frequency line. This clearly shows the effect of wave directionality. Comparing the (a) and (b) parts of these figures shows that while there are slight differences in the QTFs over this bi-frequency range, they are not significantly affected by first-order body motions.

The computation of the hydrodynamic load QTFs in the bidirectional case involves considerably more computational effort than the corresponding unidirectional calculations. Therefore, one approach that has been suggested to estimate the effect of wave directionality is to evaluate the load QTFs in unidirectional waves with an angle of

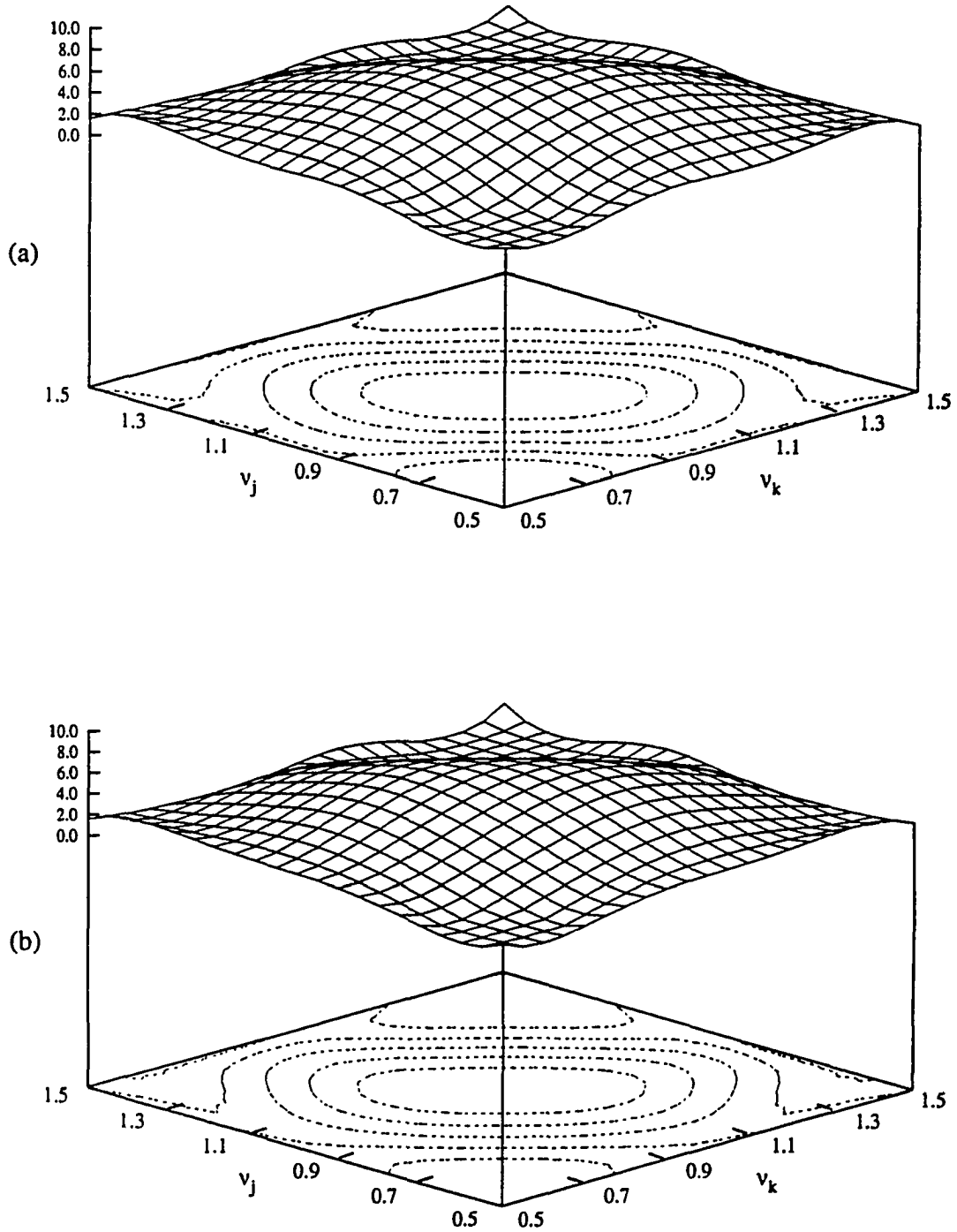


Fig. 4.7 Sum-frequency hydrodynamic surge force QTF, $H^+(\omega_j, \omega_k; \beta_j, \beta_k)$, for the ISSC TLP with $\beta_j = 0^\circ$, $\beta_k = 45^\circ$. Notations: (a) Fixed TLP, (b) Tethered TLP.

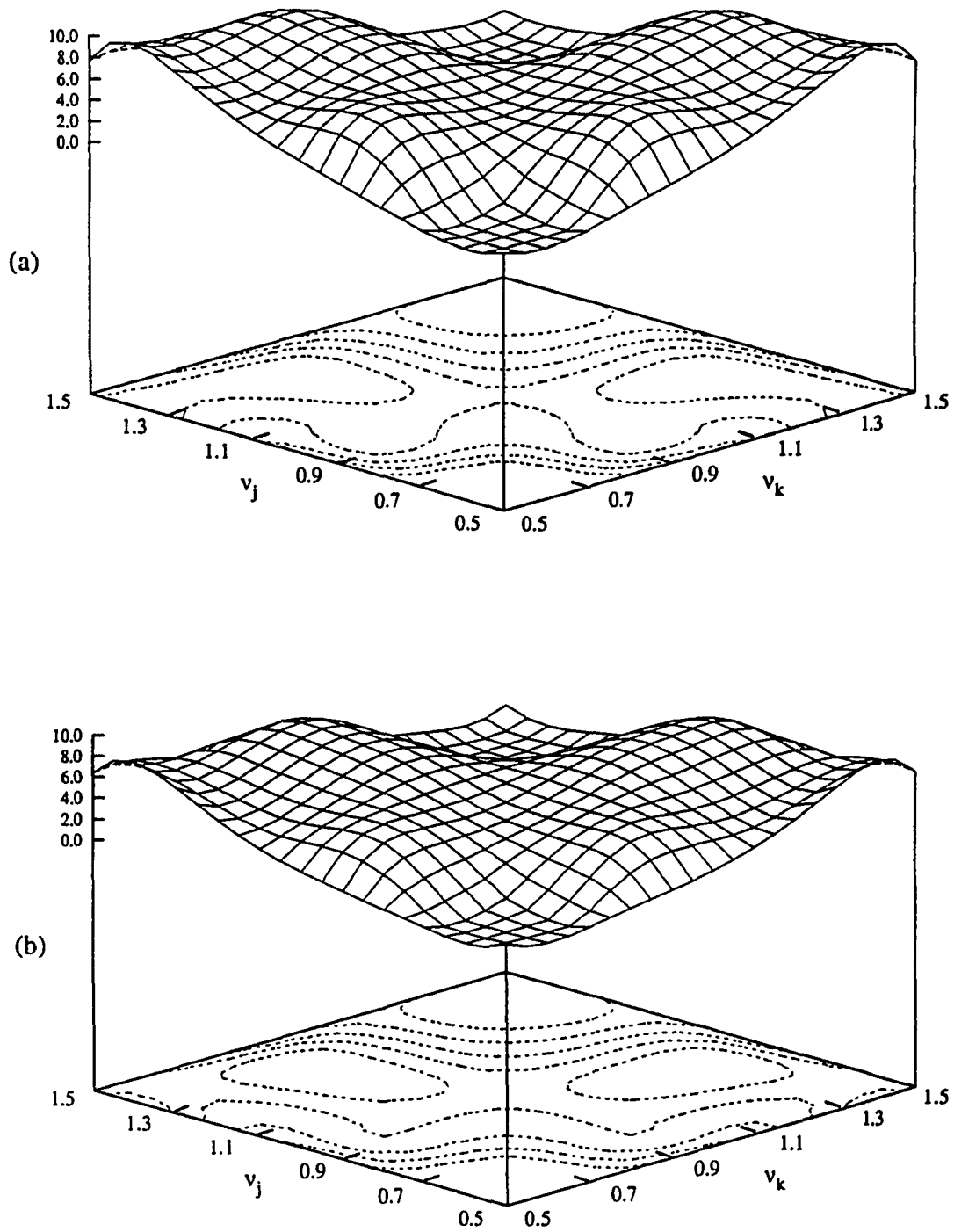


Fig. 4.8 Sum-frequency hydrodynamic surge force QTF, $H^+(\omega_j, \omega_k; \beta_j, \beta_k)$, for the ISSC TLP with $\beta_j = 45^\circ$, $\beta_k = 0^\circ$. Notations: (a) Fixed TLP, (b) Tethered TLP.

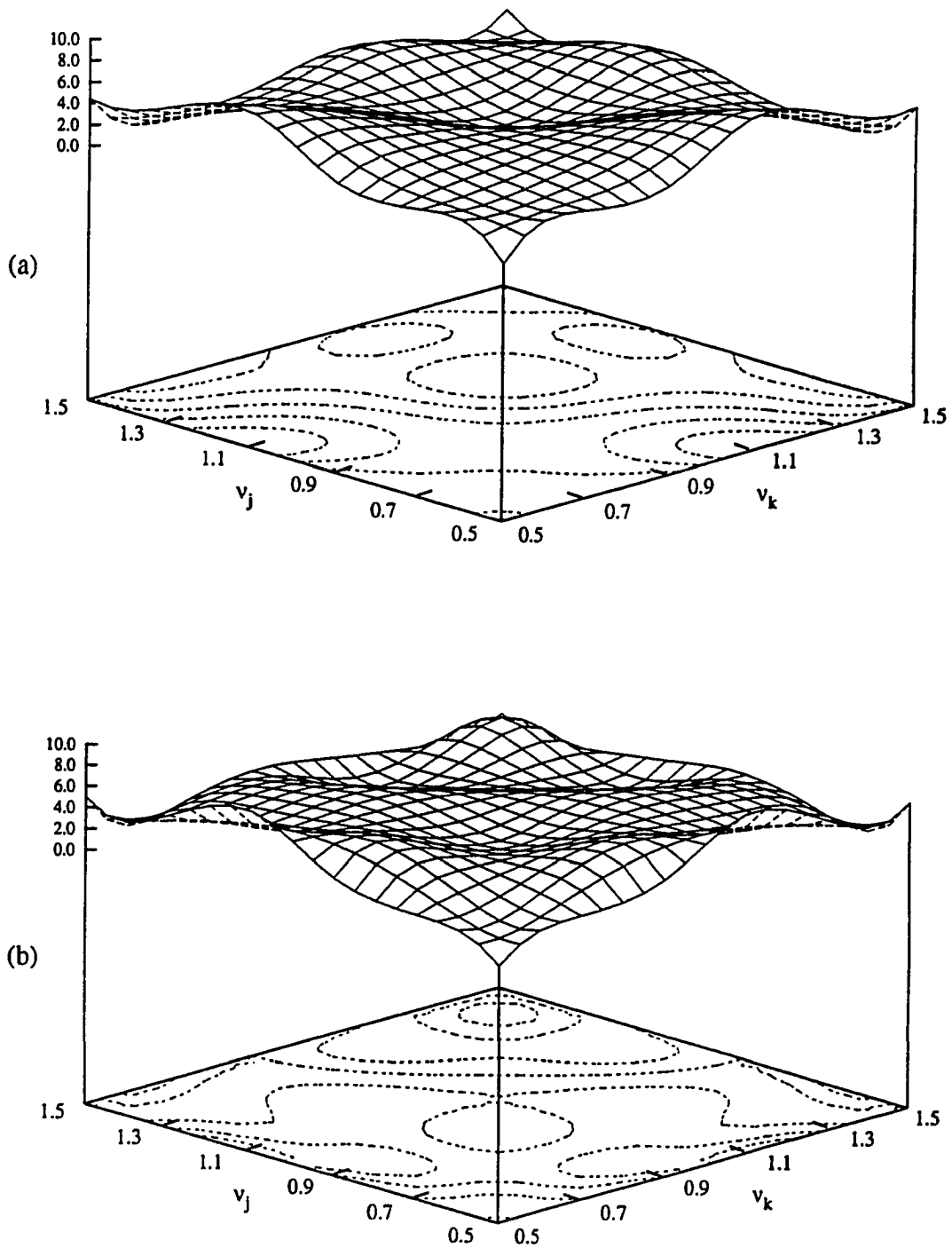


Fig. 4.9 Sum-frequency hydrodynamic surge force QTF, $H^+(\omega_j, \omega_k; \beta_j, \beta_k)$, for the ISSC TLP with $\beta_j = \beta_k = 22.5^\circ$. Notations: (a) Fixed TLP, (b) Tethered TLP.

incidence equal to the average angle of the two wave components. In this case, the unidirectional angle is 22.5° . The surge sum-frequency QTFs are shown in Fig. 4.9 corresponding to incident wave angles $\beta_j = \beta_k = 22.5^\circ$. In this case, the oscillatory nature of the surge QTFs is seen to be more pronounced and, as expected, the QTF values are significantly different from those in Figs. 4.7 and 4.8. Not only are the QTFs in Fig. 4.9 more oscillatory than those in Figs. 4.7 and 4.8, they are also larger in magnitude over wider frequency ranges. For the tethered ISSC TLP, the QTFs vary in a more severe form reaching dimensionless values up to 10.0. Regarding the effect of first-order body motions on the QTFs, it is seen from parts (a) and (b) of Fig. 4.9 that they are more significant in the unidirectional case than in the previous bidirectional cases considered. It appears that the lack of symmetry in the incident wave components results in an additive contribution to the second-order loads, as compared to the 0° and 45° cases, which have symmetry at each of the the first-order wave components. It is also seen that the most significant contribution of the first-order body motions to the unidirectional QTFs occurs in the vicinity of monochromatic waves indicating a strong dependency on whether the first-order body motions caused by each of the wave components are in phase with each other.

Figures 4.10 - 4.12 show the corresponding sum-frequency QTFs for the sway loading. As expected, the sway QTF values are lower than the corresponding surge QTFs due to the larger projection of the wave components onto the x-axis than the y-axis. In this case, however, the unidirectional QTFs corresponding to $\beta_j = \beta_k = 22.5^\circ$ are seen to be more uniform than the bidirectional cases. Comparing Figs. 4.10 and 4.11, the effect of wave directionality is again easily seen. Along the $\nu_k = 0.5$ line, the QTF values in Fig. 4.10 oscillate between 0.0 and 2.0, while those in Fig. 4.11, while oscillatory, have an almost linear variation from dimensionless values of 1.0 to 3.0. As was the case for

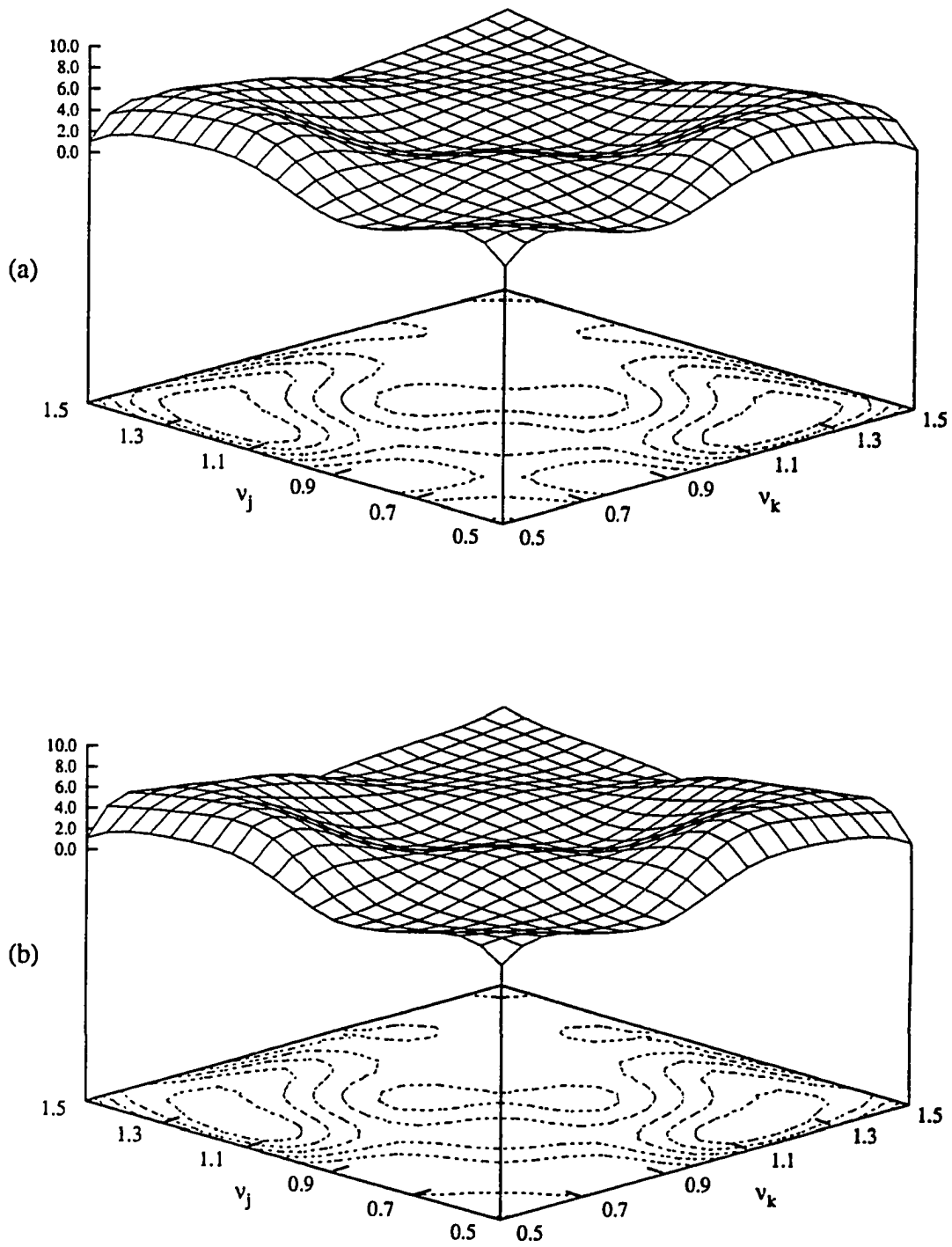


Fig. 4.10 Sum-frequency hydrodynamic sway force QTF, $H^+(\omega_j, \omega_k; \beta_j, \beta_k)$, for the ISSC TLP with $\beta_j = 0^\circ$, $\beta_k = 45^\circ$. Notations: (a) Fixed TLP, (b) Tethered TLP.

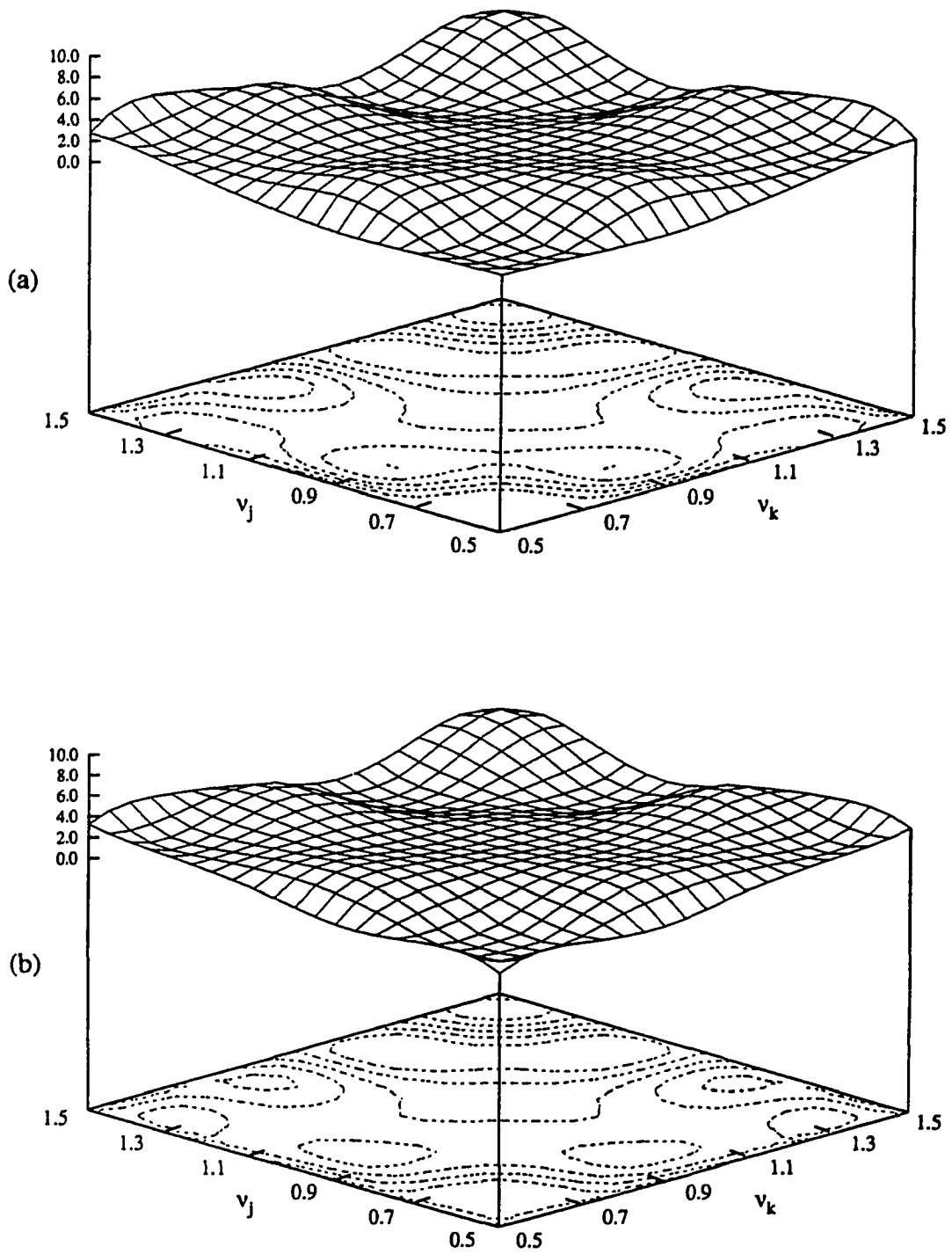


Fig. 4.11 Sum-frequency hydrodynamic sway force QTF, $H^+(\omega_j, \omega_k; \beta_j, \beta_k)$, for the ISSC TLP with $\beta_j = 45^\circ$, $\beta_k = 0^\circ$. Notations: (a) Fixed TLP, (b) Tethered TLP.

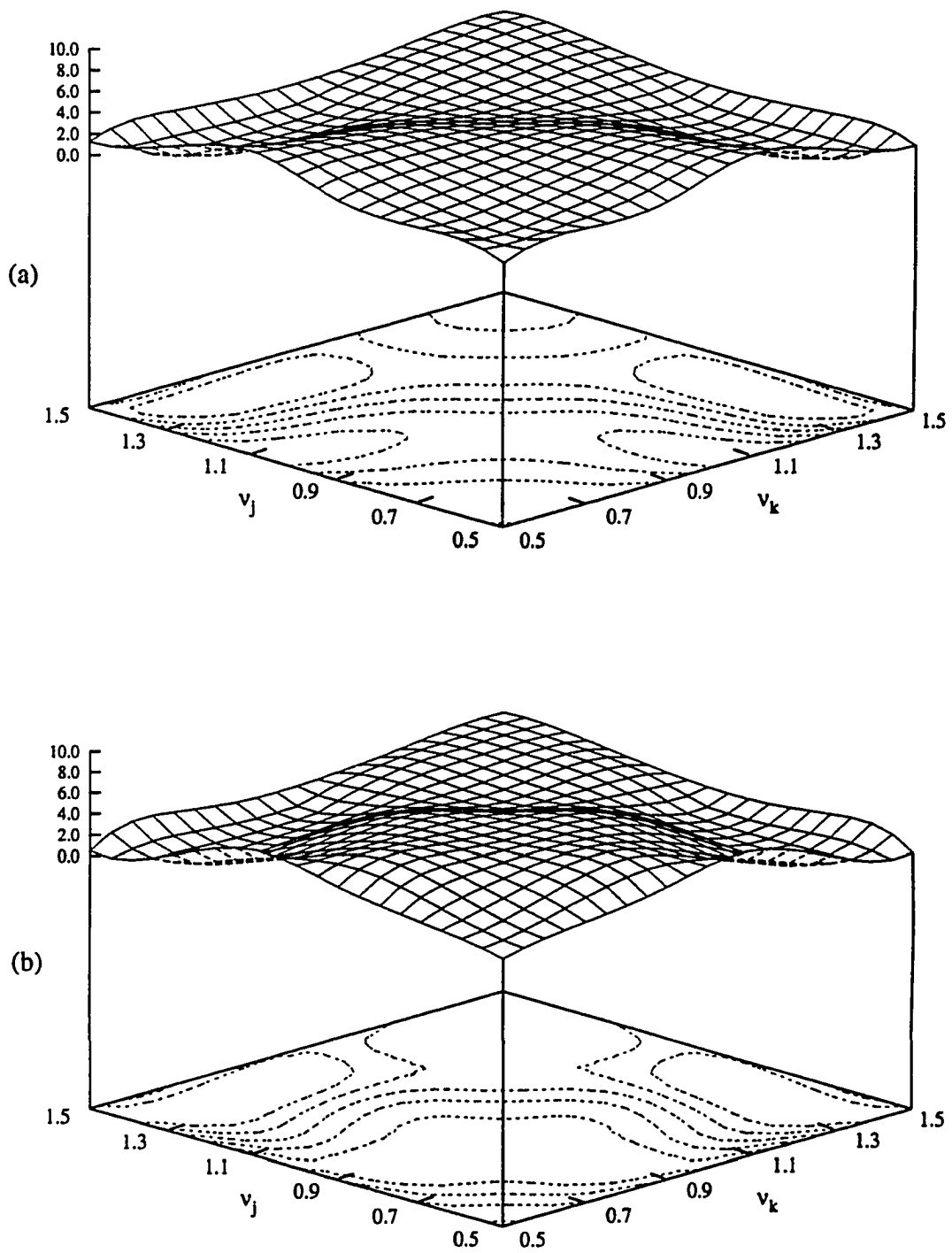


Fig. 4.12 Sum-frequency hydrodynamic sway force QTF, $H^+(\omega_j, \omega_k; \beta_j, \beta_k)$, for the ISSC TLP with $\beta_j = \beta_k = 22.5^\circ$. Notations: (a) Fixed TLP, (b) Tethered TLP.

surge QTFs, the effect of first-order body motions is rather small for the bidirectional case, but more pronounced in the unidirectional case.

Although the surge and sway loads are important at the sum-frequency, more emphasis is placed in the QTFs for heave, roll and pitch at the higher frequencies. This emphasis is due to the fact that in these vertical modes the TLP has a much higher natural frequency than at the horizontal modes of oscillation. Thus, accurate predictions of the second-order exciting loads in heave, roll and pitch are essential to predict the high frequency response of the structure. In this study, the second-order response is not computed. The emphasis is in recognizing the fact that wave directionality significantly affects the second-order exciting loads and therefore the structural response at this order.

Figures 4.13 - 4.21 present the sum-frequency QTFs in heave, roll and pitch for the ISSC TLP. As was the case for the surge and sway modes, the influence of wave directionality is seen by comparing consecutive sets of three figures (i.e., Figs. 4.13 - 4.15 for heave, 4.16 - 4.18 for roll, and 4.19 - 4.21 for pitch). Figure 4.13 shows that the heave sum-frequency QTFs for $\beta_j = 0^\circ$, $\beta_k = 45^\circ$ is relatively uniform with a peak at a monochromatic wave frequency $\nu = 1.1$. This behavior is also true for the heave QTFs shown in Fig. 4.14 which correspond to incident wave angles $\beta_j = 45^\circ$, $\beta_k = 0^\circ$. For the unidirectional case, $\beta_j = \beta_k = 22.5^\circ$, this is true only for the QTFs corresponding to a fixed TLP. The effect of first-order body motions on the heave QTFs in the unidirectional case ($\beta_j = \beta_k = 22.5^\circ$) is seen to be very significant. Body motions lead to a large increase in the heave QTFs. Although not explicitly shown here, it has been found that the increases in these QTFs are not the result of the free-surface integral, nor the first-order potential contribution to the second-order force. Instead, they are the result of the term arising from the structural boundary condition relating the assisting radiated potential directly to the first-order body motions. As stated above for the surge QTFs, the

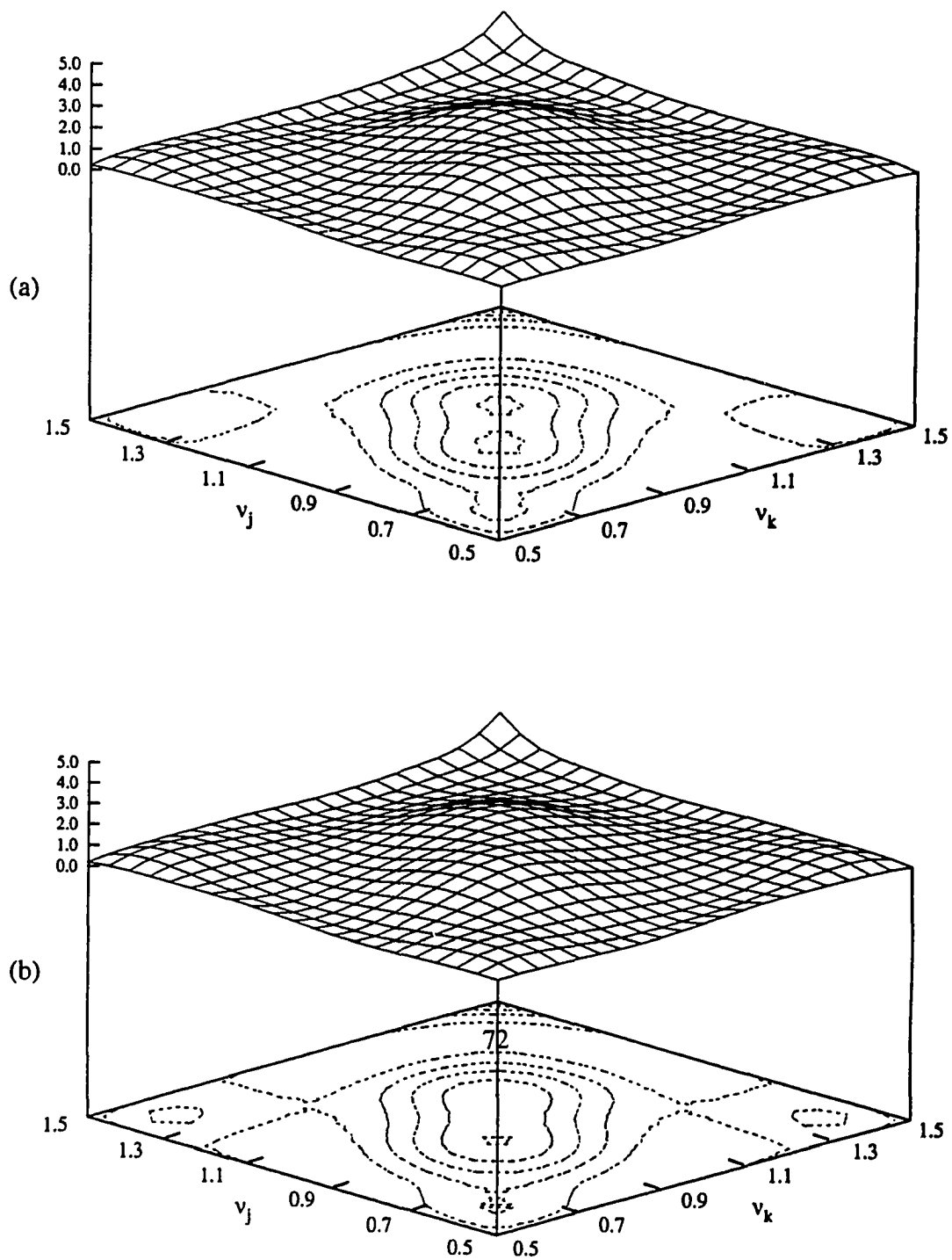


Fig. 4.13 Sum-frequency hydrodynamic heave force QTF, $H^+(\omega_j, \omega_k; \beta_j, \beta_k)$, for the ISSC TLP with $\beta_j = 0^\circ$, $\beta_k = 45^\circ$. Notations: (a) Fixed TLP, (b) Tethered TLP.

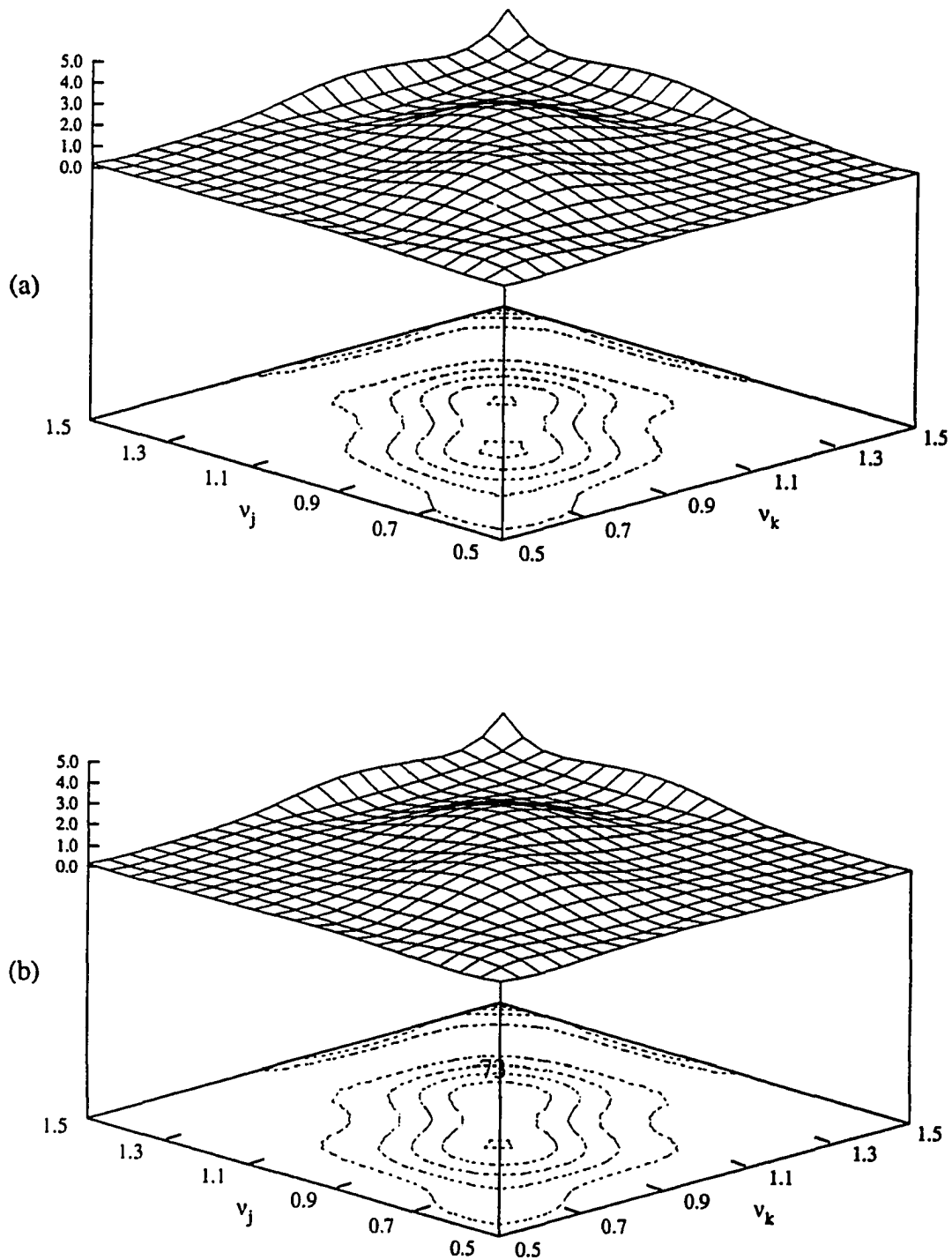


Fig. 4.14 Sum-frequency hydrodynamic heave force QTF, $H^+(\omega_j, \omega_k; \beta_j, \beta_k)$, for the ISSC TLP with $\beta_j = 45^\circ$, $\beta_k = 0^\circ$. Notations: (a) Fixed TLP, (b) Tethered TLP.

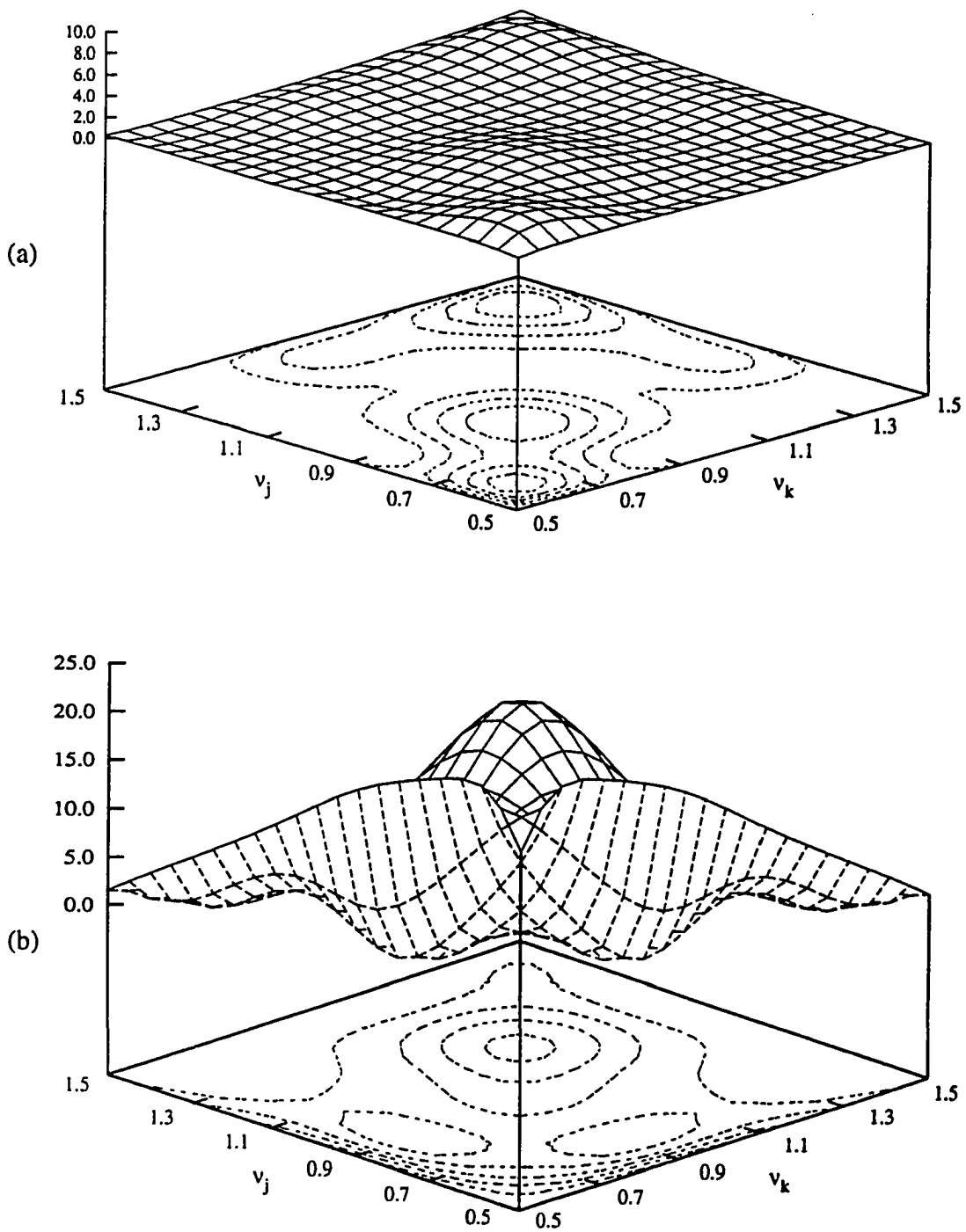


Fig. 4.15 Sum-frequency hydrodynamic heave force QTF, $H^+(\omega_j, \omega_k; \beta_j, \beta_k)$, for the ISSC TLP with $\beta_j = \beta_k = 22.5^\circ$. Notations: (a) Fixed TLP, (b) Tethered TLP.

lack of symmetry in the incident waves seems to be the source of the significant additive contribution to the second-order loads. Figures 4.16 - 4.21 show the variation of the sum-frequency QTFs on the ISSC TLP in the roll and pitch modes. In general, their behavior is similar to those exhibited by the sway and surge QTFs. For this reason, the effect of first-order body motions is not as pronounced in these modes as was for the heave mode. The influence of body motions is, again, more evident in the unidirectional case.

As indicated above, the emphasis of this study is in providing evidence that the effects of wave directionality and first-order body motions, while not always observed, must be acknowledged as possible controlling aspects for the design of floating offshore structures. One of the most significant implications of bidirectional waves is the resulting non-zero yaw moments arising from waves at angles of incidence of 0° and 45° , which, by themselves, do not produce yaw moments on symmetric structures. This result, more than any of the other results, highlights the importance of accounting for wave directionality when present in the design of floating offshore structures. Figures 4.22 - 4.24 show the sum-frequency yaw moment QTFs for the different incident wave angle combinations. As was the case with the surge and sway loads, the QTF values are oscillatory and increasing with increasing frequency. Again, the QTF values for the $\beta_j = 0^\circ$, $\beta_k = 45^\circ$ case are, in general, larger than those for the $\beta_j = 45^\circ$, $\beta_k = 0^\circ$ case. It is also seen that the QTFs for the unidirectional case exhibit a significantly different behavior than those for the bidirectional cases. For this mode, the first-order body motions do not seem to significantly influence the QTFs, even in the unidirectional case.

Results for the second-order difference-frequency load QTFs on the ISSC TLP in bichromatic bidirectional waves are presented in Figs. 4.25 - 4.42. As for the sum-frequency case, three incident wave angle combinations are used: $\beta_j = 0^\circ$, $\beta_k = 45^\circ$; $\beta_j = 45^\circ$, $\beta_k = 0^\circ$; and $\beta_j = \beta_k = 22.5^\circ$. In general, for the frequency range considered, the

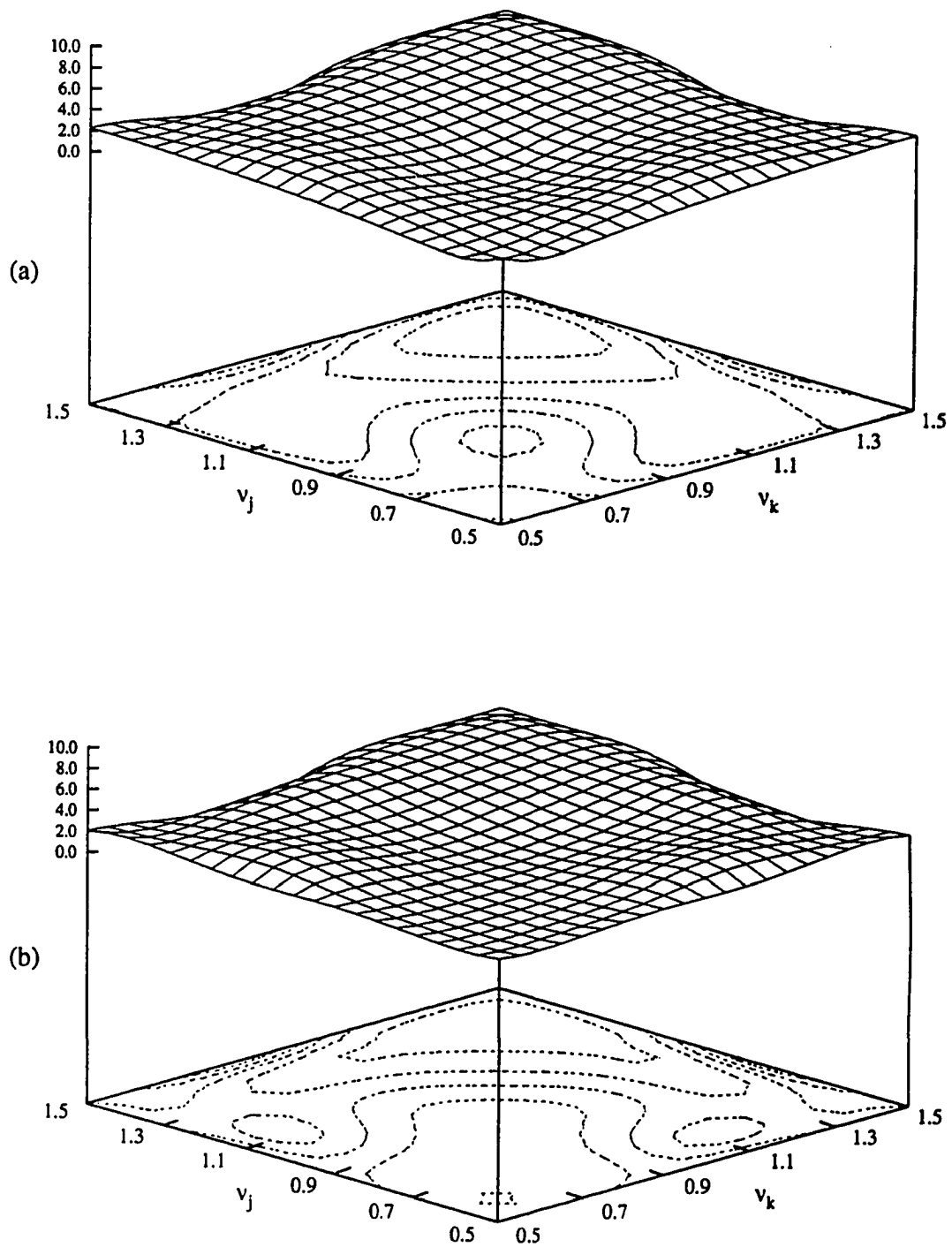


Fig. 4.16 Sum-frequency hydrodynamic roll moment QTF, $H^+(\omega_j, \omega_k; \beta_j, \beta_k)$, for the ISSC TLP with $\beta_j = 0^\circ$, $\beta_k = 45^\circ$. Notations: (a) Fixed TLP, (b) Tethered TLP.

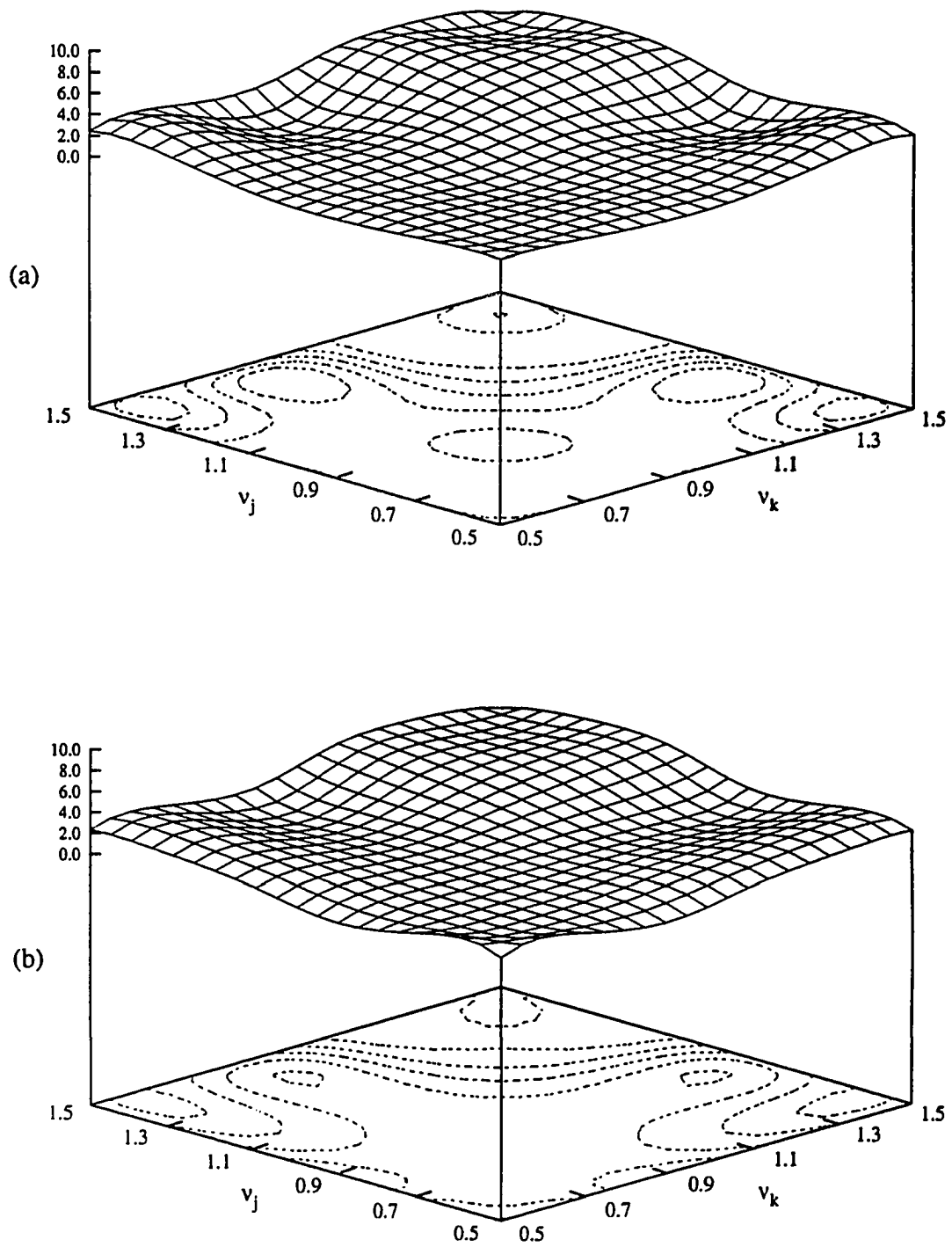


Fig. 4.17 Sum-frequency hydrodynamic roll moment QTF, $H^+(\omega_j, \omega_k; \beta_j, \beta_k)$, for the ISSC TLP with $\beta_j = 45^\circ$, $\beta_k = 0^\circ$. Notations: (a) Fixed TLP, (b) Tethered TLP.

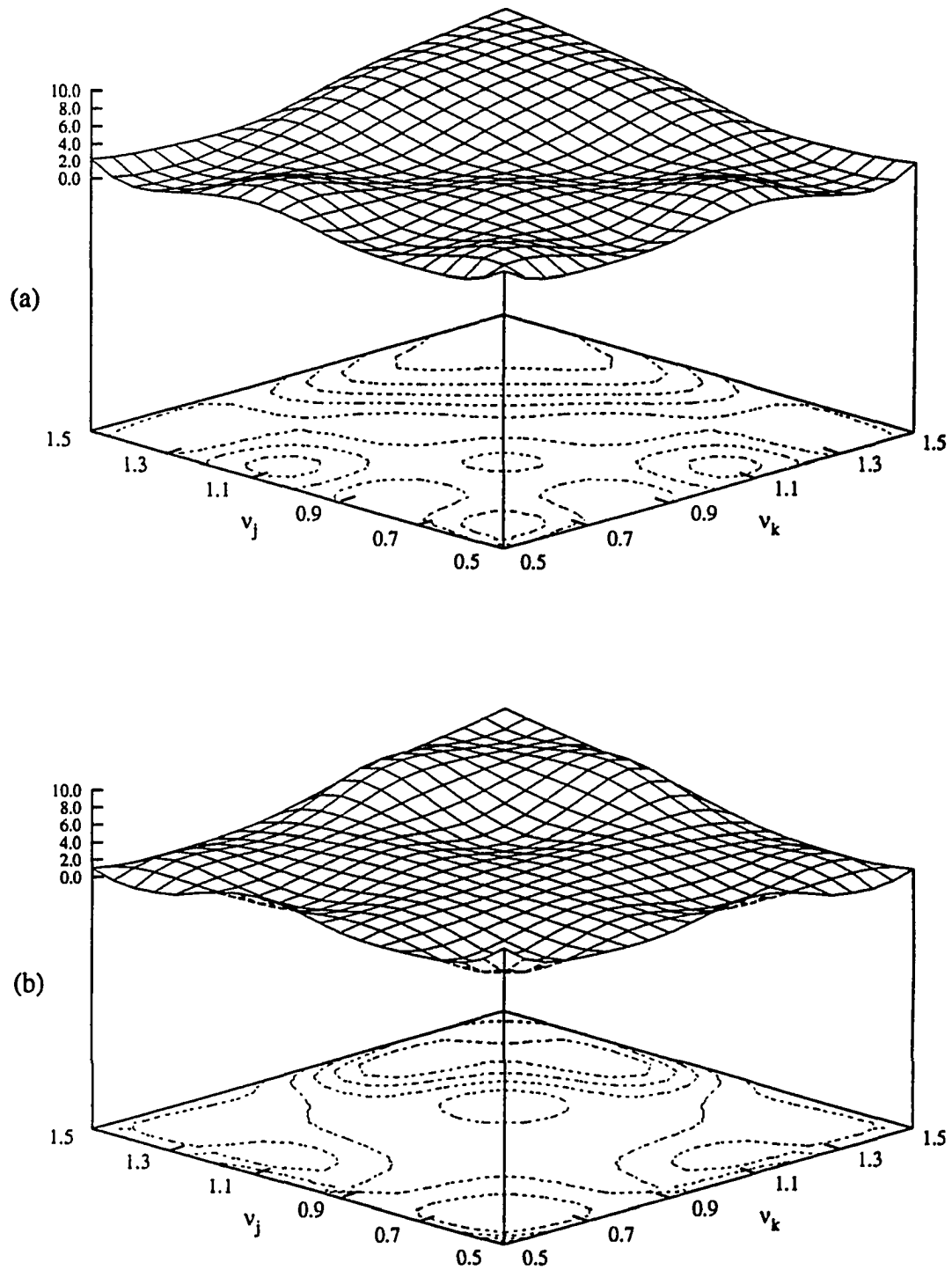


Fig. 4.18 Sum-frequency hydrodynamic roll moment QTF, $H^+(\omega_j, \omega_k; \beta_j, \beta_k)$, for the ISSC TLP with $\beta_j = \beta_k = 22.5^\circ$. Notations: (a) Fixed TLP, (b) Tethered TLP.

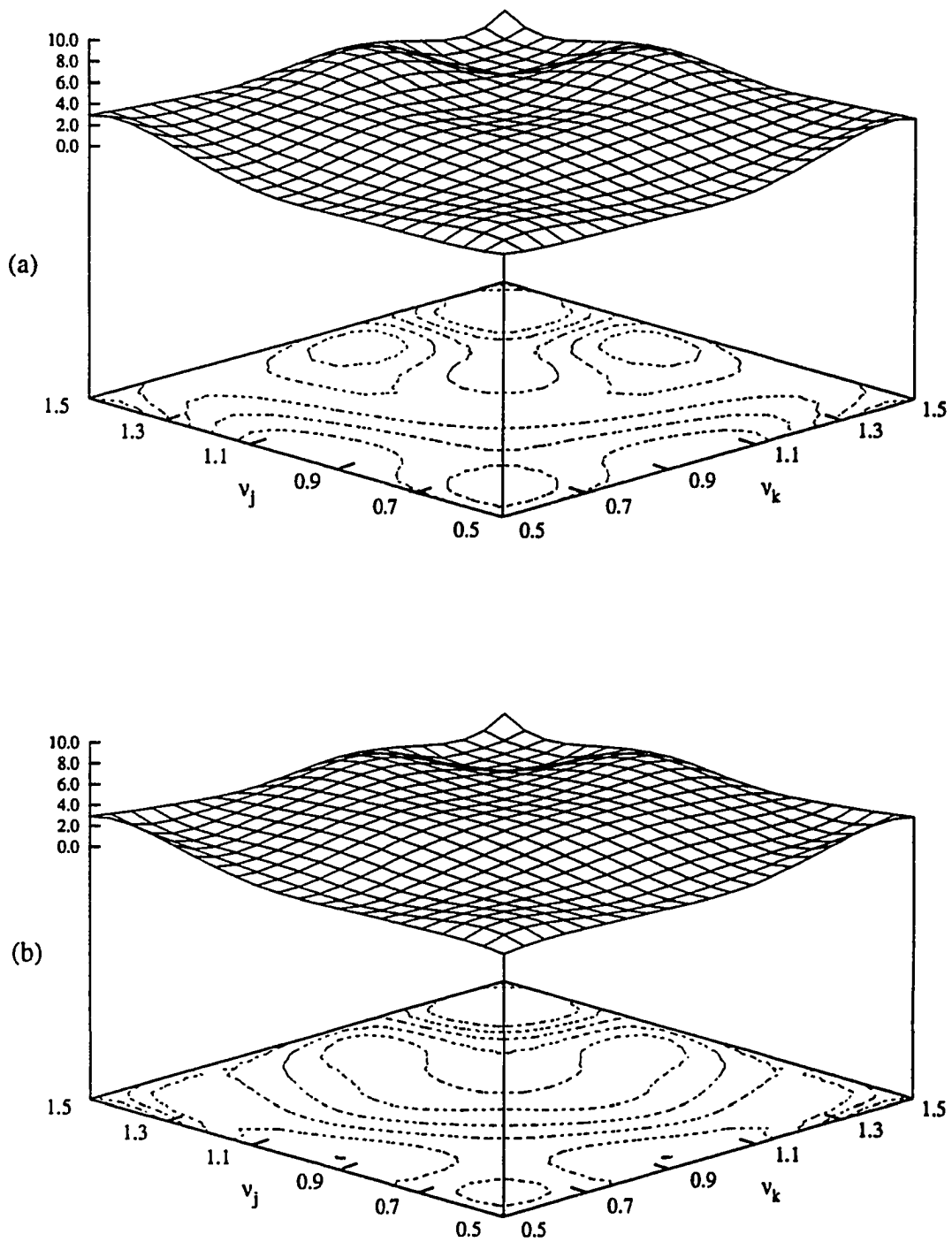


Fig. 4.19 Sum-frequency hydrodynamic pitch moment QTF, $H^+(\omega_j, \omega_k; \beta_j, \beta_k)$, for the ISSC TLP with $\beta_j = 0^\circ$, $\beta_k = 45^\circ$. Notations: (a) Fixed TLP, (b) Tethered TLP.

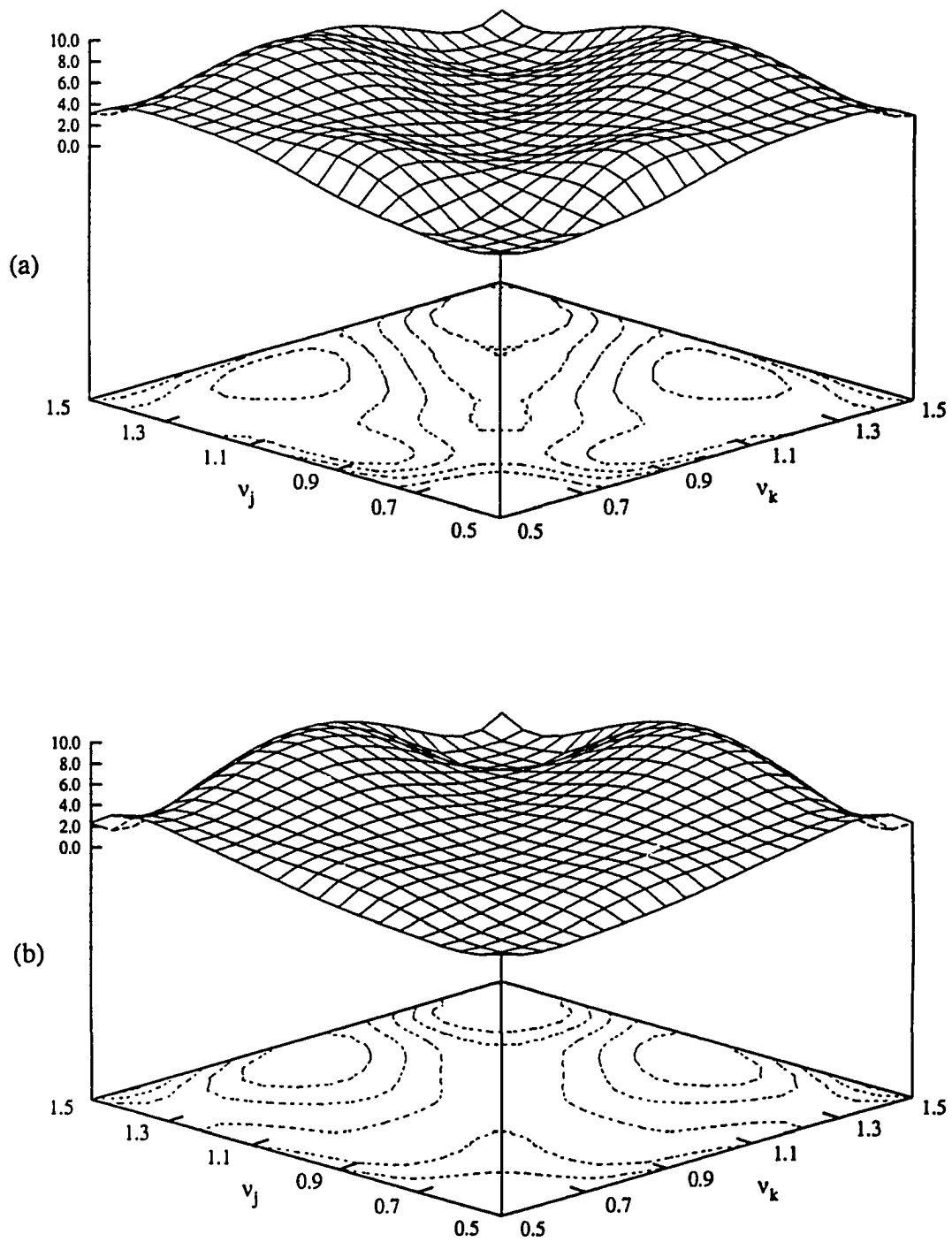


Fig. 4.20 Sum-frequency hydrodynamic pitch moment QTF, $H^+(\omega_j, \omega_k; \beta_j, \beta_k)$, for the ISSC TLP with $\beta_j = 45^\circ$, $\beta_k = 0^\circ$. Notations: (a) Fixed TLP, (b) Tethered TLP.

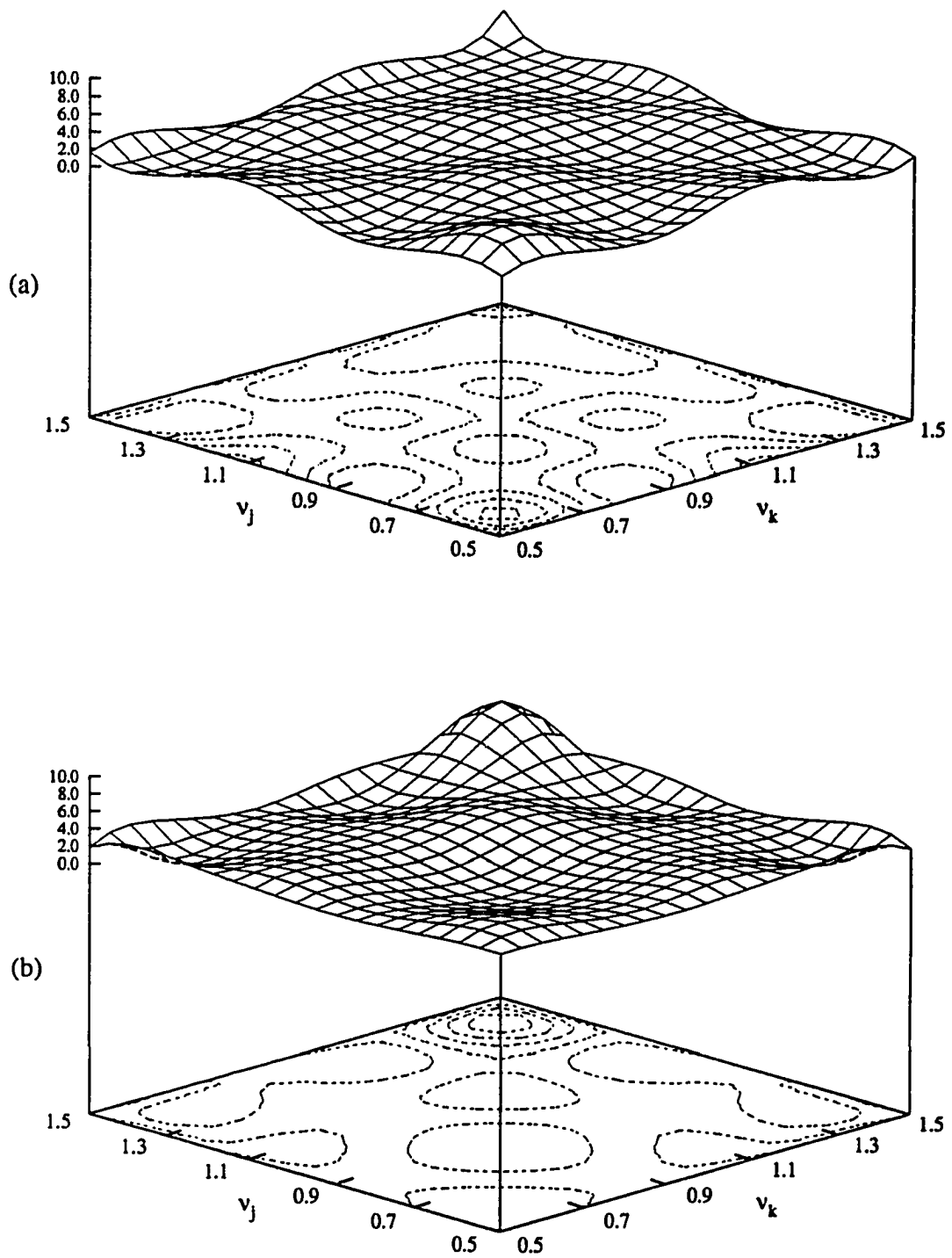


Fig. 4.21 Sum-frequency hydrodynamic pitch moment QTF, $H^+(\omega_j, \omega_k; \beta_j, \beta_k)$, for the ISSC TLP with $\beta_j = \beta_k = 22.5^\circ$. Notations: (a) Fixed TLP, (b) Tethered TLP.

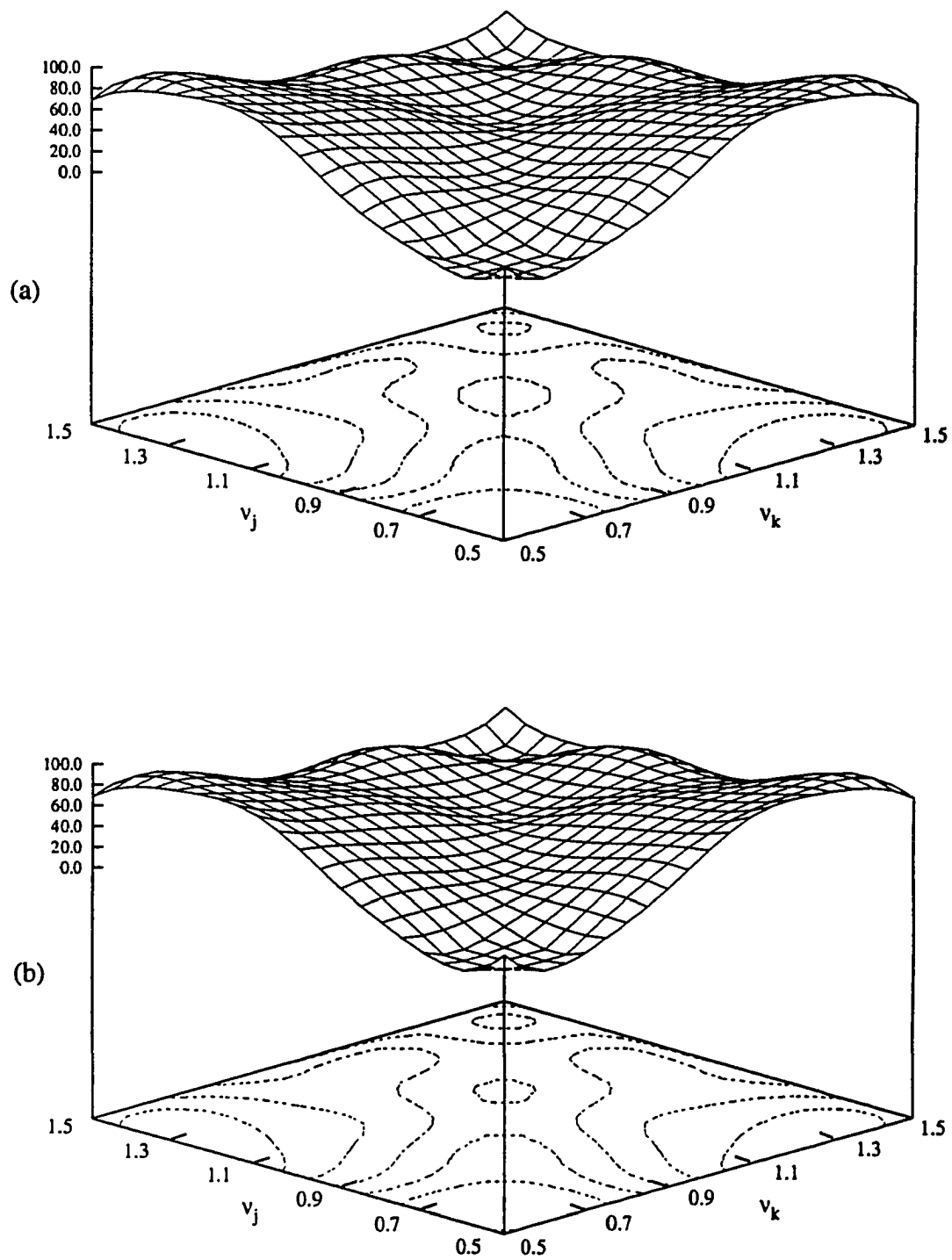


Fig. 4.22 Sum-frequency hydrodynamic yaw moment QTF, $H^+(\omega_j, \omega_k; \beta_j, \beta_k)$, for the ISSC TLP with $\beta_j = 0^\circ$, $\beta_k = 45^\circ$. Notations: (a) Fixed TLP, (b) Tethered TLP.

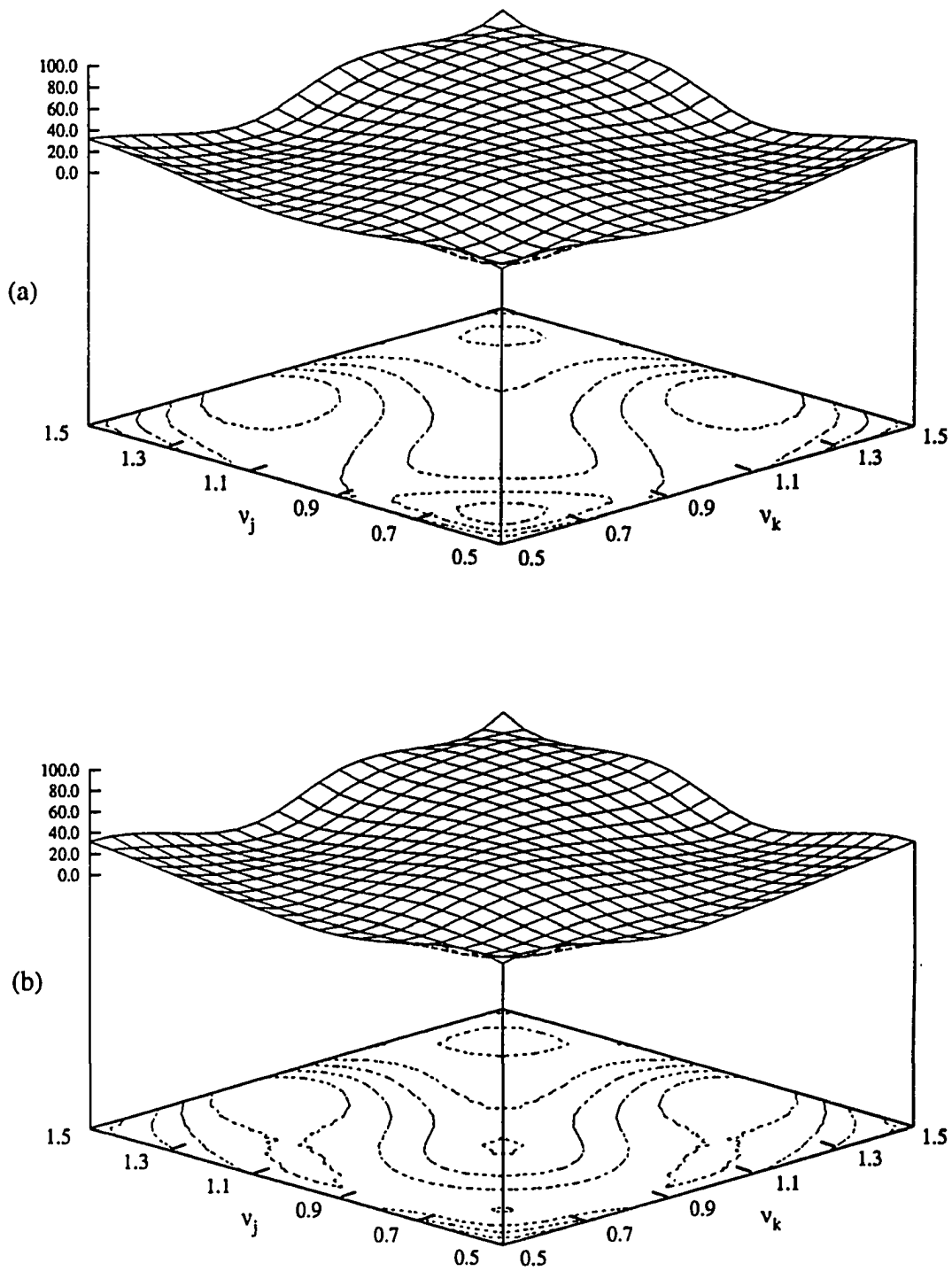


Fig. 4.23 Sum-frequency hydrodynamic yaw moment QTF, $H^+(\omega_j, \omega_k; \beta_j, \beta_k)$, for the ISSC TLP with $\beta_j = 45^\circ$, $\beta_k = 0^\circ$. Notations: (a) Fixed TLP, (b) Tethered TLP.

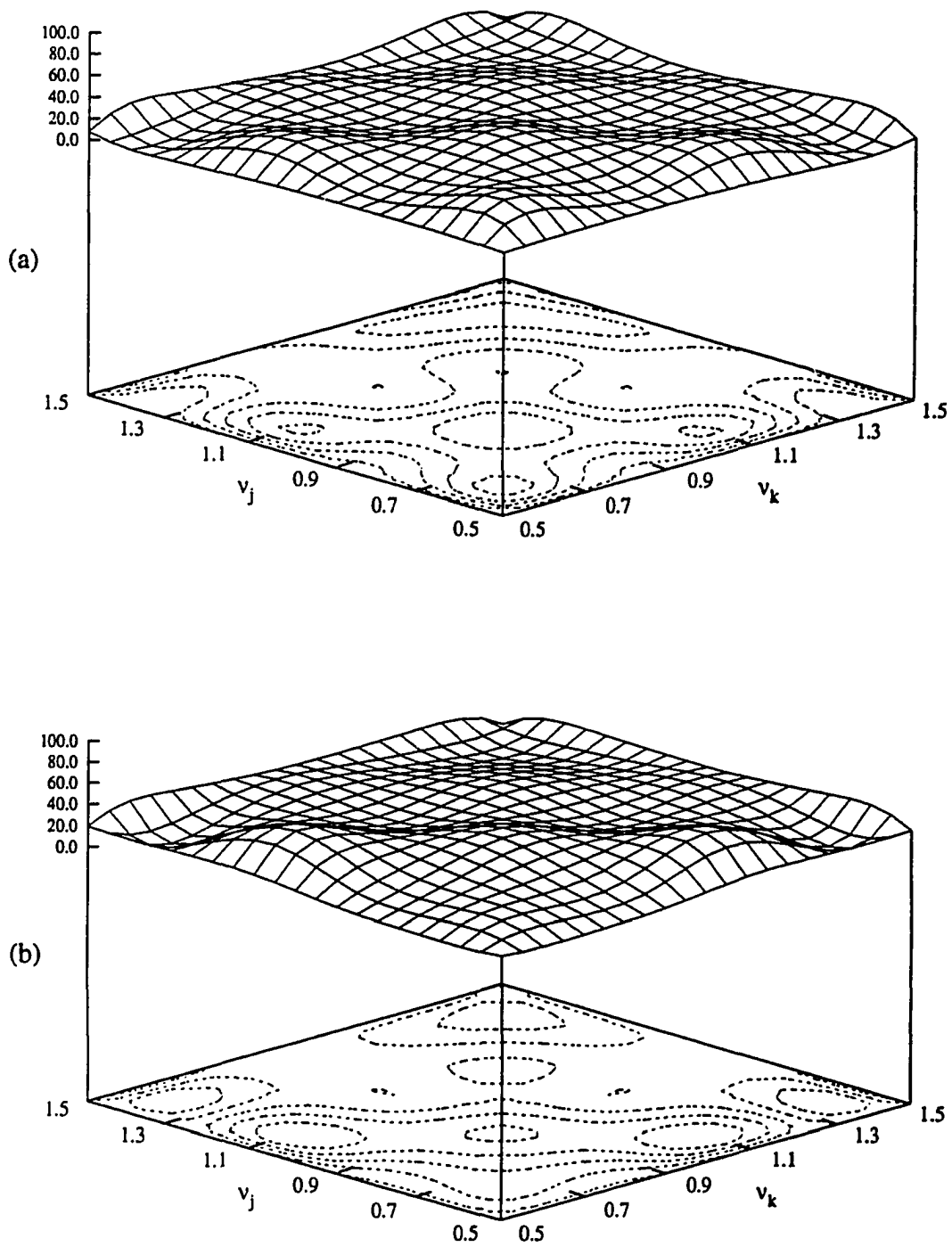


Fig. 4.24 Sum-frequency hydrodynamic yaw moment QTF, $H^+(\omega_j, \omega_k; \beta_j, \beta_k)$, for the ISSC TLP with $\beta_j = \beta_k = 22.5^\circ$. Notations: (a) Fixed TLP, (b) Tethered TLP.

effect of first-order body motions is seen to be almost insignificant for the difference-frequency case. For the most part, in all six modes of loading both the (a) and (b) figures possess similar behavior and exhibit similar magnitudes. It is also seen that for the two bidirectional cases considered, the difference-frequency QTFs are more uniform than the corresponding sum-frequency QTFs. This behavior is not true for unidirectional waves, due to the hydrodynamic interactions between the wave components and the columns of the TLP. Despite the relatively mild variation of the sway difference-frequency QTFs, there is a distinct difference between the $\beta_j = 0^\circ, \beta_k = 45^\circ$ case and the $\beta_j = 45^\circ, \beta_k = 0^\circ$ case. The former exhibits dimensionless QTF values less than 4.0, while in the latter case the QTFs can attain values up to 7.0. The results obtained for the difference-frequency load QTFs are in agreement with those observed by Kim (1992) indicating that the assumption of wave uni-directionality is not necessarily conservative as far as low-frequency loading is concerned.

In order to more distinctly see the effect of wave directionality on the second-order load QTFs, Tables 4.3 and 4.4 present ratios of the maximum vertical force, and overturning moment (i.e., the combined effect of roll and pitch) sum-frequency QTFs in bidirectional waves to the corresponding quantities in unidirectional waves. Only the vertical mode ratios are shown at the sum-frequency because, as stated earlier, they are relevant in the high frequency design of TLPs. A similar table for maximum horizontal force difference-frequency QTFs (combined surge and sway) is presented in Table 4.5. The first two rows of Table 4.3 present the ratios of maximum sum-frequency heave QTF for bidirectional waves with $\beta_j = 0^\circ, \beta_k = 45^\circ$ to those arising from unidirectional waves at $\beta_j = \beta_k = 0^\circ$ and $\beta_j = \beta_k = 45^\circ$. Rows three and four contain the ratios of the maximum heave sum-frequency QTF for bidirectional waves with $\beta_j = 45^\circ, \beta_k = 0^\circ$ to those arising from unidirectional waves at $\beta_j = \beta_k = 0^\circ$ and $\beta_j = \beta_k = 45^\circ$. Tables 4.4 and 4.5 present similar ratios for combined roll and pitch sum-frequency QTFs, and for combined surge

and sway difference-frequency QTFs. These loads were combined to allow for a better comparison of the wave loading at the different wave directions. It was not possible to compare individual modes since for the unidirectional 0° case, sway and roll QTFs are identically zero for a symmetric structure. The fact that there is no table presenting the QTF ratios associated with yaw mode in itself points out to the relevance of bidirectionality. All these ratios are, of course, infinite since, for symmetric structures such as the ISSC TLP, unidirectional waves at 0° and 45° do not cause any yaw moment. In the tables, the upper triangle contains the results for the tethered ISSC TLP, while the lower triangle contains the results for a fixed TLP. For each frequency pair, the ratios are presented so as to compare row one to row two, row three to row four, and then further compare rows one and two to rows three and four (i.e., compare the bidirectional 0-45 case with the $0^\circ-0^\circ$ and $45^\circ-45^\circ$ case, then the $45^\circ-0^\circ$ case with the $0^\circ-0^\circ$ and $45^\circ-45^\circ$ case, and finally, compare the ratios themselves for the $0^\circ-45^\circ$ and $45^\circ-0^\circ$ cases). In these tables it is seen that the QTF ratios vary significantly from unity. Furthermore, some of these values are significantly larger than one, indicating that for some wave frequency combinations bidirectional waves result in higher load QTFs than those obtained from unidirectional waves, and therefore bidirectionality should be accounted for in the design of floating offshore structures such as TLPs.

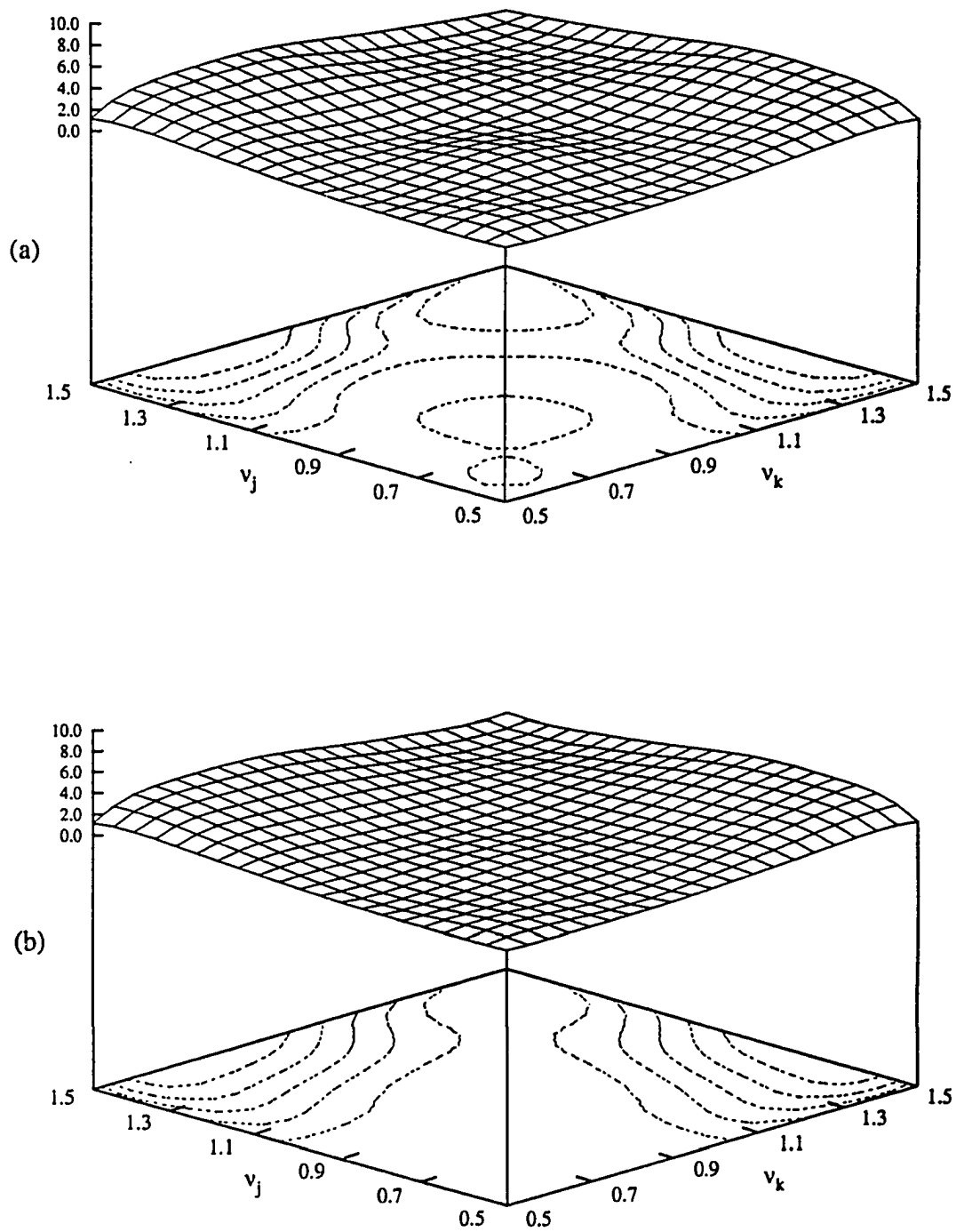


Fig. 4.25 Difference-frequency hydrodynamic surge force QTF, $H(\omega_j, \omega_k; \beta_j, \beta_k)$, for the ISSC TLP with $\beta_j = 0^\circ$, $\beta_k = 45^\circ$. Notations: (a) Fixed TLP, (b) Tethered TLP.

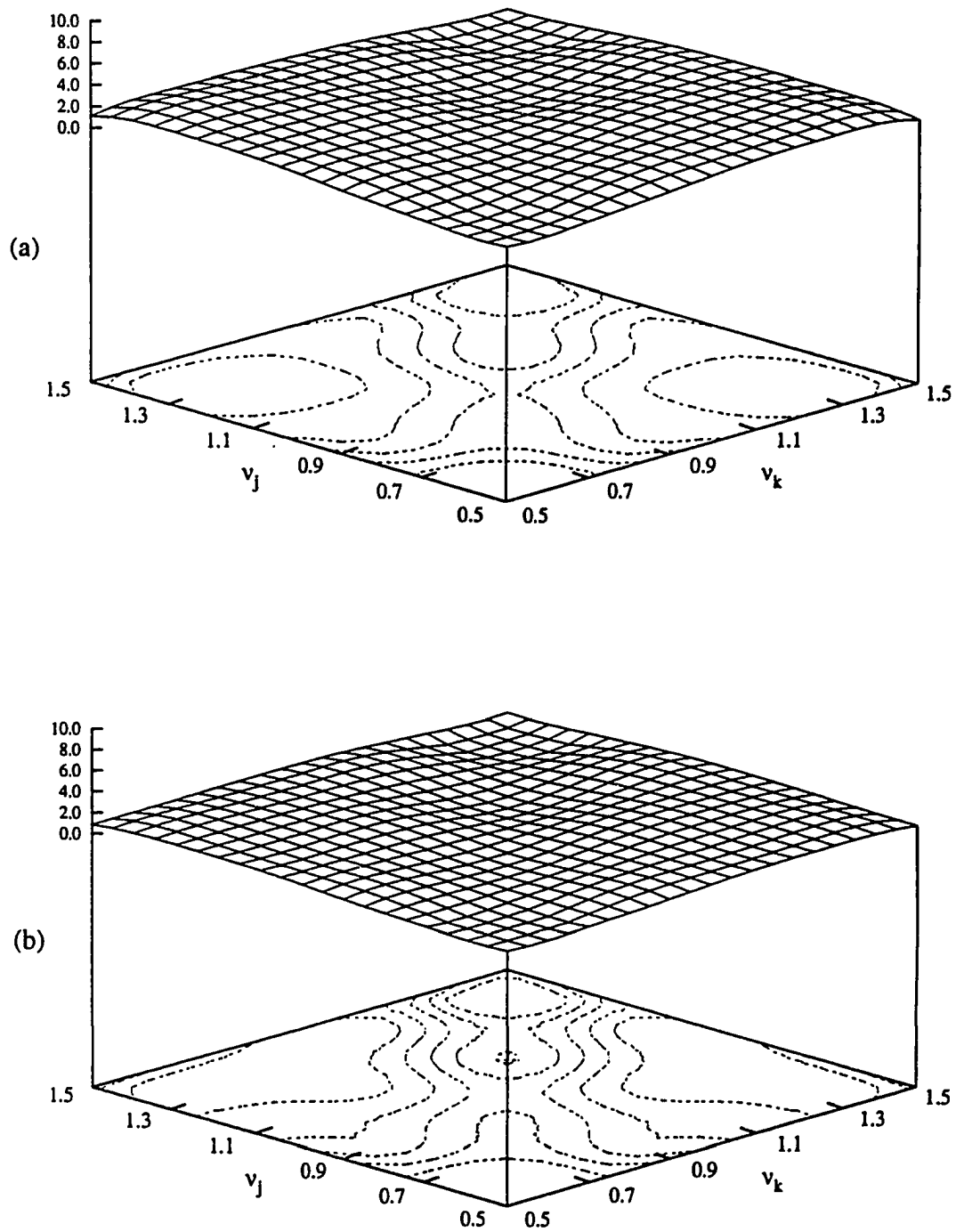


Fig. 4.26 Difference-frequency hydrodynamic surge force QTF, $H^*(\omega_j, \omega_k; \beta_j, \beta_k)$, for the ISSC TLP with $\beta_j = 45^\circ$, $\beta_k = 0^\circ$. Notations: (a) Fixed TLP, (b) Tethered TLP.

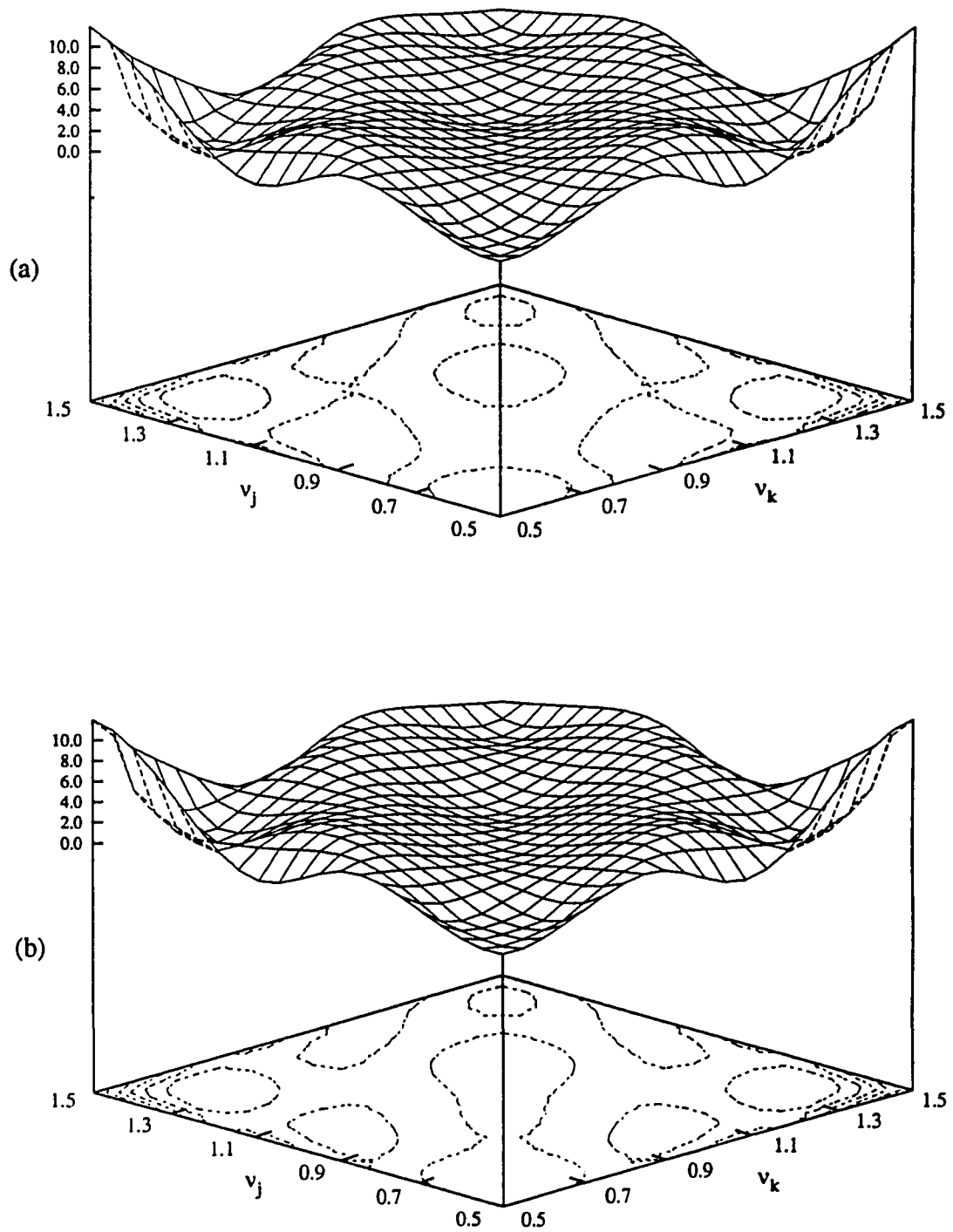


Fig. 4.27 Difference-frequency hydrodynamic surge force QTF, $H^*(\omega_j, \omega_k; \beta_j, \beta_k)$, for the ISSC TLP with $\beta_j = \beta_k = 22.5^\circ$. Notations: (a) Fixed TLP, (b) Tethered TLP.

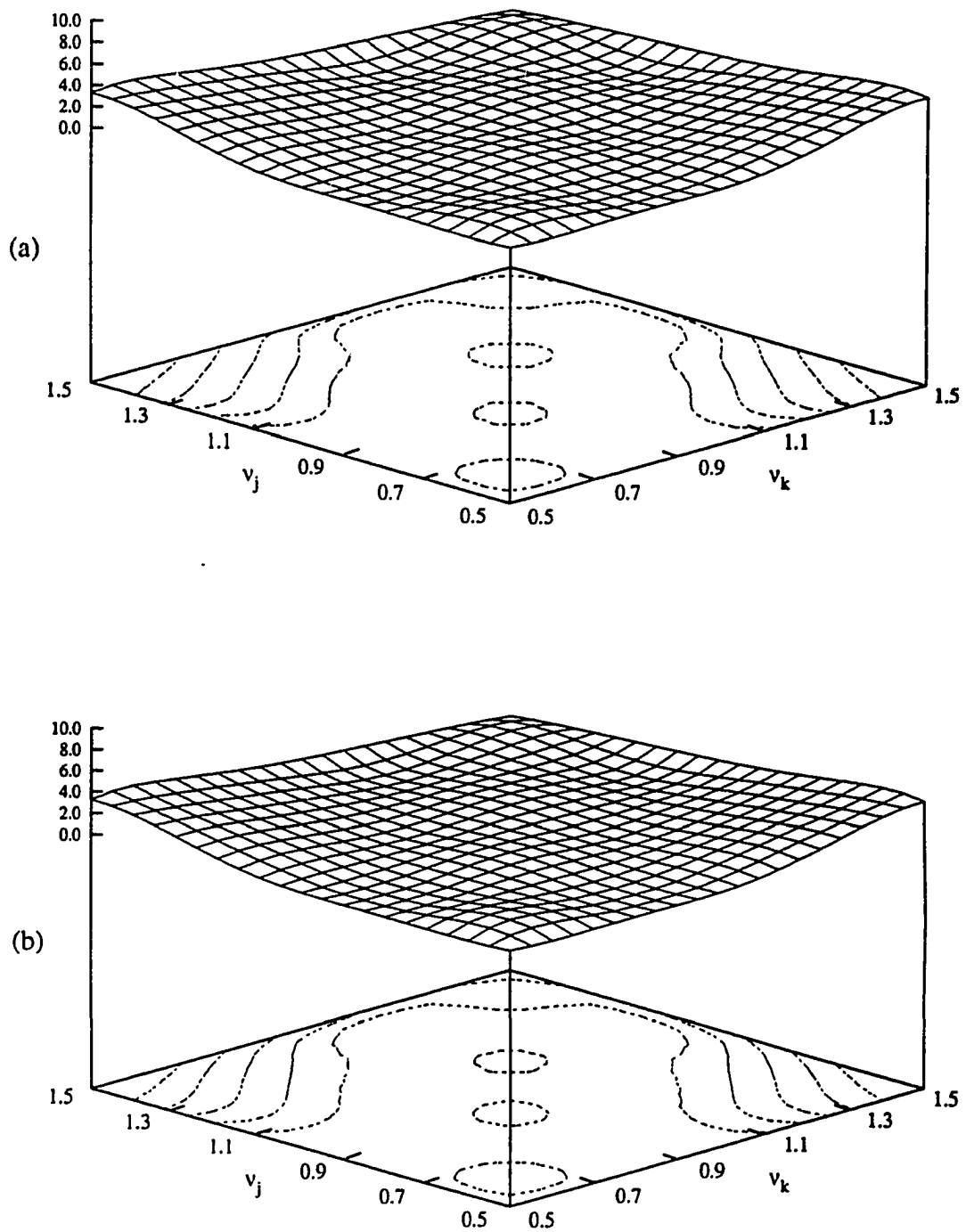


Fig. 4.28 Difference-frequency hydrodynamic sway force QTF, $H^-(\omega_j, \omega_k; \beta_j, \beta_k)$, for the ISSC TLP with $\beta_j = 0^\circ$, $\beta_k = 45^\circ$. Notations: (a) Fixed TLP, (b) Tethered TLP.

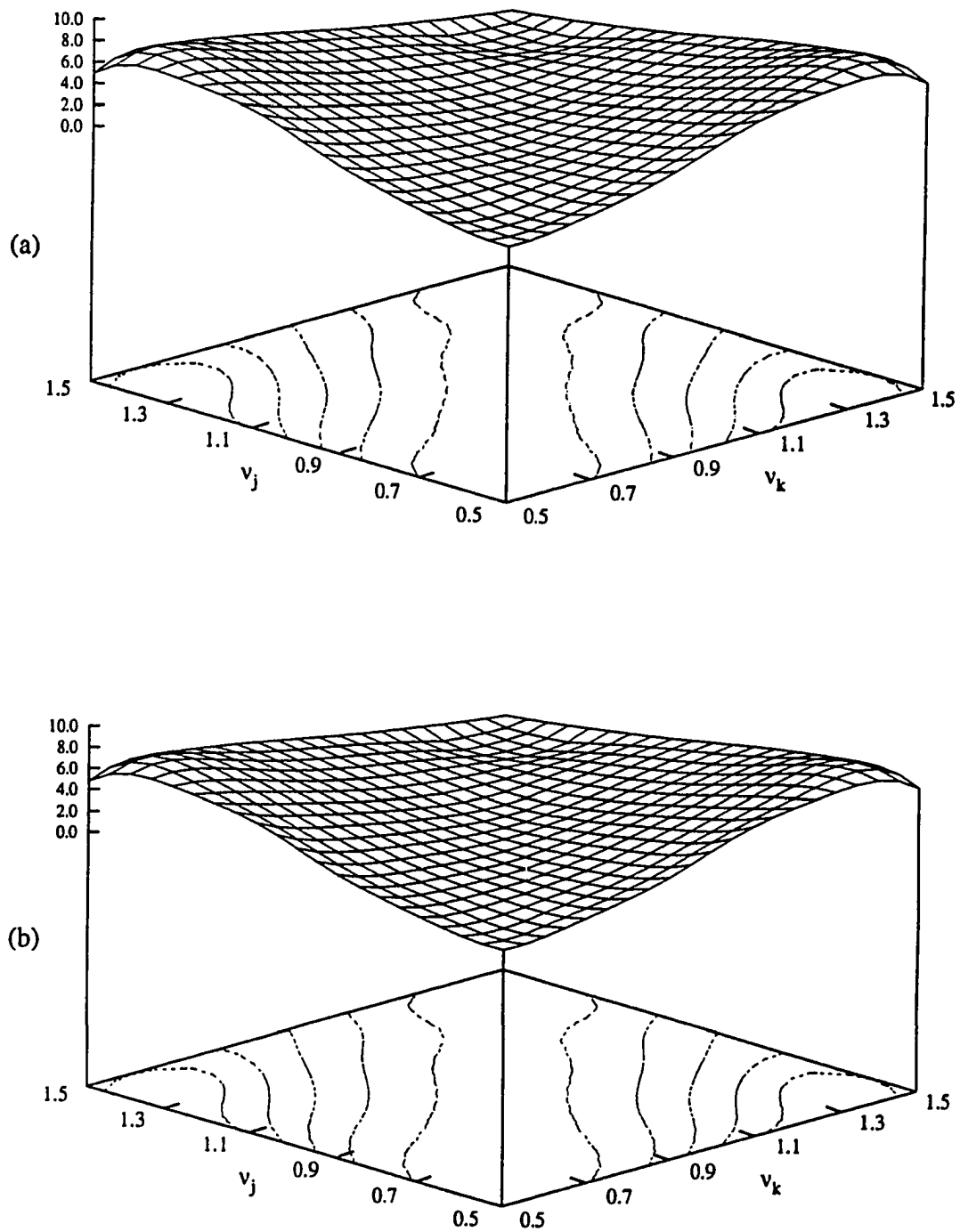


Fig. 4.29 Difference-frequency hydrodynamic sway force QTF, $H^*(\omega_j, \omega_k; \beta_j, \beta_k)$, for the ISSC TLP with $\beta_j = 45^\circ$, $\beta_k = 0^\circ$. Notations: (a) Fixed TLP, (b) Tethered TLP.

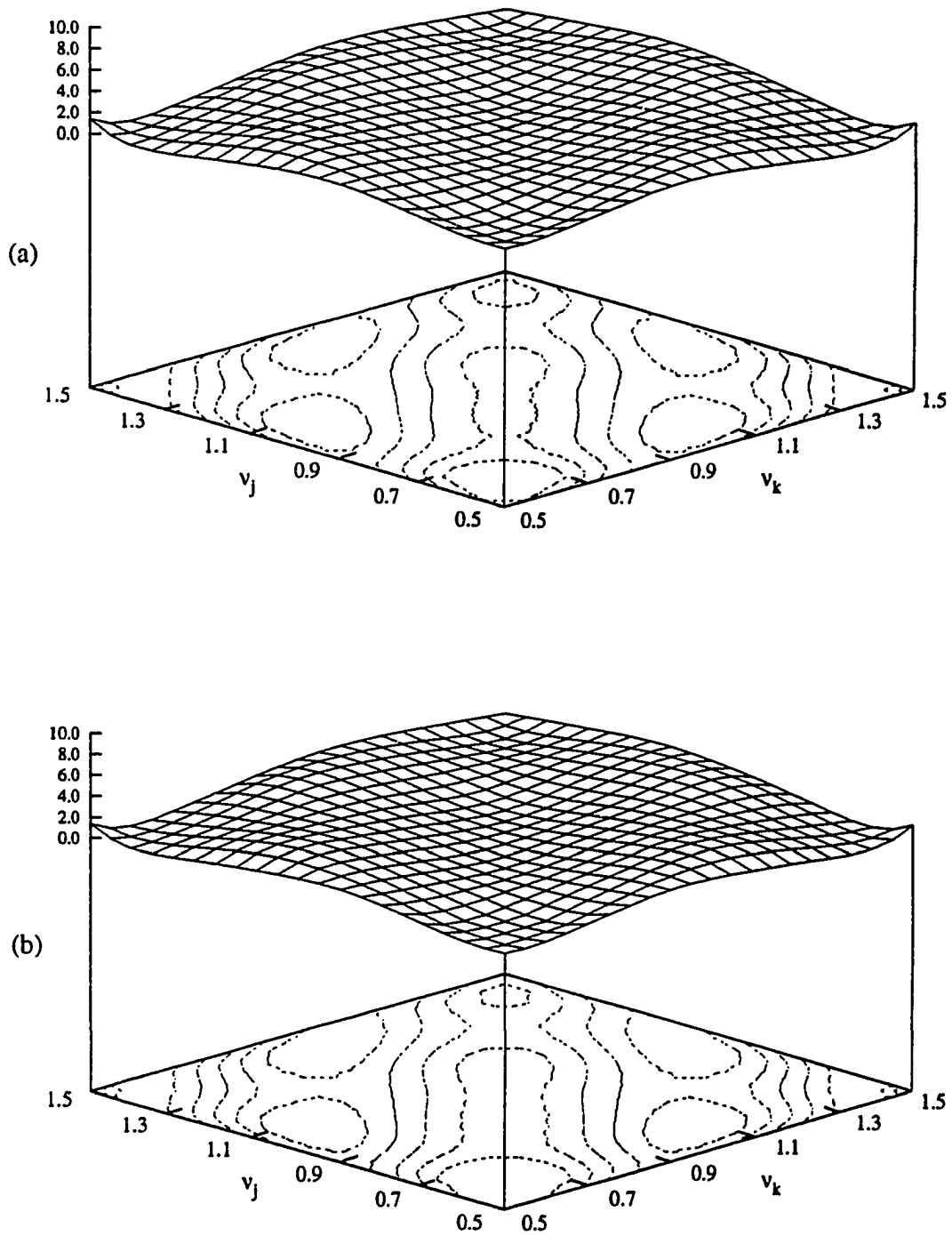


Fig. 4.30 Difference-frequency hydrodynamic sway force QTF, $H^*(\omega_j, \omega_k; \beta_j, \beta_k)$, for the ISSC TLP with $\beta_j = \beta_k = 22.5^\circ$. Notations: (a) Fixed TLP, (b) Tethered TLP.

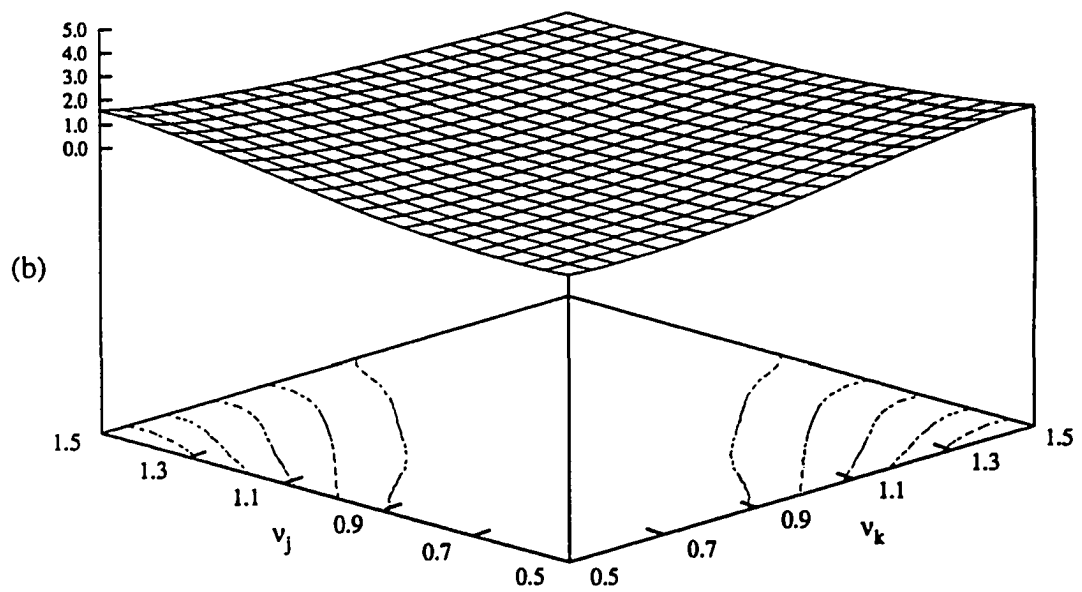
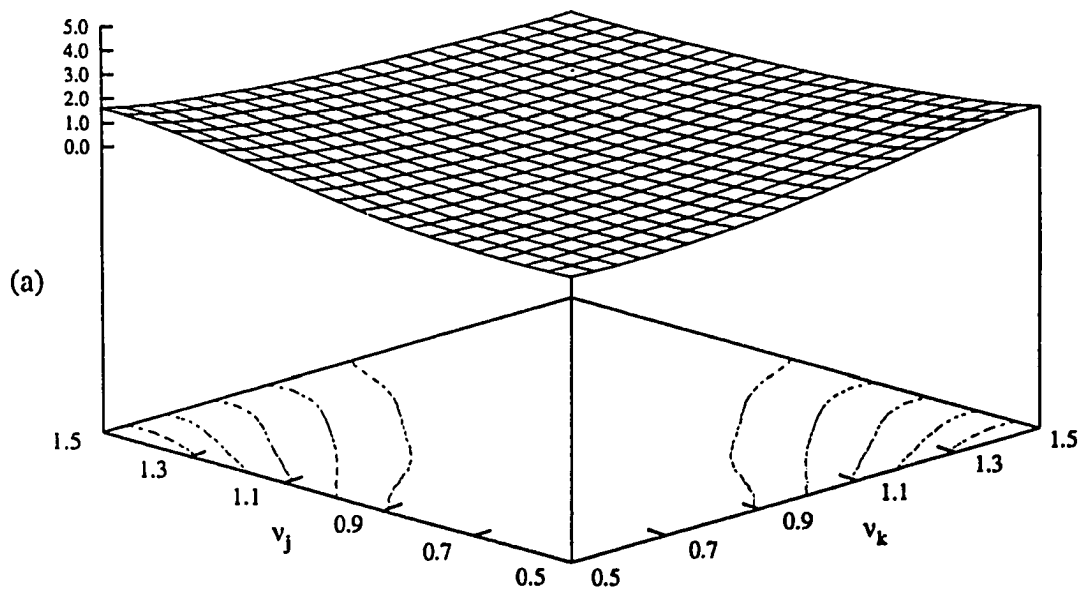


Fig. 4.31 Difference-frequency hydrodynamic heave force QTF, $H^-(\omega_j, \omega_k; \beta_j, \beta_k)$, for the ISSC TLP with $\beta_j = 0^\circ$, $\beta_k = 45^\circ$. Notations: (a) Fixed TLP, (b) Tethered TLP.

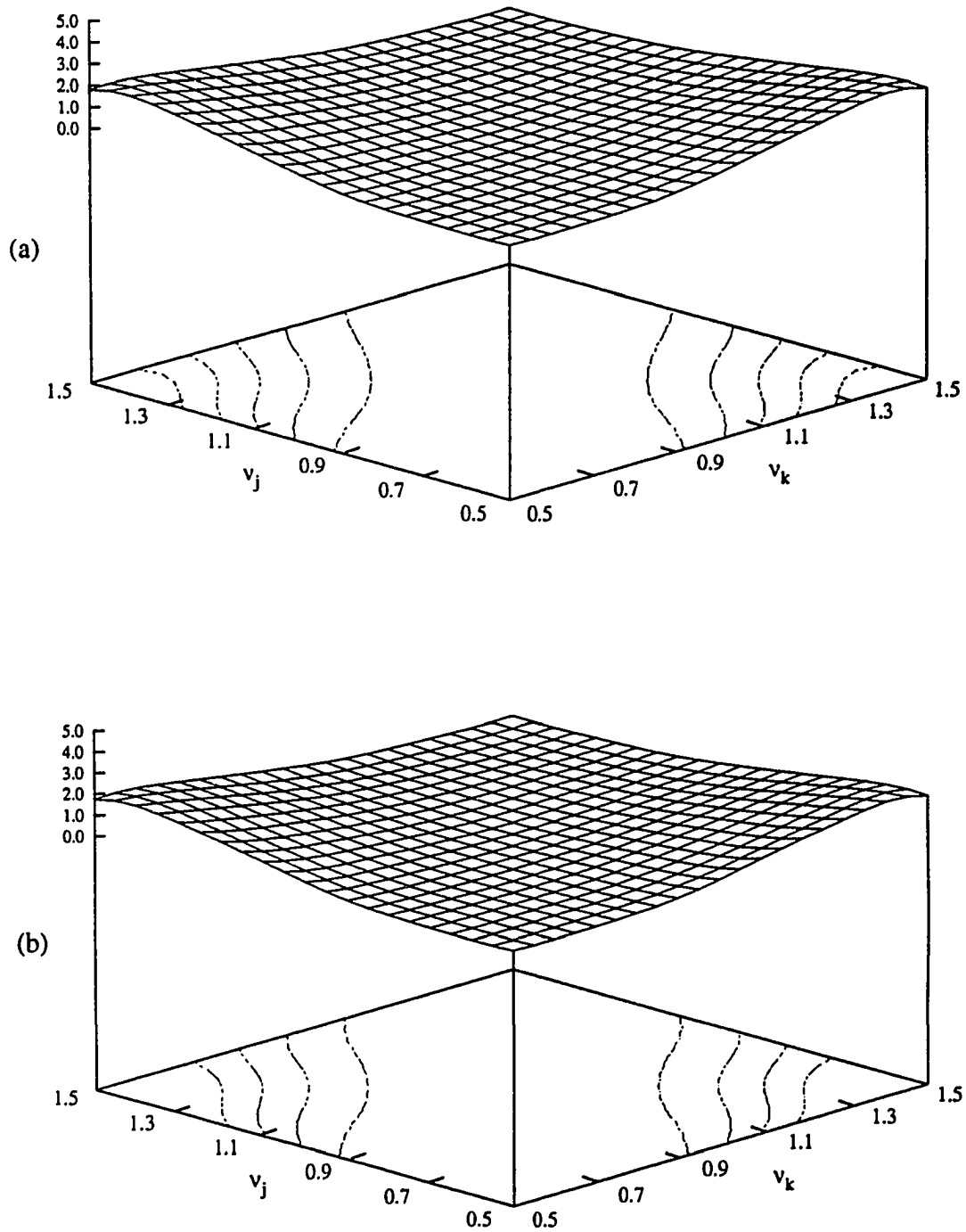


Fig. 4.32 Difference-frequency hydrodynamic heave force QTF, $H^-(\omega_j, \omega_k; \beta_j, \beta_k)$, for the ISSC TLP with $\beta_j = 45^\circ$, $\beta_k = 0^\circ$. Notations: (a) Fixed TLP, (b) Tethered TLP.

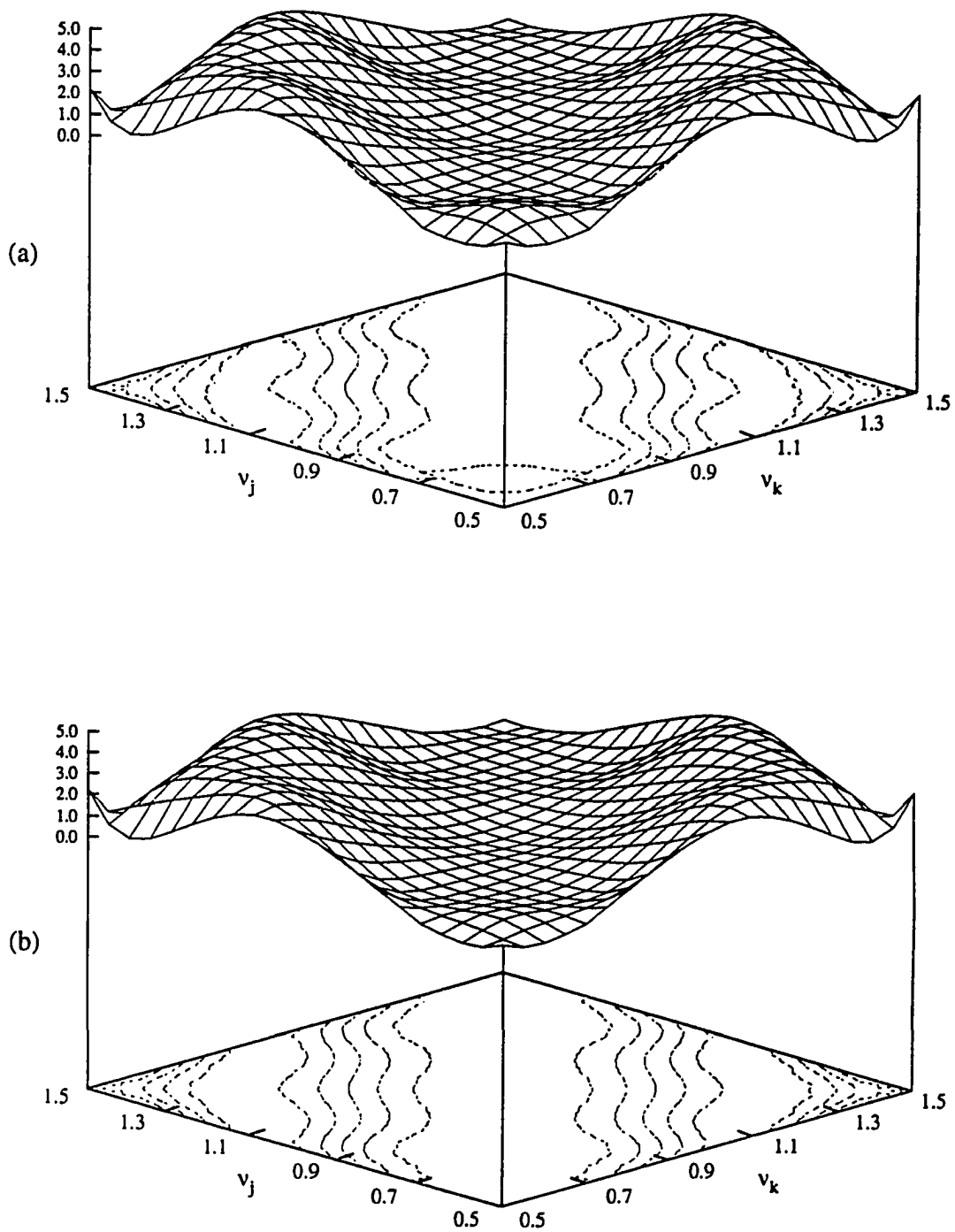


Fig. 4.33 Difference-frequency hydrodynamic heave force QTF, $H^-(\omega_j, \omega_k; \beta_j, \beta_k)$, for the ISSC TLP with $\beta_j = \beta_k = 22.5^\circ$. Notations: (a) Fixed TLP, (b) Tethered TLP.

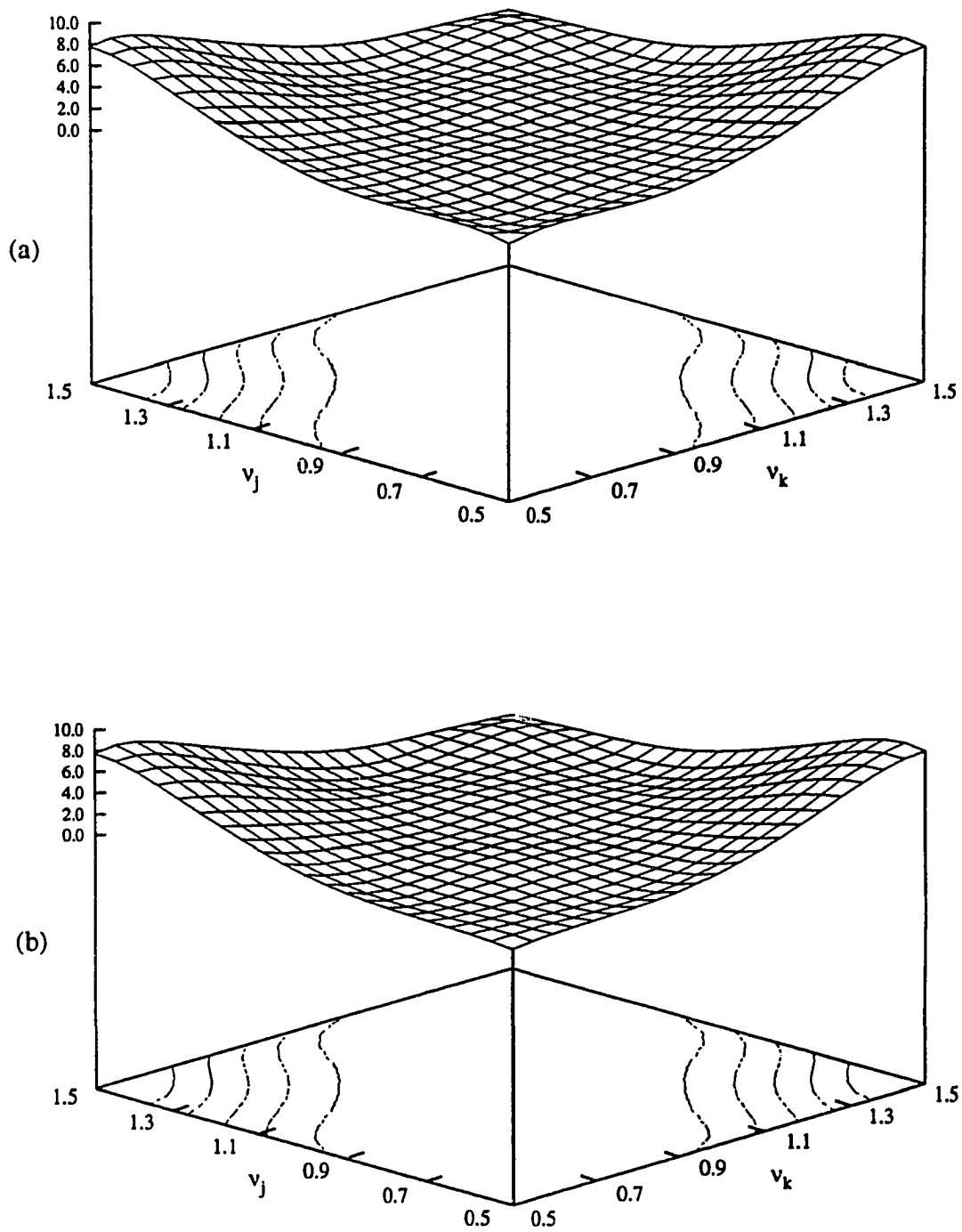


Fig. 4.34 Difference-frequency hydrodynamic roll moment QTF, $H^*(\omega_j, \omega_k; \beta_j, \beta_k)$, for the ISSC TLP with $\beta_j = 0^\circ$, $\beta_k = 45^\circ$. Notations: (a) Fixed TLP, (b) Tethered TLP.

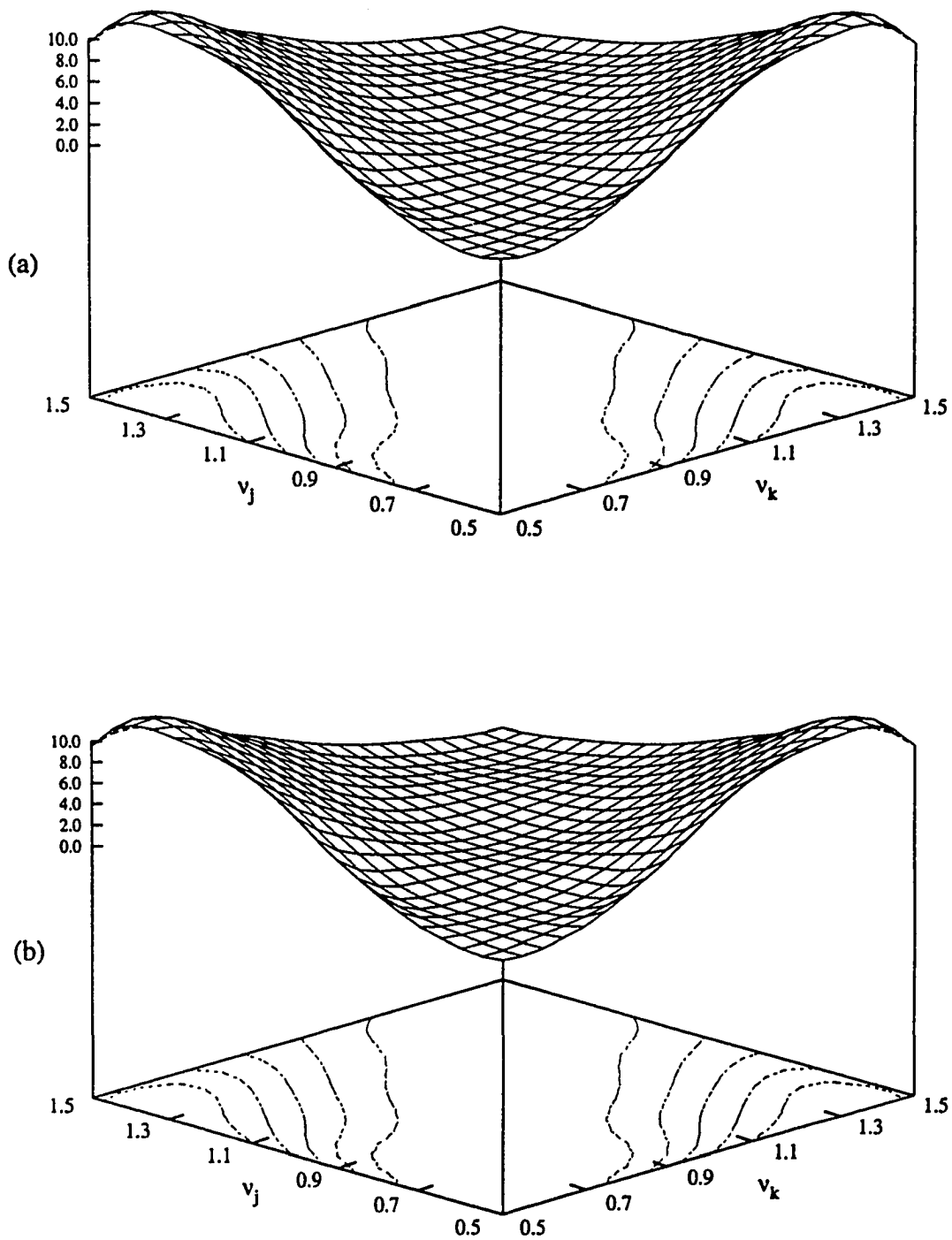


Fig. 4.35 Difference-frequency hydrodynamic roll moment QTF, $H^-(\omega_j, \omega_k; \beta_j, \beta_k)$, for the ISSC TLP with $\beta_j = 45^\circ$, $\beta_k = 0^\circ$. Notations: (a) Fixed TLP, (b) Tethered TLP.

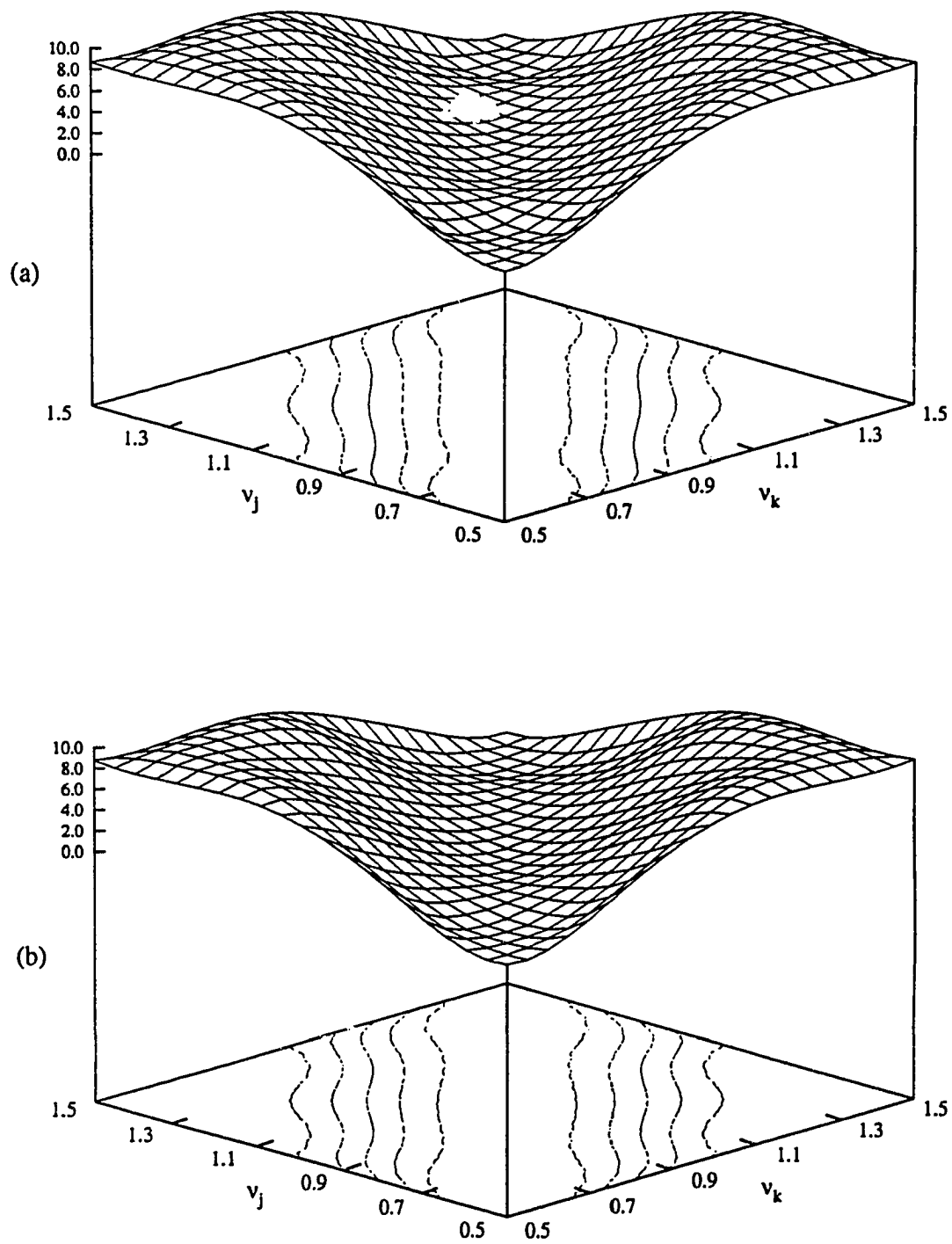


Fig. 4.36 Difference-frequency hydrodynamic roll moment QTF, $H^-(\omega_j, \omega_k; \beta_j, \beta_k)$, for the ISSC TLP with $\beta_j = \beta_k = 22.5^\circ$. Notations: (a) Fixed TLP, (b) Tethered TLP.

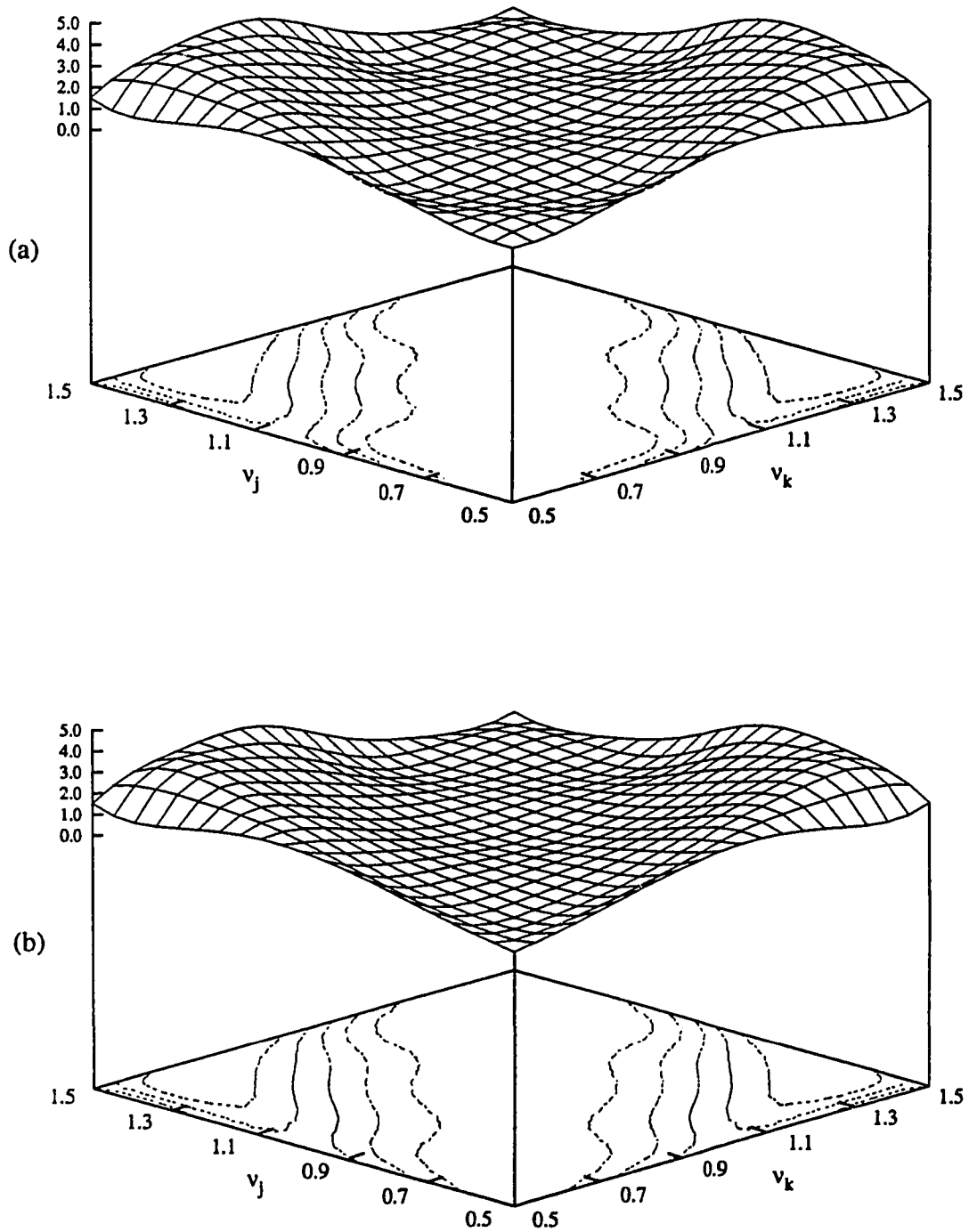


Fig. 4.37 Difference-frequency hydrodynamic pitch moment QTF, $H^-(\omega_j, \omega_k; \beta_j, \beta_k)$, for the ISSC TLP with $\beta_j = 0^\circ$, $\beta_k = 45^\circ$. Notations: (a) Fixed TLP, (b) Tethered TLP.

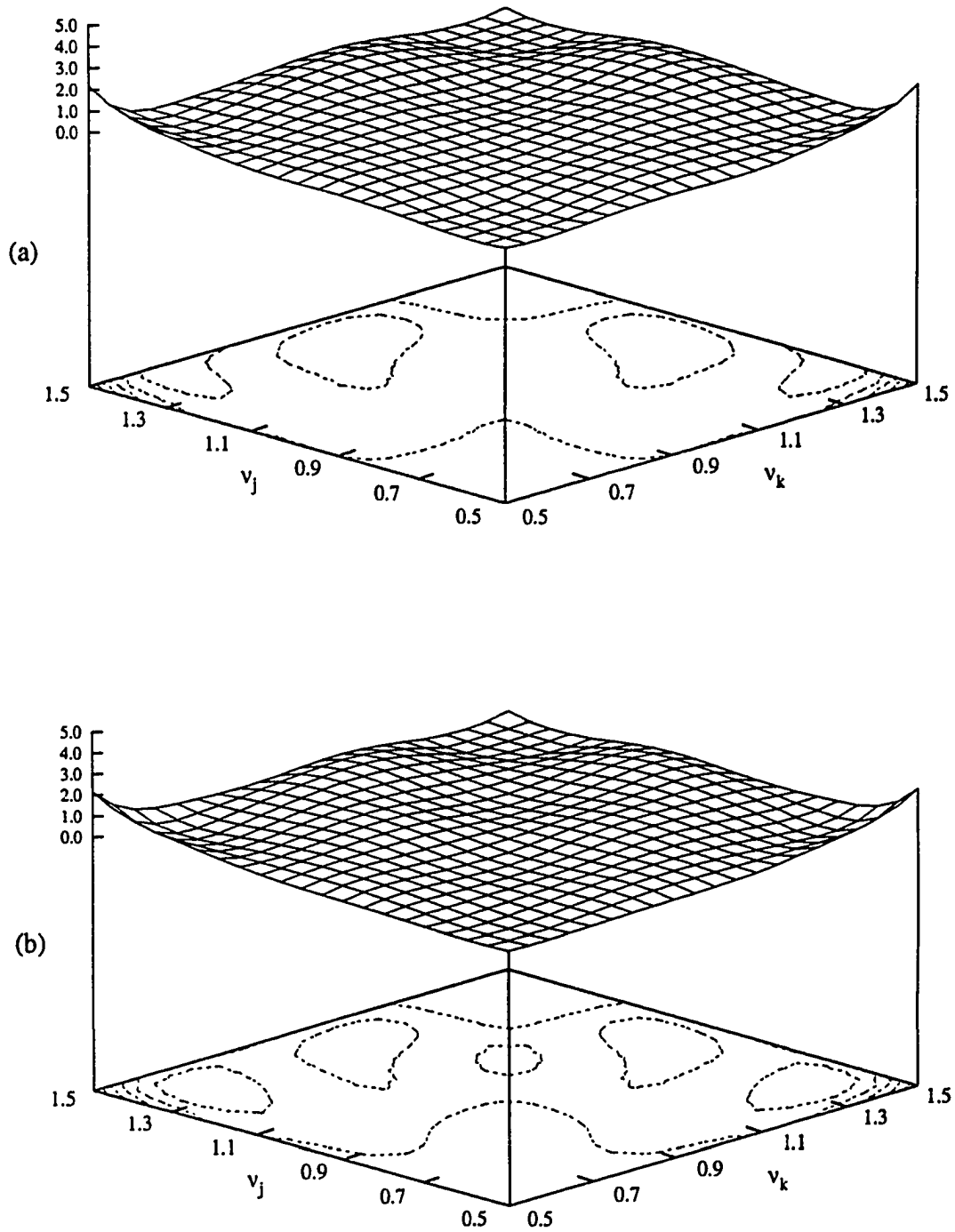


Fig. 4.38 Difference-frequency hydrodynamic pitch moment QTF, $H^-(\omega_j, \omega_k; \beta_j, \beta_k)$, for the ISSC TLP with $\beta_j = 45^\circ$, $\beta_k = 0^\circ$. Notations: (a) Fixed TLP, (b) Tethered TLP.

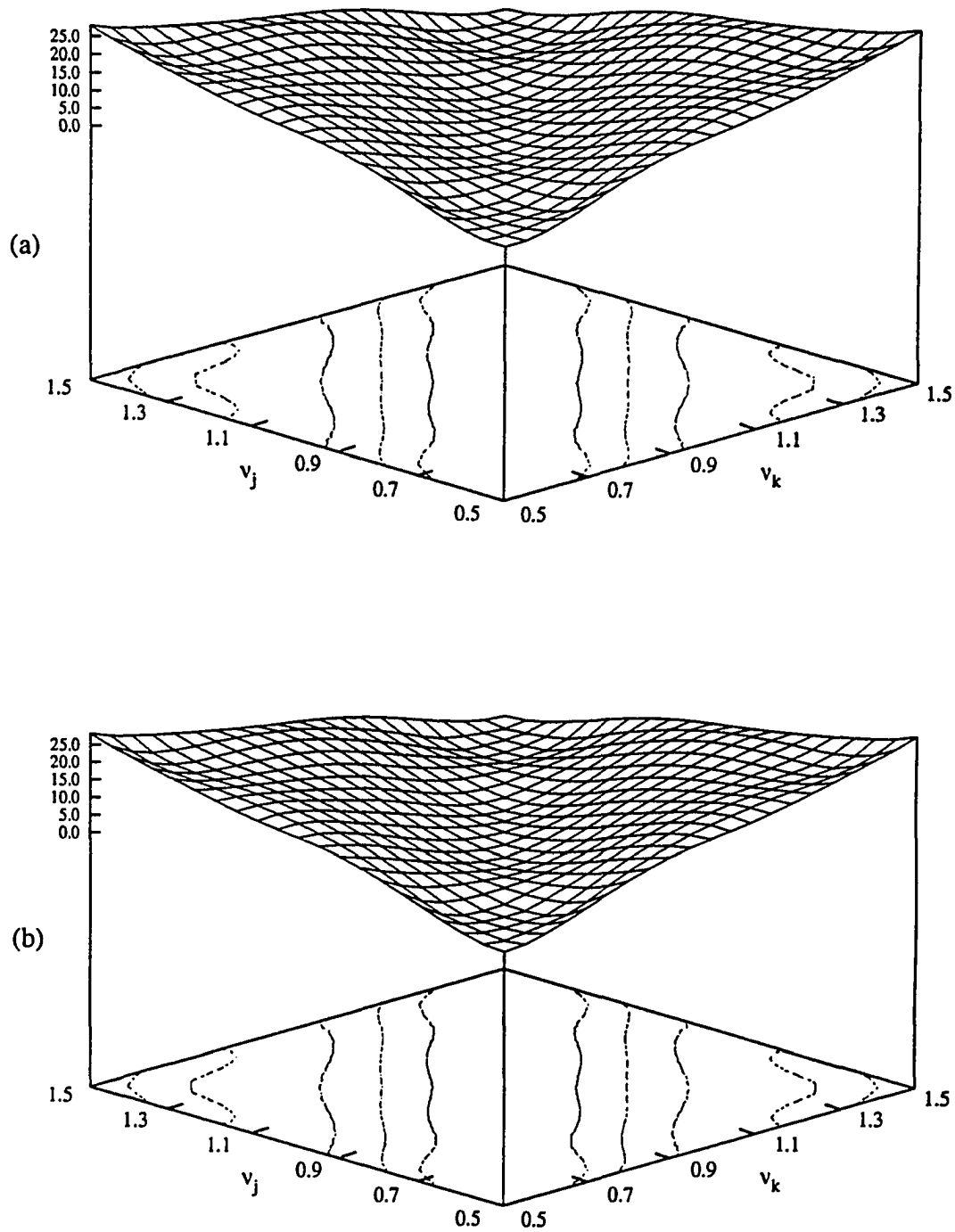


Fig. 4.39 Difference-frequency hydrodynamic pitch moment QTF, $H^-(\omega_j, \omega_k; \beta_j, \beta_k)$, for the ISSC TLP with $\beta_j = \beta_k = 22.5^\circ$. Notations: (a) Fixed TLP, (b) Tethered TLP.

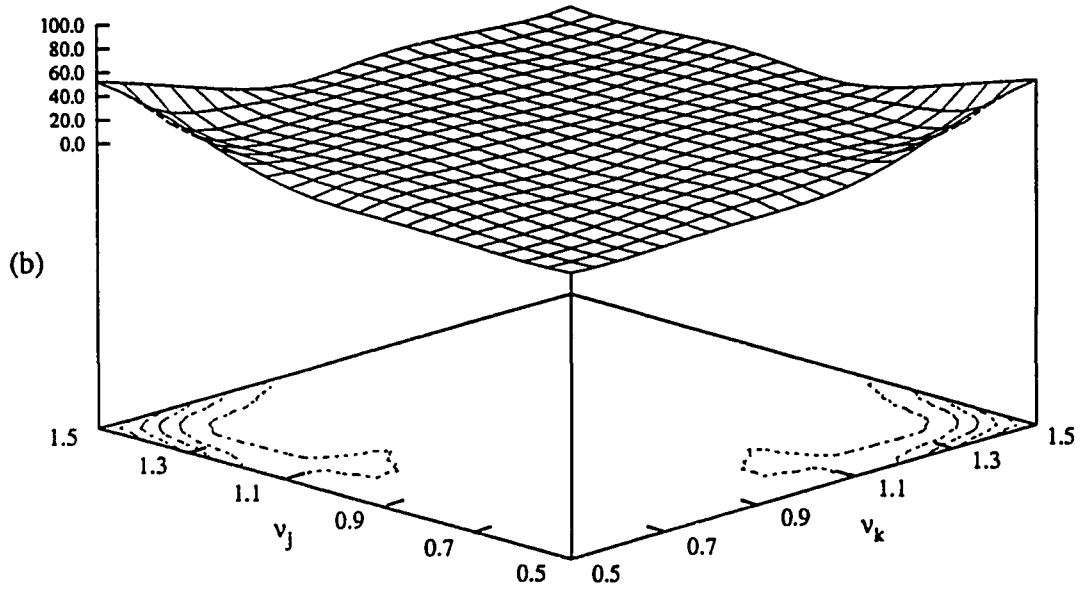
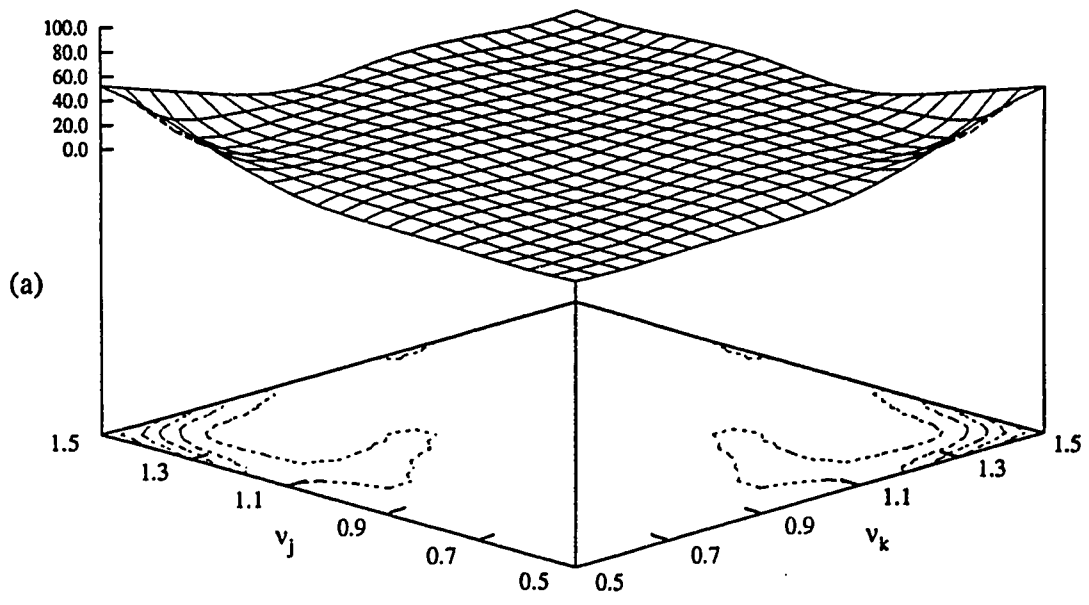


Fig. 4.40 Difference-frequency hydrodynamic yaw moment QTF, $H^-(\omega_j, \omega_k; \beta_j, \beta_k)$, for the ISSC TLP with $\beta_j = 40^\circ$, $\beta_k = 45^\circ$. Notations: (a) Fixed TLP, (b) Tethered TLP.

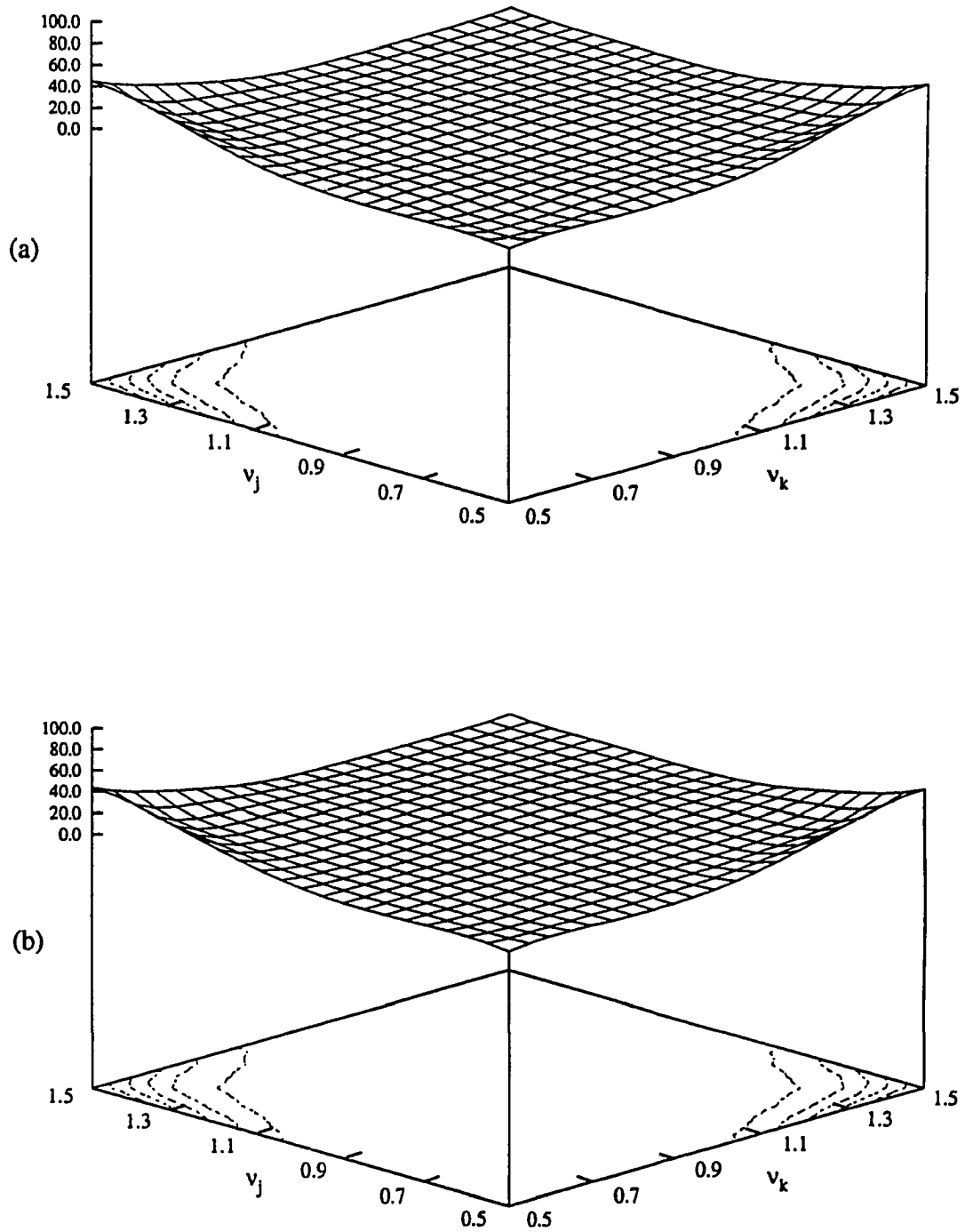


Fig. 4.41 Difference-frequency hydrodynamic yaw moment QTF, $H^-(\omega_j, \omega_k; \beta_j, \beta_k)$, for the ISSC TLP with $\beta_j = 45^\circ$, $\beta_k = 0^\circ$. Notations: (a) Fixed TLP, (b) Tethered TLP.

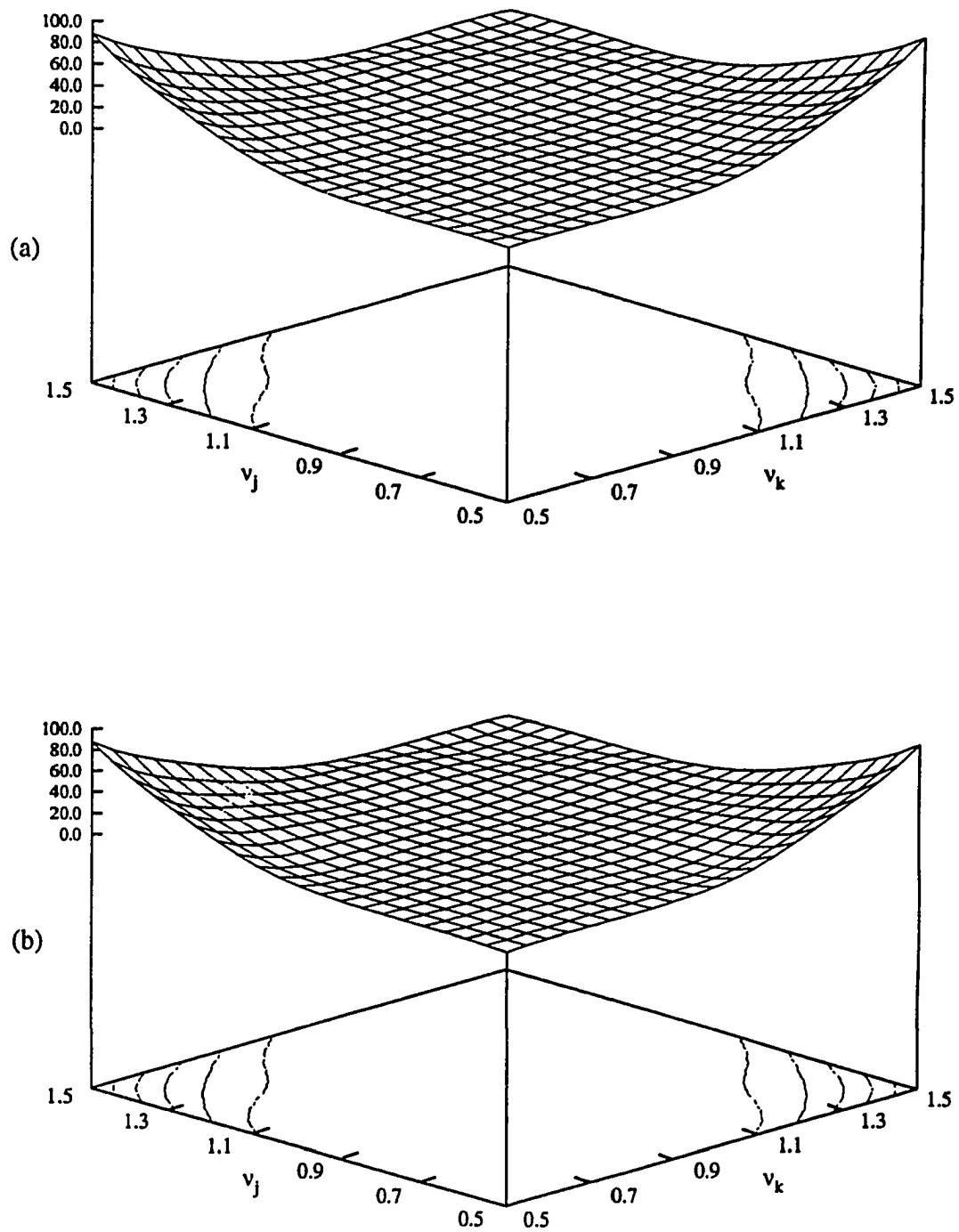


Fig. 4.42 Difference-frequency hydrodynamic yaw moment QTF, $H^*(\omega_j, \omega_k; \beta_j, \beta_k)$, for the ISSC TLP with $\beta_j = \beta_k = 22.5^\circ$. Notations: (a) Fixed TLP, (b) Tethered TLP.

Table 4.3 Ratio of the maximum second-order sum-frequency vertical force QTF with different angles of wave incidence $H^+(\omega_j, \omega_k; \beta_j, \beta_k)$ to those resulting from unidirectional waves $H^+(\omega_j, \omega_k; \beta_q, \beta_q)$. The upper right triangular matrix contains the QTF ratios for a tethered ISSC TLP, the lower left triangle contains the QTF ratios for a fixed ISSC TLP. In row 1, $\beta_j = 0^\circ$, $\beta_k = 45^\circ$, and $\beta_q = 0^\circ$; in row 2, $\beta_j = 0^\circ$, $\beta_k = 45^\circ$, and $\beta_q = 45^\circ$; in row 3, $\beta_j = 45^\circ$, $\beta_k = 0^\circ$, and $\beta_q = 0^\circ$; in row 4, $\beta_j = 0^\circ$, $\beta_k = 45^\circ$, and $\beta_q = 45^\circ$.

$v_j =$		0.5	0.7	0.9	1.1	1.3	1.5
$v_k =$	0.18	0.74	0.31	0.22	9.90	1.40	0.67
	0.15	0.19	0.30	0.37	0.83	2.20	0.46
0.5	0.18	0.74	0.26	0.81	7.29	0.52	0.49
	0.15	0.18	0.26	1.37	0.61	0.82	0.34
0.7	0.17	0.34	0.56	1.41	0.53	1.08	0.79
	0.33	3.16	3.92	2.31	0.69	1.51	0.99
	0.23	0.34	0.54	1.62	1.12	0.49	0.17
	0.45	3.16	3.76	2.65	1.44	0.69	0.22
0.9	0.32	0.83	1.29	2.43	1.34	0.35	0.65
	0.62	2.77	5.09	4.69	2.21	0.78	1.48
	1.11	0.99	1.29	2.42	1.21	0.37	0.65
	2.12	3.30	5.09	4.67	1.98	0.82	1.48
1.1	1.36	0.22	1.94	1.02	0.79	0.31	0.32
	0.69	0.37	1.64	1.10	1.30	0.98	0.65
	1.20	0.60	1.76	1.02	0.78	0.28	1.48
	0.61	1.02	1.49	1.10	1.30	0.91	2.99
1.3	1.49	0.88	0.32	0.36	0.07	0.07	0.55
	1.65	0.97	0.76	0.73	0.10	0.13	0.41
	0.90	0.57	0.38	0.32	0.07	0.07	0.86
	0.99	0.62	0.90	0.63	0.10	0.12	0.65
1.5	0.55	0.95	0.86	0.46	0.71	1.38	1.11
	0.52	1.41	1.59	0.72	0.43	1.48	2.30
	0.45	0.29	1.29	1.76	1.04	1.38	1.10
	0.42	0.42	2.39	2.75	0.64	1.48	2.28
$v_j =$		0.5	0.7	0.9	1.1	1.3	1.5

Table 4.4 Ratio of the maximum second-order sum frequency overturning moment QTF with different angles of wave incidence $H^+(\omega_j, \omega_k; \beta_j, \beta_k)$ to those resulting from unidirectional waves $H^+(\omega_j, \omega_k; \beta_q, \beta_q)$. The upper right triangular matrix contains the QTF ratios for a tethered ISSC TLP, the lower left triangle contains the QTF ratios for a fixed ISSC TLP. In row 1, $\beta_j = 0^\circ$, $\beta_k = 45^\circ$, and $\beta_q = 0^\circ$; in row 2, $\beta_j = 0^\circ$, $\beta_k = 45^\circ$, and $\beta_q = 45^\circ$; in row 3, $\beta_j = 45^\circ$, $\beta_k = 0^\circ$, and $\beta_q = 0^\circ$; in row 4, $\beta_j = 0^\circ$, $\beta_k = 45^\circ$, and $\beta_q = 45^\circ$.

$v_j =$		0.5	0.7	0.9	1.1	1.3	1.5
$v_k =$	0.62	0.71	0.65	0.45	0.38	2.67	1.57
	1.14	0.99	1.15	0.82	0.45	1.07	1.27
0.5	0.62	0.72	0.60	0.25	0.58	3.89	1.39
	1.14	1.00	1.06	0.46	0.70	1.55	1.12
0.7	0.24	0.44	0.60	0.64	0.55	1.04	0.57
	0.49	0.70	1.11	0.59	1.06	1.55	0.73
	0.45	0.44	0.60	1.11	0.87	1.89	0.95
	0.93	0.70	1.10	1.03	1.66	2.83	1.22
0.9	0.43	0.27	0.50	3.06	2.27	1.11	0.37
	0.57	0.50	0.45	0.71	0.79	1.53	0.28
	0.63	0.76	0.50	3.06	2.53	2.12	1.45
	0.83	1.44	0.45	0.71	0.88	2.92	1.11
1.1	0.41	0.91	3.90	3.09	3.08	4.54	0.66
	0.42	0.89	0.75	1.07	1.05	0.67	0.66
	0.91	1.68	4.86	3.09	3.07	5.19	1.15
	0.93	1.64	0.93	1.07	1.05	0.77	1.15
1.3	2.25	0.78	0.88	3.04	3.82	3.00	1.19
	0.77	1.03	1.67	0.63	0.50	0.53	0.57
	4.26	1.67	1.58	3.28	3.82	3.00	1.90
	1.46	2.20	3.00	0.68	0.50	0.53	0.91
1.5	1.98	1.18	0.57	0.72	1.20	1.00	0.88
	1.19	0.75	0.44	0.83	0.42	0.42	0.65
	2.14	1.96	1.45	1.07	2.07	1.00	0.88
	1.28	1.25	1.13	1.23	0.72	0.42	0.65
$v_j =$		0.5	0.7	0.9	1.1	1.3	1.5

Table 4.5 Ratio of the maximum second-order difference-frequency horizontal force QTF with different angles of wave incidence $H^-(\omega_j, \omega_k; \beta_j, \beta_k)$ to those resulting from unidirectional waves $H^-(\omega_j, \omega_k; \beta_q, \beta_q)$. The upper right triangular matrix contains the QTF ratios for a tethered ISSC TLP, the lower left triangle contains the QTF ratios for a fixed ISSC TLP. In row 1, $\beta_j = 0^\circ$, $\beta_k = 45^\circ$, and $\beta_q = 0^\circ$; in row 2, $\beta_j = 0^\circ$, $\beta_k = 45^\circ$, and $\beta_q = 45^\circ$; in row 3, $\beta_j = 45^\circ$, $\beta_k = 0^\circ$, and $\beta_q = 0^\circ$; in row 4, $\beta_j = 0^\circ$, $\beta_k = 45^\circ$, and $\beta_q = 45^\circ$.

$v_j =$		0.5	0.7	0.9	1.1	1.3	1.5
$v_k =$	0.42	1.49	0.05	0.05	0.84	0.21	0.15
	0.25	0.28	0.05	0.04	0.20	2.62	1.65
	0.5	0.42	1.49	0.43	0.71	5.98	0.59
	0.25	0.28	0.42	0.57	1.44	7.36	2.26
0.7	0.03	0.30	0.69	0.07	0.16	4.07	0.40
	0.04	1.04	1.20	0.06	0.13	0.62	4.41
	0.35	0.30	0.69	0.39	0.70	8.61	0.51
	0.45	1.04	1.20	0.37	0.55	1.30	5.72
0.9	0.05	0.11	0.46	0.53	0.11	0.33	33.62
	0.05	0.13	0.42	0.39	0.10	0.27	0.94
	0.65	0.39	0.46	0.53	0.39	0.63	41.70
	0.62	0.46	0.42	0.39	0.37	0.52	1.16
1.1	1.38	0.11	0.03	0.28	0.29	0.17	0.36
	0.19	0.09	0.03	0.26	0.34	0.20	0.37
	11.10	0.73	0.46	0.28	0.29	0.34	0.49
	1.53	0.62	0.41	0.26	0.34	0.39	0.51
1.3	0.21	4.00	0.34	0.19	0.17	0.16	0.17
	2.37	0.56	0.25	0.18	0.22	0.27	0.24
	0.63	9.37	0.73	0.37	0.17	0.16	0.26
	7.04	1.31	0.54	0.36	0.22	0.27	0.38
1.5	0.15	0.39	8.01	0.42	0.22	0.06	0.13
	1.62	3.39	0.90	0.39	0.29	0.11	0.26
	0.21	0.53	10.04	0.53	0.27	0.06	0.13
	2.29	4.64	1.13	0.50	0.36	0.11	0.26
$v_j =$		0.5	0.7	0.9	1.1	1.3	1.5

CHAPTER FIVE

ARRAYS OF BOTTOM-MOUNTED, SURFACE-PIERCING CYLINDERS IN BICHROMATIC BIDIRECTIONAL WAVES

Consider a structure consisting of an array of M bottom-mounted, surface-piercing vertical cylinders of arbitrary, uniform cross-sections bounded by $C_0 = C_1 \cup C_2 \dots \cup C_M$, situated in water of constant depth d . In this chapter, a numerical solution is presented for the second-order sum- and difference-frequency hydrodynamic loads in bichromatic bidirectional waves. This derivation has many similarities with that obtained in Chapter Three for arbitrarily-shaped structures in deep water. The main difference between the two cases is that for the array of bottom-mounted cylinders case, the second-order loads on each of the cylinders may be of interest, requiring the computation of the assisting radiated potential due to the oscillation of each of the cylinders making up the array while holding all others fixed. The other difference is, of course, in the solution to the first-order potentials that each of the cases requires.

This chapter starts with a derivation of a solution for the first-order scattered potential and the assisting radiated potential needed for the computation of the second-order sum- and difference-frequency loads due to the interaction of the array of cylinders with a bichromatic wave system represented by the superposition of two waves of amplitudes Γ_j with frequencies ω_j , and incident direction β_j $j = 1, 2$. The boundary-value problem for the first-order scattered potential is similar to that for the ocean structure in deep water, with the exception of an additional bottom boundary condition requiring that the vertical velocity at the sea bed be zero. Also, for fixed structures such as this one, $V_n = 0$, therefore the body motions are zero and there is no need to compute a first-order radiation potential. An

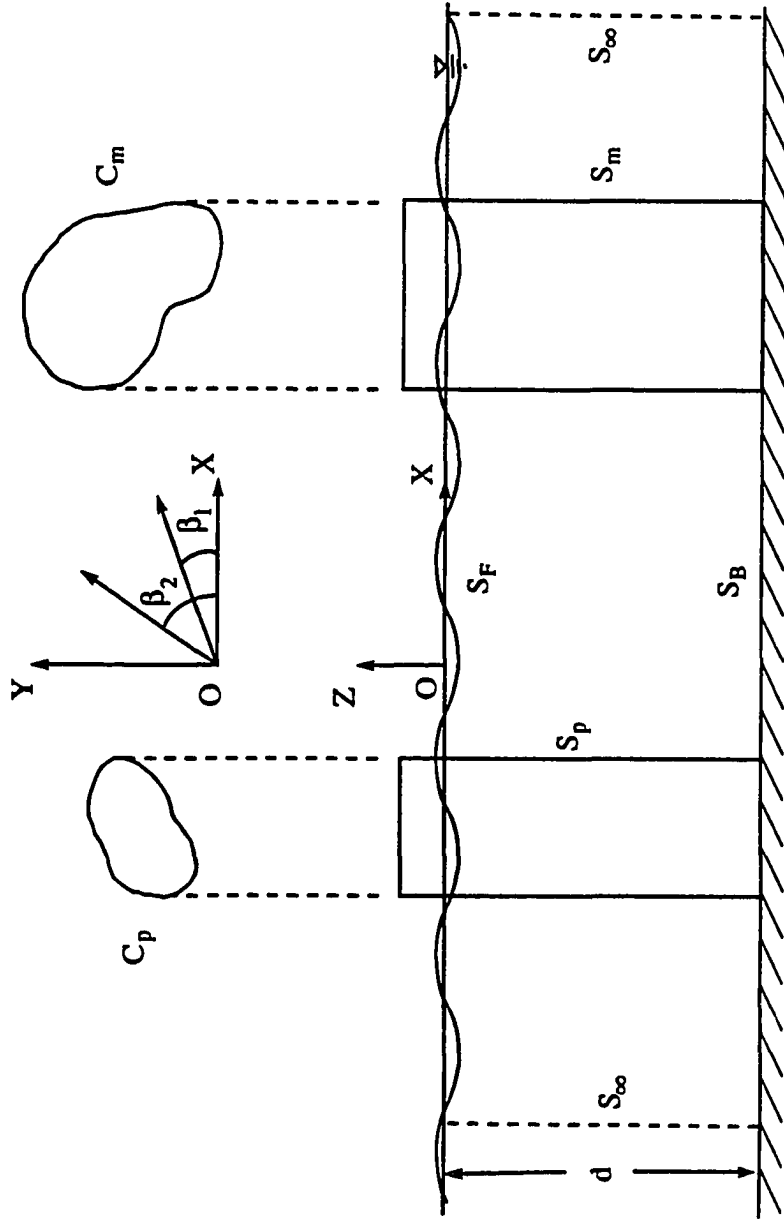


Fig. 5.1 Definition Sketch.

assisting radiated potential, however, is still needed for the computation of the second-order hydrodynamic loads on the array.

As in Chapter Three, the j th component of the first-order potential is decomposed into incident and scattered potentials. The spatial component of the incident potential is given by

$$\Phi_{jI}^{(1)} = -\frac{ig\Gamma_j}{\omega_j} \frac{\cosh k_{oj}(z+d)}{\cosh k_{oj}d} \Psi_{jI}^{(1)}(x,y), \quad (5.1a)$$

in which

$$\Psi_{jI}^{(1)} = e^{ik_{oj}(x \cos \beta_j + y \sin \beta_j)}, \quad (5.1b)$$

where Γ_j is the amplitude of the j th incident wave component and k_{oj} its associated wavenumber related to the wave frequency by the dispersion relation $\omega_j^2 = gk_{oj} \tanh [k_{oj}d]$.

5.1 First-Order Scattered Potential Solution

For wave diffraction by an array of structures possessing arbitrary cross-sections which are uniform with depth, the j th component of the first-order scattered potential may be written as

$$\Phi_{jS}^{(1)}(\underline{X}) = -\frac{ig\Gamma_j}{\omega_j} \frac{\cosh k_{oj}(z+d)}{\cosh k_{oj}d} \Psi_{jS}^{(1)}(\underline{r}), \quad (5.2)$$

where $\underline{X} = \{x,y,z\}$ and $\underline{r} = \{x,y\}$.

The boundary-value problem for $\Psi_{jS}^{(1)}$ can be shown to be

$$\nabla^2 \Psi_{jS}^{(1)} + k_{oj}^2 \Psi_{jS}^{(1)} = 0 \quad \text{in } \bar{V}, \quad (5.3)$$

$$\frac{\partial \Psi_{jS}^{(1)}}{\partial n} = - \frac{\partial \Psi_{jI}^{(1)}}{\partial n} \quad \text{on } C_m \quad m = 1, 2, \dots, M, \quad (5.4)$$

$$\lim_{r \rightarrow \infty} \sqrt{r} \left\{ \frac{\partial \Psi_{jS}^{(1)}}{\partial r} - ik_{oj} \Psi_{jS}^{(1)} \right\} = 0. \quad (5.5)$$

In Eq. (5.3), \bar{V} is the fluid domain in any horizontal plane. It is noted that the form for $\Phi_{jS}^{(1)}$ given by Eq. (5.2) identically satisfies the boundary conditions on S_F and S_B . The above problem for $\Psi_{jS}^{(1)}$ will be solved utilizing a source distribution method in two dimensions. The j th component of the scattered potential is taken to be of the form

$$\Psi_{jS}^{(1)}(\mathbf{L}_0) = \int_{C_0} \sigma_{jS}(\mathbf{r}') G_0(\omega_j; \mathbf{L}_0, \mathbf{r}') dL. \quad (5.6)$$

A suitable Green's function $G_0(\omega_j; \mathbf{r}, \mathbf{r}')$ is given by

$$G_0(\omega_j; \mathbf{r}, \mathbf{r}') = \frac{1}{4i} H_0^{(1)}(k_{oj} R_1), \quad (5.7)$$

where $H_0^{(1)}$ is the Hankel function of the first kind of order zero, $\mathbf{r}' = (x', y')$ and $R_1 = \sqrt{(x - x')^2 + (y - y')^2}$.

Letting \mathbf{L}_0 be a point on C_m , then Eq. (5.6) may be used to express the scattered velocity normal to the structure at \mathbf{L}_0 as

$$\frac{\partial \Psi_{jS}^{(1)}}{\partial n}(\mathbf{L}_0) = \gamma(\mathbf{L}_0) \sigma_{jS}(\mathbf{L}_0) + \int_{C_0} \sigma_{jS}^{(1)}(\mathbf{r}') \frac{\partial G_0}{\partial n}(\omega_j; \mathbf{L}_0, \mathbf{r}') dL, \quad (5.8)$$

in which $\gamma(\mathbf{L}_0)$ is the interior angle at \mathbf{L}_0 . For smooth contours, $\gamma(\mathbf{L}_0)$ takes a value of π .

The cylinder contours are now discretized into a total of M' higher-order line elements each described in terms of N_e nodes for a total of N_T nodes on the cylinder contours. Next, the variation of the scattered source strengths over each of these elements is expressed in terms of its corresponding values at the nodes and appropriate shape functions. For \mathbf{L}_0 at the n^{th} node ($\mathbf{L}_0 = \mathbf{L}_n$), after applying the structural boundary condition, Eq. (5.4), equation (5.8) becomes

$$-\frac{\partial \Psi_{i\mathbf{L}}^{(1)}}{\partial n}(\mathbf{L}_0) = \gamma(\mathbf{L}_0) \sigma_{jS}(\mathbf{L}_0) + \sum_{m'=1}^{M'} \sum_{i=1}^{N_e} \sigma_{jS}^{(1)}(\mathbf{L}_{i^*}) \int_{\Delta C_m} N_i \frac{\partial G_o}{\partial n}(\omega_j; \mathbf{L}_0; \mathbf{L}') dL, \quad (5.9)$$

where i^* is the node number associated with the i^{th} node of the m^{th} element in the global system. Allowing n to vary from $n = 1$ to $n = N_T$ results in a system of $N_T \times N_T$ linear equations which can be solved for the unknown source strength values at the nodes. The contour integrals are carried out utilizing standard one-dimensional Gauss quadrature.

Once the source strength values at the nodes are computed, the velocity potential at any point \mathbf{L}_n in the plane may be determined from the discretized version of Eq. (5.6), namely

$$\Psi_{jS_n}^{(1)} = \sum_{m'=1}^{M'} \sum_{i=1}^{N_e} \sigma_{jS}^{(1)}(\mathbf{L}_{i^*}) \int_{\Delta C_m} N_i G_o(\omega_j; \mathbf{L}_n; \mathbf{L}') dL. \quad (5.10)$$

Taking derivatives of Eq. (5.10) with respect to x and y yields

$$\frac{\partial \Psi_{jS_n}^{(1)}}{\partial x_n} = \sum_{m'=1}^{M'} \sum_{i=1}^{N_e} \sigma_{jS}^{(1)}(\underline{r}_{i*}) \int_{\Delta C_m} N_i \frac{\partial G_o}{\partial x_n}(\omega_j, \underline{r}_n; \underline{r}') dL, \quad (5.11a)$$

and

$$\frac{\partial \Psi_{jS_n}^{(1)}}{\partial y_n} = \sum_{m'=1}^{M'} \sum_{i=1}^{N_e} \sigma_{jS}^{(1)}(\underline{r}_{i*}) \int_{\Delta C_m} N_i \frac{\partial G_o}{\partial y_n}(\omega_j, \underline{r}_n; \underline{r}') dL. \quad (5.11b)$$

These expressions, combined with Eq. (5.2) are used to express the velocity potential and water particle velocities at any point strictly inside the fluid domain V as

$$\Phi_{jS}^{(1)}(\underline{X}_n) = -\frac{ig\Gamma_j}{\omega_j} \frac{\cosh k_{oj}(z_n+d)}{\cosh k_{oj}d} \sum_{m'=1}^{M'} \sum_{i=1}^{N_e} \sigma_{jS}^{(1)}(\underline{r}_{i*}) \int_{\Delta C_m} N_i G_o(\omega_j, \underline{r}_n; \underline{r}') dL, \quad (5.12a)$$

$$\frac{\partial \Phi_{jS}^{(1)}}{\partial x}(\underline{X}_n) = -\frac{ig\Gamma_j}{\omega_j} \frac{\cosh k_{oj}(z_n+d)}{\cosh k_{oj}d} \sum_{m'=1}^{M'} \sum_{i=1}^{N_e} \sigma_{jS}^{(1)}(\underline{r}_{i*}) \int_{\Delta C_m} N_i \frac{\partial G_o}{\partial x_n}(\omega_j, \underline{r}_n; \underline{r}') dL, \quad (5.12b)$$

$$\frac{\partial \Phi_{jS}^{(1)}}{\partial y}(\underline{X}_n) = -\frac{ig\Gamma_j}{\omega_j} \frac{\cosh k_{oj}(z_n+d)}{\cosh k_{oj}d} \sum_{m'=1}^{M'} \sum_{i=1}^{N_e} \sigma_{jS}^{(1)}(\underline{r}_{i*}) \int_{\Delta C_m} N_i \frac{\partial G_o}{\partial y_n}(\omega_j, \underline{r}_n; \underline{r}') dL, \quad (5.12c)$$

and

$$\frac{\partial \Phi_{jS}^{(1)}}{\partial z}(\underline{X}_n) = k_{oj} \tanh k_{oj}(z_n+d) \Phi_{jS}^{(1)}(\underline{X}_n). \quad (5.12d)$$

5.2 Radiated Potential Solution

In the computation of the second-order hydrodynamic loads, the solution to the assisting radiated potential is required. In particular, the solution for the velocity potential generated by the oscillation of the m th cylinder in the p th mode. Although the cylinders are bottom mounted (i.e., fixed), the solution of the potential due to the fictitious motion of the cylinders is possible. For an array of bottom mounted cylinders of constant cross-section, the heave ($p=3$) mode of oscillation cannot be determined. Therefore, in the subsequent derivation, p may take values 1, 2, 4, 5, and 6; associated with oscillations in surge, sway, roll, pitch, and yaw modes, respectively. It should be noted; however, that the yaw mode of oscillation is only relevant when discussing the oscillation of the entire cylinder array as a single unit.

For an array of vertical cylinders of arbitrary cross-section, the z -dependency of the linearized assisting radiation potential, due to the oscillation of the m th cylinder in the p th mode, may be expanded in terms of eigenfunctions,

$$\Phi_{mp}^{\pm}(\mathbf{X}) = \frac{\cosh \lambda_o^{\pm}(z+d)}{\cosh \lambda_o^{\pm}d} \Psi_{mp}^{o\pm}(\mathbf{r}) + \sum_{q=1}^{\infty} \frac{\cos \lambda_q^{\pm}(z+d)}{\cos \lambda_q^{\pm}d} \Psi_{mp}^{q\pm}(\mathbf{r}), \quad (5.13)$$

where the wave numbers are given by the positive real roots of the dispersion relations, $(\omega_j \pm \omega_k)^2 = g \lambda_o^{\pm} \tanh \lambda_o^{\pm} d$ and $(\omega_j \pm \omega_k)^2 = -g \lambda_q^{\pm} \tan \lambda_q^{\pm} d$.

Using Eq. (5.13), the boundary-value problems satisfied by $\Psi_{mp}^{o\pm}(\mathbf{r})$ and $\Psi_{mp}^{q\pm}(\mathbf{r})$, $q = 1, 2, \dots$ can be shown to be

$$\nabla^2 \Psi_{mp}^{o\pm} + \lambda_o^{\pm 2} \Psi_{mp}^{o\pm} = 0 \quad \text{in } \bar{V}, \quad (5.14)$$

$$\frac{\partial \Psi_{mp}^{\circ\pm}}{\partial n} = \frac{2 \sinh 2\lambda_o^\pm d}{2\lambda_o^\pm d + \sinh 2\lambda_o^\pm d} V_{mpn_p} \quad \text{on } C_m, p = 1, 2, 6, \quad (5.15a)$$

$$\frac{\partial \Psi_{mp}^{\circ\pm}}{\partial n} = \frac{4 \cosh \lambda_o^\pm d [1 - \cosh \lambda_o^\pm d]}{\lambda_o^\pm [2\lambda_o^\pm d + \sinh 2\lambda_o^\pm d]} V_{mpn_p} \quad \text{on } C_m, p = 4, 5, \quad (5.15b)$$

$$\frac{\partial \Psi_{np}^{\circ\pm}}{\partial n} = 0 \quad \text{on } C_n, n = 1, 2, \dots, M \quad (n \neq m), \quad (5.15c)$$

$p = 1, 2, 4, 5, 6,$

$$\lim_{r \rightarrow \infty} \sqrt{r} \left\{ \frac{\partial \Psi_{mp}^{\circ\pm}}{\partial r} - i\lambda_o^\pm \Psi_{mp}^{\circ\pm} \right\} = 0, \quad (5.16)$$

$$\nabla^2 \Psi_{mp}^{\circ\pm} - \lambda_q^{\pm 2} \Psi_{mp}^{\circ\pm} = 0 \quad \text{in } \bar{V}, \quad (5.17)$$

$$\frac{\partial \Psi_{mp}^{\circ\pm}}{\partial n} = \frac{2 \sin 2\lambda_q^\pm d}{2\lambda_q^\pm d + \sin 2\lambda_q^\pm d} V_{mpn_p} \quad \text{on } C_m, p = 1, 2, 6, \quad (5.18a)$$

$$\frac{\partial \Psi_{mp}^{\circ\pm}}{\partial n} = \frac{4 \cos \lambda_q^\pm d [-1 + \cos \lambda_q^\pm d]}{\lambda_q^\pm [2\lambda_q^\pm d + \sin 2\lambda_q^\pm d]} V_{mpn_p} \quad \text{on } C_m, p = 4, 5, \quad (5.18b)$$

$$\frac{\partial \Psi_{mp}^{\circ\pm}}{\partial n} = 0 \quad \text{on } C_n, n = 1, 2, \dots, M \quad (n \neq m), \quad (5.18c)$$

$p = 1, 2, 4, 5, 6,$

$$\Psi_{mp}^{\circ\pm} \rightarrow 0 \quad \text{as } r \rightarrow \infty, \quad (5.19)$$

where the z-dependency in Eqs. (5.14) - (5.19) has been removed by invoking the orthogonality of the vertical eigenfunctions.

The solution to the assisting radiated potential is similar in form to that for the j th component of the scattered potential. The propagating component of the assisting radiated potential at the sum- and difference-frequency is taken to be of the form,

$$\Psi_{mp}^{\omega^{\pm}}(\underline{r}_0) = \int_{C_0} \sigma_{mp}^{\omega^{\pm}}(\underline{r}') G_0(\omega^{\pm}; \underline{r}, \underline{r}') dL, \quad (5.20a)$$

while the q th evanescent component is given by

$$\Psi_{mp}^{\omega^{\pm}}(\underline{r}_0) = \int_{C_0} \sigma_{mp}^{\omega^{\pm}}(\underline{r}') G_q(\omega^{\pm}; \underline{r}, \underline{r}') dL. \quad (5.20b)$$

Suitable Green's functions $G_0(\omega^{\pm}; \underline{r}, \underline{r}')$, and $G_q(\omega^{\pm}; \underline{r}, \underline{r}')$, $q = 1, 2, \dots$ for the above representations of the radiated potential are given by

$$G_0(\omega^{\pm}; \underline{r}, \underline{r}') = \frac{1}{4i} H_0^{(1)}(\lambda_0^{\pm} R_1) \quad (5.21a)$$

and

$$G_q(\omega^{\pm}; \underline{r}, \underline{r}') = -\frac{1}{2\pi} K_0(\lambda_q^{\pm} R_1), \quad (5.21b)$$

in which K_0 denotes the modified Bessel function of the second kind of order zero.

After discretization of the cylinder contours and application of the boundary condition at $\underline{r}_0 = \underline{r}_n$ located at the n th node, the following equations are obtained for the source strengths associated with the propagating mode of the assisting radiated potential at the sum- difference-frequency:

$$\begin{aligned}
& \sum_{m'=1}^{M'} \sum_{i=1}^{N_e} \sigma_{mp}^{o\pm}(\underline{r}_{i*}) \int_{\Delta C_m} N_i \frac{\partial G_o}{\partial n}(\omega^\pm; \underline{r}_n, \underline{r}') dL + \gamma(\underline{r}_n) \sigma_{mp}^{o\pm}(\underline{r}_n) \\
& = \frac{2 \sinh 2\lambda_o^\pm d}{2\lambda_o^\pm d + \sinh 2\lambda_o^\pm d} [V_{mpn_p}] (\underline{r}_n) \quad p = 1, 2, 6, n \text{ on } C_m, \quad (5.22a)
\end{aligned}$$

$$\begin{aligned}
& \sum_{m'=1}^{M'} \sum_{i=1}^{N_e} \sigma_{mp}^{o\pm}(\underline{r}_{i*}) \int_{\Delta C_m} N_i \frac{\partial G_o}{\partial n}(\omega^\pm; \underline{r}_n, \underline{r}') dL + \gamma(\underline{r}_n) \sigma_{mp}^{o\pm}(\underline{r}_n) \\
& = \frac{4 \cosh \lambda_o^\pm d [1 \cdot \cosh \lambda_o^\pm d]}{\lambda_o^\pm [2\lambda_o^\pm d + \sinh 2\lambda_o^\pm d]} [V_{mpn_p}] (\underline{r}_n) \quad p = 4, 5, n \text{ on } C_m, \quad (5.22b)
\end{aligned}$$

$$\begin{aligned}
& \sum_{m'=1}^{M'} \sum_{i=1}^{N_e} \sigma_{mp}^{o\pm}(\underline{r}_{i*}) \int_{\Delta C_m} N_i \frac{\partial G_o}{\partial n}(\omega^\pm; \underline{r}_n, \underline{r}') dL + \gamma(\underline{r}_n) \sigma_{mp}^{o\pm}(\underline{r}_n) = 0 \\
& \quad p = 1, 2, 3, 5, 6, n \text{ not on } C_m. \quad (5.22c)
\end{aligned}$$

The corresponding equations for the qth evanescent component are

$$\begin{aligned}
& \sum_{m'=1}^{M'} \sum_{i=1}^{N_e} \sigma_{mp}^{q\pm}(\underline{r}_{i*}) \int_{\Delta C_m} N_i \frac{\partial G_q}{\partial n}(\omega^\pm; \underline{r}_n, \underline{r}') dL + \gamma(\underline{r}_n) \sigma_{mp}^{q\pm}(\underline{r}_n) \\
& = \frac{2 \sin 2\lambda_q^\pm d}{2\lambda_q^\pm d + \sin 2\lambda_q^\pm d} [V_{mpn_p}] (\underline{r}_n) \quad p = 1, 2, 6, n \text{ on } C_m, \quad (5.23a)
\end{aligned}$$

$$\begin{aligned}
& \sum_{m'=1}^{M'} \sum_{i=1}^{N_e} \sigma_{mp}^{q\pm}(\underline{r}_{i*}) \int_{\Delta C_m} N_i \frac{\partial G_q}{\partial n}(\omega^{\pm}; \underline{r}_n, \underline{r}') dL + \gamma(\underline{r}_n) \sigma_{mp}^{q\pm}(\underline{r}_n) \\
&= \frac{4 \cos \lambda_q^{\pm} d [-1 + \cos \lambda_q^{\pm} d]}{\lambda_q^{\pm} [2 \lambda_q^{\pm} d + \sin 2 \lambda_q^{\pm} d]} [V_{mpn_p}] (\underline{r}_n) \quad p = 4, 5, n \text{ on } C_m, \quad (5.23b)
\end{aligned}$$

$$\begin{aligned}
& \sum_{m'=1}^{M'} \sum_{i=1}^{N_e} \sigma_{mp}^{q\pm}(\underline{r}_{i*}) \int_{\Delta C_m} N_i \frac{\partial G_q}{\partial n}(\omega^{\pm}; \underline{r}_n, \underline{r}') dL + \gamma(\underline{r}_n) \sigma_{mp}^{q\pm}(\underline{r}_n) = 0 \\
& \quad p = 1, 2, 3, 5, 6; n \text{ not on } C_m. \quad (5.23c)
\end{aligned}$$

Allowing n to vary from $n = 1$ to $n = N_T$ results in a system of $N_T \times N_T$ linear equations which can be solved for the unknown source strengths at the nodes for $q = 0, 1, 2, \dots, \bar{Q}$; where \bar{Q} is sufficiently large to ignore the contributions of the larger evanescent modes to the radiated potential. Once the source strength values at the nodes are computed, the velocity potential at any point \underline{r}_n in the fluid domain may be determined from Eqs. (5.13) and (5.20) as

$$\begin{aligned}
\Phi_{mp}^{\pm}(\underline{x}_n) &= \frac{\cosh \lambda_0^{\pm}(z+d)}{\cosh \lambda_0^{\pm} d} \sum_{m'=1}^{M'} \sum_{i=1}^{N_e} \sigma_{mp}^{0\pm}(\underline{r}_{i*}) \int_{\Delta C_m} N_i G_0(\omega^{\pm}; \underline{r}_n, \underline{r}') dL \\
&+ \sum_{q=1}^{\bar{Q}} \frac{\cos \lambda_q^{\pm}(z+d)}{\cos \lambda_q^{\pm} d} \sum_{m'=1}^{M'} \sum_{i=1}^{N_e} \sigma_{mp}^{q\pm}(\underline{r}_{i*}) \int_{\Delta C_m} N_i G_q(\omega^{\pm}; \underline{r}_n, \underline{r}') dL. \quad (5.24)
\end{aligned}$$

5.3 Approximation of Hydrodynamic Loads on Deep Draft Floating Structures

As discussed in Chapter One, the solution to the problem of wave diffraction by an array of cylinders may be used to approximate that of wave interactions with a deep draft multi-column structure. For instance, the first-order body motions of a multi-column floating structure of a given draft (with the exception of heave motion) may be computed utilizing the above solution for the first-order problem resulting in considerable savings in computational effort compared to that required in the full three-dimensional solution. Furthermore, the computation of the second-order sum-frequency hydrodynamic loads on deep draft multi-column structures may also be approximated by the solution to the cylinder array problem.

Consider a structure consisting of M columns of arbitrary cross-section and draft b . Given the rapid decay of the velocity potential with depth, it is assumed that the solution for the velocity potential presented in Section 5.2 is valid for the truncated column problem. However, when computing the first-order hydrodynamic loads, the pressure integrals are carried out only from $z=-b$ to $z=0$. The computation of the added mass and radiation damping coefficients needed for the solution of the equation of motion requires a slight modification to the structural boundary condition given by Eqs. (5.15) and (5.18), as only a portion of the bottom-mounted structure (from $z = -b$ to $z = 0$) is allowed to oscillate. Furthermore, the structure oscillates as a unit, as opposed to section by section as was the case in the assisting radiated potential problem. The modification to the structural boundary condition essentially scales the results from the bottom mounted case at each of the evanescent modes and the propagating mode. It is noted that this is not a simple scaling of the final radiated potential.

The expressions for the complex form of the exciting and reaction loads for the truncated structure are given by

$$\begin{aligned}
F_{j\dot{p}}^{(e)} &= i\omega_j \rho \int_{S_o} \Phi_j^{(1)} n_p dS \\
&= i\omega_j \rho \left\{ \frac{-ig\Gamma_j}{\omega_j \cosh k_{oj}d} \int_{-b}^0 \cosh k_{oj}(z+d) dz \right\} \int_{C_o} [\Psi_{Sj}^{(1)} + \Psi_{Ij}^{(1)}] n_p dL \\
&= \frac{\rho g \Gamma_j [\sinh k_{oj}d - \sinh k_{oj}(d-b)]}{k_{oj} \cosh k_{oj}d} \sum_{m'=1}^{M'} \sum_{i=1}^{N_e} [\Psi_{Sj}^{(1)} + \Psi_{Ij}^{(1)}]_{i^*} \int_{\Delta C_m} N_i n_p dL,
\end{aligned} \tag{5.25}$$

$$\begin{aligned}
F_{j\dot{m}p}^{(r)} &= i\omega_j \rho \int_{S_o} \Phi_{jm}^{(1)} n_p dS \\
&= i\omega_j \rho \left\{ \frac{1}{\cosh k_{oj}d} \int_{-b}^0 \cosh k_{oj}(z+d) dz \int_{C_o} \Psi_{ojm}^{(1)} n_p dL \right. \\
&\quad \left. + \sum_{q=1}^Q \frac{1}{\cos k_{qj}d} \int_{-b}^0 \cos k_{qj}(z+d) dz \int_{C_o} \Psi_{qjm}^{(1)} n_p dL \right\} \\
&= i\omega_j \rho \left\{ \frac{[\sin k_{qj}d - \sin k_{qj}(d-b)]}{k_{qj} \cos k_{qj}d} \sum_{m'=1}^{M'} \sum_{i=1}^{N_e} [\Psi_{ojm}^{(1)}]_{i^*} \int_{\Delta C_m} N_i n_p dL \right. \\
&\quad \left. - \sum_{q=1}^Q \frac{[\sin k_{qj}d - \sin k_{qj}(d-b)]}{k_{qj} \cos k_{qj}d} \sum_{m'=1}^{M'} \sum_{i=1}^{N_e} [\Psi_{qjm}^{(1)}]_{i^*} \int_{\Delta C_m} N_i n_p dL \right\}.
\end{aligned} \tag{5.26}$$

5.4 Second-Order Hydrodynamic Loads

The expressions for the second-order loads on the cylinders are similar to those derived in Chapter Three. The free-surface integral is treated in a similar manner to that discussed previously. In order to obtain the coefficients needed for the integral in the exterior region of the free-surface, S_{F2} , the asymptotic expansions of the potentials are needed. These expressions are similar to those presented in section 3.6. given for infinite water depth, with the exception that the z -dependency is no longer e^{kz} , but rather it is now of the form $\cosh[k(z+d)] / \cosh[kd]$ to account for the finite depth. Also, in the expression for asymptotic tail of the free-surface integral, Eq. (3.90), the expressions for C_1^\pm and C_2^\pm associated with waves of finite depth are given by

$$C_1^\pm = -k_{oj}^2 (1 - \tanh^2 k_{oj}d) - k_{ok}^2 (1 - \tanh^2 k_{ok}d) + (\omega_j \pm \omega_k) k_{oj} k_{ok} \tanh k_{oj}d \tanh k_{ok}d, \quad (5.27a)$$

and

$$C_2^\pm = C_1^\pm \mp (\omega_j \pm \omega_k) k_{oj} k_{ok}. \quad (5.27b)$$

One of the advantages of the constant cross-section of the cylinders is that the z -dependency of the potentials and velocities is known, enabling the z -integrations to be carried out analytically, and requiring only contour integrals. With this in mind, the expression for the sum- and difference-frequency loads on the m th cylinder in a direction associated with the p th mode, F_{2mp}^\pm , are given by

$$F_{2mp}^\pm = \frac{i\rho(\omega_j \pm \omega_k) (q_{jkl}^\pm + q_{kil}^{\pm*})}{2V_{mp}} \int_{C_o} \left\{ \Psi_1^\pm \left[L_o^\pm \frac{\partial \Psi_{mp}^{o\pm}}{\partial n} + \sum_{q=1}^{\infty} L_q^\pm \frac{\partial \Psi_{mp}^{q\pm}}{\partial n} \right] - \frac{\partial \Psi_1^\pm}{\partial n} \left[L_o^\pm \Psi_{m\alpha}^{o\pm} + \sum_{q=1}^{\infty} L_q^\pm \Psi_{mp}^{q\pm} \right] \right\} dL$$

$$+ \frac{i\rho g(\omega_j \pm \omega_k) (q_{jkl}^\pm + q_{kjl}^{\pm*})}{2V_{mp}} \int_{S_F} \left\{ \Psi_{mp}^{o\pm} + \sum_{q=1}^{\infty} \Psi_{mp}^{q\pm} \right\} \left\{ p_{jk}^\pm + p_{kj}^{\pm*} \right\} dS, \quad (5.28a)$$

where

$$q_{jkl}^\pm = \pm \frac{i\omega_k}{2g} \Phi_{kl}^{(1)*} \left(\omega_j^2 \frac{\partial \Phi_{jl}^{(1)}}{\partial z} - g \frac{\partial^2 \Phi_{jl}^{(1)}}{\partial z^2} \right) \pm i\omega_k \nabla \Phi_{jl}^{(1)} \cdot \nabla \Phi_{kl}^{(1)*}, \quad (5.28b)$$

$$p_{jk}^\pm = \left(-\frac{i\Gamma_k \Gamma_j}{\omega_j} \right) \left\{ \nabla \Psi_{jl}^{(1)} \cdot \nabla \Psi_{ks}^{(1)*} + \nabla \Psi_{kl}^{(1)*} \cdot \nabla \Psi_{js}^{(1)} + \nabla \Psi_{ks}^{(1)*} \cdot \nabla \Psi_{js}^{(1)} + \left[-\frac{k_{oj}^2}{2} (1 - \tanh^2 k_{oj}d) + k_{oj}k_{ok} \tanh k_{oj}d \tanh k_{ok}d \right] \left[\Psi_{jl}^{(1)} \Psi_{ks}^{(1)*} + \Psi_{kl}^{(1)*} \Psi_{js}^{(1)} + \Psi_{ks}^{(1)*} \Psi_{js}^{(1)} \right] \right\}, \quad (5.28c)$$

and the constants L_0^\pm and L_q^\pm , $q = 1, 2, \dots$ are given by the definite integrals,

$$L_0^\pm = \int_{-d}^0 \frac{\cosh \kappa^\pm(z+d)}{\cosh \kappa^\pm d} \frac{\cosh \lambda_0^\pm(z+d)}{\cosh \lambda_0^\pm d} dz, \quad (5.28d)$$

and

$$L_q^\pm = \int_{-d}^0 \frac{\cosh \kappa^\pm(z+d)}{\cosh \kappa^\pm d} \frac{\cos \lambda_q^\pm(z+d)}{\cos \lambda_q^\pm d} dz. \quad (5.28e)$$

CHAPTER SIX

IMPLEMENTING NUMERICAL COMPUTATION OF SECOND-ORDER SUM-FREQUENCY LOADS ON A FOUR-CYLINDER STRUCTURE

As mentioned previously, an array of bottom-mounted surface-piercing cylinders may be used to model deep draft, multi-column structures where, due to the deep draft, the effect of the pontoons is assumed negligible. In this section, a four-cylinder array is utilized to model a typical deep draft TLP. The structure consists of four circular cylinders of radius a , center-to-center spacing $s = 5a$, situated in water depth $d = 4a$. Therefore, the cylinder centers are located at $(x,y) = (-2.5a, -2.5a)$, $(+2.5a, -2.5a)$, $(+2.5a, +2.5a)$, and $(-2.5a, +2.5a)$ respectively (see Figure 6.1). This structure was selected as a model of a deep draft TLP. It is assumed that due to deep draft, the effect of the pontoons is negligible. As indicated in Chapter Five, the solution to the first-order problem for the array of cylinders is reduced to a two-dimensional problem. This results in a considerable saving in the required computational effort. This simplification also allows for increased accuracy in the modeling of deep draft structures over a wider frequency range.

Before obtaining numerical results for the second-order hydrodynamic sum-frequency loads, a study was performed to assess the convergence characteristics of the numerical technique adopted. The insights gained from the convergence study were then applied to the implementation of the theory developed in Chapter Five.

6.1 Convergence of Linear Solutions.

In order to obtain high accuracy in the solution, numerical testing was carried out to select the optimum size of boundary elements and the number of terms in the evanescent

series and to ensure that the numerical results obtained were indeed convergent. It is clear that obtaining meaningful results for the second-order hydrodynamic loads depends critically on the accuracy of the solution for the scattered and radiated potentials. In the following, the integrations over a boundary element of the Green's functions and their derivatives were carried out numerically utilizing a 16-point Gauss quadrature over a parametric line element.

The four-cylinder structure used to model a deep draft TLP was discretized using different numbers of quadratic elements per cylinder. Also, the solution to the radiated potential was obtained with different numbers of terms in the evanescent series. These different combinations were used to obtain solutions for both the scattered and radiated potentials at dimensionless frequency $\nu = \omega^2 a/g = 2.0$. For all cases where the mesh was being tested, the series for the radiated potential was truncated at $\bar{Q} = 30$. For the case where the value of \bar{Q} was being tested, the cylinder was discretized with 16 elements per cylinder. The results of this convergence study are presented graphically in Figs. 6.2 - 6.4 as variations of the computed velocity potentials around the cylinder contours. The convention for the cylinder numbering is shown in Fig. 6.1.

Figures 6.2 show the variation of the real and imaginary parts of the scattered potential $\Psi_S^{(1)}$ around each of the four cylinders with different mesh discretizations for an incident wave angle $\beta = 22.5^\circ$. Three mesh discretizations are investigated: mesh 1 consists of (the minimal) four quadratic elements per cylinder; mesh 2 has four times as many elements (i.e., 16 elements per cylinder); and mesh 3 has 64 elements per cylinder. It can be seen that numerical convergence is achieved as the number of elements increases. The variation around each of the four cylinders of both the real and imaginary parts of the scattered potential as computed with the 16 elements per cylinder mesh is seen to be in

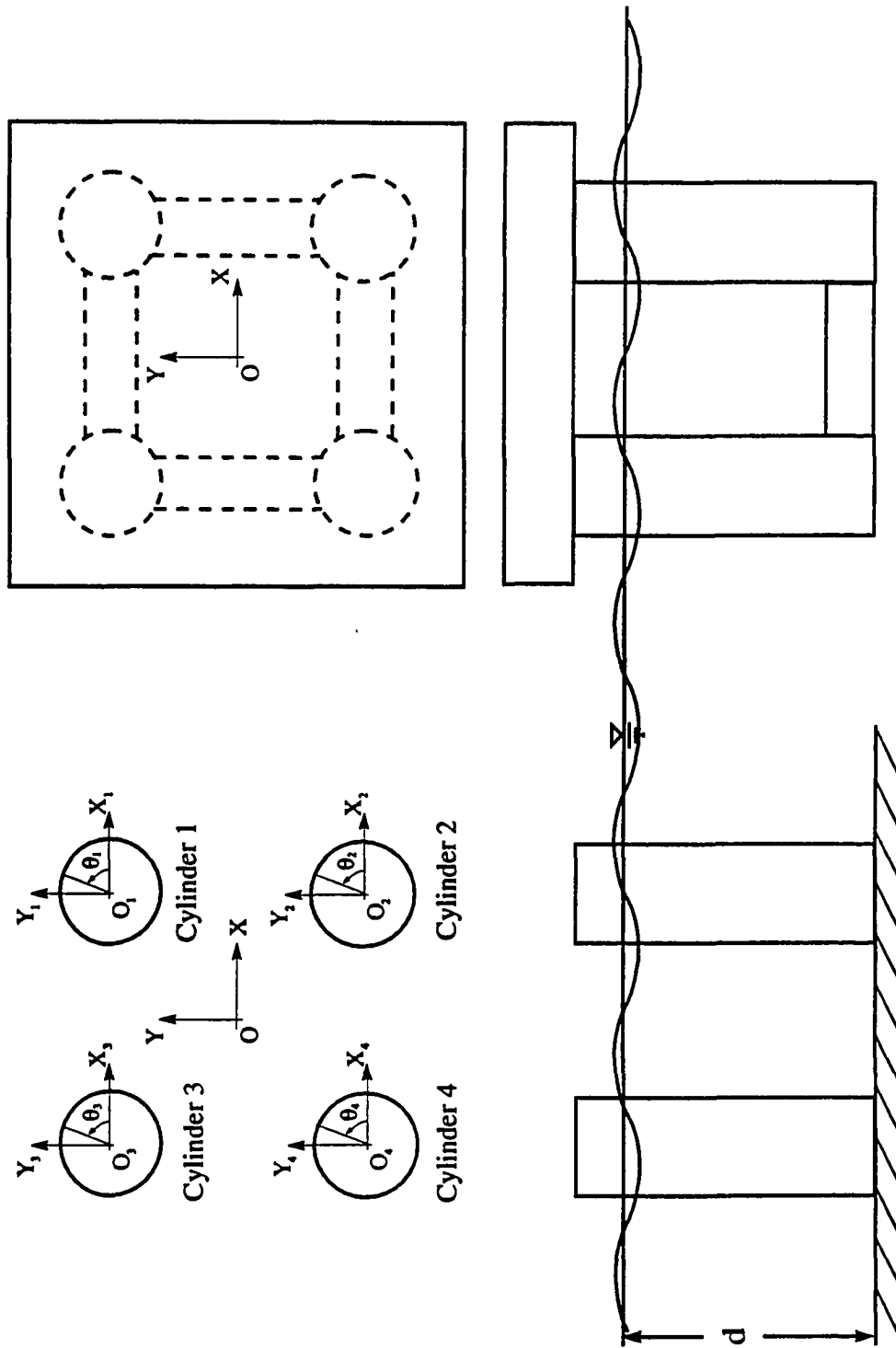


Fig. 6.1 Four cylinder array as an approximation to a four column, deep draft TLP.

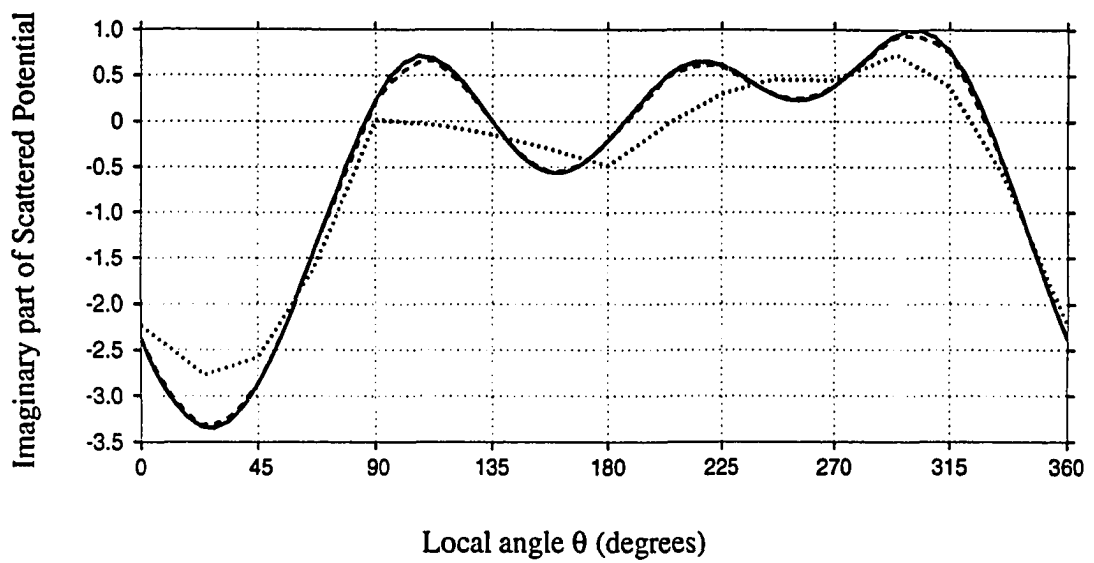
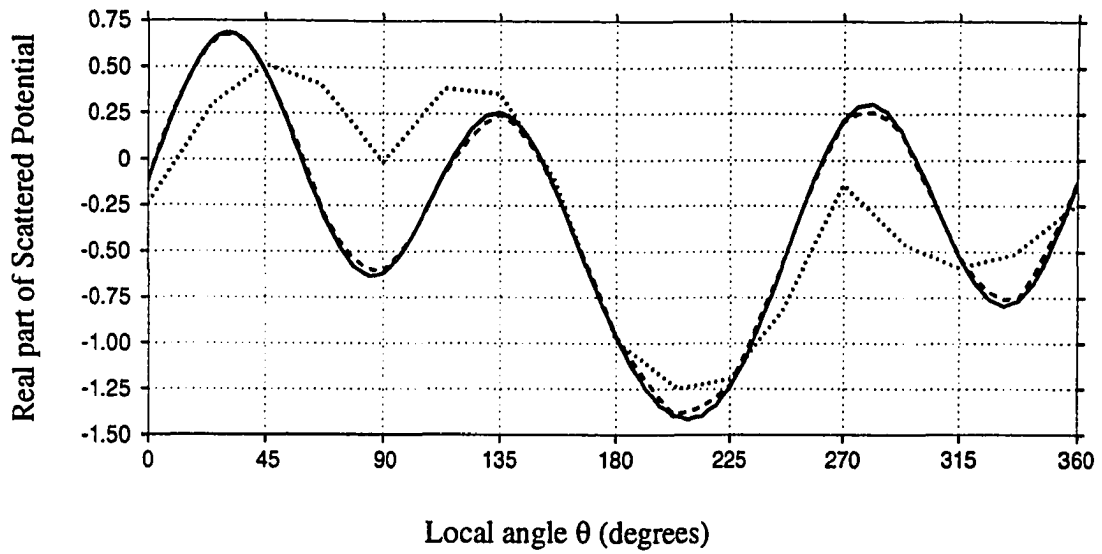


Fig. 6.2a Variation of scattered potential on cylinder 1 with body discretization for $\beta = 22.5^\circ$. Notation: four elements per cylinder, --- 16 elements per cylinder, and — 64 elements per cylinder.

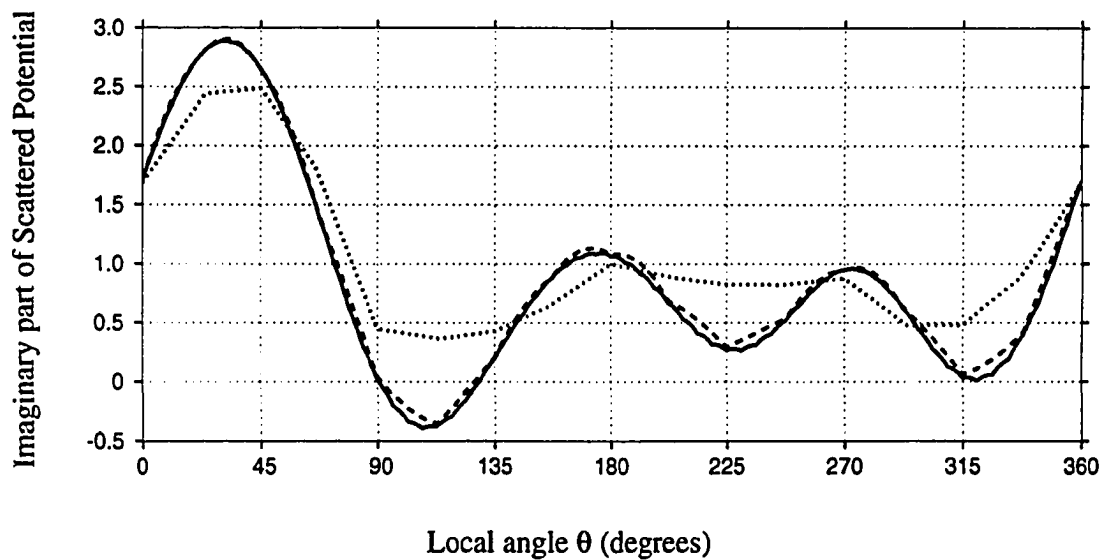
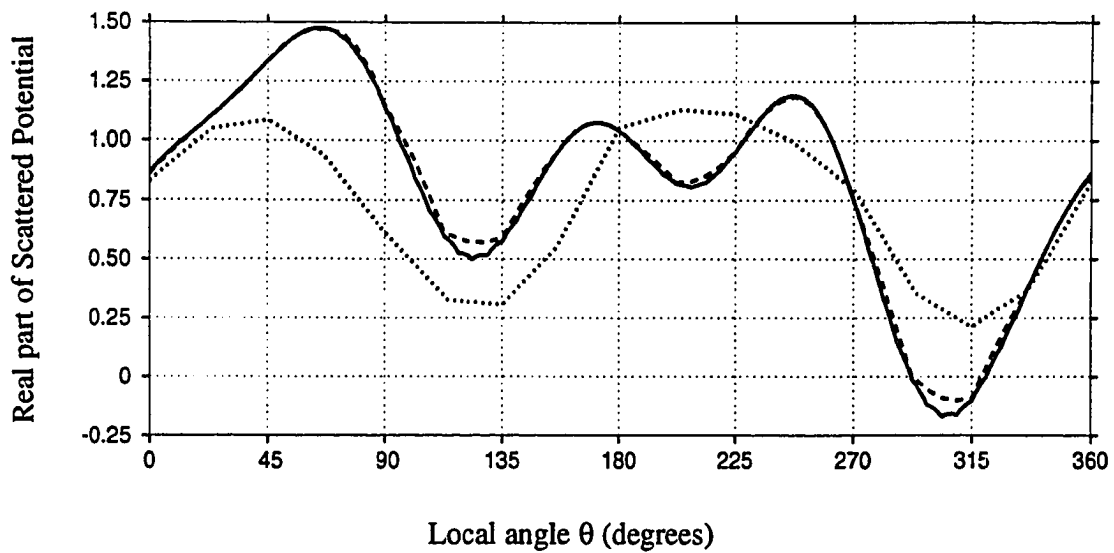


Fig. 6.2b Variation of scattered potential on cylinder 2 with body discretization for $\beta = 22.5^\circ$. Notation: four elements per cylinder, --- 16 elements per cylinder, and — 64 elements per cylinder.

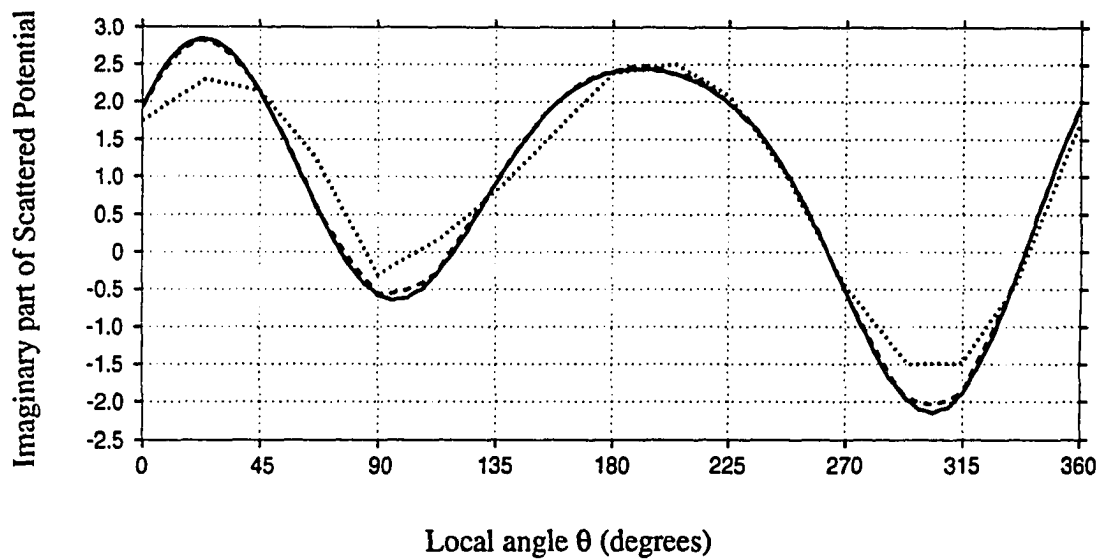
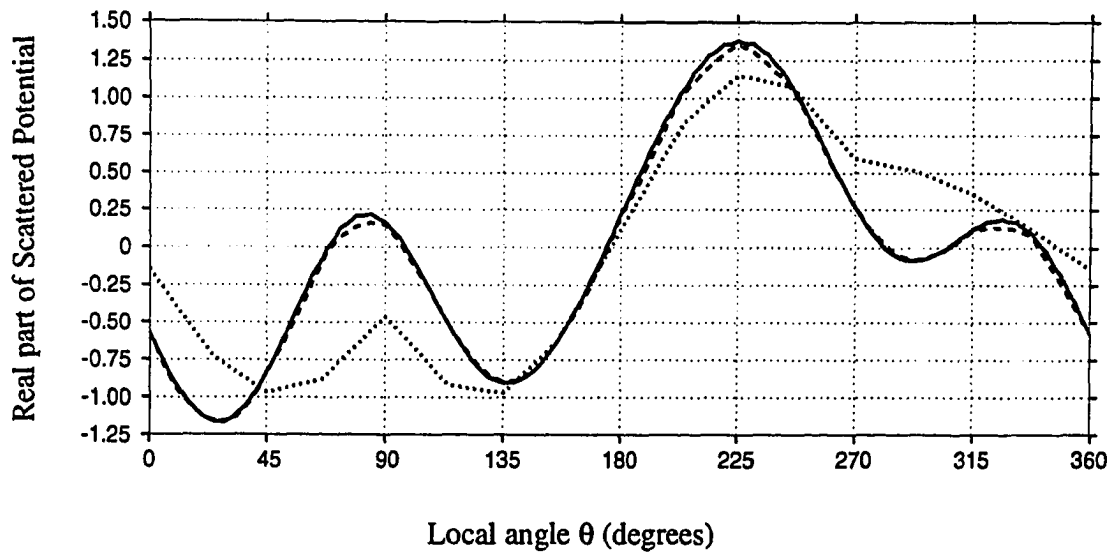


Fig. 6.2c Variation of scattered potential on cylinder 3 with body discretization for $\beta = 22.5^\circ$. Notation: four elements per cylinder, --- 16 elements per cylinder, and — 64 elements per cylinder.

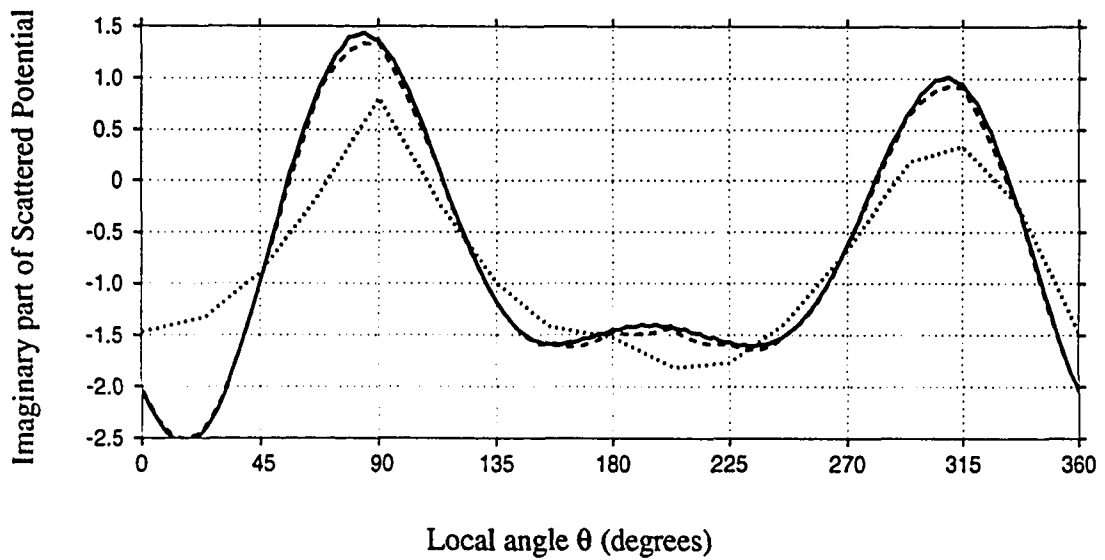
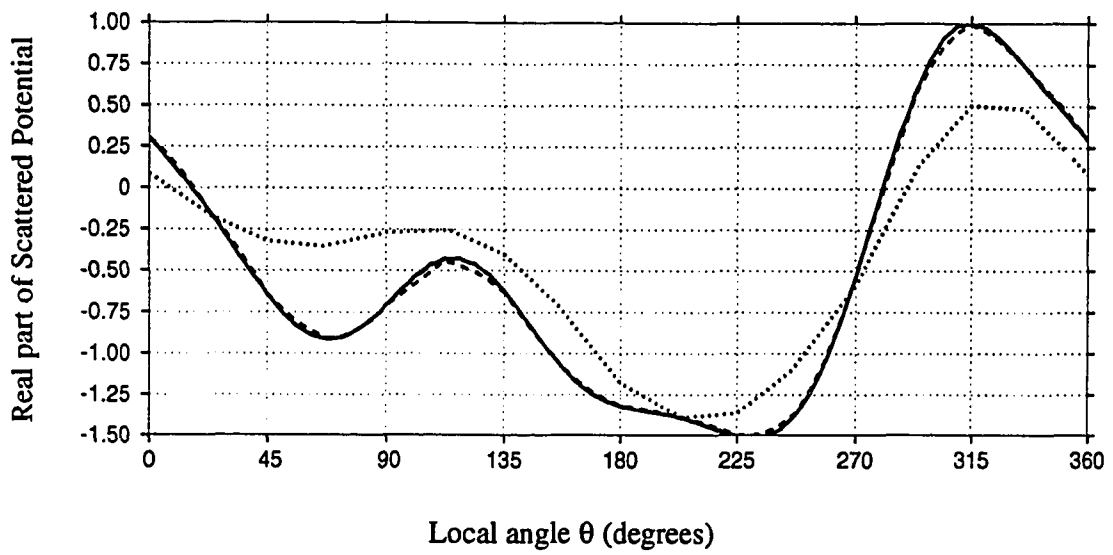


Fig. 6.2d Variation of scattered potential on cylinder 4 with body discretization for $\beta = 22.5^\circ$. Notation: four elements per cylinder, --- 16 elements per cylinder, and — 64 elements per cylinder.

good agreement with the corresponding values obtained with the 64 elements per cylinder mesh.

Figure 6.3 presents the variation of the real and imaginary parts of the radiated potential Ψ_p around cylinder 1 due to the oscillation of the entire structure in three different modes, $p=1$ (surge), $p=5$ (pitch) and $p=6$ (yaw), with different discretizations. Due to the symmetry of the structure, the variation of these potentials is similar over the other three cylinders and is therefore not presented. Also, due to the symmetry of the structure, the potentials in sway and roll modes are similar to those in surge and pitch, and are therefore not presented. As was the case for the scattered potential, numerical convergence is achieved with a mesh of 16 elements per cylinder. It should be noted that while the values of the potentials at the nodes may be well approximated even with a smaller number of elements, say eight elements per cylinder, the variation of the potential within the element may not be correctly described due to the fact that the wave kinematics vary more rapidly than the quadratic variation assumed within each boundary element. For this reason, it is recommended that the minimum number of elements be such that the maximum spacing between consecutive nodes is no greater than one-eighth of the wavelength.

Figure 6.4 presents the variation of the real part of the surge and pitch radiated potential around cylinder 1 resulting from truncating the evanescent series at different values, \bar{Q} . It should be noted that the imaginary part of the radiated potential is unaffected by the evanescent terms of the series and, therefore, it remains unchanged from the values presented in Fig. 6.3. Results are presented for values of $\bar{Q} = 0, 2, 5$ and 20. It is seen that the curves associated with $\bar{Q} = 5$ and $\bar{Q} = 20$ are in good agreement with each other indicating numerical convergence.

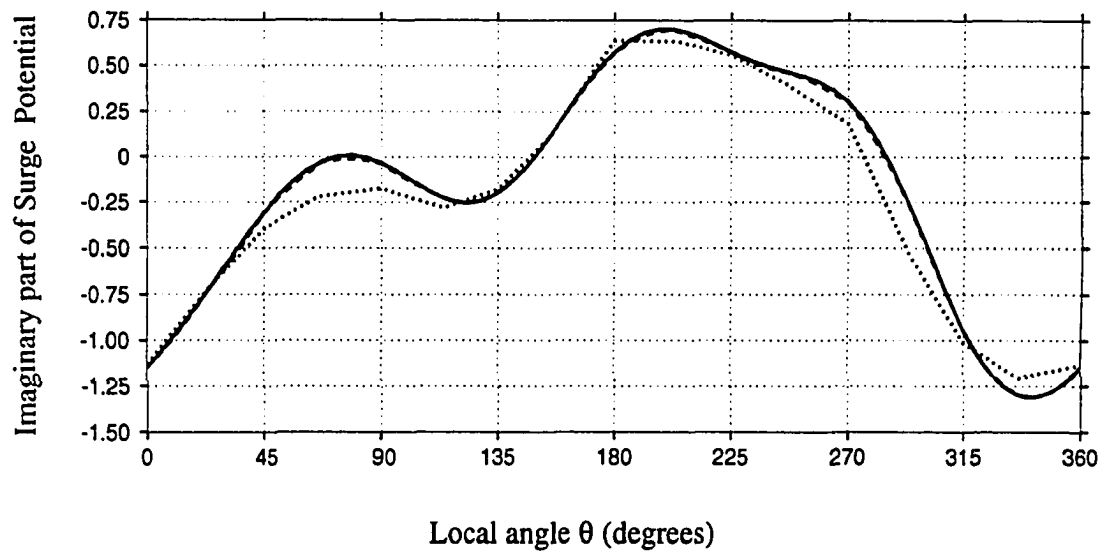
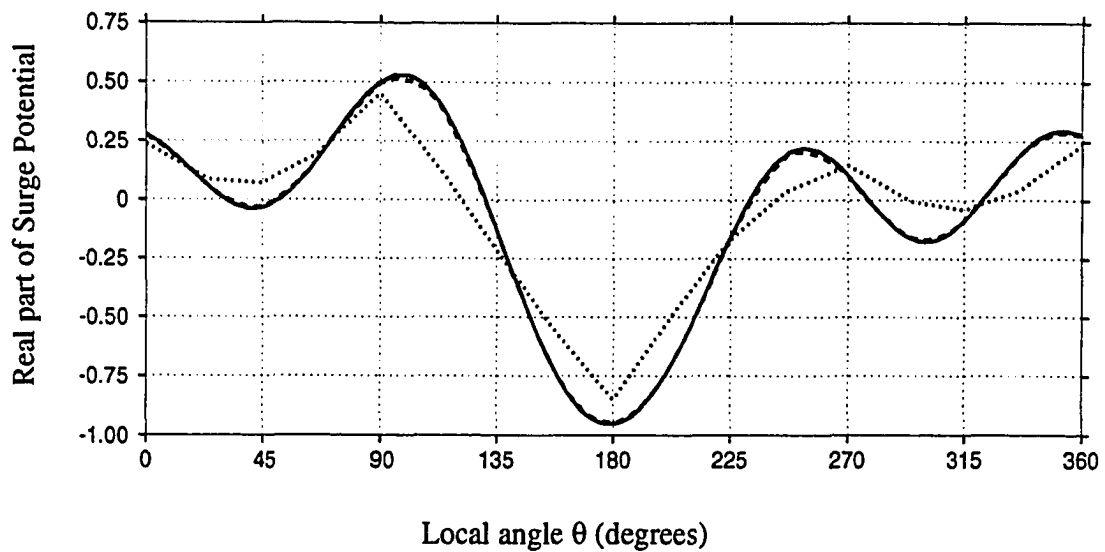


Fig. 6.3a Variation of surge radiated potential on cylinder 1 with body discretization
 Notation: four elements per cylinder, --- 16 elements per cylinder, and
 — 64 elements per cylinder.

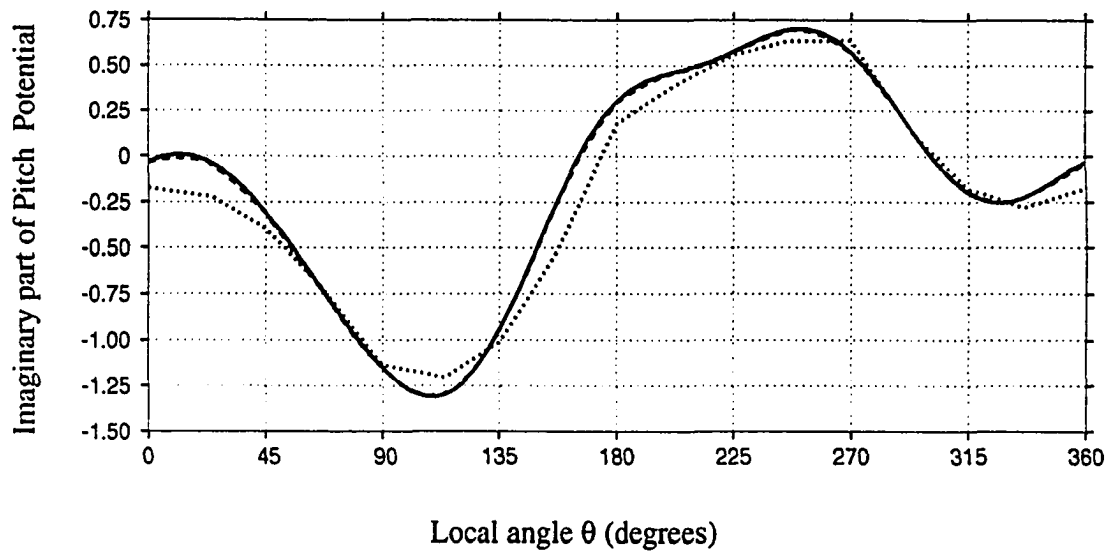
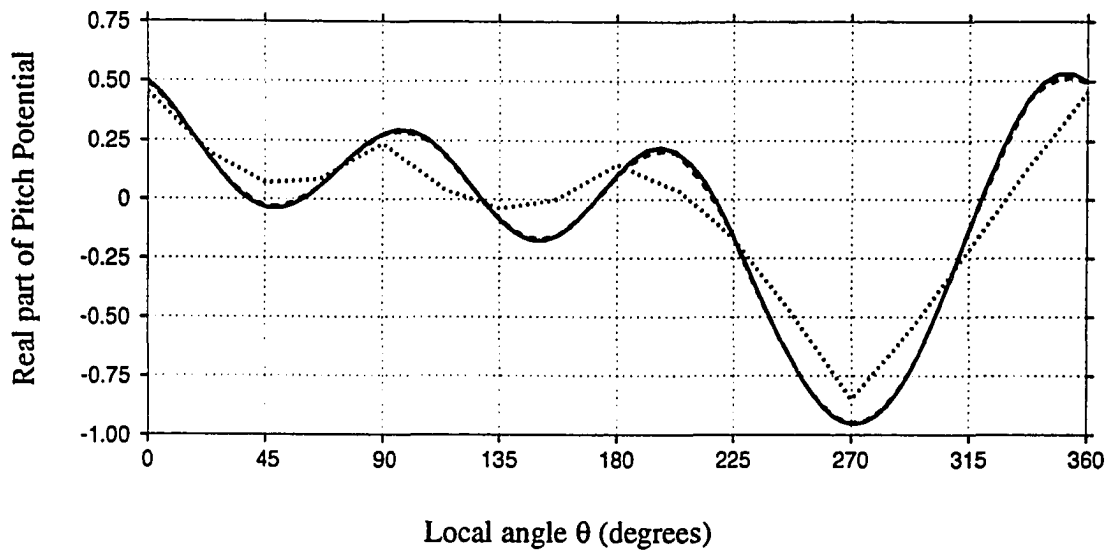


Fig. 6.3b Variation of pitch radiated potential on cylinder 1 with body discretization
 Notation: four elements per cylinder, --- 16 elements per cylinder, and
 — 64 elements per cylinder.

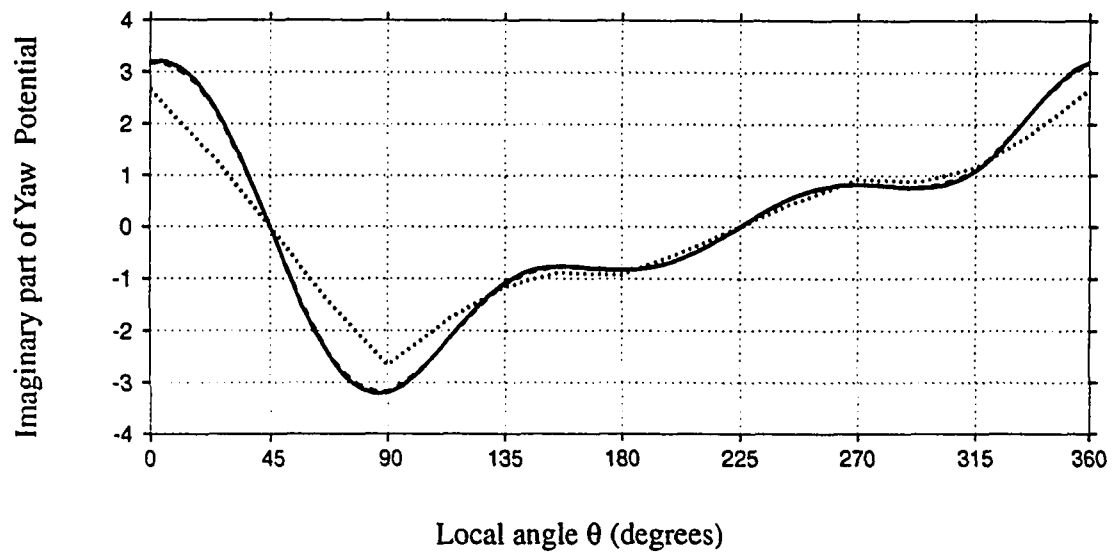
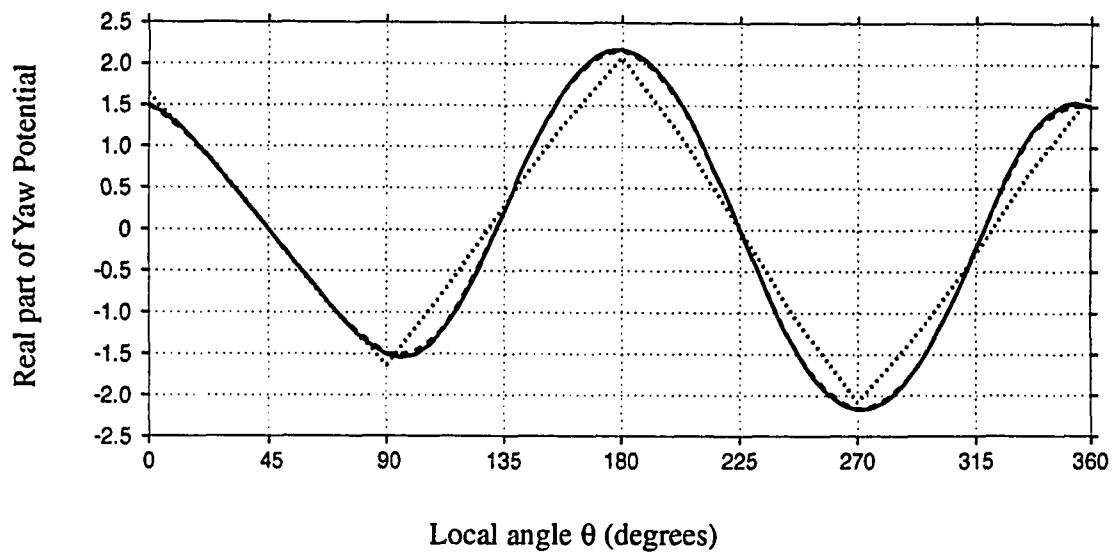


Fig. 6.3c Variation of yaw radiated potential on cylinder 1 with body discretization
 Notation: four elements per cylinder, --- 16 elements per cylinder, and
 ——— 64 elements per cylinder.

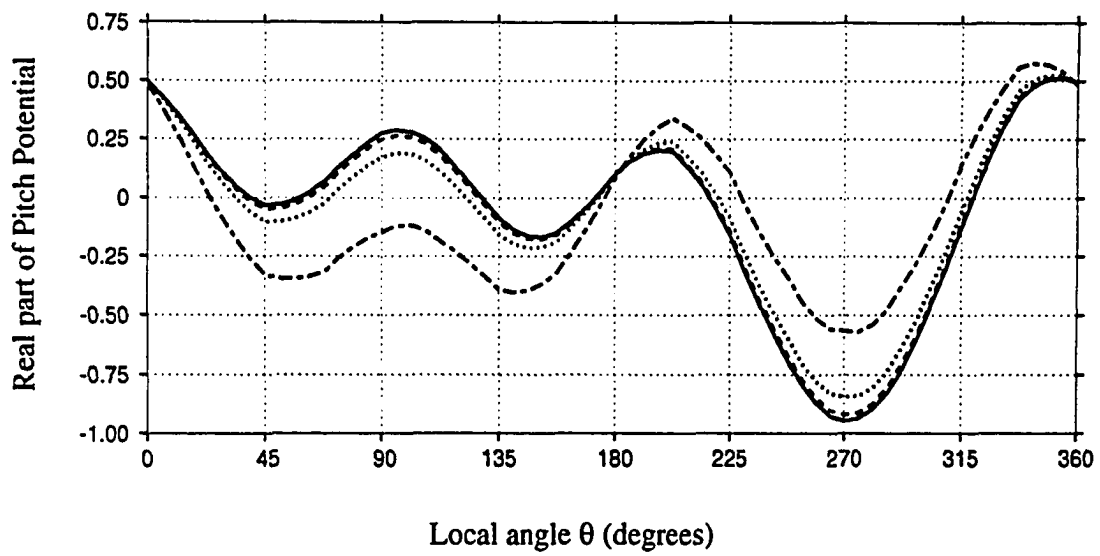
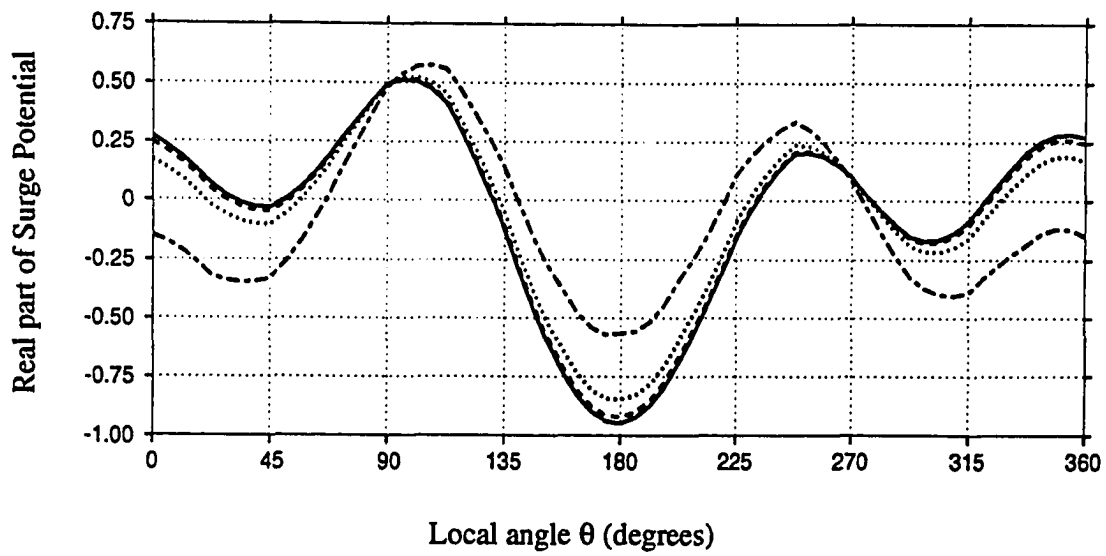


Fig. 6.4 Variation of the real part of surge/pitch potential on cylinder 1 with different number of evanescent modes \bar{Q} . Notation: ----- $\bar{Q} = 0$, $\bar{Q} = 2$, --- $\bar{Q} = 5$, and ——— $\bar{Q} = 20$.

Based on the results shown in Figs. 6.2 and 6.3, the number of boundary elements per cylinder was taken to be 36 for the computation of the scattered and associated radiated potentials to be used in the computation of the second-order sum-frequency hydrodynamic loads. This requirement of a seemingly large number of elements is indeed necessary to capture the variation of the assisting radiated potential at the sum-frequency. It is precisely for this reason that the modeling of deep draft structures by bottom-mounted arrays of cylinders is so appealing since achieving an adequate discretization at this frequency range for a general three-dimensional structure would require a much more significant effort. As far as the number of evanescent terms in the computation of the assisting radiated potential, the series was truncated at $\bar{Q} = 30$ to account for the higher frequencies.

6.2 Element Convergence on SF₁₁

The element discretization over the inner region and its effect on the accuracy of the free-surface integral was investigated by varying the element mesh size. Four different triangular element meshes (1, 2, 3 and 4 containing 608, 1382, 2592 and 3828 triangular elements respectively) for the array of four cylinders are shown in Figure 6.5. It should be noted that these meshes are not coincident with those adopted on the cylinder contours. Indeed, these meshes start from a distance $0.1a$ away from the cylinders and extend to a distance $6a$. The reason for the meshes not starting from the cylinders is purely a matter of convenience. Since the solution to the water particle velocities at points on the cylinder contour requires an extra term related to the source strength at that point, the section immediately surrounding the cylinders is treated separately from the rest of the region SF₁₁. This distinction does not, in any way, affect the results presented herein, as the purpose of the different discretizations is to show convergence with element distribution within a defined region.

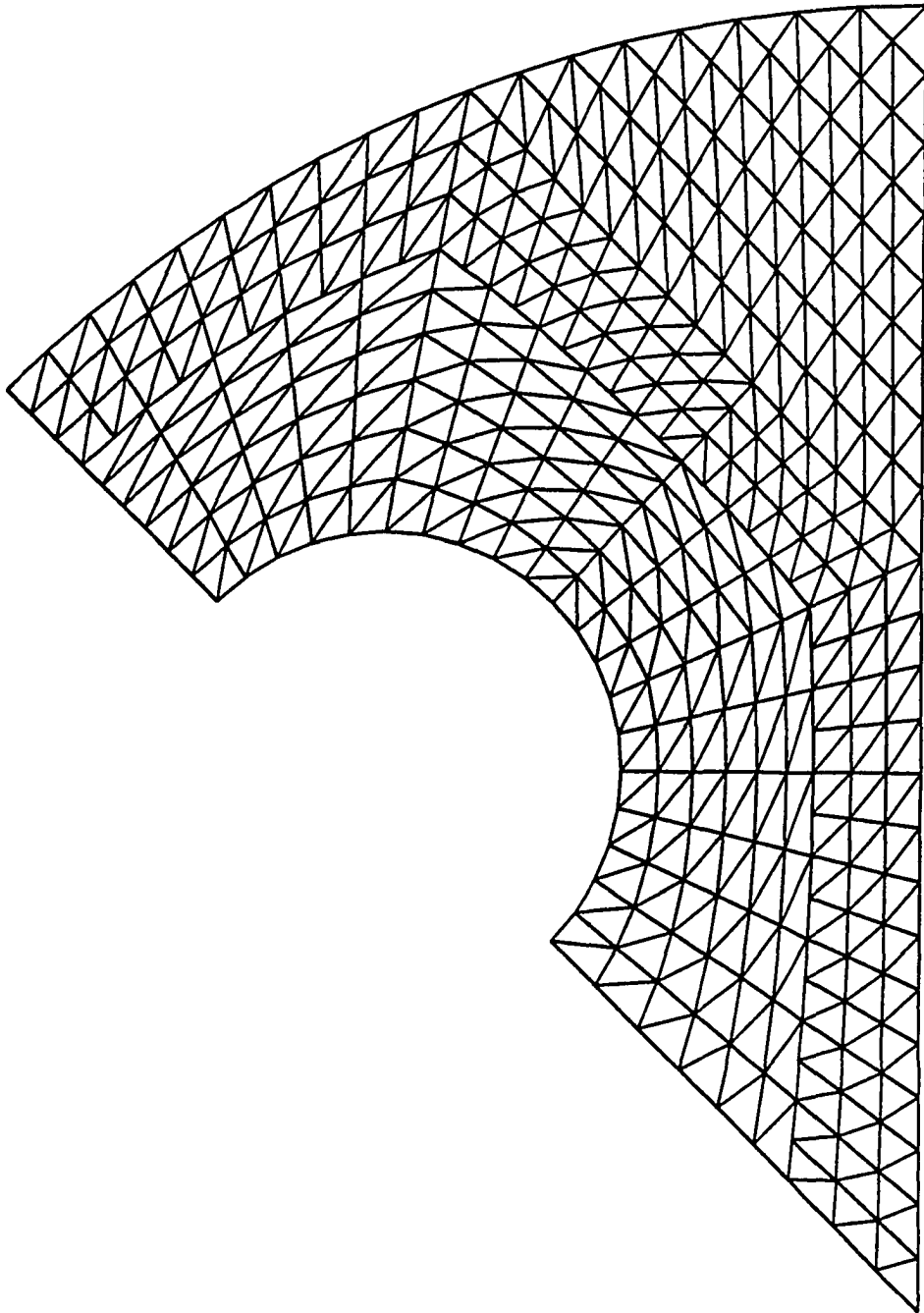


Fig. 6.5a One-eighth interior free-surface mesh for four-cylinder array. Mesh 1: 354 nodes, 608 linear elements.

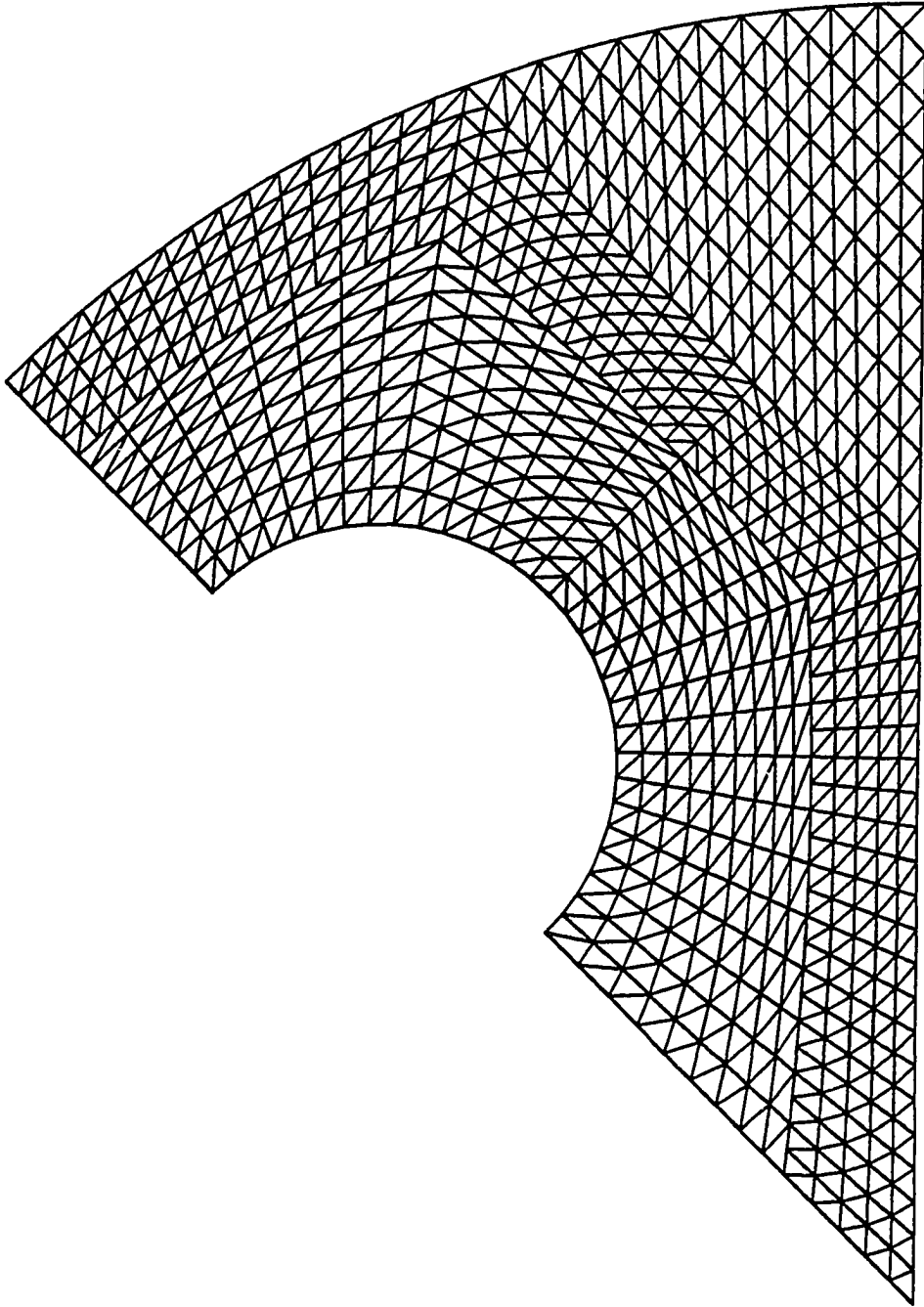


Fig. 6.5b One-eighth interior free-surface mesh for four-cylinder array. Mesh 2: 766 nodes, 1382 linear elements.

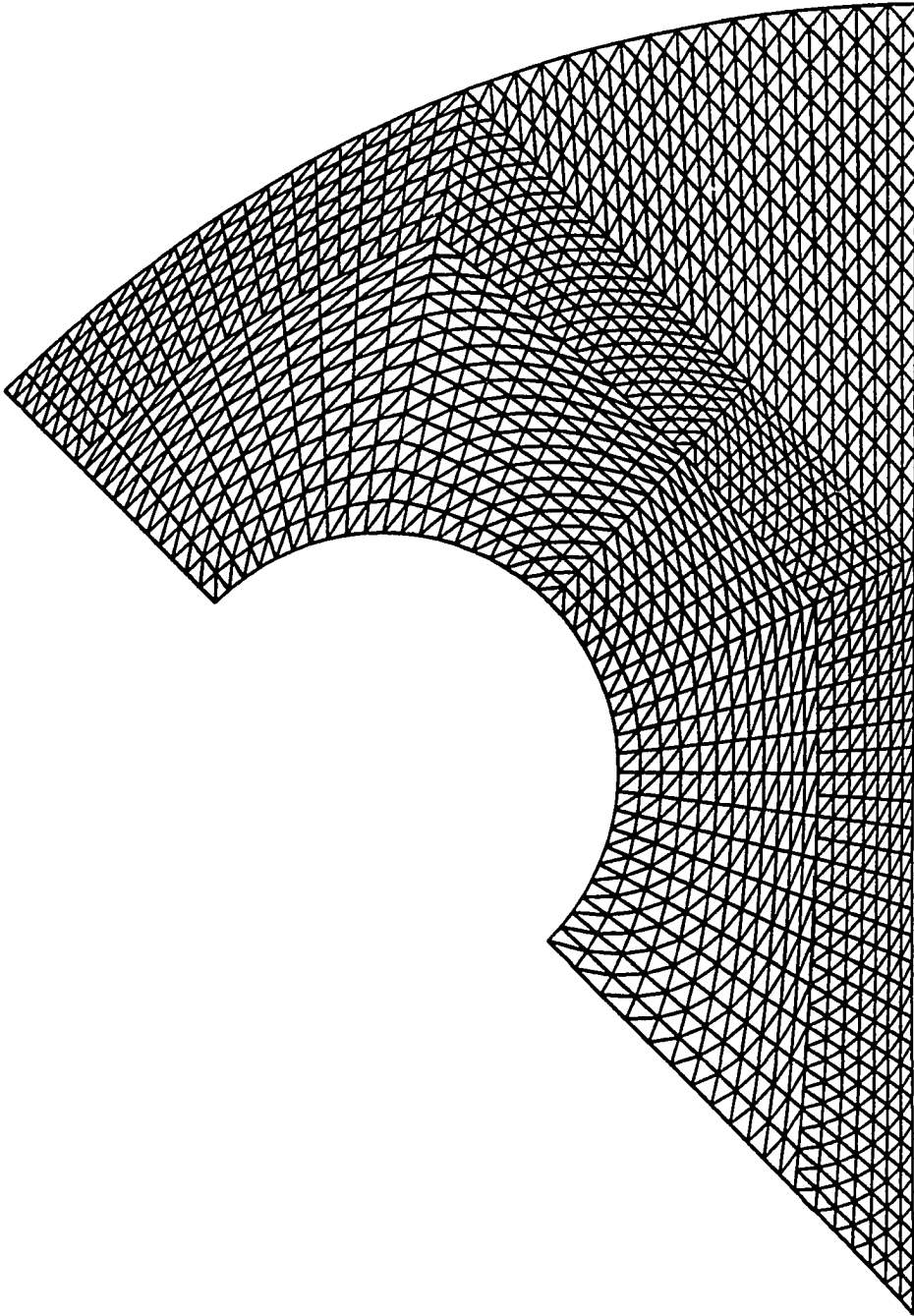


Fig. 6.5c One-eighth interior free-surface mesh for four-cylinder array. Mesh 3: 1396 nodes, 2592 linear elements.

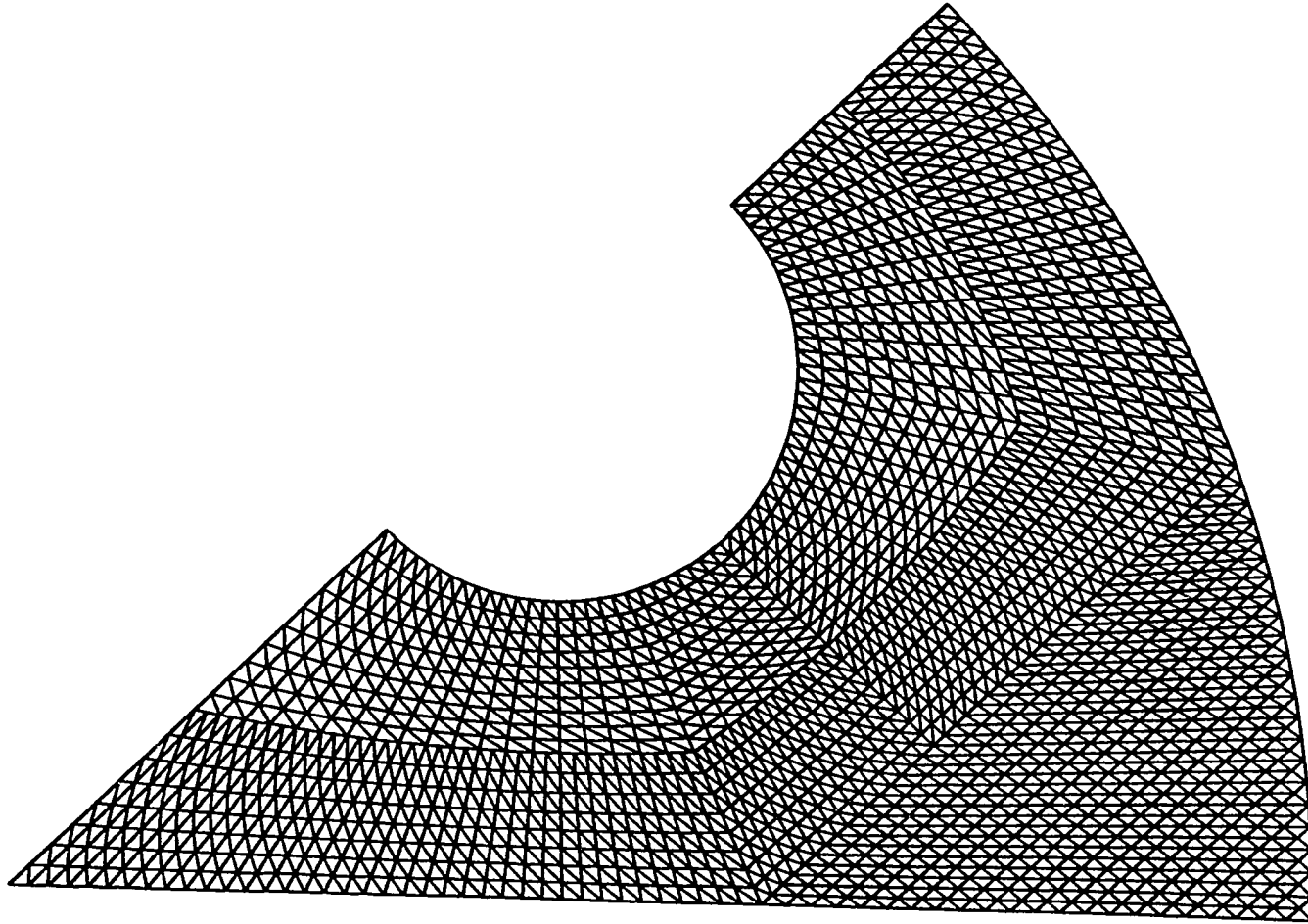


Fig. 6.5d One-eighth interior free-surface mesh for four-cylinder array. Mesh 4: 2043 nodes, 3828 linear elements.

The influence of element mesh size on the computation of the sum-frequency free-surface integral contribution to the forces and moments in a portion of SF_{11} is presented in Table 6.1 for a typical frequency pair $\nu_j = 1.4$, $\nu_k = 1.2$. Three different incident wave combinations are considered in the numerical testing: $\beta_j = 0^\circ$, $\beta_k = 45^\circ$; $\beta_j = 45^\circ$, $\beta_k = 0^\circ$; and $\beta_j = \beta_k = 22.5^\circ$. It can be seen that the contribution to the second-order sum-frequency loads due to the free-surface integral in this region converges as the number of elements used to discretize the free-surface domain increases. For the computation of the second-order sum-frequency loads over the range $(\nu_j, \nu_k) = (1.0, 1.0)$ to $(\nu_j, \nu_k) = (2.0, 2.0)$, mesh number 3 was adopted. The selection of this mesh is consistent with the above observations regarding the minimum spacing of nodes.

6.3 Convergence of Free-Surface Integral

The question of convergence of the complex free-surface integral with varying distance R (radius of the imaginary circular truncation boundary) is now addressed. The radial distance R was obtained by examining the behavior of the terms containing the modified Bessel function K_0 while varying the radius R . For the sum-frequency case, the partition distance, R , must be such that the asymptotic representations of the first-order scattered potentials are valid. In the difference-frequency case, however, it is the frequency of the assisting radiated potential that dictates the location of the artificial boundary.

Figure 6.6 presents the variation of the amplitudes of the free-surface contribution to the sum-frequency pitch and roll moment QTFs, $|I_F^+|$, for various values of R for the previously described geometry at three incident wave angle combinations: $\beta_j = 0^\circ$, $\beta_k = 45^\circ$; $\beta_j = 45^\circ$, $\beta_k = 0^\circ$; and $\beta_j = \beta_k = 22.5^\circ$. As in the previous case, a typical frequency pair $\nu_j = 1.4$, $\nu_k = 1.2$ was used. The number of elements on the structural contours and the

Table 6.1 Convergence of sum-frequency free-surface integral on interior region with different mesh discretizations. Hydrodynamic load components are computed for dimensionless frequency $v_j = 1.4$, $v_k = 1.2$.

Mesh	$\beta_j = 0^\circ, \beta_k = 45^\circ$	$\beta_j = 45^\circ, \beta_k = 0^\circ$	$\beta_j = \beta_k = 22.5^\circ$
Mesh 1: 354 nodes 608 elements	$F_x = (-3.656, -4.391)$ $F_y = (-2.336, 3.398)$ $M_x = (4.131, 4.617)$ $M_y = (0.142, -1.178)$ $M_z = (21.207, -12.348)$	$F_x = (-5.908, -4.496)$ $F_y = (8.300, 2.898)$ $M_x = (5.141, 3.679)$ $M_y = (-8.030, -3.387)$ $M_z = (3.988, 1.689)$	$F_x = (-6.963, -0.994)$ $F_y = (4.752, 1.141)$ $M_x = (6.032, 1.752)$ $M_y = (-3.734, 0.117)$ $M_z = (8.775, -10.745)$
Mesh 2: 766 nodes 1382 elements	$F_x = (-3.708, -4.573)$ $F_y = (-2.341, 3.425)$ $M_x = (4.181, 4.675)$ $M_y = (0.053, -1.187)$ $M_z = (22.186, -12.438)$	$F_x = (-6.094, -4.762)$ $F_y = (8.398, 2.955)$ $M_x = (5.203, 3.747)$ $M_y = (-8.239, -3.611)$ $M_z = (3.961, 1.952)$	$F_x = (-7.209, -1.079)$ $F_y = (4.796, 1.143)$ $M_x = (6.121, 1.769)$ $M_y = (-3.826, 0.113)$ $M_z = (9.244, -10.871)$
Mesh 3: 1396 nodes 2592 elements	$F_x = (-3.715, -4.635)$ $F_y = (-2.346, 3.434)$ $M_x = (4.195, 4.695)$ $M_y = (0.037, -1.177)$ $M_z = (22.496, -12.388)$	$F_x = (-6.159, -4.850)$ $F_y = (8.429, 2.976)$ $M_x = (5.221, 3.767)$ $M_y = (-8.308, -3.698)$ $M_z = (3.898, 2.013)$	$F_x = (-7.280, -1.102)$ $F_y = (4.812, 1.147)$ $M_x = (6.146, 1.775)$ $M_y = (-3.853, 0.103)$ $M_z = (9.367, -10.814)$
Mesh 4: 2043 nodes 3828 elements	$F_x = (-3.674, -4.657)$ $F_y = (-2.351, 3.442)$ $M_x = (4.197, 4.704)$ $M_y = (0.049, -1.189)$ $M_z = (22.748, -12.166)$	$F_x = (-6.151, -4.892)$ $F_y = (8.445, 2.991)$ $M_x = (5.226, 3.774)$ $M_y = (-8.323, -3.764)$ $M_z = (3.836, 2.077)$	$F_x = (-7.281, -1.142)$ $F_y = (4.820, 1.148)$ $M_x = (6.154, 1.781)$ $M_y = (-3.859, 0.089)$ $M_z = (9.471, -10.712)$

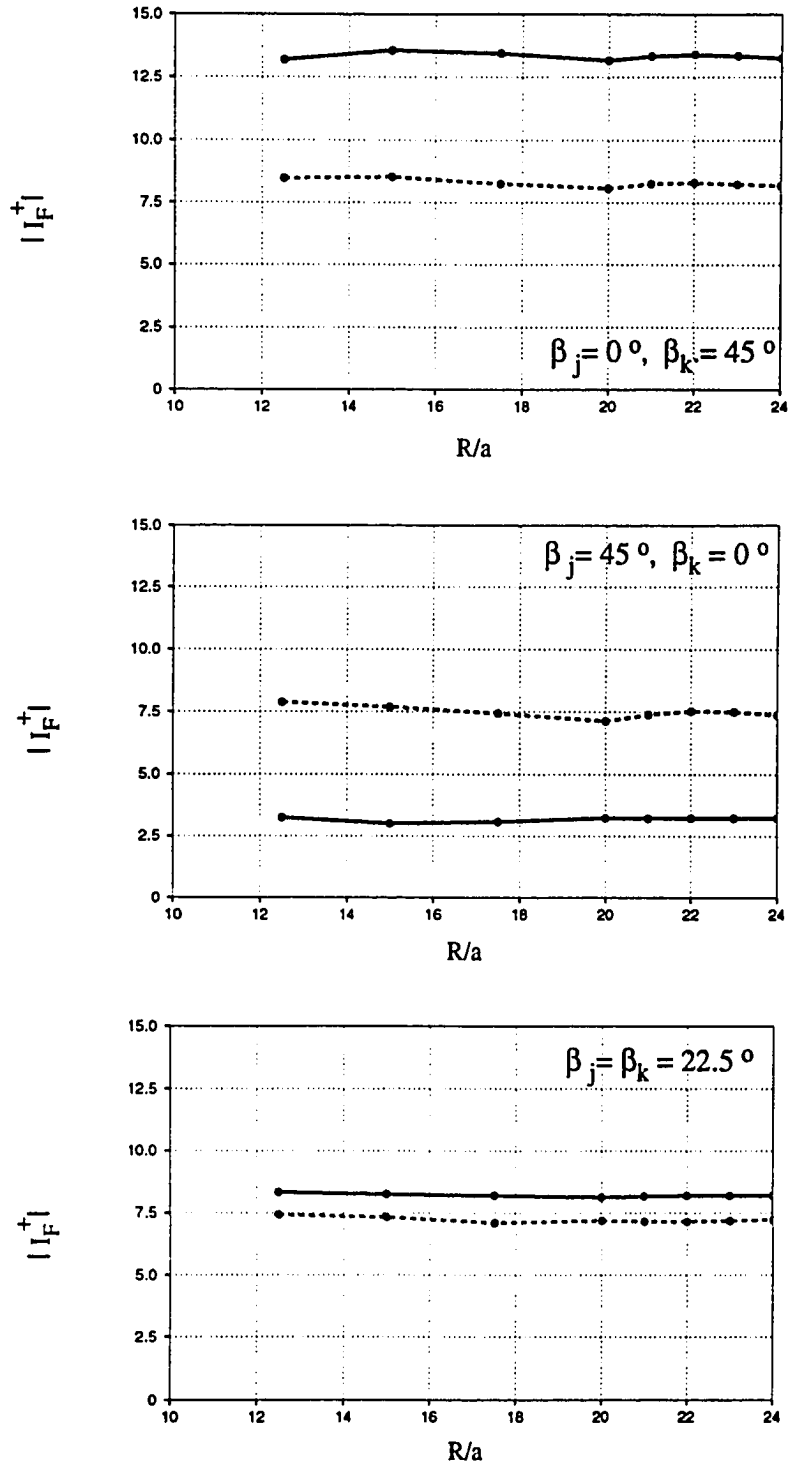


Fig. 6.6 Variation of the amplitude of the free-surface contribution to the sum-frequency moment QTF, $|I_F^+|$, with partition distance, R/a , for the four cylinder structure at $v_j = 1.4, v_k = 1.2$. Notation: $\text{---}\bullet\text{---}$ Pitch, $\text{--}\bullet\text{--}$ Roll.

infinite series truncations are as outlined above. It can be seen from the figure, that the estimates of the free-surface integrals converge as R/a increases.

6.4 Numerical Results and Discussion

Numerical results will now be presented for the sum-frequency hydrodynamic force and moment QTFs (with respect to the still water level) for the four cylinder array described above. Three incident wave directions are considered: $\beta_j = 0^\circ, \beta_k = 45^\circ$; $\beta_j = 45^\circ, \beta_k = 0^\circ$; and $\beta_j = \beta_k = 22.5^\circ$. The forces are nondimensionalized by $\rho g a \Gamma_j \Gamma_k$, and the moments by $\rho g a^2 \Gamma_j \Gamma_k$. The dimensionless frequency range considered is $1.0 \leq \nu = \omega^2 a / g \leq 2.0$. The numerical results presented herein have been obtained with each cylinder contour discretized into 36 quadratic elements (i.e. total number of nodes on the structural contour is equal to 288). The infinite series in the radiation potentials was truncated after 30 terms. The region $S_{F_{11}}$ extends to $r = 6a$, the region $S_{F_{12}}$ extends to a radial distance of $30a$ as suggested by Moubayed (1992b). Mesh 3 was utilized to discretize the free-surface domain in the interior region (See Fig. 6.5).

The hydrodynamic loads are presented as QTF surface plots (and corresponding contour plots) of the dimensionless frequency components ν_j, ν_k , for different combinations of angles of wave incidence. In all cases, the QTFs satisfy the symmetry relation resulting in surface plots that are symmetric about the line $\nu_j = \nu_k$. The figures are ordered to facilitate comparisons between similar load components (i.e. surge, sway, etc.) for different combinations of incident wave directions. The effect of wave directionality may be quantified by comparing sets of three consecutive figures corresponding to the incident wave combinations: $\beta_j = 0^\circ, \beta_k = 45^\circ$; $\beta_j = 45^\circ, \beta_k = 0^\circ$; and $\beta_j = \beta_k = 22.5^\circ$. The unidirectional set is presented to show that the hydrodynamic load QTFs resulting from

waves at 0° and 45° are in general not equal to those arising from a unidirectional analysis at the "average angle" of 22.5° .

Figure 6.7 presents the second-order sum-frequency surge QTF on the four cylinder structure for the incident wave combination $\beta_j = 0^\circ$, $\beta_k = 45^\circ$. It can be seen from the figure that the QTF values are oscillatory and that, in general, they increase with increasing frequency. Due to the relatively large column spacing (as compared to the wavelengths), the oscillatory nature of the QTFs is not very pronounced. For this particular case, the variation of the QTF at constant frequency $\nu_j = 1.0$ is seen to be almost uniform. This is not the case observed in Fig. 6.8 which presents the corresponding QTFs for an incident wave combination $\beta_j = 45^\circ$, $\beta_k = 0^\circ$. These differences clearly indicate the effect of wave directionality in the computation of the second-order sum-frequency loads. While these two cases show remarkably different behavior throughout most of the frequency range considered, they do agree with each other along the line $\nu_j = \nu_k$, corresponding to monochromatic incident waves.

As indicated in Chapter Four, one approach that has been suggested to estimate the effect of wave directionality on the second-order sum-frequency loads is to evaluate the load QTFs in unidirectional waves with an angle of incidence equal to the average angle of the two wave components. In this case, the unidirectional angle is 22.5° . The surge sum-frequency QTFs corresponding to incident wave angles $\beta_j = \beta_k = 22.5^\circ$ are shown in Fig. 6.9. In this figure it can be seen that the QTFs are more oscillatory than in the previous two cases. This is attributed to the interaction with the cylinders of the non-symmetric wave field associated with incident waves at 22.5° (i.e., in the previous two cases, although the second-order wave field is not symmetric, the first-order scattered wave field is. The 22.5° case does not possess symmetry even at the first-order).

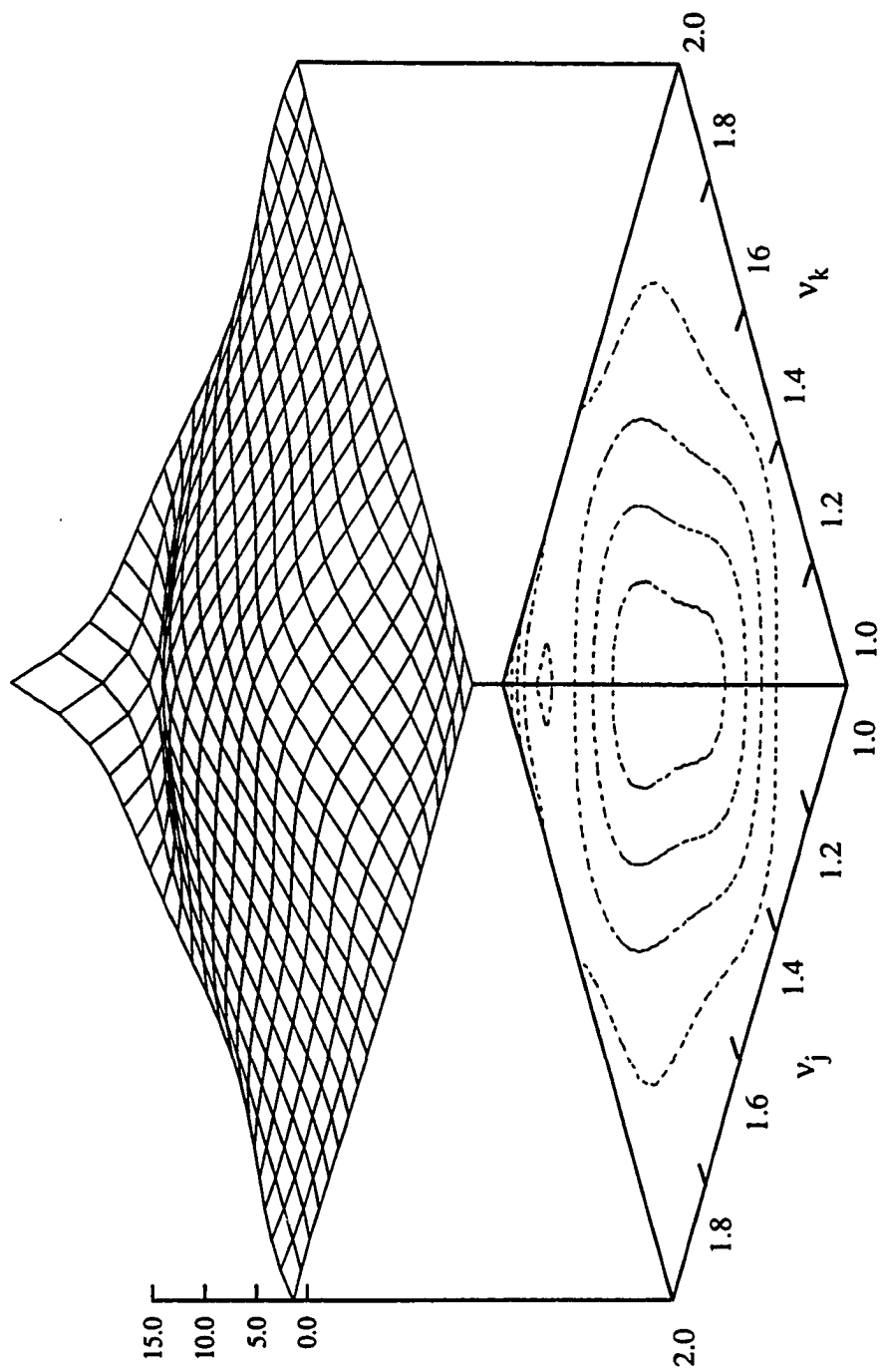


Fig. 6.7 Hydrodynamic sum-frequency surge force QTF, $H^+(\omega_j, \omega_k; \beta_j, \beta_k)$, for four-cylinder structure with $\beta_j = 0^\circ$, $\beta_k = 45^\circ$.

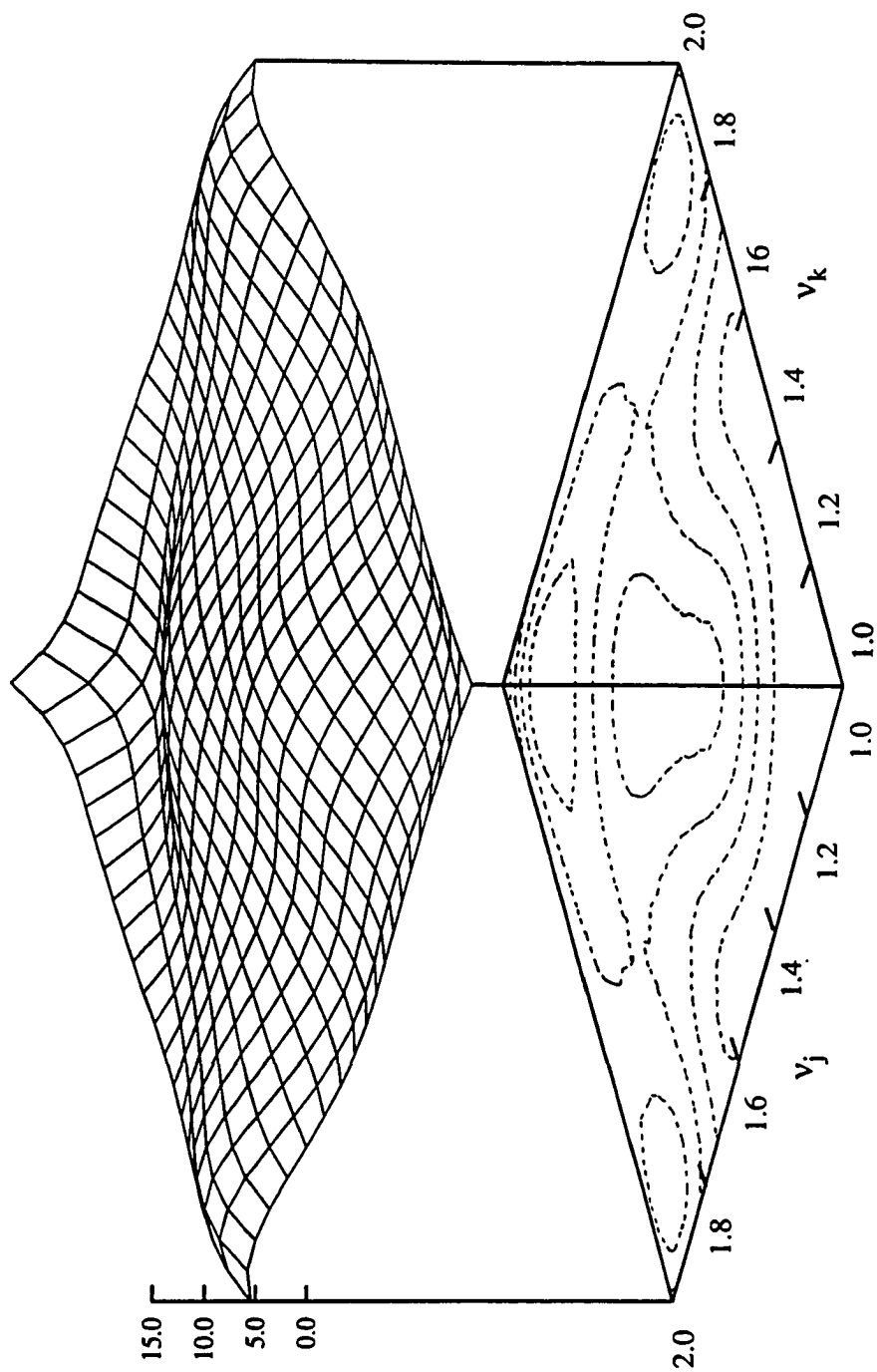


Fig. 6.8 Hydrodynamic sum-frequency surge force QTF, $H^+(\omega_j, \omega_k; \beta_j, \beta_k)$, for four-cylinder structure with $\beta_j = 45^\circ$, $\beta_k = 0^\circ$.

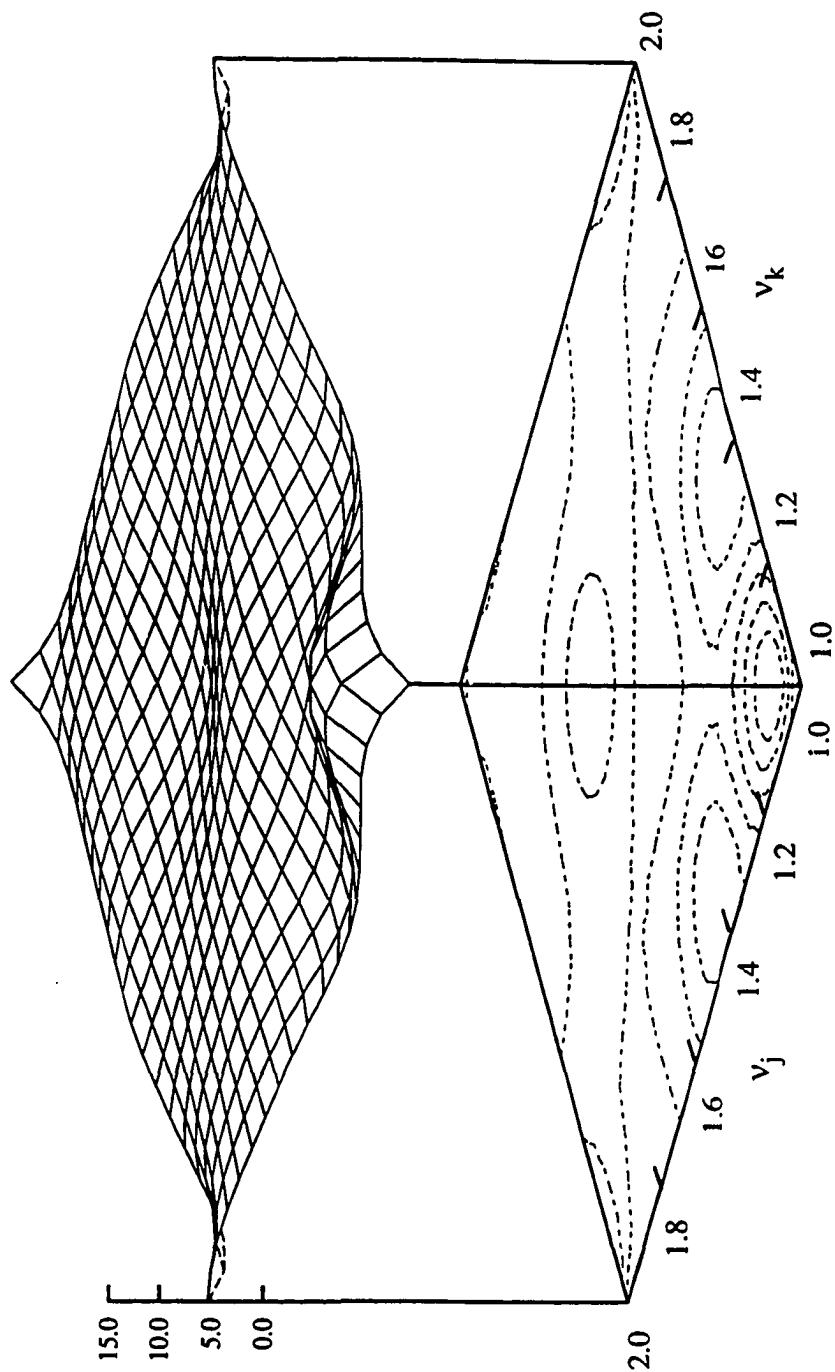


Fig. 6.9 Hydrodynamic sum-frequency surge force QTF, $H^+(\omega_j, \omega_k; \beta_j, \beta_k)$, for four-cylinder structure with $\beta_j = \beta_k = 22.5^\circ$.

Figures 6.10 - 6.12 show the corresponding sum-frequency QTFs for the sway forces. In this mode, the QTFs are significantly more oscillatory, even in the bidirectional cases, and, in general, are larger for the $\beta_j = 45^\circ$, $\beta_k = 0^\circ$ case, than for the $\beta_j = 0^\circ$, $\beta_k = 45^\circ$ case. For the unidirectional case, the QTFs are seen to vary in a less oscillatory fashion (i.e. the QTFs are seen to gradually increase with increasing frequency).

One of the drawbacks of using an array of bottom-mounted cylinders to model deep draft structures is that the second-order heave force cannot be determined by the indirect assisting radiated potential method since the structure cannot be oscillated in this mode. Kim (1992) presented an approximate way to determine the second-harmonic loads on arrays of bottom-mounted circular cylinders when used to model deep draft structures. This approach, which obtains the second-order loads by integrating the second-order potential, is based on the assumption that the second-order pressure at the bottom of the structures is relatively constant. Therefore the second-order heave force may be obtained by multiplying the area of the cylinder by the "average" pressure at the desired level on the cylinder. In the present method, however, the second-order scattered potential is not computed, and therefore, the heave forces may not be approximated. For this reason, the roll and pitch QTFs are seen to behave in a manner similar to the surge and sway QTFs.

The sum-frequency QTFs in roll and pitch for the four cylinder structure are presented in Figs. 6.13 - 6.18. As expected, due to the deep draft of the structure, the roll and pitch moment QTFs behave in similar manner as the corresponding sway and surge force QTFs. Again, it is seen that the roll moment QTFs are significantly more oscillating than the corresponding pitch moment QTFs. These results are in contrast with those found in chapter Four for the ISSC TLP, where it was seen that the roll and pitch moment QTFs did not behave in an entirely similar manner as the corresponding surge and sway force

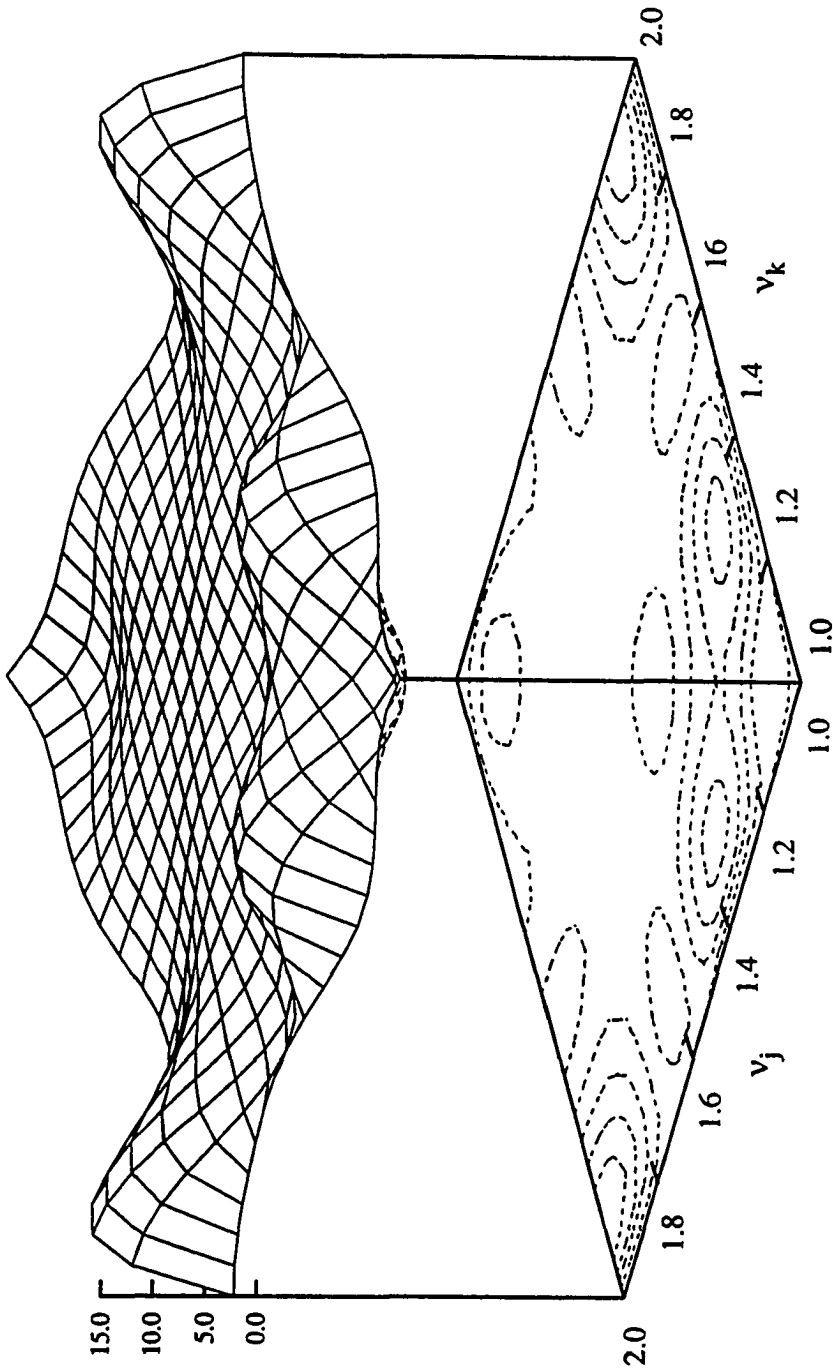


Fig. 6.10 Hydrodynamic sum-frequency sway force QTF, $H^+(\omega_j, \omega_k; \beta_j, \beta_k)$, for four-cylinder structure with $\beta_j = 0^\circ$, $\beta_k = 45^\circ$.

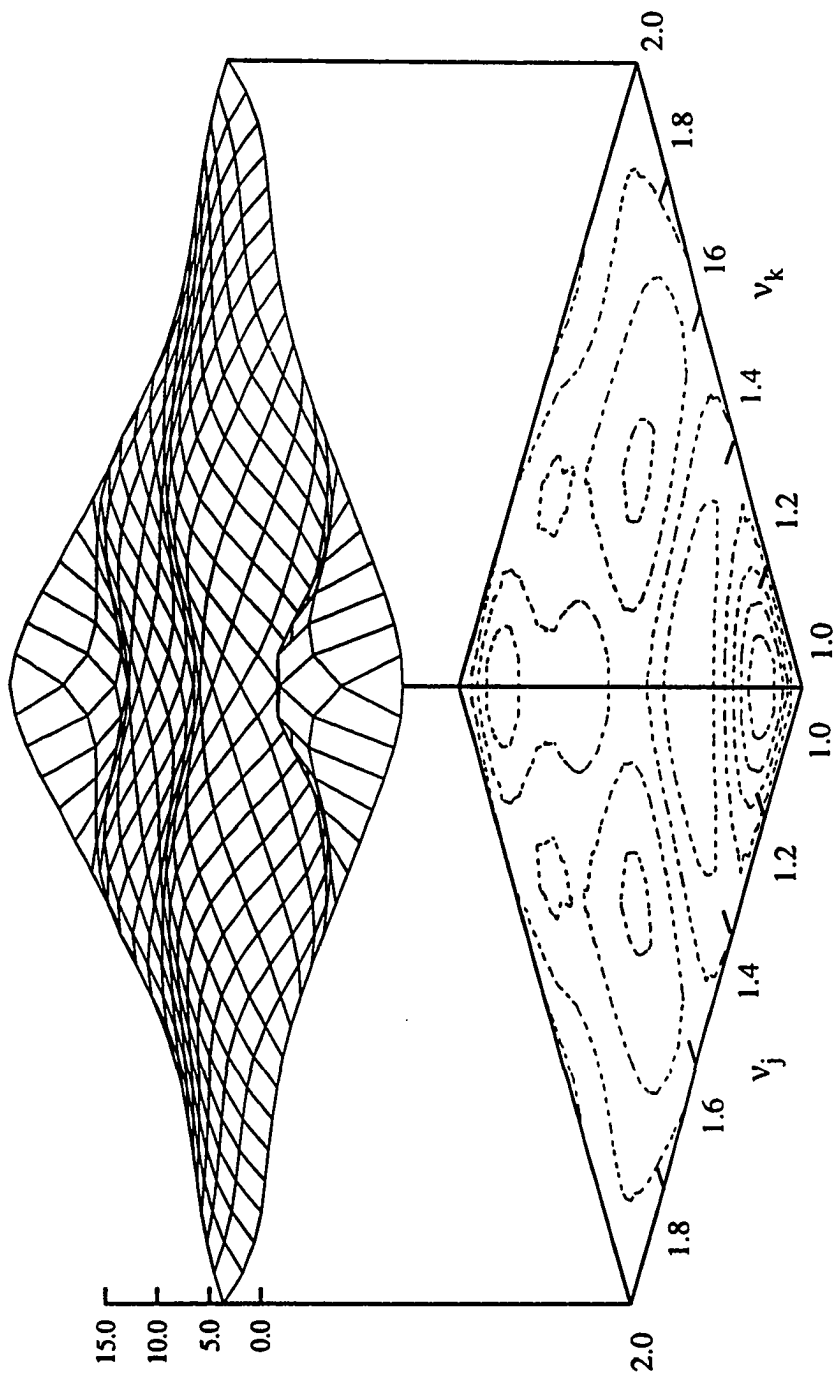


Fig. 6.11 Hydrodynamic sum-frequency sway force QTF, $H^+(\omega_j, \omega_k; \beta_j, \beta_k)$, for four-cylinder structure with $\beta_j = 45^\circ$, $\beta_k = 0^\circ$.

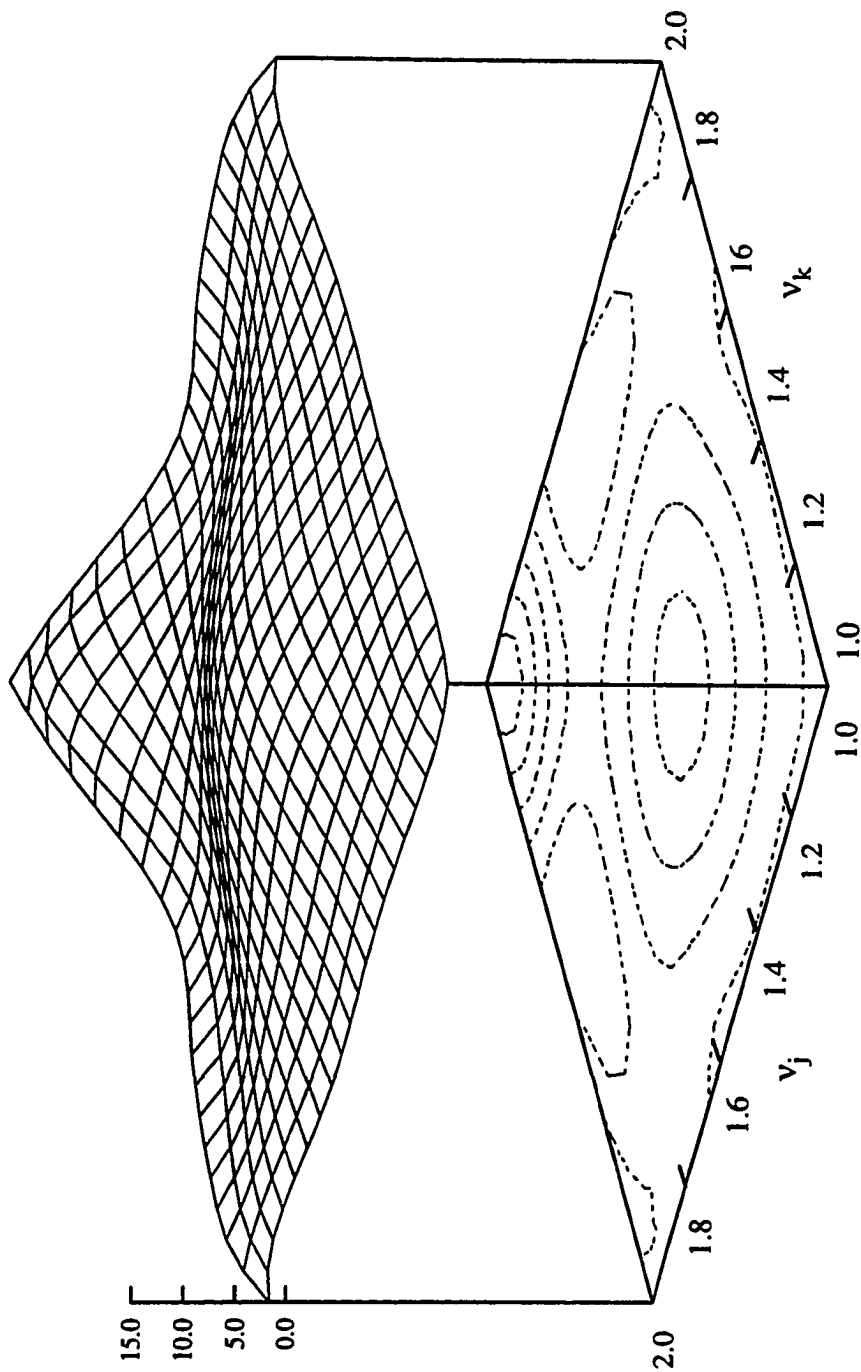


Fig. 6.12 Hydrodynamic sum-frequency sway force QTF, $H^+(\omega_j, \omega_k; \beta_j, \beta_k)$, for four-cylinder structure with $\beta_j = \beta_k = 22.5^\circ$.

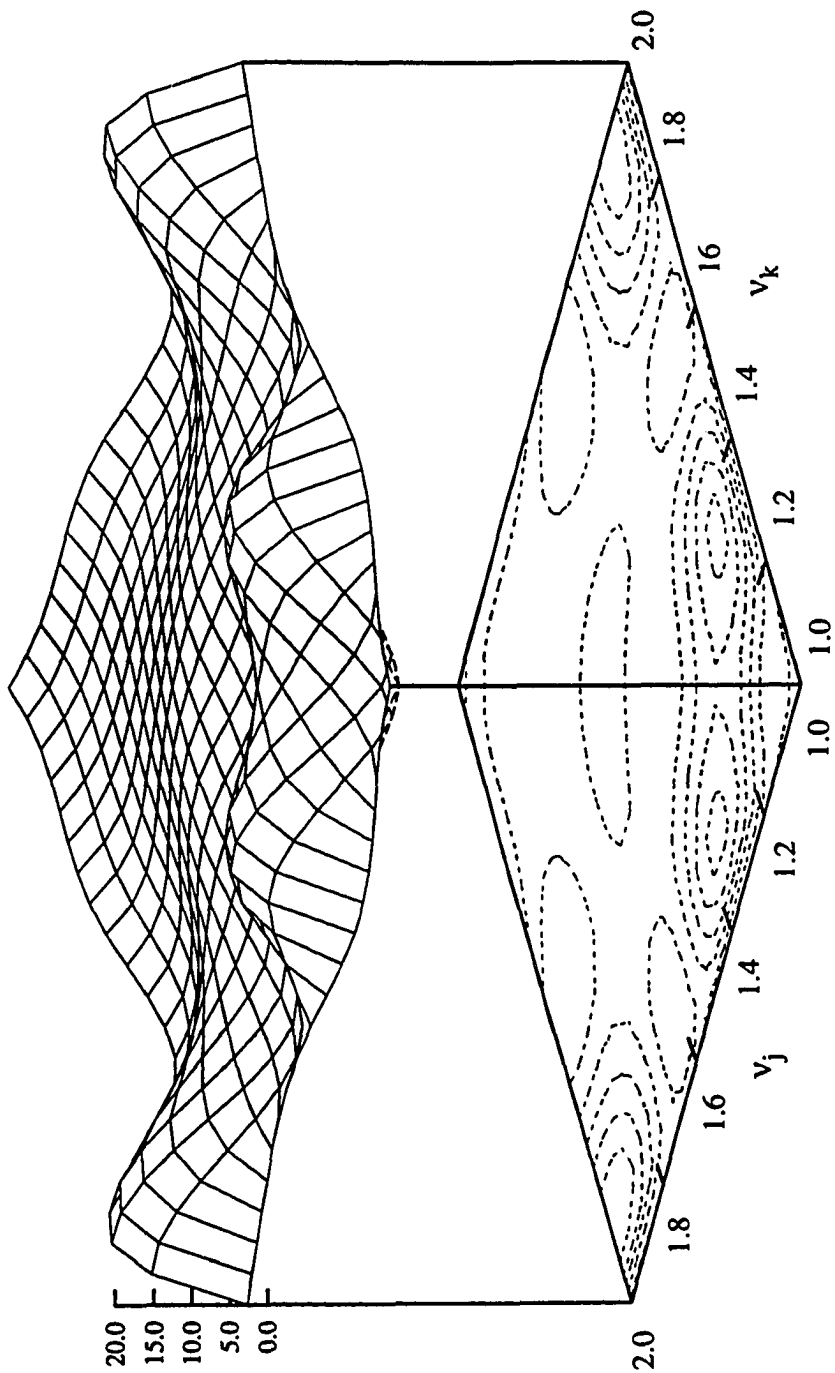


Fig. 6.13 Hydrodynamic sum-frequency roll moment QTF, $H^+(\omega_j, \omega_k; \beta_j, \beta_k)$, for four-cylinder structure with $\beta_j = 0^\circ$, $\beta_k = 45^\circ$.

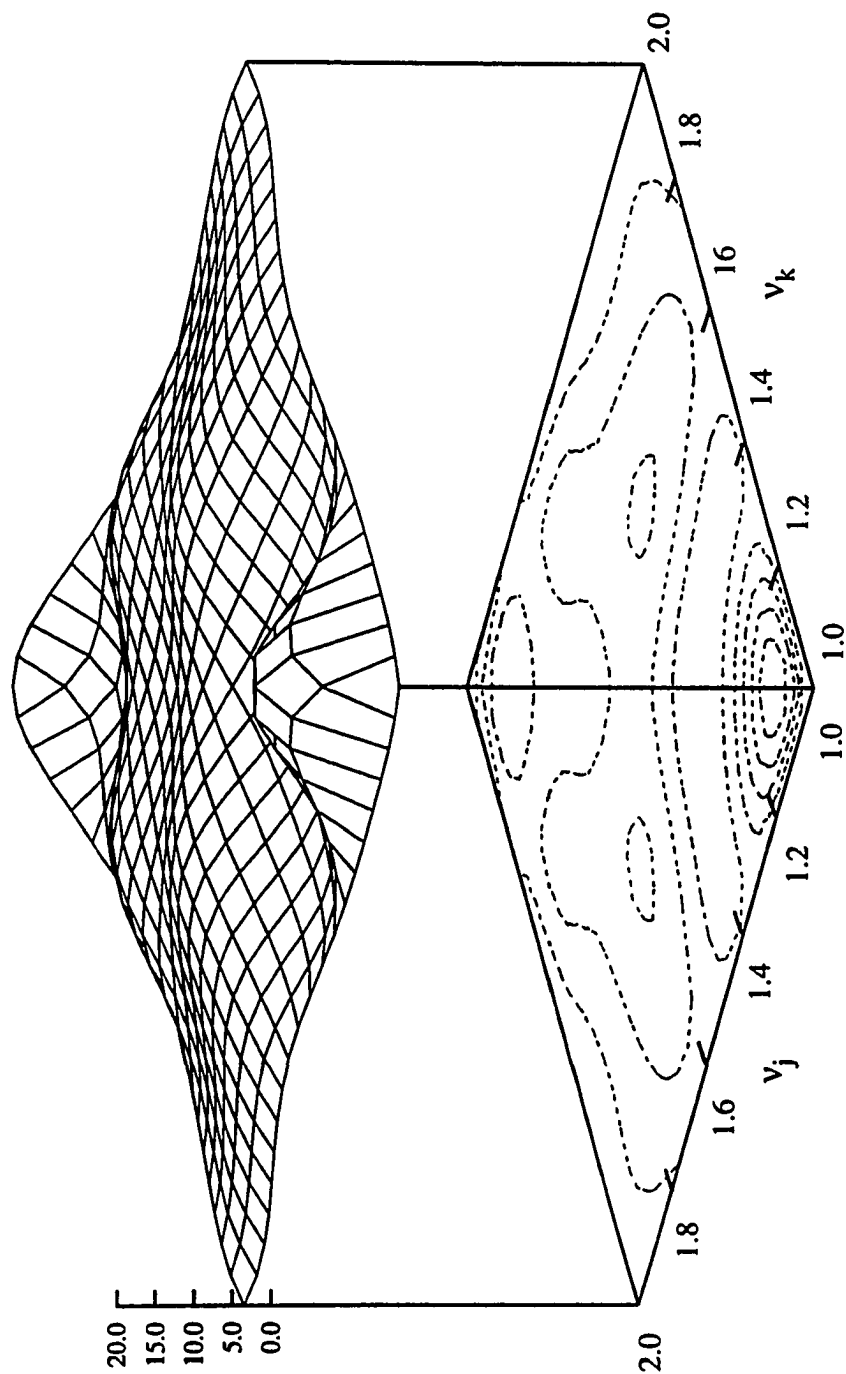


Fig. 6.14 Hydrodynamic sum-frequency roll moment QTF, $H^+(\omega_j, \omega_k; \beta_j, \beta_k)$, for four-cylinder structure with $\beta_j = 45^\circ$, $\beta_k = 0^\circ$.

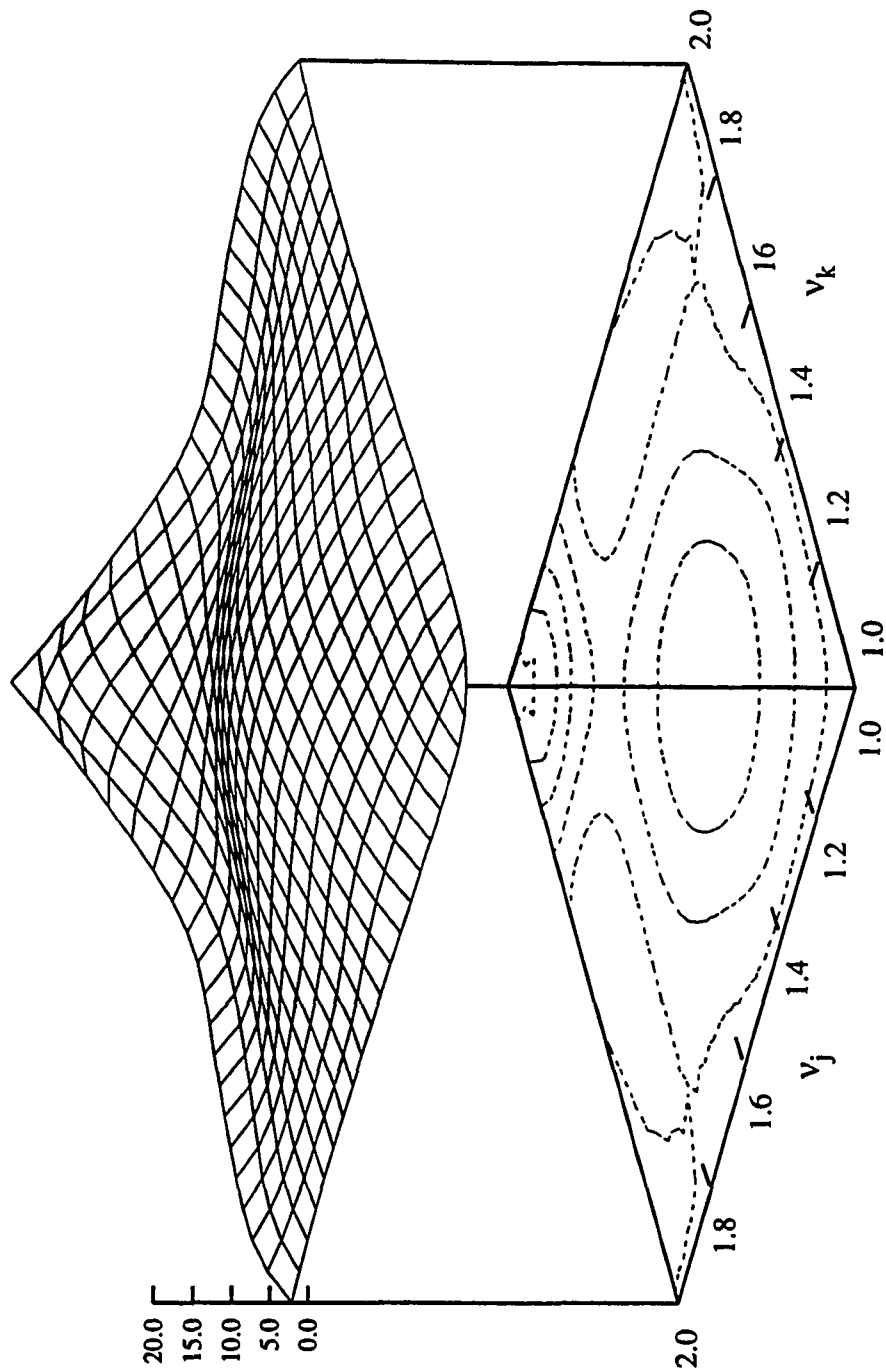


Fig. 6.15 Hydrodynamic sum-frequency roll moment QTF, $H^+(\omega_j, \omega_k; \beta_j, \beta_k)$, for four-cylinder structure with $\beta_j = \beta_k = 22.5^\circ$.

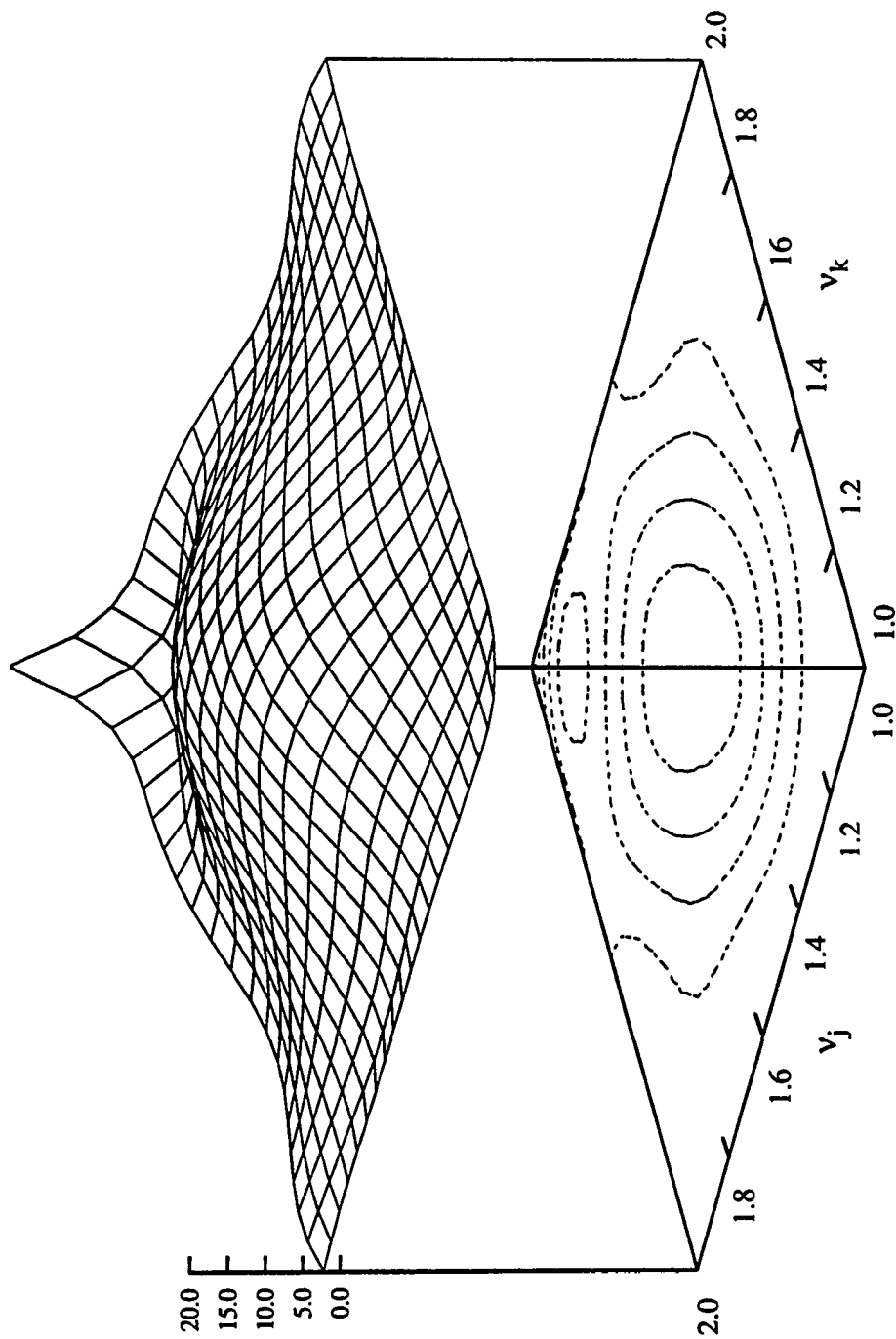


Fig. 6.16 Hydrodynamic sum-frequency pitch moment QTF, $H^+(\omega_j, \omega_k; \beta_j, \beta_k)$, for four-cylinder structure with $\beta_j = 0^\circ$, $\beta_k = 45^\circ$.

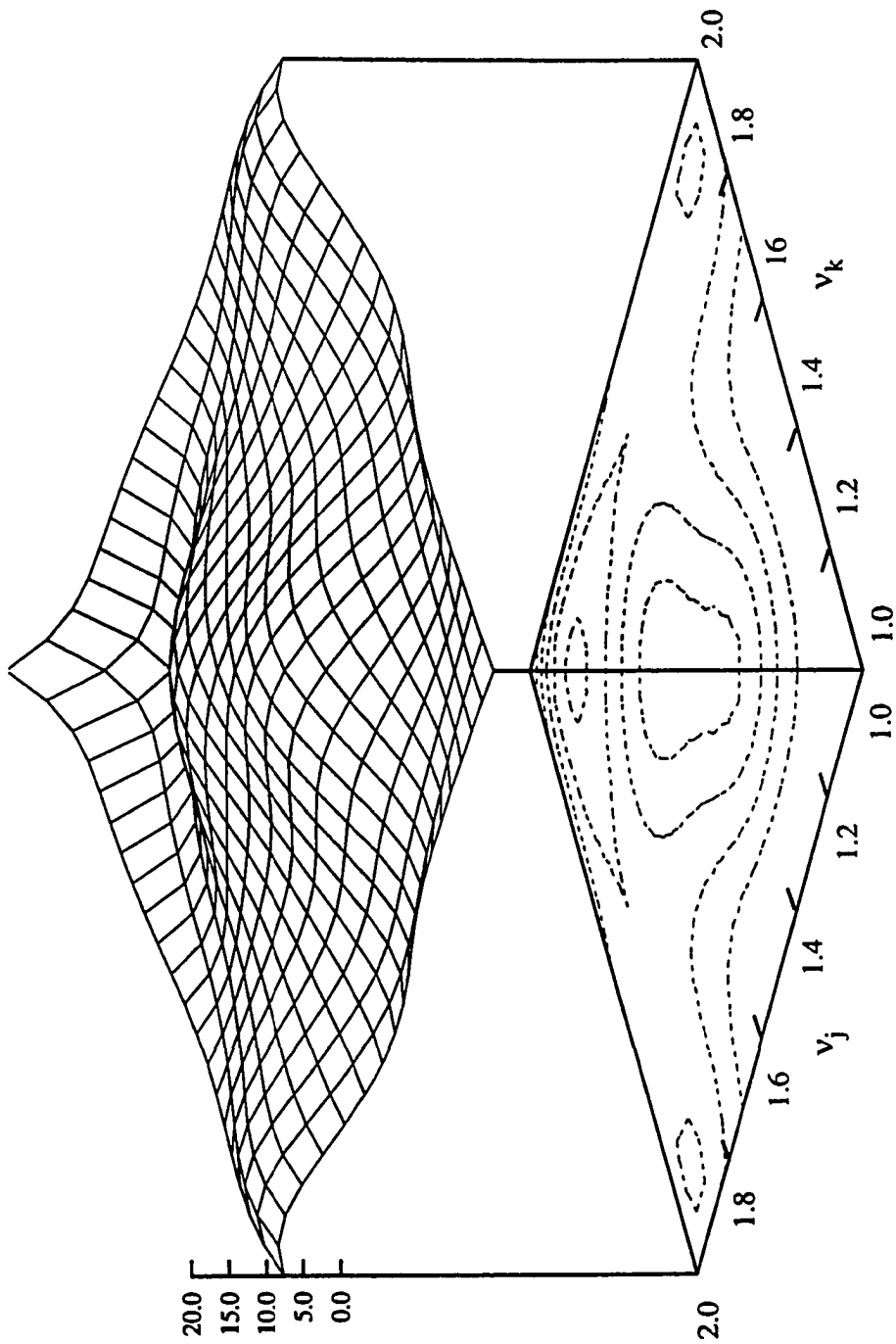


Fig. 6.17 Hydrodynamic sum-frequency pitch moment QTF, $H^+(\omega_j, \omega_k; \beta_j, \beta_k)$, for four-cylinder structure with $\beta_j = 45^\circ$, $\beta_k = 0^\circ$.

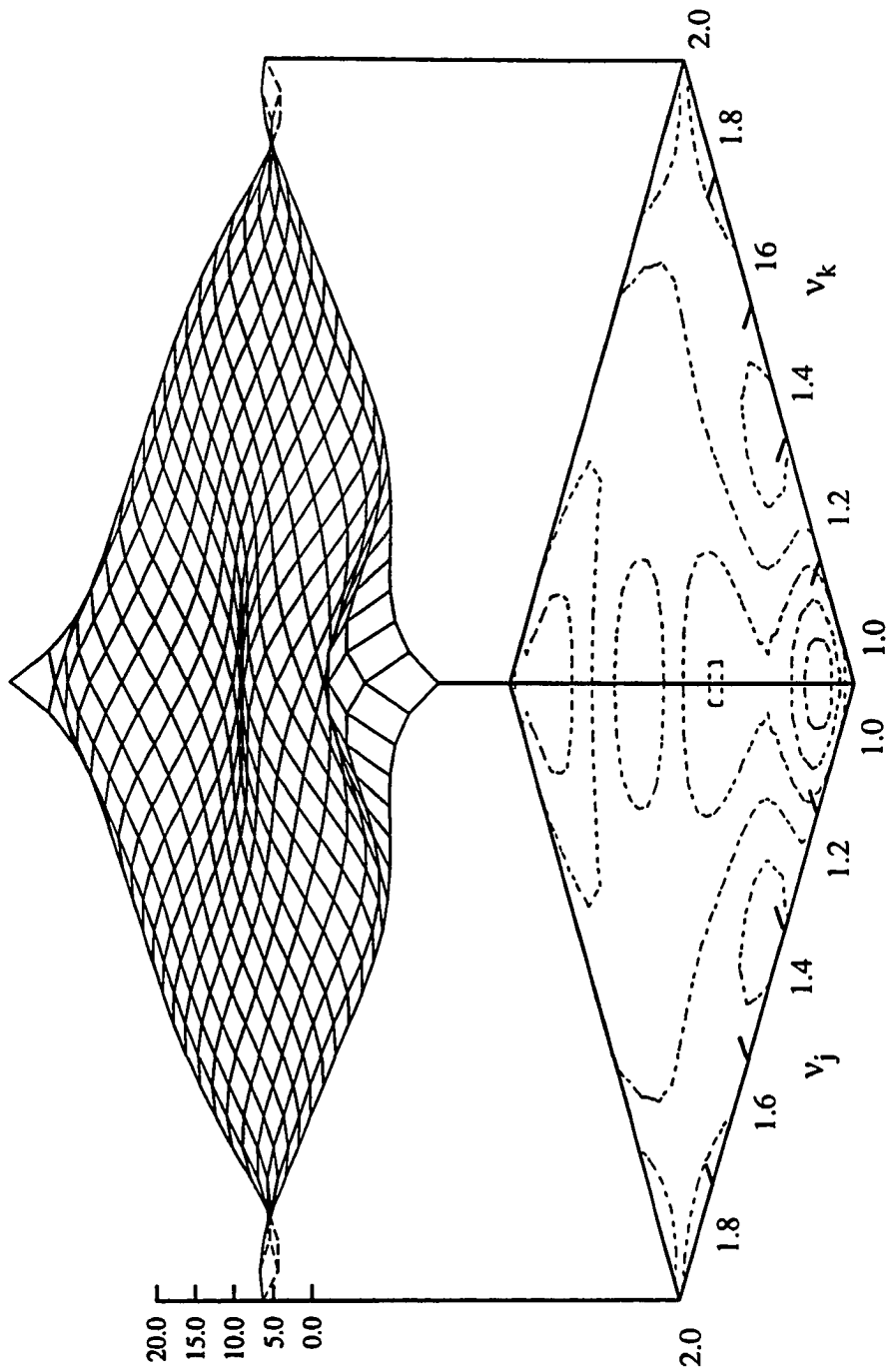


Fig. 6.18 Hydrodynamic sum-frequency pitch moment QTF, $H^*(\omega_j, \omega_k; \beta_j, \beta_k)$, for four-cylinder structure with $\beta_j = \beta_k = 22.5^\circ$.

QTFs. It should be reiterated here that, for the frequency range considered in Chapter Four, the ISSC TLP is not considered a deep draft structure.

Finally, Figs. 6.19 - 6.21 present the second-order sum-frequency yaw moment QTF's for the four-cylinder structure at three incident wave angle combinations. It is seen that in the lower frequency region, ($v_j < 1.5, v_k < 1.5$), where the sway force QTFs are larger than the corresponding surge force QTFs, the yaw moment QTFs behave as the former QTFs. At the higher frequencies, however, the yaw moment QTFs are more influenced by the surge force component. In comparing Fig. 6.19 to Fig. 6.20, the effect of wave directionality is clearly seen.

As observed in Chapter Four in Tables 4.3 - 4.5, the QTF values for the different loadings in bidirectional waves may be significantly higher than those obtained from a unidirectional wave analysis. Therefore, the effect of wave directionality should be considered in the design of offshore structures. The purpose of this research is to point out the effect of wave directionality in the second-order wave loading of offshore structures, and therefore, throughout the presentation of the results, the actual values of the QTFs have not been discussed in detail. This approach is in keeping with the goal of only presenting evidence that wave directionality plays a role and may be a controlling aspect in the design of offshore structures. The actual values of the sum-frequency QTFs are dependent on the frequency range of interest, and on the relative dimensions and spacing of the various components of the structure considered.

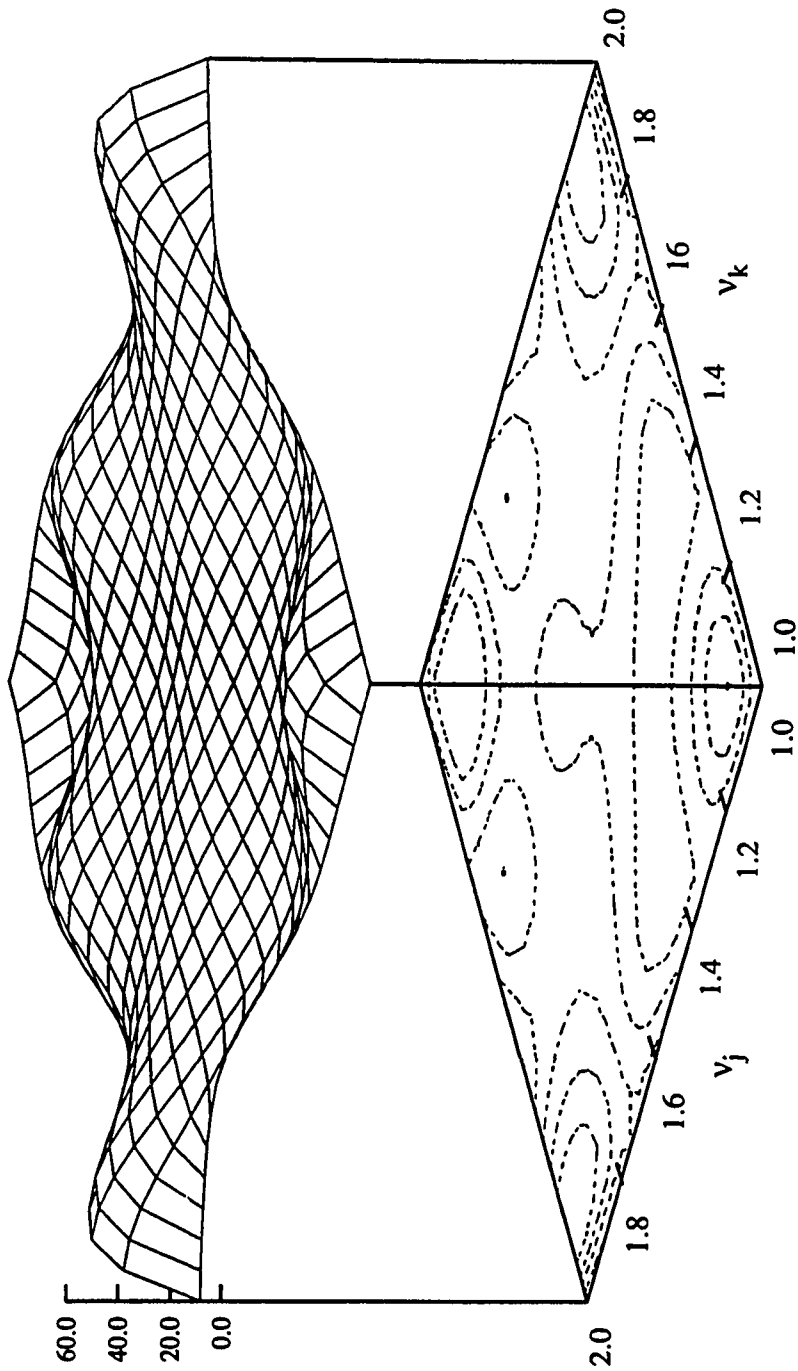


Fig. 6.19 Hydrodynamic sum-frequency yaw moment QTF, $H^+(\omega_j, \omega_k; \beta_j, \beta_k)$, for four-cylinder structure with $\beta_j = 0^\circ$, $\beta_k = 45^\circ$.

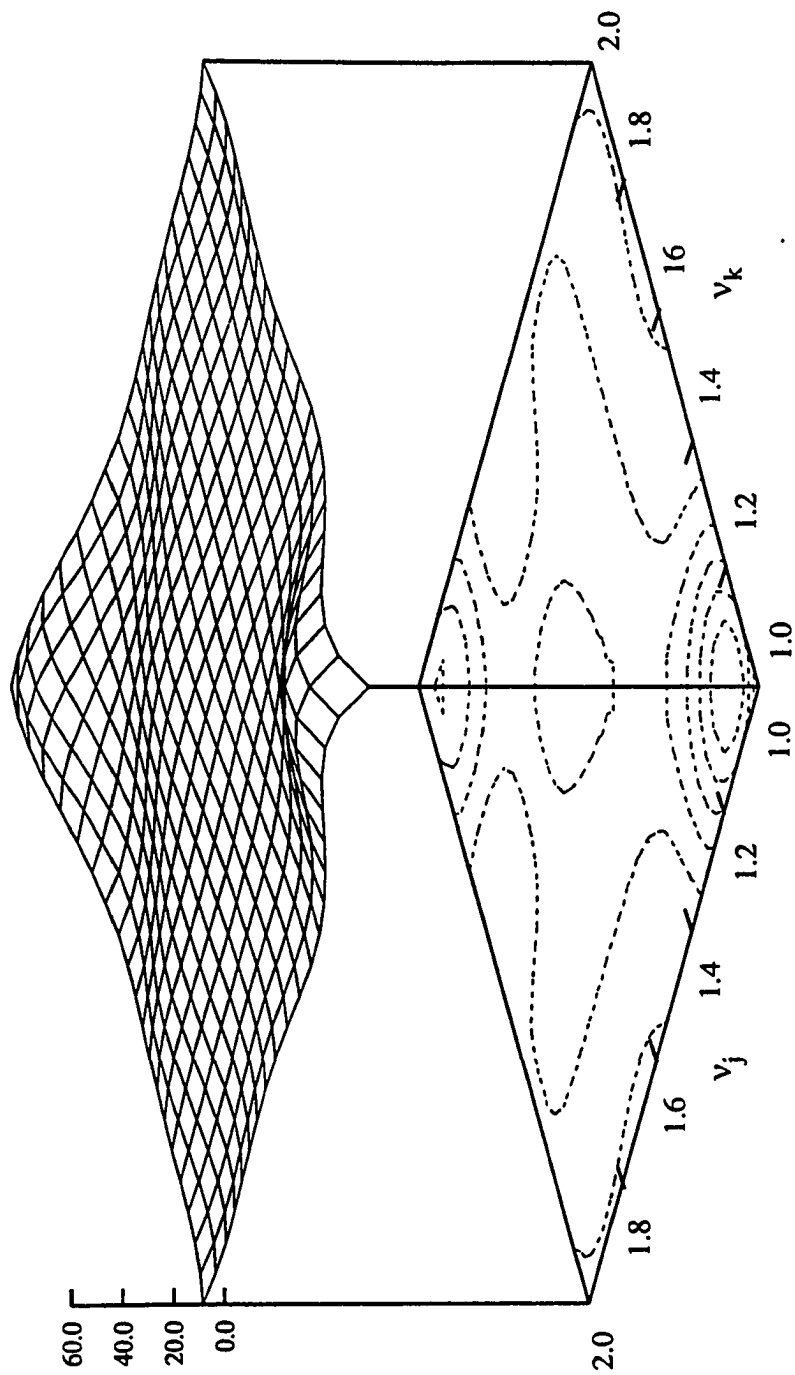


Fig. 6.20 Hydrodynamic sum-frequency yaw moment QTF, $H^+(\omega_j, \omega_k; \beta_j, \beta_k)$, for four-cylinder structure with $\beta_j = 45^\circ$, $\beta_k = 0^\circ$.

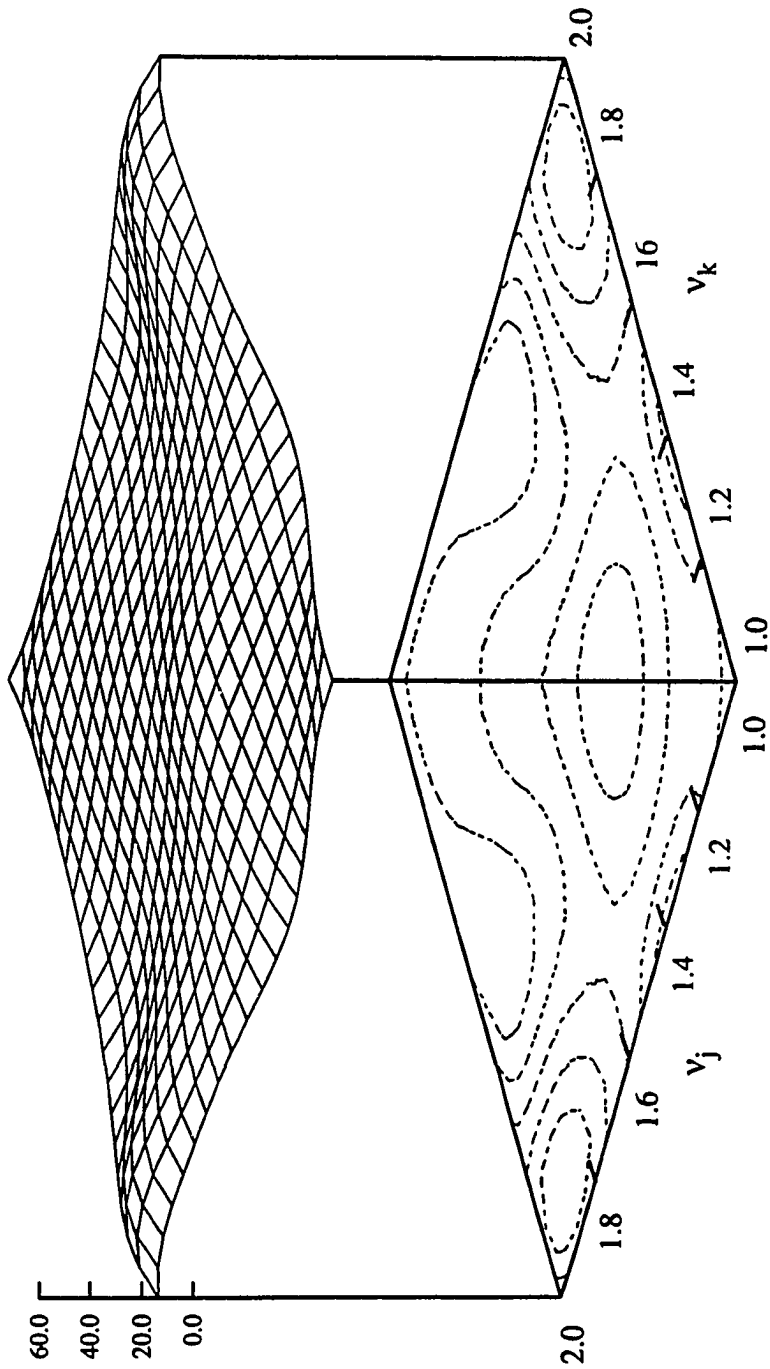


Fig. 6.21 Hydrodynamic sum-frequency yaw moment QTF, $H^*(\omega_j, \omega_k; \beta_j, \beta_k)$, for four-cylinder structure with $\beta_j = \beta_k = 22.5^\circ$.

CHAPTER SEVEN

SUMMARY AND CONCLUSIONS

In this research a complete second-order solution is developed for the hydrodynamic loads on ocean structures in bichromatic, bidirectional waves. The solution to the first-order problem is obtained utilizing a Green's function approach using higher-order boundary elements. The solution of the first-order diffraction problem yields the excitation forces and moments on the structure, while the solution to the radiation problem yields the corresponding first-order added-mass and radiation damping coefficients utilized in the solution of the linear equations of motion. Through the application of Green's second identity, the second-order hydrodynamic loads explicitly due to the second-order potential components are computed without the explicit computation of the second-order scattered potential. An efficient numerical technique, that accounts for the directionality of the waves and the asymptotic behavior of the integrand is presented to treat the free-surface integral which appears in the second-order load formulation.

In the first part of this research, a numerical technique utilizing quadratic surface elements is presented to obtain the second-order sum- and difference-frequency loads on an arbitrarily shaped three dimensional structure situated in infinite water depth. Numerical results are presented for the sum- and difference-frequency load QTFs on a stationary as well as on the tethered ISSC TLP. The results shown illustrate the sensitivity of the second-order wave loading to wave directionality at both the sum- and difference-frequency. Also seen in the results presented for the ISSC TLP is the effect of first-order body motions on the second-order sum- and difference-frequency hydrodynamic loading. It is seen that, for the most part, first-order body motions do not significantly contribute

to these loadings, but at certain frequency- and angles of wave incidence-combinations, they may account for a significant component of the second-order loading.

In the second part of this research, an array of bottom-mounted, surface piercing cylinders is used for the computation of the second-order sum-frequency loads on a deep draft TLP. By exploiting the constant cross-section of the cylinder array, the z-dependency of the solution may be obtained analytically, thereby rendering the numerical problem two-dimensional. This results in a considerable saving in the required computational effort. This simplification also allows for increased accuracy in the modeling of deep draft structures which would otherwise be impossible to analyze due to limitations of local computer resources. To illustrate this point, numerical results for the sum-frequency QTFs are presented for a four-column structure to represent a deep draft TLP.

The numerical results suggest that wave directionality may have a significant influence on the second-order hydrodynamic loads on large ocean structures at both sum- and difference-frequencies and that the assumption of unidirectional waves does not always lead to conservative estimates of the second-order loading. It is also found that while the effect of first-order body motions is not significant throughout the entire frequency range considered, they may have considerable influence at certain wave frequency and incident angle combinations. Wave directionality and first-order body motions are seen to play a significant role in the second-order loading, and should therefore be accounted for in the engineering design of offshore structures.

REFERENCES

- Abramowitz, M. and Stegun, I.A. (1972) Handbook of Mathematical Functions. Dover Publications, Mineola, New York.
- Abul-Azm, A.G. and Williams, A.N. (1988). Second-Order Diffraction Loads on Truncated Cylinders. *Journal of Waterways, Port, Coastal and Ocean Division, ASCE*, **114**, pp. 436-454.
- Abul-Azm, A.G. and Williams, A.N. (1989a) Approximation of Second-Order Diffraction Loads on Arrays of Vertical Circular Cylinders. *Journal of Fluids and Structures*, **3**, pp. 17-36.
- Abul-Azm, A.G. and Williams, A.N. (1989b) Second-Order Diffraction Loads on Arrays of Semi-Immersed Circular Cylinder. *Journal of Fluids and Structures*, **3**, pp. 365-388.
- Chen, X.B. and Molin, B. (1990). High Frequency Interactions Between TLP Legs. *Proc. 5th Intl. Workshop on Water Waves and Floating Bodies*, Manchester, England.
- Eatock Taylor, R.E. and Jeffreys, E.R. (1986). Variability of Hydrodynamic Load Predictions for a Tension Leg Platform. *Ocean Engineering*, **13**, pp. 449-490.
- Eatock Taylor, R.E., Hung, S.M. and Mitchell, K.L. (1988). Advances in the Prediction of Low-Frequency Drift Behaviour. *Proc. BOSS 88*, Trondheim, Norway, pp. 651-666.
- Eatock Taylor, R.E. and Chau, F.P. (1991). Wave Diffraction - Some Developments in Linear and Nonlinear Theory. *Proc. 11th Intl. Offshore Mechanics and Arctic Eng. Conf.*, Stavanger, Norway, pp. 19-28.
- Eatock Taylor, R.E. and Teng, B. (1993). The Effect of Corners on Diffraction/Radiation Forces and Wave Drift Damping. *OTC Proceedings*, Houston Texas, USA., pp. 571-581.

- Ghalayini, S.A. and Williams, A.N. (1989). Nonlinear Wave Forces on Vertical Cylinders of Arbitrary Cross-Section. *Journal of Waterways, Port, Coastal and Ocean Division ASCE*, **115**, pp. 809-830.
- Ghalayini, S.A. and Williams, A.N. (1991). Nonlinear Wave Forces on Vertical Cylinder Arrays. *Journal of Fluids and Structures*, **5**, pp. 1-32.
- Kim, M.-H. and Yue, D.K.P. (1989). Slowly-Varying Wave Drift Forces in Short-Crested Irregular Seas. *Applied Ocean Research*, **11**, pp. 2-18.
- Kim, M.-H. (1992). Difference-Frequency Wave Loads on a Large Body in Multi-Directional Waves. *Applied Ocean Research*, **14**, pp. 353-370.
- Kim, M.-H. (1993). Second-Harmonic Vertical Wave Loads on Arrays of Deep-Draft Circular Cylinders in Monochromatic Uni- and Multi-Directional Waves. *Applied Ocean Research*, **15**, pp. 245-262.
- Korsmeyer, F.T., Lee, C.- H., Newman, J.N., and Sclavounos, P.D. (1988). The Analysis of Wave Effects on Tension Leg Platforms. *Proc. Seventh Offshore Mechanics and Arctic Engineering Conf.*, Houston, Texas, USA., pp. 1-14.
- Lee, C.-H., Kim, M.H., Newman, J.N. and Yue, D.K.P. (1991) The Computation of Second-Order Wave Loads. *Proc. 11th Intl. Offshore Mechanics and Arctic Eng. Conf.*, Stavanger, Norway, pp. 113-124.
- Linton, C.M. and Evans, D.V. (1990). The Interaction of Waves with Arrays of Vertical Circular Cylinders. *Journal of Fluid Mechanics*, **215**, pp. 129-139.
- Lighthill, M.J. (1979). Waves and Hydrodynamic Loading. *Proc. BOSS 79*, London, UK, pp. 1-40.
- Maeda, H., Morooka, C.K. and Kasahara, A. (1986). Motions of Floating Type Offshore Structures in Directional Waves. *Proc. 5th Intl. Offshore Mechanics and Arctic Engineering Conf.*, Tokyo, Japan, pp. 94-101.

- Maeda, H., Morooka, C.K. and Miyajima, S. (1988). Motions of Floating Offshore Structures in Multi-Directional Waves. *Proc. 7th Intl. Offshore Mechanics and Arctic Engineering Conf.*, Houston Texas, USA., pp. 309-316.
- Maeda, H., Jo, H.J. and Miyajima, S. (1992). Effect of Directional Waves on the Low Frequency Motions of Moored Floating Structures. *Proc. 2nd Intl. Offshore and Polar Engineering Conf.*, San Francisco, California, USA, pp. 489-495.
- Matsui, T., Suzuki, T., and Sakoh, Y. (1992). Second-Order Diffraction Forces on Floating Three-Dimensional Bodies in Regular Waves. *International Journal of Offshore and Polar Engineering*, **2**, pp. 175-185.
- McIver, P. and Evans, D.V. (1984). Approximation of Wave Forces on Cylinder Arrays. *Applied Ocean Research*, **6.**, pp. 101-107.
- Molin, B., (1979). Second-Order Diffraction Loads Upon Three-Dimensional Bodies. *Applied Ocean Research*, **1**, pp. 197-202.
- Moubayed, W.I. and Williams, A.N. (1992a). Second-Order Hydrodynamic Interactions Between a Pair of Vertical Cylinders in Irregular Waves. *Proc. 5th Conf. Civil Eng. in the Oceans*, College Station, Texas, USA., pp. 188-202.
- Moubayed, W.I. (1992) Nonlinear Hydrodynamics of Offshore Structures in Bichromatic Seas. Doctoral Dissertation. University of Houston, Houston Texas, USA.
- Natvig, B.J. (1994) A Proposed Ringing Analysis Model for Higher Order Tether Response. *Proc. 4th Intl. Offshore and Polar Eng. Conf.*, Osaka, Japan, pp. 40-50.
- Newman, J.N. (1974). Second-Order Slowly Varying Forces on Vessels in Irregular Waves. *Proc. Symp. on Dynamics of Marine Vehicles and Structures in Waves*, London, U.K, pp. 193-197.
- Newman J.N. and Lee, C.-H. (1992). Sensitivity of Wave Loads to the Discretization of Bodies. *Proc. BOSS 92*, London, U.K, pp. 50-64.

- Nwogu, O. and Isaacson, M. (1991). Drift motions of a Floating Barge in Random Multi-Directional Waves. *Journal of Offshore Mechanics and Arctic Engineering ASME*, **113**, pp. 37-42.
- Stoker, J.J. (1957) *Water Waves: The Mathematical Theory with Applications*. Wiley Interscience, New York.
- Telste, J.G. and Noblesse, F. (1986). Numerical Evaluation of the Green Function of Water-Wave Radiation and Diffraction. *Journal of Ship Research*, **30**, pp. 69-84.
- Vazquez, J.H. and Williams, A.N. (1994). Second-Order Diffraction Loads on an Array of Vertical Cylinders in Bichromatic, Bidirectional Waves. *Proc. 14th Intl. Offshore Mechanics and Arctic Eng. Conf.*, Houston, Texas, USA., pp. 73-82.
- Wehausen J.V. and Laitone, E.V. (1960) Surface Waves, *Encyclopedia of Physics*, **IX**.
- Williams, A.N., Abul-Azm, A.G. and Ghalayini, S.A. (1990). A Comparison of Complete and Approximate Solutions for Second-Order Diffraction Loads on Arrays of Vertical Cylinders. *Ocean Engineering*, **17**, pp. 427-446.
- Zaraphonitis, G.N. and Papanikolaou, A.D. (1993). Second-Order Theory and Calculations of Motions and Loads of Arbitrary Shaped 3D Bodies in Waves. *Marine Structures*, **6**, pp.165-185.

APPENDIX A

QUADRATIC SHAPE FUNCTIONS FOR SURFACE AND LINE ELEMENTS

When using shape functions to describe the variation of a given parameter over a line element or a surface element, the order of the approximation depends on the number of nodes (or sampling points) utilized to define the shape functions. The number of shape functions required to describe n th order variation over a line element is $n+1$. For quadrilateral surface elements, the number of shape functions required to describe n th order variation over the element is either $(n+1)^2$ or $(n+1)^2 - (n-1)^2$ depending on whether all nodes in the matrix or only the nodes on the boundary are used. For instance, eight or nine nodes may be used to achieve quadratic variation over a quadrilateral surface element. Similarly, twelve or sixteen shape functions may be used to achieve cubic variation over quadrilateral surface elements. For triangular surface elements, the number of nodes (shape functions) required to describe n th order variation over the element is $[(n+1)^2 + (n+1)] / 2$. For instance, six and ten shape functions are required to describe quadratic and cubic variation. Obviously, the more shape functions used to describe the variation over an element, the more accurately it represents the actual variation. However, using the elements having nodes only on the boundary has a great advantage: it requires fewer overall nodes to describe any given parameter for any given order of element variation. For this reason, in the following section, the shape functions for quadratic variation over surface elements will be given only in terms of the eight-node representation.

A.1 Line elements

In general, the form of the shape functions may be found by Legendre's formula:

$$L_i^{(n)} = \frac{\sum_{j=1}^{n+1} (\xi - \xi_j)}{\sum_{\substack{j=1 \\ j \neq i}}^{n+1} (\xi_i - \xi_j)}, \quad (\text{A.1})$$

where ξ_i are the nodal coordinates.

Taking the parametric element in the range $-1 \leq \xi \leq 1$, with nodes at $\xi_1 = -1$, $\xi_2 = 0$, and $\xi_3 = 1$, results in the following expressions for the quadratic shape functions:

$$L_1 = \frac{\xi}{4} (\xi - 1) \quad \text{for the node at } \xi = -1, \quad (\text{A.2a})$$

$$L_2 = \frac{1}{4} (\xi + 1) (\xi - 1) \quad \text{for the node at } \xi = 0, \quad (\text{A.2b})$$

and

$$L_3 = \frac{\xi}{4} (\xi + 1) \quad \text{for the node at } \xi = 1. \quad (\text{A.2c})$$

A.2 Surface elements

The shape functions for surface elements may be obtained using the serendipity method. Surface elements may be represented with either quadrilateral or triangular elements. Depending on the application, one type of element may be more desirable over the other.

For a parametric surface element with four sides of length 2 and origin at its center, either eight or nine nodes are used to obtain quadratic variation. In the interest of savings in computational effort, eight-node representation is preferred over nine-node representation.

Taking the parametric element in the range $-1 \leq \xi \leq 1$, $-1 \leq \eta \leq 1$, (see Fig. A.1), results in the following expressions for the quadratic shape functions:

$$N_1 = \frac{\xi}{4} (1 + \eta) (1 + \xi) \quad \text{for the node at } (\xi, \eta) = (1, 1), \quad (\text{A.3a})$$

$$N_2 = \frac{1}{2} (1 + \eta) (1 - \xi^2) \quad \text{for the node at } (\xi, \eta) = (0, 1), \quad (\text{A.3b})$$

$$N_3 = \frac{\xi}{4} (1 + \eta) (\xi - 1) \quad \text{for the node at } (\xi, \eta) = (-1, 1), \quad (\text{A.3c})$$

$$N_4 = \frac{1}{2} (1 - \xi) (1 - \eta^2) \quad \text{for the node at } (\xi, \eta) = (-1, 0), \quad (\text{A.3d})$$

$$N_5 = \frac{\xi}{4} (1 - \eta) (\xi - 1) \quad \text{for the node at } (\xi, \eta) = (-1, -1), \quad (\text{A.3e})$$

$$N_6 = \frac{1}{2} (1 - \eta) (1 - \xi^2) \quad \text{for the node at } (\xi, \eta) = (0, -1), \quad (\text{A.3f})$$

$$N_7 = \frac{\xi}{4} (1 - \eta) (1 + \xi) \quad \text{for the node at } (\xi, \eta) = (1, -1), \quad (\text{A.3g})$$

and

$$N_8 = \frac{1}{2} (1 + \xi) (1 - \eta^2) \quad \text{for the node at } (\xi, \eta) = (1, 0). \quad (\text{A.3h})$$

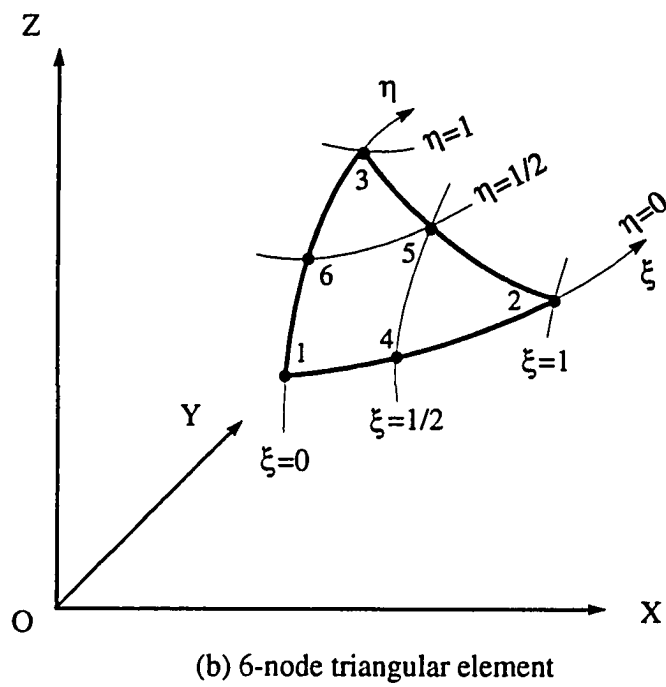
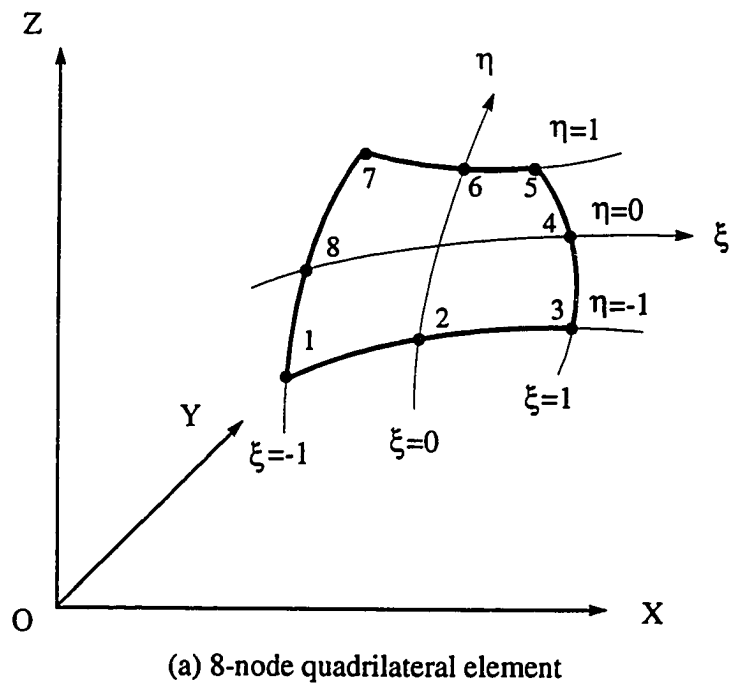


Fig. A.1 Quadratic quadrilateral and triangular elements.

For a parametric surface element with three sides, six nodes are used to obtain quadratic variation. When working with triangular elements, natural triangular coordinates are preferred over rectangular coordinates for the simplicity of their use. Triangular natural coordinates, ξ_i , at a point within the element are defined by $\xi_i = \frac{A_i}{A}$ for $i = 1, 2, 3$ (see Fig. A.2), where A is the total area of the triangle, and A_i is the area of the triangle formed by connecting the point of interest to the side opposite node i . It should be noted that regardless of the actual area of the triangle, by their definition the natural coordinates vary such that $\xi_3 = 1 - \xi_1 - \xi_2$, and therefore only two coordinates are necessary to define the triplet.

Utilizing the natural triangular coordinates, the shape functions for a six node triangular element are given by

$$N_1 = \xi_1(2\xi_1 - 1) \quad \text{for the node at } (\xi_1, \xi_2, \xi_3) = (1, 0, 0), \quad (\text{A.4a})$$

$$N_2 = \xi_2(2\xi_2 - 1) \quad \text{for the node at } (\xi_1, \xi_2, \xi_3) = (0, 1, 0), \quad (\text{A.4b})$$

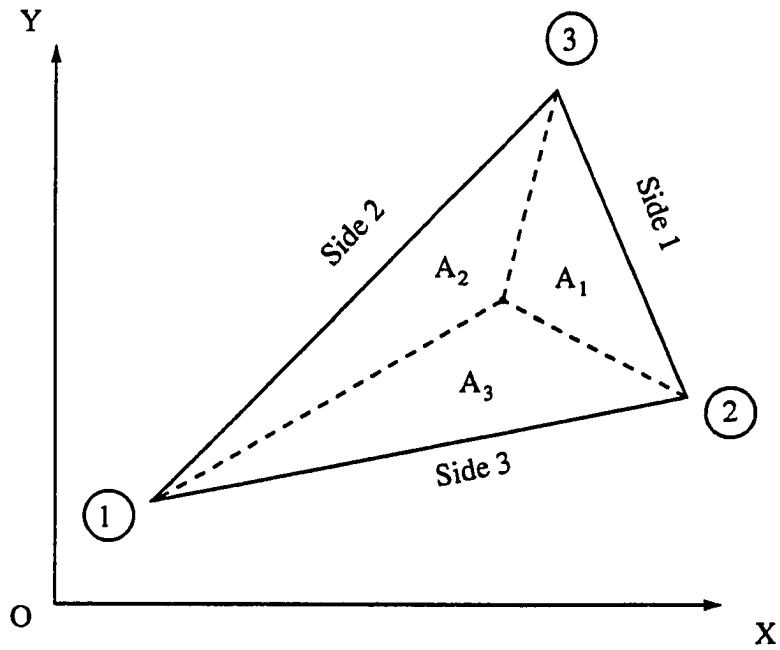
$$N_3 = \xi_3(2\xi_3 - 1) \quad \text{for the node at } (\xi_1, \xi_2, \xi_3) = (0, 0, 1), \quad (\text{A.4c})$$

$$N_4 = 4 \xi_1 \xi_2 \quad \text{for the node at } (\xi_1, \xi_2, \xi_3) = \left(\frac{1}{2}, \frac{1}{2}, 0\right), \quad (\text{A.4d})$$

$$N_5 = 4 \xi_2 \xi_3 \quad \text{for the node at } (\xi_1, \xi_2, \xi_3) = \left(0, \frac{1}{2}, \frac{1}{2}\right), \quad (\text{A.4e})$$

and

$$N_6 = 4 \xi_1 \xi_3 \quad \text{for the node at } (\xi_1, \xi_2, \xi_3) = \left(\frac{1}{2}, 0, \frac{1}{2}\right). \quad (\text{A.4f})$$



$$A = A_1 + A_2 + A_3$$

$$\xi_1 = \frac{A_1}{A} \quad \xi_2 = \frac{A_2}{A} \quad \xi_3 = \frac{A_3}{A}$$

$$\xi_3 = 1 - \xi_1 - \xi_2$$

Fig. A.2 Natural triangular coordinates.

A.3 Numerical Integration Over Elements

The numerical integrations over arbitrarily shaped elements are achieved through a mapping of the element into parametric space. A point on the physical three-dimensional surface element $\underline{r} = (x,y,z)$ is mapped into the parametric element at point (ξ,η) . Similarly, for line elements, a point (x,y) is mapped in to parametric space ξ . The original integral is reduced to the standard integration of the original function multiplied by the magnitude of the appropriate reduced Jacobian. It should be noted that although the parametric elements are either one- or two-dimensional, they are used to integrate over two- and three-dimensional boundaries. It is through the reduced Jacobian and the unit normal to the element that this integration is possible. The reduced Jacobian is obtained as function of the the derivatives of the shape functions as follows:

A.3.1 Line Elements

A differential segment is given by

$$dL = |G| d\xi, \quad (\text{A.5})$$

where G is is the reduced Jacobian and its magnitude, $|G|$, is equal to the magnitude of the two-dimensional normal vector \underline{n} , given by

$$\underline{n} = (g_1, g_2) = \left(\frac{\partial x}{\partial \xi}, \frac{\partial y}{\partial \xi} \right) \quad (\text{A.6})$$

Hence, $|G|$ is given by

$$|G| = \sqrt{g_1^2 + g_2^2} . \quad (\text{A.7})$$

These relationships are now used to evaluate the integrals of any function over the physical line elements as

$$\int_{\Gamma_e} f(x,y) dL = \int_{\Gamma_p} f(x,y) |G| d\xi. \quad (\text{A.8})$$

A.3.2 Surface Elements

A differential area is given by

$$dS = |G| d\xi d\eta, \quad (\text{A.9})$$

where G is the reduced Jacobian and its magnitude, $|G|$, is equal to the magnitude of the three-dimensional normal vector \underline{n} , given by

$$\underline{n} = (g_1, g_2, g_3) = \frac{\partial \underline{r}}{\partial \xi} \times \frac{\partial \underline{r}}{\partial \eta}, \quad (\text{A.10a})$$

$$g_1 = \left(\frac{\partial y}{\partial \xi} \frac{\partial z}{\partial \eta} - \frac{\partial y}{\partial \eta} \frac{\partial z}{\partial \xi} \right) \quad (\text{A.10b})$$

$$g_2 = \left(\frac{\partial z}{\partial \xi} \frac{\partial x}{\partial \eta} - \frac{\partial z}{\partial \eta} \frac{\partial x}{\partial \xi} \right) \quad (\text{A.10c})$$

$$g_3 = \left(\frac{\partial x}{\partial \xi} \frac{\partial y}{\partial \eta} - \frac{\partial x}{\partial \eta} \frac{\partial y}{\partial \xi} \right) \quad (\text{A.10d})$$

Hence, $|G|$ is given by

$$|G| = \sqrt{g_1^2 + g_2^2 + g_3^2}. \quad (\text{A.11})$$

These relationships are now used to evaluate the integrals of any function over the physical surface elements as

$$\int_{S_e} f(x,y,z) dS = \int_{S_p} f(x,y,z) |G| d\xi d\eta. \quad (\text{A.12})$$

APPENDIX B

REDUCTION OF $O(1/R)$ SINGULARITY BY POLAR COORDINATE TRANSFORMATION

Consider a typical integral over an element, S_e , of the function $f(x,y,z)$ which has singular behavior of order $O(1/R)$ or $O(1/R)^2$ near one of the nodes which describe the element. This integral is performed over a parametric element, S_p , and is given by

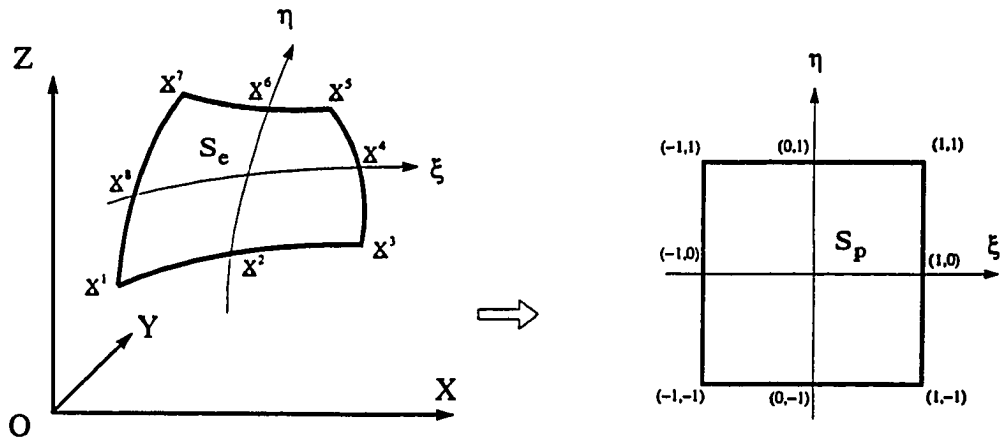
$$I = \int_{S_e} f(x,y,z) dS = \int_{S_p} f(x,y,z) |G(\xi,\eta)| d\xi d\eta, \quad (\text{B.1})$$

where the position vector $\underline{r} = (x,y,z)$ is related to the parametric coordinates (ξ,η) through appropriate shape functions and the position vectors at the element nodes.

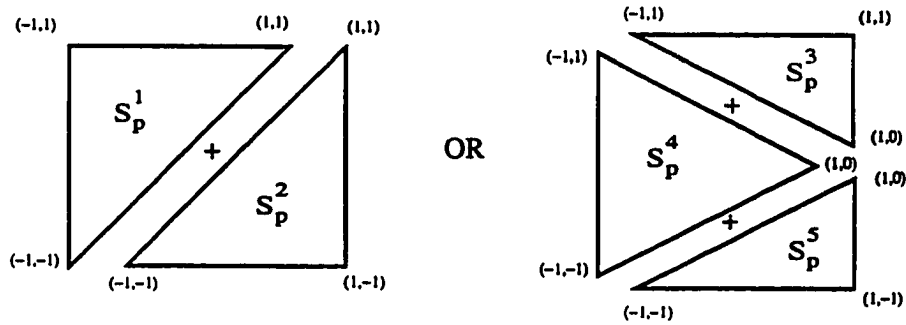
The parametric square element S_p is a square element of side length equal to 2 with origin at its center. Depending on the location of the singular node, the element is divided into two or three triangular elements corresponding to the singular node being at the corner, or the side of the element respectively. Then, for the case of the singular node being at one of the corners (i.e., S_p is divided into two triangles),

$$I = \sum_{j=1}^2 \int_{S_p^j} f(x,y,z) |G(\xi,\eta)| d\xi d\eta. \quad (\text{B.2})$$

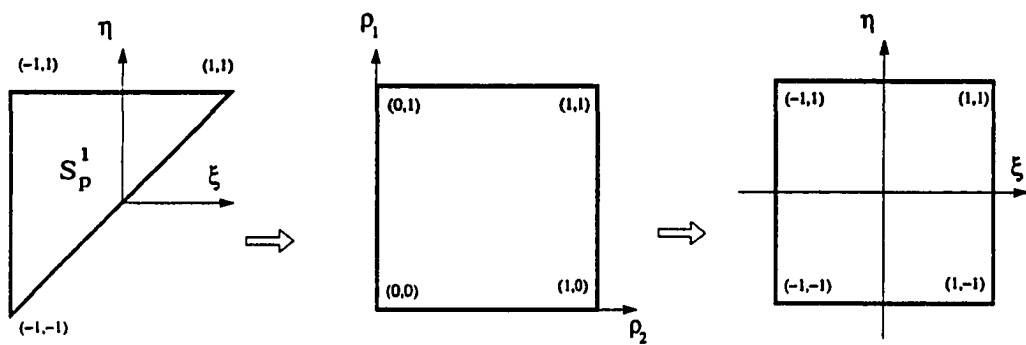
Employing triangular polar coordinates, each of the subelements, S_p^j , is mapped onto a unit square (see Fig. B.1). The corresponding shape functions for this mapping are given by



(a) Mapping of S_e onto S_p by isoparametric quadratic transformation



(b) Subdivision of S_p into triangular elements



(c) Mapping of S_p^1 onto a unit square by polar coordinates and further mapping onto a square of length 2.

Fig. B.1 Triangular polar coordinate transformation.

$$N_1 = (1 - \rho_1), \quad (B.3a)$$

$$N_2 = \rho_1(1 - \rho_2), \quad (B.3b)$$

and

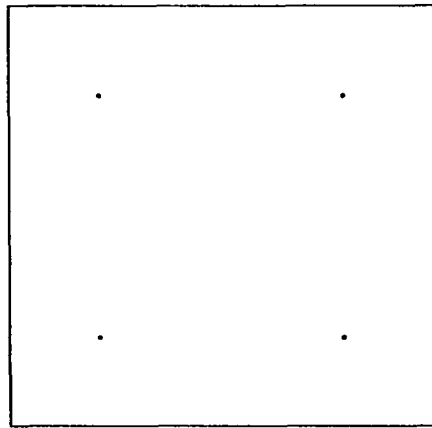
$$N_3 = \rho_1\rho_2. \quad (B.3c)$$

Equation (B.2) can now be written as

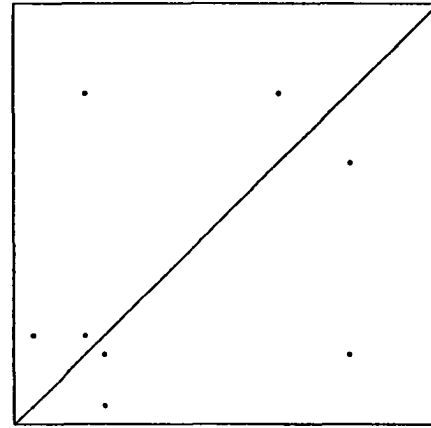
$$I = \sum_{j=1}^2 \int_{S_p^j} f(x,y,z) |G(\xi,\eta)| [2 \rho_1 A_j] d\rho_1 d\rho_2, \quad (B.4)$$

where A_j is the area of the triangular subelement S_p^j . The term in the square brackets accounts for the mapping from the triangle to the unit square. In particular, the term ρ_1 , which is directly related to the distance between the singular node and the integration point on the element (i.e., ρ_1 is proportional to R), serves to reduce the order of the singularity in the integrand facilitating the subsequent numerical integration.

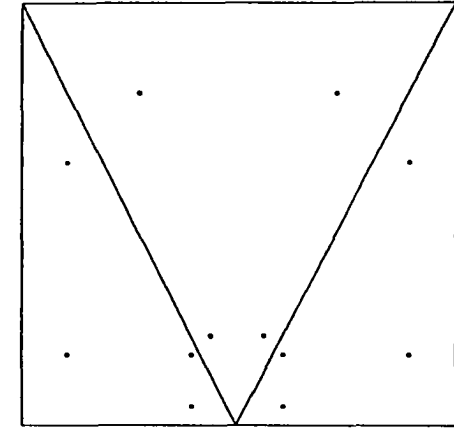
A final coordinate transformation is invoked to carry out the numerical integration. It consists of mapping the unit square, S_p^j , onto a square of side length 2 with origin at its center. The numerical integration is carried out utilizing a suitable Gauss quadrature in two dimensions. One of the effects of the sequence of transformations is that they result in a greater concentration of the Gauss integration points near the singular node. The concentration of integration sampling points is clearly seen in Fig. B2 which shows the location of the integration points on a square element with and without the above coordinate transformation utilizing 2x2 and 4x4 Gauss integration.



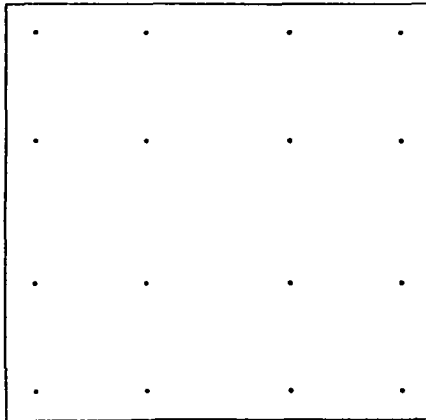
2x2 standard



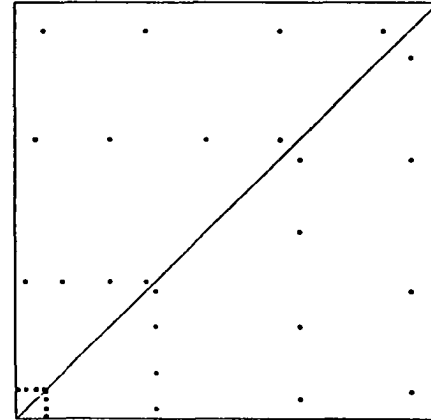
2x2 singular node at lower left corner



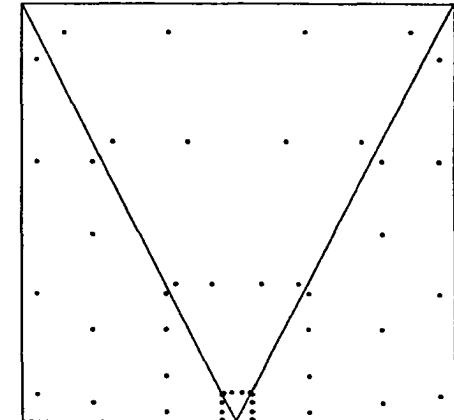
2x2 singular node on bottom



4x4 standard



4x4 singular node at lower left corner



4x4 singular node on bottom

Fig. B.2 Distribution of integration points for 2x2 and 4x4 Gauss quadrature.

APPENDIX C

GEOMETRICAL SYMMETRY

Typical floating offshore structures such as TLPs possess symmetry to some degree. Typical structures may have single, double or triple symmetry (see Fig. C.1). In the solution to the first-order potentials, the coefficient matrix containing the different integrals of the Green's function over the discretized equilibrium surface of the structure is therefore seen to have similar sets of submatrices. This is important in that it significantly reduces the effort required to obtain the first-order solution. Since the computational effort required to solve a linear system of equations increases greatly with the number of equations, a reduction in the size of the systems to be solved is of great advantage.

The matrix equation (3.20) may be written as

$$\begin{bmatrix} C_{11} & C_{12} & \cdot & \cdot & \cdot & C_{1n_s} \\ C_{21} & & & & & C_{2n_s} \\ \cdot & \cdot & & & & \cdot \\ \cdot & \cdot & & & & \cdot \\ \cdot & \cdot & & & & \cdot \\ C_{n_s 1} & C_{n_s 2} & \cdot & \cdot & \cdot & C_{n_s n_s} \end{bmatrix} \begin{Bmatrix} S_1 \\ S_2 \\ \cdot \\ \cdot \\ \cdot \\ S_{n_s} \end{Bmatrix} = \begin{Bmatrix} R_1 \\ R_2 \\ \cdot \\ \cdot \\ \cdot \\ R_{n_s} \end{Bmatrix}, \quad (C.1)$$

where n_s is the number of similar geometrical sections needed to define the entire structure (i.e., $n_s = 2, 4$ or 8).

Recognizing that due to the geometrical symmetry of the structure, all submatrices in the coefficient matrix may be related to the submatrices in the first column (or row), the above system of $n_s \times n_s$ matrix equations may be modified accordingly to give

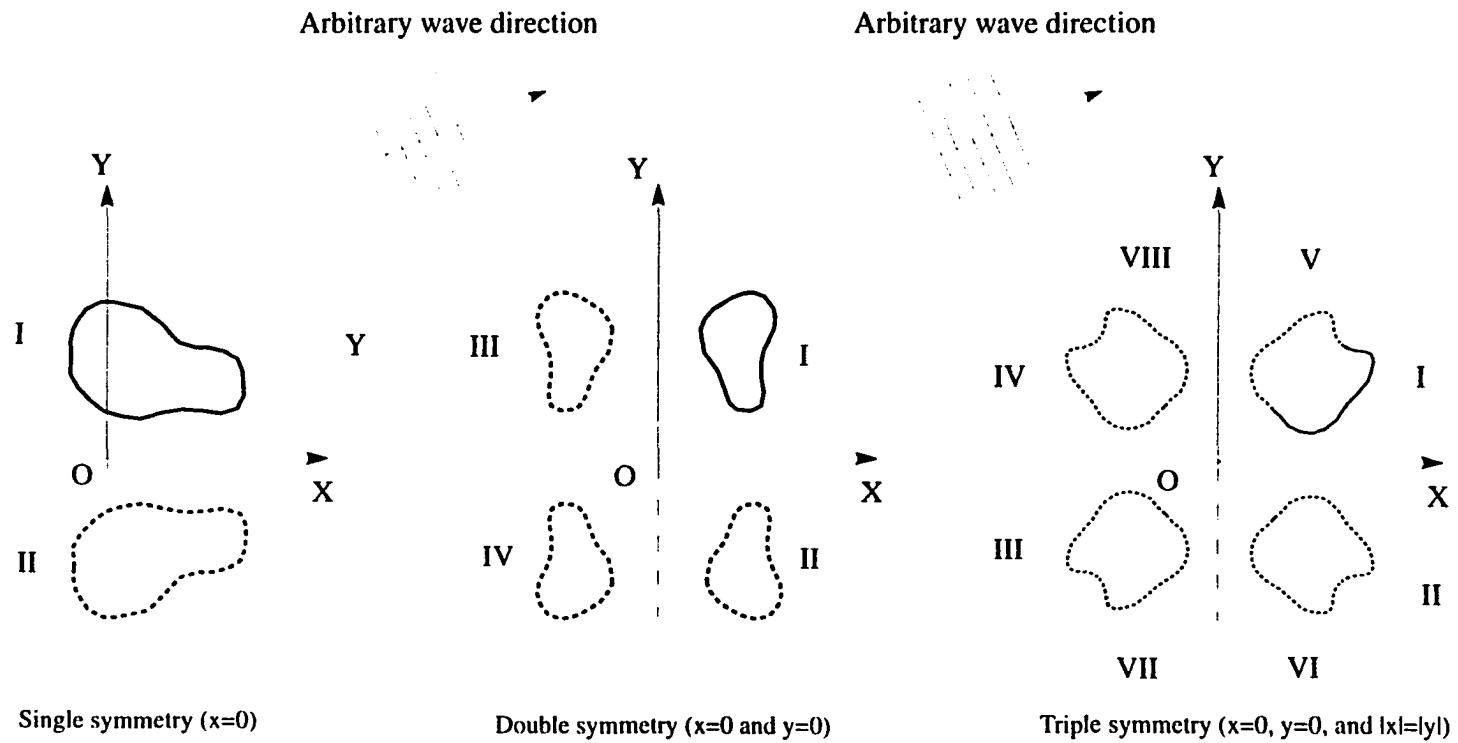


Fig. C.1 Planes of symmetry.

$$([T][C][T]^{-1}) ([T]\{S\}) = ([T]\{R\}) \quad (C.2a)$$

or

$$[\bar{C}]\{\bar{S}\} = \{\bar{R}\}, \quad (C.2b)$$

where the transformation matrix, $[T]$ consists of a set of null and identity matrices so arranged as to assure the property that $[T]^{-1} = \frac{1}{n_s} [T]$. (i.e. $[T][T] = \frac{1}{n_s} [I]$).

Because of this relationship, the solution vector, $\{S\}$, may be obtained from the vector $\{\bar{S}\}$ by

$$\{S\} = \frac{1}{n_s} [T] \{\bar{S}\}. \quad (C.3)$$

Due to the properties of the coefficient matrix (i.e, the symmetry of the structure) and the orthogonality of the transformation matrix, the original system of equations is decoupled (completely or partially), thus requiring solutions to smaller systems of equations. The derivation leading to the decoupling of the system of equations for structures possessing single, double, or triple geometrical symmetry is presented below. The savings due to the geometrical symmetry originate from two sources. Firstly, the assembly of the coefficient matrix is reduced by a factor of n_s . Secondly, the task of computing the solution to the original system of equations is replaced by that of solving several smaller systems of equations, resulting in a considerable saving of computational effort. The exact proportion of time savings relative to the original problem depends on the computational effort required to assemble the coefficient matrix relative to that required to solve the linear system of equations.

C.1 Single Symmetry (Two Equal Sections)

For the case of single symmetry about $y = 0$, only one half of the structure is discretized utilizing n_2 nodes. The resulting coefficient matrix is thus $2n_2 \times 2n_2$ in size. The coefficient and transformation matrices may be written as

$$[C] = \begin{bmatrix} C_{11} & C_{12} \\ C_{21} & C_{22} \end{bmatrix} = \begin{bmatrix} C_{11} & C_{12} \\ C_{12} & C_{11} \end{bmatrix}, \quad (\text{C.4a})$$

$$[T] = \begin{bmatrix} I_{n_2} & I_{n_2} \\ I_{n_2} & -I_{n_2} \end{bmatrix}, \quad (\text{C.4b})$$

$$\{S\} = \begin{Bmatrix} S_1 \\ S_2 \end{Bmatrix}, \quad (\text{C.4c})$$

$$\{R\} = \begin{Bmatrix} R_1 \\ R_2 \end{Bmatrix}, \quad (\text{C.4d})$$

where $[I_{n_2}]$ is an $n_2 \times n_2$ identity matrix.

Carrying out the symbolic multiplications, Eqn. (C.2b) takes the following form,

$$\begin{bmatrix} \bar{C}_{11} & 0_{n_2} \\ 0_{n_2} & \bar{C}_{22} \end{bmatrix} \begin{Bmatrix} \bar{S}_1 \\ \bar{S}_2 \end{Bmatrix} = \begin{Bmatrix} \bar{R}_1 \\ \bar{R}_2 \end{Bmatrix}, \quad (\text{C.5})$$

where

$$[\bar{C}_{11}] = [C_{11}] + [C_{12}], \quad [\bar{C}_{22}] = [C_{11}] - [C_{12}],$$

$$\begin{Bmatrix} \bar{S}_1 \\ \bar{S}_2 \end{Bmatrix} = \begin{Bmatrix} S_1 + S_2 \\ S_1 - S_2 \end{Bmatrix}, \quad \begin{Bmatrix} \bar{R}_1 \\ \bar{R}_2 \end{Bmatrix} = \begin{Bmatrix} R_1 + R_2 \\ R_1 - R_2 \end{Bmatrix},$$

and $[0_{n_2}]$ is an $n_2 \times n_2$ null matrix.

The $2n_2 \times 2n_2$ matrix equation (C.5) is now decomposed into two independent $n_2 \times n_2$ systems which may be solved directly for $\{\bar{S}\}$. This vector is, in turn, combined with the transformation matrix to obtain the solution for the original system, namely,

$$\begin{Bmatrix} S_1 \\ S_2 \end{Bmatrix} = \frac{1}{2} \begin{Bmatrix} \bar{S}_1 + \bar{S}_2 \\ \bar{S}_1 - \bar{S}_2 \end{Bmatrix}. \quad (C.6)$$

C.2 Double Symmetry (Four Equal Sections)

For the case of double symmetry, about $y = 0$ and about $x = 0$, only one quarter of the structure is discretized utilizing n_4 nodes. The resulting coefficient matrix is thus $4n_4 \times 4n_4$ in size. The coefficient and transformation matrices may be written as

$$[C] = \begin{bmatrix} C_{11} & C_{12} & C_{13} & C_{14} \\ C_{21} & C_{22} & C_{23} & C_{24} \\ C_{31} & C_{32} & C_{33} & C_{34} \\ C_{41} & C_{42} & C_{43} & C_{44} \end{bmatrix} = \begin{bmatrix} C_{11} & C_{12} & C_{13} & C_{14} \\ C_{12} & C_{11} & C_{14} & C_{13} \\ C_{13} & C_{14} & C_{11} & C_{12} \\ C_{14} & C_{13} & C_{12} & C_{11} \end{bmatrix}, \quad (C.7a)$$

$$[T] = \begin{bmatrix} I_{n_4} & I_{n_4} & I_{n_4} & I_{n_4} \\ I_{n_4} & I_{n_4} & -I_{n_4} & -I_{n_4} \\ I_{n_4} & -I_{n_4} & -I_{n_4} & I_{n_4} \\ I_{n_4} & -I_{n_4} & I_{n_4} & -I_{n_4} \end{bmatrix}, \quad (C.7b)$$

$$\{ \mathbf{S} \} = \begin{Bmatrix} \mathbf{S}_1 \\ \mathbf{S}_2 \\ \mathbf{S}_3 \\ \mathbf{S}_4 \end{Bmatrix}, \quad (\text{C.7c})$$

$$\{ \mathbf{R} \} = \begin{Bmatrix} \mathbf{R}_1 \\ \mathbf{R}_2 \\ \mathbf{R}_3 \\ \mathbf{R}_4 \end{Bmatrix}, \quad (\text{C.7d})$$

where $[\mathbf{I}_{n_4}]$ is an $n_4 \times n_4$ identity matrix.

Carrying out the symbolic multiplications, Eqn. (C.2b) takes the following form,

$$\begin{bmatrix} \bar{\mathbf{C}}_{11} & \mathbf{0}_{n_4} & \mathbf{0}_{n_4} & \mathbf{0}_{n_4} \\ \mathbf{0}_{n_4} & \bar{\mathbf{C}}_{22} & \mathbf{0}_{n_4} & \mathbf{0}_{n_4} \\ \mathbf{0}_{n_4} & \mathbf{0}_{n_4} & \bar{\mathbf{C}}_{33} & \mathbf{0}_{n_4} \\ \mathbf{0}_{n_4} & \mathbf{0}_{n_4} & \mathbf{0}_{n_4} & \bar{\mathbf{C}}_{44} \end{bmatrix} \begin{Bmatrix} \bar{\mathbf{S}}_1 \\ \bar{\mathbf{S}}_2 \\ \bar{\mathbf{S}}_3 \\ \bar{\mathbf{S}}_4 \end{Bmatrix} = \begin{Bmatrix} \bar{\mathbf{R}}_1 \\ \bar{\mathbf{R}}_2 \\ \bar{\mathbf{R}}_3 \\ \bar{\mathbf{R}}_4 \end{Bmatrix}, \quad (\text{C.8})$$

where

$$[\bar{\mathbf{C}}_{11}] = [\mathbf{C}_{11}] + [\mathbf{C}_{12}] + [\mathbf{C}_{13}] + [\mathbf{C}_{14}],$$

$$[\bar{\mathbf{C}}_{22}] = [\mathbf{C}_{11}] + [\mathbf{C}_{12}] - [\mathbf{C}_{13}] - [\mathbf{C}_{14}],$$

$$[\bar{\mathbf{C}}_{33}] = [\mathbf{C}_{11}] - [\mathbf{C}_{12}] - [\mathbf{C}_{13}] + [\mathbf{C}_{14}],$$

$$[\bar{\mathbf{C}}_{44}] = [\mathbf{C}_{11}] - [\mathbf{C}_{12}] + [\mathbf{C}_{13}] - [\mathbf{C}_{14}],$$

$$\begin{Bmatrix} \bar{\mathbf{S}}_1 \\ \bar{\mathbf{S}}_2 \\ \bar{\mathbf{S}}_3 \\ \bar{\mathbf{S}}_4 \end{Bmatrix} = \begin{Bmatrix} \mathbf{S}_1 + \mathbf{S}_2 + \mathbf{S}_3 + \mathbf{S}_4 \\ \mathbf{S}_1 + \mathbf{S}_2 - \mathbf{S}_3 - \mathbf{S}_4 \\ \mathbf{S}_1 - \mathbf{S}_2 - \mathbf{S}_3 + \mathbf{S}_4 \\ \mathbf{S}_1 - \mathbf{S}_2 + \mathbf{S}_3 - \mathbf{S}_4 \end{Bmatrix}, \quad \begin{Bmatrix} \bar{\mathbf{R}}_1 \\ \bar{\mathbf{R}}_2 \\ \bar{\mathbf{R}}_3 \\ \bar{\mathbf{R}}_4 \end{Bmatrix} = \begin{Bmatrix} \mathbf{R}_1 + \mathbf{R}_2 + \mathbf{R}_3 + \mathbf{R}_4 \\ \mathbf{R}_1 + \mathbf{R}_2 - \mathbf{R}_3 - \mathbf{R}_4 \\ \mathbf{R}_1 - \mathbf{R}_2 - \mathbf{R}_3 + \mathbf{R}_4 \\ \mathbf{R}_1 - \mathbf{R}_2 + \mathbf{R}_3 - \mathbf{R}_4 \end{Bmatrix},$$

and $[\mathbf{0}_{n_4}]$ is an $n_4 \times n_4$ null matrix.

The $4n_4 \times 4n_4$ matrix equation (C.8) is now decomposed into four independent $n_4 \times n_4$ systems which may be solved directly for $\{\bar{S}\}$. This vector is, in turn, combined with the transformation matrix to obtain the solution for the original system, namely,

$$\begin{Bmatrix} S_1 \\ S_2 \\ S_3 \\ S_4 \end{Bmatrix} = \frac{1}{4} \begin{Bmatrix} \bar{S}_1 + \bar{S}_2 + \bar{S}_3 + \bar{S}_4 \\ \bar{S}_1 + \bar{S}_2 - \bar{S}_3 - \bar{S}_4 \\ \bar{S}_1 - \bar{S}_2 - \bar{S}_3 + \bar{S}_4 \\ \bar{S}_1 - \bar{S}_2 + \bar{S}_3 - \bar{S}_4 \end{Bmatrix}. \quad (C.9)$$

C.3 Triple Symmetry (Eight Equal Sections)

For the case of triple symmetry, about $y = 0$, about $x = 0$, and about $|x| = |y|$, only one eighth of the structure is discretized utilizing n_8 nodes. The resulting coefficient matrix is thus $8n_8 \times 8n_8$ in size. The coefficient and transformation matrices may be written as

$$[C] = \begin{bmatrix} C_{11} & C_{12} & C_{13} & C_{14} & C_{15} & C_{16} & C_{17} & C_{18} \\ C_{21} & C_{22} & C_{23} & C_{24} & C_{25} & C_{26} & C_{27} & C_{28} \\ C_{31} & C_{32} & C_{33} & C_{34} & C_{35} & C_{36} & C_{37} & C_{38} \\ C_{41} & C_{42} & C_{43} & C_{44} & C_{45} & C_{46} & C_{47} & C_{48} \\ C_{51} & C_{52} & C_{53} & C_{54} & C_{55} & C_{56} & C_{57} & C_{58} \\ C_{61} & C_{62} & C_{63} & C_{64} & C_{65} & C_{66} & C_{67} & C_{68} \\ C_{71} & C_{72} & C_{73} & C_{74} & C_{75} & C_{76} & C_{77} & C_{78} \\ C_{81} & C_{82} & C_{83} & C_{84} & C_{85} & C_{86} & C_{87} & C_{88} \end{bmatrix} = \begin{bmatrix} C_{11} & C_{12} & C_{13} & C_{14} & C_{15} & C_{16} & C_{17} & C_{18} \\ C_{12} & C_{11} & C_{14} & C_{13} & C_{16} & C_{15} & C_{18} & C_{17} \\ C_{13} & C_{14} & C_{11} & C_{12} & C_{17} & C_{18} & C_{15} & C_{16} \\ C_{14} & C_{13} & C_{12} & C_{11} & C_{18} & C_{17} & C_{16} & C_{15} \\ C_{15} & C_{18} & C_{17} & C_{16} & C_{11} & C_{14} & C_{13} & C_{12} \\ C_{18} & C_{15} & C_{16} & C_{17} & C_{14} & C_{11} & C_{12} & C_{13} \\ C_{17} & C_{16} & C_{15} & C_{18} & C_{13} & C_{12} & C_{11} & C_{14} \\ C_{16} & C_{17} & C_{18} & C_{15} & C_{12} & C_{13} & C_{14} & C_{11} \end{bmatrix}, \quad (C.10a)$$

$$[T] = \begin{bmatrix} I_{n_8} & I_{n_8} & I_{n_8} & I_{n_8} & I_{n_8} & I_{n_8} & I_{n_8} & I_{n_8} \\ I_{n_8} & -I_{n_8} & I_{n_8} & -I_{n_8} & I_{n_8} & -I_{n_8} & I_{n_8} & -I_{n_8} \\ I_{n_8} & I_{n_8} & -I_{n_8} & -I_{n_8} & I_{n_8} & I_{n_8} & -I_{n_8} & -I_{n_8} \\ I_{n_8} & -I_{n_8} & -I_{n_8} & I_{n_8} & I_{n_8} & -I_{n_8} & -I_{n_8} & I_{n_8} \\ I_{n_8} & I_{n_8} & I_{n_8} & I_{n_8} & -I_{n_8} & -I_{n_8} & -I_{n_8} & -I_{n_8} \\ I_{n_8} & -I_{n_8} & I_{n_8} & -I_{n_8} & -I_{n_8} & I_{n_8} & -I_{n_8} & I_{n_8} \\ I_{n_8} & I_{n_8} & -I_{n_8} & -I_{n_8} & -I_{n_8} & -I_{n_8} & I_{n_8} & I_{n_8} \\ I_{n_8} & -I_{n_8} & -I_{n_8} & I_{n_8} & -I_{n_8} & I_{n_8} & I_{n_8} & -I_{n_8} \end{bmatrix} \quad (C.10b)$$

$$\{ S \} = \begin{Bmatrix} S_1 \\ S_2 \\ S_3 \\ S_4 \\ S_5 \\ S_6 \\ S_7 \\ S_8 \end{Bmatrix}, \quad (C.10c)$$

$$\{ R \} = \begin{Bmatrix} R_1 \\ R_2 \\ R_3 \\ R_4 \\ R_5 \\ R_6 \\ R_7 \\ R_8 \end{Bmatrix}, \quad (C.10d)$$

where I_{n_8} is an $n_8 \times n_8$ identity matrix.

In this case, carrying out the symbolic multiplications, does not result in 8 independent systems of equations, as was the case for single and double symmetry. Instead 4 ($n_8 \times n_8$) and 2 ($2n_8 \times 2n_8$) systems are identified. These systems are given below:

$$[\bar{C}_{11}] \{\bar{S}_1\} = \{\bar{R}_1\}, \quad (C.11a)$$

$$[\bar{C}_{22}] \{\bar{S}_2\} = \{\bar{R}_2\}, \quad (C.11b)$$

$$[\bar{C}_{55}] \{\bar{S}_5\} = \{\bar{R}_5\}, \quad (C.11c)$$

$$[\bar{C}_{66}] \{\bar{S}_6\} = \{\bar{R}_6\}, \quad (C.11d)$$

$$\begin{bmatrix} \bar{C}_{33} & \bar{C}_{73} \\ \bar{C}_{37} & \bar{C}_{77} \end{bmatrix} \begin{Bmatrix} \bar{S}_3 \\ \bar{S}_7 \end{Bmatrix} = \begin{Bmatrix} \bar{R}_3 \\ \bar{R}_7 \end{Bmatrix}, \quad (C.11e)$$

$$\begin{bmatrix} \bar{C}_{44} & \bar{C}_{84} \\ \bar{C}_{48} & \bar{C}_{88} \end{bmatrix} \begin{Bmatrix} \bar{S}_4 \\ \bar{S}_8 \end{Bmatrix} = \begin{Bmatrix} \bar{R}_4 \\ \bar{R}_8 \end{Bmatrix}, \quad (C.11f)$$

where

$$[\bar{C}_{11}] = [C_{11}] + [C_{12}] + [C_{13}] + [C_{14}] + [C_{15}] + [C_{16}] + [C_{17}] + [C_{18}],$$

$$[\bar{C}_{22}] = [C_{11}] - [C_{12}] + [C_{13}] - [C_{14}] + [C_{15}] - [C_{16}] + [C_{17}] - [C_{18}],$$

$$[\bar{C}_{55}] = [C_{11}] + [C_{12}] + [C_{13}] + [C_{14}] - [C_{15}] - [C_{16}] - [C_{17}] - [C_{18}],$$

$$[\bar{C}_{66}] = [C_{11}] - [C_{12}] + [C_{13}] - [C_{14}] - [C_{15}] + [C_{16}] - [C_{17}] + [C_{18}],$$

$$[\bar{C}_{33}] = [C_{11}] - [C_{13}] + [C_{15}] - [C_{17}],$$

$$[\bar{C}_{37}] = [C_{12}] - [C_{14}] - [C_{16}] + [C_{18}],$$

$$[\bar{C}_{44}] = [C_{11}] - [C_{13}] + [C_{15}] - [C_{17}],$$

$$[\bar{C}_{48}] = -[C_{12}] + [C_{14}] + [C_{16}] - [C_{18}],$$

$$[\bar{C}_{73}] = [C_{12}] - [C_{14}] + [C_{16}] - [C_{18}],$$

$$[\bar{C}_{77}] = [C_{11}] - [C_{13}] - [C_{15}] + [C_{17}],$$

$$[\bar{C}_{84}] = -[C_{12}] + [C_{14}] - [C_{16}] + [C_{18}],$$

$$[\bar{C}_{88}] = [C_{11}] - [C_{13}] - [C_{15}] + [C_{17}];$$

$$\{\bar{S}_1\} = \{S_1\} + \{S_2\} + \{S_3\} + \{S_4\} + \{S_5\} + \{S_6\} + \{S_7\} + \{S_8\},$$

$$\{\bar{S}_2\} = \{S_1\} - \{S_2\} + \{S_3\} - \{S_4\} + \{S_5\} - \{S_6\} + \{S_7\} - \{S_8\},$$

$$\{\bar{S}_3\} = \{S_1\} + \{S_2\} - \{S_3\} - \{S_4\} + \{S_5\} + \{S_6\} - \{S_7\} - \{S_8\},$$

$$\{\bar{S}_4\} = \{S_1\} - \{S_2\} - \{S_3\} + \{S_4\} + \{S_5\} - \{S_6\} - \{S_7\} + \{S_8\},$$

$$\begin{aligned}
\{ \bar{S}_5 \} &= \{ S_1 \} + \{ S_2 \} + \{ S_3 \} + \{ S_4 \} - \{ S_5 \} - \{ S_6 \} - \{ S_7 \} - \{ S_8 \}, \\
\{ \bar{S}_6 \} &= \{ S_1 \} - \{ S_2 \} + \{ S_3 \} - \{ S_4 \} - \{ S_5 \} + \{ S_6 \} - \{ S_7 \} + \{ S_8 \}, \\
\{ \bar{S}_7 \} &= \{ S_1 \} + \{ S_2 \} - \{ S_3 \} - \{ S_4 \} - \{ S_5 \} - \{ S_6 \} + \{ S_7 \} + \{ S_8 \}, \\
\{ \bar{S}_8 \} &= \{ S_1 \} - \{ S_2 \} - \{ S_3 \} + \{ S_4 \} - \{ S_5 \} + \{ S_6 \} + \{ S_7 \} - \{ S_8 \};
\end{aligned}$$

and

$$\begin{aligned}
\{ \bar{R}_1 \} &= \{ R_1 \} + \{ R_2 \} + \{ R_3 \} + \{ R_4 \} + \{ R_5 \} + \{ R_6 \} + \{ R_7 \} + \{ R_8 \}, \\
\{ \bar{R}_2 \} &= \{ R_1 \} - \{ R_2 \} + \{ R_3 \} - \{ R_4 \} + \{ R_5 \} - \{ R_6 \} + \{ R_7 \} - \{ R_8 \}, \\
\{ \bar{R}_3 \} &= \{ R_1 \} + \{ R_2 \} - \{ R_3 \} - \{ R_4 \} + \{ R_5 \} + \{ R_6 \} - \{ R_7 \} - \{ R_8 \}, \\
\{ \bar{R}_4 \} &= \{ R_1 \} - \{ R_2 \} - \{ R_3 \} + \{ R_4 \} + \{ R_5 \} - \{ R_6 \} - \{ R_7 \} + \{ R_8 \}, \\
\{ \bar{R}_5 \} &= \{ R_1 \} + \{ R_2 \} + \{ R_3 \} + \{ R_4 \} - \{ R_5 \} - \{ R_6 \} - \{ R_7 \} - \{ R_8 \}, \\
\{ \bar{R}_6 \} &= \{ R_1 \} - \{ R_2 \} + \{ R_3 \} - \{ R_4 \} - \{ R_5 \} + \{ R_6 \} - \{ R_7 \} + \{ R_8 \}, \\
\{ \bar{R}_7 \} &= \{ R_1 \} + \{ R_2 \} - \{ R_3 \} - \{ R_4 \} - \{ R_5 \} - \{ R_6 \} + \{ R_7 \} + \{ R_8 \}, \\
\{ \bar{R}_8 \} &= \{ R_1 \} - \{ R_2 \} - \{ R_3 \} + \{ R_4 \} - \{ R_5 \} + \{ R_6 \} + \{ R_7 \} - \{ R_8 \}.
\end{aligned}$$

The six sets of equations, (C.11a) - (C.11f), are now solved for $\{ \bar{S} \}$. This vector is, in turn, used to determine the solution to the original system of equations, namely,

$$\begin{aligned}
\{ S_1 \} &= \frac{1}{8} (\{ \bar{S}_1 \} + \{ \bar{S}_2 \} + \{ \bar{S}_3 \} + \{ \bar{S}_4 \} + \{ \bar{S}_5 \} + \{ \bar{S}_6 \} + \{ \bar{S}_7 \} + \{ \bar{S}_8 \}), \\
\{ S_2 \} &= \frac{1}{8} (\{ \bar{S}_1 \} - \{ \bar{S}_2 \} + \{ \bar{S}_3 \} - \{ \bar{S}_4 \} + \{ \bar{S}_5 \} - \{ \bar{S}_6 \} + \{ \bar{S}_7 \} - \{ \bar{S}_8 \}), \\
\{ S_3 \} &= \frac{1}{8} (\{ \bar{S}_1 \} + \{ \bar{S}_2 \} - \{ \bar{S}_3 \} - \{ \bar{S}_4 \} + \{ \bar{S}_5 \} + \{ \bar{S}_6 \} - \{ \bar{S}_7 \} - \{ \bar{S}_8 \}), \\
\{ S_4 \} &= \frac{1}{8} (\{ \bar{S}_1 \} - \{ \bar{S}_2 \} - \{ \bar{S}_3 \} + \{ \bar{S}_4 \} + \{ \bar{S}_5 \} - \{ \bar{S}_6 \} - \{ \bar{S}_7 \} + \{ \bar{S}_8 \}), \\
\{ S_5 \} &= \frac{1}{8} (\{ \bar{S}_1 \} + \{ \bar{S}_2 \} + \{ \bar{S}_3 \} + \{ \bar{S}_4 \} - \{ \bar{S}_5 \} - \{ \bar{S}_6 \} - \{ \bar{S}_7 \} - \{ \bar{S}_8 \}), \\
\{ S_6 \} &= \frac{1}{8} (\{ \bar{S}_1 \} - \{ \bar{S}_2 \} + \{ \bar{S}_3 \} - \{ \bar{S}_4 \} - \{ \bar{S}_5 \} + \{ \bar{S}_6 \} - \{ \bar{S}_7 \} + \{ \bar{S}_8 \}), \\
\{ S_7 \} &= \frac{1}{8} (\{ \bar{S}_1 \} + \{ \bar{S}_2 \} - \{ \bar{S}_3 \} - \{ \bar{S}_4 \} - \{ \bar{S}_5 \} - \{ \bar{S}_6 \} + \{ \bar{S}_7 \} + \{ \bar{S}_8 \}), \\
\{ S_8 \} &= \frac{1}{8} (\{ \bar{S}_1 \} - \{ \bar{S}_2 \} - \{ \bar{S}_3 \} + \{ \bar{S}_4 \} - \{ \bar{S}_5 \} + \{ \bar{S}_6 \} + \{ \bar{S}_7 \} - \{ \bar{S}_8 \}).
\end{aligned}$$

APPENDIX D

STIFFNESS MATRIX FOR TETHERED STRUCTURE

The stiffness matrix \mathbf{K} defined by $\underline{\mathbf{T}} = -\mathbf{K} \underline{\mathbf{x}}$ in Eq. (3.56) is given in this appendix.

Consider a single (representative) cable n anchored at a point $\mathbf{r}_n^- = (x_n^-, y_n^-, z_n^-)$ and to the structure at a point whose equilibrium position is given by $\mathbf{r}_n^+ = (x_n^+, y_n^+, z_n^+)$. Let the equilibrium tension (pretension) in the cable be given by T_0 , its equilibrium length be L , and its cross-sectional area and modulus of elasticity be given by A_c and E_c , respectively. The six-component displacement $\underline{\mathbf{x}}$ of the structure results in a displacement $\Delta \mathbf{r}_n$ at \mathbf{r}_n^+ which is given by

$$\Delta \mathbf{r}_n = (x_1, x_2, x_3) + (\mathbf{r}_G - \mathbf{r}_n^+) \times (x_4, x_5, x_6), \quad (\text{D.1})$$

where \mathbf{r}_G represents the center of gravity of the structure.

This results in a force $\Delta \mathbf{T}^n$ on the structure whose components to the first-order in small quantities are given by

$$\Delta T_i^n = - \sum_{j=1}^6 \left\{ \frac{T_0}{L} P_{ij}^n x_j + \frac{(T_0 - A_c E_c)}{L^3} [\mathbf{r}_n^+ - \mathbf{r}_n^-]_i Q_j^n x_j \right\}, \quad (\text{D.2})$$

$i = 1, 2, 3$ in which the 3×6 matrix \mathbf{P}^n is defined by

$$\mathbf{P}^n = \left\{ \begin{array}{cccccc} 1 & 0 & 0 & 0 & z_n^+ - z_G & -(y_n^+ - y_G) \\ 0 & 1 & 0 & -(z_n^+ - z_G) & 0 & x_n^+ - x_G \\ 0 & 0 & 1 & y_n^+ - y_G & -(x_n^+ - x_G) & 0 \end{array} \right\}, \quad (\text{D.3})$$

and the vector \underline{Q}^n is defined by

$$[\underline{Q}^n]^T = \left\{ \begin{array}{l} -(x_n^+ - x_n^-) \\ -(y_n^+ - y_n^-) \\ -(z_n^+ - z_n^-) \\ -(z_n^+ - z_G)(y_n^+ - y_n^-) + (y_n^+ - y_G)(z_n^+ - z_n^-) \\ -(x_n^+ - x_G)(z_n^+ - z_n^-) + (z_n^+ - z_G)(x_n^+ - x_n^-) \\ -(y_n^+ - y_G)(x_n^+ - x_n^-) + (x_n^+ - x_G)(y_n^+ - y_n^-) \end{array} \right\}. \quad (D.4)$$

The moments caused by the cable tension forces may be written as

$$[(x_4, x_5, x_6) \times (\underline{r}_n^+ - \underline{r}_G)] \times \frac{T_0}{L} (\underline{r}_n^- - \underline{r}_n^+) + (\underline{r}_n^+ - \underline{r}_G) \times \Delta \underline{T}^n. \quad (D.5)$$

This expression may be evaluated explicitly to yield the following moment components, for $i = 1, 2, 3$,

$$- \sum_{j=1}^6 \left\{ \frac{T_0}{L} (R_{ij}^n + S_{ij}^n) x_j + \frac{(T_0 - A_c E_c)}{L^3} [(\underline{r}_n^+ - \underline{r}_G) \times (\underline{r}_n^+ - \underline{r}_n^-)]_i Q_j^n x_j \right\}, \quad (D.6)$$

in which the 3×6 matrix \underline{R}^n is defined by

$$\underline{R}^n = \begin{bmatrix} 0 & 0 & 0 & (y_n^- - y_G)(y_n^- - y_n^+) + (z_n^- - z_G)(z_n^- - z_n^+) \\ 0 & 0 & 0 & -(y_n^- - y_G)(x_n^- - x_n^+) \\ 0 & 0 & 0 & -(z_n^- - z_G)(x_n^- - x_n^+) \end{bmatrix}$$

$$\begin{array}{cc}
- (x_n^- - x_G)(y_n^- - y_n^+) & - (x_n^- - x_G)(z_n^- - z_n^+) \\
(x_n^- - x_G)(x_n^- - x_n^+) + (z_n^- - z_G)(z_n^- - z_n^+) & - (y_n^- - y_G)(z_n^- - z_n^+) \\
- (z_n^- - z_G)(y_n^- - y_n^+) & (x_n^- - x_G)(x_n^- - x_n^+) + (y_n^- - y_G)(y_n^- - y_n^+)
\end{array} \Bigg] ,$$

(D.7)

and the elements of \underline{S}^n are given by

$$S_{1j}^n = (y_n^+ - y_G) P_{3j}^n - (z_n^+ - z_G) P_{2j}^n, \quad (D.8a)$$

$$S_{2j}^n = (z_n^+ - z_G) P_{1j}^n - (x_n^+ - x_G) P_{3j}^n, \quad (D.8b)$$

$$S_{3j}^n = (x_n^+ - x_G) P_{2j}^n - (y_n^+ - y_G) P_{1j}^n. \quad (D.8c)$$

The above cable forces ΔT_i^n in Eq. (D.2) may be identified with the terms of the cable stiffness matrix associated with cable n as

$$\Delta T_i^n = - \sum_{j=1}^6 K_{ij}^n x_j, \quad (D.9)$$

to yield

$$K_{ij}^n = \frac{T_o}{L} P_{ij}^n + \frac{(T_o - A_c E_c)}{L^3} [L_n^+ - L_n^-]_i Q_j^n, \quad (D.10)$$

for $i = 1, 2, 3$ and $j = 1, 2, 3, 4, 5, 6$. The remaining elements of the stiffness matrix \underline{K} may be obtained from the corresponding moments which are given by Eq. (D.6). Thus, we have

$$K_{ij}^n = \frac{T_o}{L} (R_{qj}^n + S_{qj}^n) + \frac{(T_o - A_c E_c)}{L^3} [(L_n^+ - L_n^-) \times (L_n^+ - L_n^-)]_q Q_j^n, \quad (D.11)$$

for $i = 4, 5, 6$; $j = 1, 2, 3, 4, 5, 6$; and $q = i - 3$. For a structure possessing an array of identical cables or tethers, the combined stiffness matrix may be obtained by linearly adding the stiffness matrices from the individual cables, that is,

$$\underline{\mathbf{K}} = \sum_{n=1}^{N_c} \underline{\mathbf{K}}^n, \quad (\text{D.12})$$

where N_c is the number of cables in the system.

APPENDIX E

FRESNEL INTEGRALS

The Fresnel cosine and sine functions $C(x)$ and $S(x)$, are defined by Abramowitz and Stegun (1972) as

$$C(x) = \int_0^x \cos\left(\frac{\pi t^2}{2}\right) dt, \quad (\text{E.1a})$$

and

$$S(x) = \int_0^x \sin\left(\frac{\pi t^2}{2}\right) dt. \quad (\text{E.1b})$$

Combining Eqs. (C.1a) and (C.1b) into a complex form gives

$$C(x) + i S(x) = \int_0^x \left(\cos\left(\frac{\pi t^2}{2}\right) + i \sin\left(\frac{\pi t^2}{2}\right) \right) dt = \int_0^x e^{i\frac{\pi t^2}{2}} dt. \quad (\text{E.2})$$

Substituting $T = \sqrt{\frac{\pi}{2p}} t$ in Eq. (E.2) and expressing the integral in terms of T leads to

$$\int_0^x e^{i\frac{\pi t^2}{2}} dt = \sqrt{\frac{2p}{\pi}} \int_0^{\beta x} e^{ipT^2} dT, \quad (\text{E.3})$$

where

$$\beta = \sqrt{\frac{\pi}{2p}},$$

which leads to

$$\sqrt{\frac{2p}{\pi}} \int_0^{\beta x} e^{ipT^2} dT = C(x) + i S(x), \quad (\text{E.4a})$$

or

$$\int_0^{\beta x} e^{ipT^2} dT = \sqrt{\frac{\pi}{2p}} (C(x) + i S(x)). \quad (\text{E.4b})$$

Similarly, we have that

$$\int_0^{\beta x_1} e^{ipT^2} dT = \sqrt{\frac{\pi}{2p}} (C(x_1) + i S(x_1)), \quad (\text{E.5})$$

and

$$\int_0^{\beta x_2} e^{ipT^2} dT = \sqrt{\frac{\pi}{2p}} (C(x_2) + i S(x_2)). \quad (\text{E.6})$$

Therefore, from Eqs. (E.5) and (E.6), we get

$$\int_{\beta x_1}^{\beta x_2} e^{ipT^2} dT = \sqrt{\frac{\pi}{2p}} (\{C(x_2) - C(x_1)\} + i \{S(x_2) - S(x_1)\}). \quad (\text{E.7})$$

Substituting $r = T^2$ in Eq. (E.7) and integrating yields

$$\int_{r_1}^{r_2} \frac{e^{ipr}}{\sqrt{r}} dr = \sqrt{\frac{2\pi}{p}} \left(\left\{ C\left(\sqrt{\frac{2pr_2}{\pi}}\right) - C\left(\sqrt{\frac{2pr_1}{\pi}}\right) \right\} + i \left\{ S\left(\sqrt{\frac{2pr_2}{\pi}}\right) - S\left(\sqrt{\frac{2pr_1}{\pi}}\right) \right\} \right). \quad (\text{E.8})$$

Now letting $r_1 = R$ and $r_2 = \infty$, and noting that $S(\infty) = C(\infty) = \frac{1}{2}$ gives

$$\int_R^{\infty} \frac{e^{ipr}}{\sqrt{r}} dr = \sqrt{\frac{2\pi}{p}} \left[\left\{ \frac{1}{2} - C\left(\sqrt{\frac{2pR}{\pi}}\right) \right\} + i \left\{ \frac{1}{2} - S\left(\sqrt{\frac{2pR}{\pi}}\right) \right\} \right]. \quad (\text{E.9})$$